Computational fracture modelling by an adaptive cracking particle method

WEILONG AI

Computational fracture modelling by an adaptive cracking particle method

Thesis by

Weilong Ai

Submitted as partial consideration towards

the degree of Doctor of Philosophy

Sustainable Infrastructure Research Challenge

Department of Engineering

Durham University

June 9, 2018

Computational fracture modelling by an adaptive cracking particle method

Weilong Ai

Abstract

Conventional element-based methods for crack modelling suffer from remeshing and mesh distortion, while the cracking particle method is meshless and requires only nodal data to discretise the problem domain so these issues are addressed. This method uses a set of crack segments to model crack paths, and crack discontinuities are obtained using the visibility criterion. It has simple implementation and is suitable for complex crack problems, but suffers from spurious cracking results and requires a large number of particles to maintain good accuracy. In this thesis, a modified cracking particle method has been developed for modelling fracture problems in 2D and 3D. To improve crack description quality, the orientations of crack segments are modified to record angular changes of crack paths, e.g. in 2D, bilinear segments replacing straight segments in the original method and in 3D, nonplanar triangular facets instead of planar circular segments, so continuous crack paths are obtained. An adaptivity approach is introduced to optimise the particle distribution, which is refined to capture high stress gradients around the crack tip and is coarsened when the crack propagates away to improve the efficiency. Based on the modified method, a multi-cracked particle method is proposed for problems with branched cracks or multiple cracks, where crack discontinuities at crack intersections are modelled by multi-split particles rather than complex enrichment functions. Different crack propagation criteria are discussed and a configurational-force-driven cracking particle method has been developed, where the crack propagating angle is directly given by the configuration force, and no decomposition of displacement and stress fields for mixed-mode fracture is required. The modified method has been applied to thermo-elastic crack problems, where the adaptivity approach is employed to capture the temperature gradients around the crack tip without using enrichment functions. Several numerical examples are used to validate the proposed methodology.

Declaration

The work in this thesis is based on research carried out at the Department of Engineering, Durham University, England. No part of this thesis has been submitted elsewhere for any other degree or qualification and it is all my own work unless referenced to the contrary in the text.

Acknowledgements

The research work of this thesis would not be possible without the financial support from both the China Scholarship Council and the Faculty of Science, Durham University. Their support is fully acknowledged.

Many very nice people from the Department of Engineering have helped me during my stay at Durham University. First of all, I would like to give my best thanks to my supervisor Prof. Charles Augarde. He is always positive, supportive and responsible during the supervision of my PhD. His knowledge and experience in the fields of solid mechanics and computational mechanics is invaluable. Although he usually has a busy schedule, he is patient to revise my reports and to discuss issues and new ideas in research work with me, which is vital to the completion of this thesis. I would also like to thank Dr. Will Coombs and Dr. Stefano Giani for their time on my reviews. Their comments are helpful to improve my research work. Special thanks go to Prof. Jon Trevelyan (my secondary supervisor). The meeting with him about the boundary element method broadens my research horizons.

In addition, I appreciate all my friends in Durham. We have many good conversations during lunch time on latest news and many outdoor activities like basketball, badminton and ping-pong together, by which I can get refreshed. I am also grateful to the members of the computational mechanics group. We often have group meals on Friday with many useful discussions.

Last but not least, the endless support from my family is much appreciated. Although I am thousands of miles from my parents, I can feel their love and encouragement. They always stand behind me, no matter what kind of problems I am facing. I would like to thank my wife Yuan Liu. She knows when to drag me away from research work and we have many unforgettable trips in UK and Europe.

This thesis is for all of the people mentioned above.

Publications and presentations

Parts of work in this thesis have been published, submitted, and presented:

Journals

- **Ai, W.**, Augarde, C.E. (2016). An adaptive cracking particle method for 2D crack propagation. *International Journal for Numerical Methods in Engineering*, 108(13), 1626-1648.
- **Ai, W.**, Augarde, C.E. (2018). An adaptive cracking particle method providing explicit and accurate description of 3D crack surfaces, *International Journal for Numerical Methods in Engineering*, 114(12), 1291-1309.
- **Ai, W.**, Augarde, C.E. (2018). A multi-cracked particle method for complex fracture problems, *Mathematics and Computers in Simulation*, 150, 1-24.

Conferences

- **Ai, W.**, Augarde C.E. (2017). Explicit 3D crack modelling by the cracking particle method, *ECCOMAS Young Investigators Conference 2017*, Milan, Italy.
- **Ai, W.**, Augarde, C.E. (2017). Explicit crack modelling in 3D by the cracking particle method. *UKACM 2017: Proceedings 25th UK Conference on Computational Mechanics*, Birmingham, UK, 130-134.
- **Ai, W.**, Augarde, C.E., Trevelyan J. (2016). Branched crack modelling with the cracking particle method, *ACME 24th Conference of the Association for Computational Mechanics in Engineering*, Cardiff, UK, 125-128.
- **Ai W.**, Augarde C.E. (2016). 2D crack modelling using a new cracking particle method combined with an adaptivity strategy, *ECCOMAS 2016: 7th European Congress on Computational Methods in Applied Sciences and Engineering*, Crete, Greece.

Acronyms

CPM	Cracking particle method
MM	Meshless method
FEM	Finite element method
BEM	Boundary element method
EFGM	Element-free Galerkin method
DEM	Diffuse element method
MLPG	Meshless local Petrov-Galerkin
XFEM	Extended finite element method
NMM	Numerical manifold method
IGA	Isogeometric analysis
RKPM	Reproducing kernel particle method
MLS	Moving least squares
SIF	Stress intensity factor
SPH	Smoothed particle hydrodynamics
PDE	Partial differential equation
PU	Partition of unity
RBF	Radial basis function
RBCM	Radial basis collocation method
RKCM	Reproducing kernel collocation method
CF	Configurational force

Nomenclature

Scalers

α_T	Coefficient of thermal expansion
$\bar{q}$	External thermal loading
$\bar{T}$	Temperature constraint
β	Penalty factor
δ_{ij}	Kronecker delta function
η, ξ	Local coordinates
η_g	Global error
η_i	Local error for background cell i
η_t	Target error
κ	Kolosov constant
λ_i	Lagrange multiplier component
μ	Shear modulus
ν	Poisson's ratio
ϕ, ψ	Level set functions
Φ_i	Shape function component for meshless method
ϕ_i	Shape function component for finite element method
Ψ_e^+, Ψ_e^-	Tension and compression strain energy
Ψ_j	Shape function component for enrichment
ρ	Material density
σ_{ij}^{aux}	Auxiliary Cauchy stress tensor component
σ_{ij}	Cauchy stress tensor component
σ_v	Von Mises stress
θ	Angle with respect to the crack tip
$\varepsilon_{ij}^{\text{aux}}$	Auxiliary Cauchy strain tensor component
ε_{ij}	Cauchy strain tensor component
a	Crack length
a_j^k, b_j	Enrichment iterm
b_x, b_y	Body force component
c	Domain size for integration
d	Phase field
d_s	Ratio between support size and average particle distance
E	Young's modulus
E_g	Global error
E_i	Local error
G	Strain energy release rate
G_c	Critical strain energy release rate
$H(\mathbf{x})$	Heaviside function
H_{ij}	Displacement gradient tensor component
I	Interaction integral
i, j, k	Index notation
J	J-integral
K_{eq}	Equivalent stress intensity factor
K_{III}	Mode III stress intensity factor
K_{II}	Mode II stress intensity factor

K_{I}	Mode I stress intensity factor
k_T	Thermal conductivity
l	half crack width for phase field
L_{coa}	Coarsening trigger
L_{fin}	Refinement trigger
l_r	Refinement level
N_i	Shape function component for Lagrange interpolation
n_i	Normal component to surface
q_i	Weight function for integration
r	Distance between two nodes
r_0	Radius of initial circular support
r_i	Support size for node i
S	Strain energy density factor
T	Temperature
T^h	Temperature approximation
T_0	Reference temperature
U	System potential energy
u^h	Displacement approximation
u_i	Displacement component
W	Strain energy
$w(\mathbf{x})$	Weight function
x, y	Global coordinates
x_i	Coordinate component
Δa	Crack increment

Vectors

$\bar{\mathbf{t}}$	External traction
$\bar{\mathbf{u}}$	Displacement constraint
$\boldsymbol{\lambda}$	Lagrange multiplier
$\boldsymbol{\phi}, \boldsymbol{\Phi}$	Shape function
$\boldsymbol{\sigma}$	Cauchy stress in Voigt notation
$\boldsymbol{\sigma}^p$	Projected Cauchy stress in Voigt notation
$\boldsymbol{\varepsilon}$	Cauchy strain in Voigt notation
$\boldsymbol{\varepsilon}_T$	Thermal strain in Voigt notation
$\mathbf{g}$	Configurational force
$\mathbf{n}$	Normal to surface
$\mathbf{p}(\mathbf{x})$	Basis function
$\mathbf{q}$	Heat flux
$\mathbf{u}$	Displacement
$\mathbf{x}$	Particle location

Tensors/matrices

$[\boldsymbol{\sigma}]$	Cauchy stress in matrix
$[\boldsymbol{\varepsilon}]$	Cauchy strain in matrix
$\boldsymbol{\Sigma}$	Eshelby stress
$\boldsymbol{H}$	Displacement gradient tensor
$\boldsymbol{I}$	Identity matrix
$\hat{\mathbf{K}}$	Global thermal stiffness matrix
$\mathbf{D}$	Constitutive matrix
$\mathbf{K}$	Global stiffness matrix
$\mathbf{k}$	Local stiffness matrix
$\mathbf{L}$	Differential operator

Others

Γ	Problem boundary
Γ_q	Heat flux boundary
Γ_T	Temperature boundary

Γ_t	Force boundary
Γ_u	Displacement boundary
$\mathcal{S}^+, \mathcal{S}^-$	Two sides of crack surfaces
Ω	Problem domain
V	Problem volume

Contents

List of Figures

List of Tables

Chapter 1

Introduction

1.1 Overview

Physical phenomena in nature are usually studied by either theoretical research or experimental analysis. Unlike practical experiments facing issues of high cost and enormous damage to the environment, theoretical research is more economic and environmental, where partial differential equations (PDEs) are developed to govern the behaviour of natural phenomena. However, only a few PDEs with simple geometries and boundary conditions can be solved analytically, while the majority are directly unsolvable and have to be approximated by numerical methods. Numerical calculations are carried out only with digital computers, and these methods can provide both effectiveness and general applicability, which make them suitable for engineering analysis.

The whole process of a numerical method for solving PDEs is generally comprised of four main steps [1]: mathematical model; discretisation; solution; verification and validation. The first is to build governing equations based on theoretical principles of mechanics, while the remaining three are the main topics of computational mechanics. A problem domain is discretised and reassembled to build the system equations, then boundary conditions and external loadings are imposed and a solution of the PDEs is obtained. At the last step, numerical results are verified and compared with experimental and theoretical results to validate the numerical method.

A large number of numerical methods have been developed for engineering analysis generally composed of two groups, mesh-based and meshless methods. The origin of the

first group can be traced back to 1940s when the main strategies of the finite element method were proposed and built up, and till now these kinds of methods have been applied to analysis of static linear elasticity, heat transfer, vibration, electromagnetism and fluid dynamics [1]. However, the finite element method meets issues of mesh distortion and volumetric locking when applied for large deformation problems with low-order elements. In contrast, meshless methods are developed to address these issues and to get rid of the dependence on meshes. One early attempt was made in the element-free Galerkin method [2] in 1994, where no elements are involved in the problem discretisation. Since then, a large number of meshless methods have been developed, e.g. the reproducing kernel particle method and the meshless local Petrov-Galerkin method, and reviews on these meshless methods are presented in [3–5]. In the following sections, these numerical methods are briefly summarised and introduced.

1.2 Finite element method

The finite element method (FEM) is the most popular numerical method in solid mechanics and has been built into several commercial software packages, e.g. ANSYS [6], ABAQUS [7] and LS-DYNA [8]. In the FEM, a problem domain is divided into a finite number of nonoverlapping "elements" where all vertices of the elements are termed "nodes". Displacements within an element are interpolated by the nodal values (as basis functions) at all vertices of the element and the weights of nodal values are called shape functions. For instance, the process can be carried out through Lagrange interpolation. The stiffness of each element is reassembled to a large system equation, and then numerical results are obtained by solving this equation, which are approximated solutions to the original PDEs.

The first use of the FEM can be traced back to efforts by Hrennikoff [9] and Courant [10] in the 1940s, where the method was developed to carry out structural analysis in civil engineering with triangular elements. The stiffness of a complete engineering structure was calculated in [11], which set up elementary principles of the FEM. Then this method was applied to plate [12] and shell [13] analysis. It was extended to three-dimensional problems in [14] where new element types were created including tetrahedral elements. The name "finite element" first appeared in [15], where triangular elements were used in

plane stress analysis of elastic solids. The FEM was further extended from static linear elastic problems to plasticity [16], structural dynamics [17] and biomechanics [18].

Despite the successes, the standard FEM faces challenges when addressing problems of fracture, damage, penetration and large deformation. There is usually a difference between the assembly of elements and the physical domain, especially for problems with curved geometries. Remeshing is inevitable for fracture problems during successive analysis steps [16, 19, 20], and this process is computationally expensive even with the most sophisticated meshing algorithms. The dependence on meshing has been partially addressed in the development of the boundary element method (BEM) [21], in which volume integrals are converted into boundary integral equations, and elements are only used at boundaries. Since the surface/volume ratio for a problem is usually small, the BEM is more computationally efficient than the FEM. Early work on the BEM can be found as far back as 1963 [22] with later extension to three dimensional stress analysis in [23, 24]. Now the BEM has been widely applied in various different fields, e.g. fracture mechanics [25–27], acoustics [28, 29] and thermoelasticity [30]. The BEM makes use of the Green's theorem to reduce the integration cost, but this also places restrictions on its applications, particularly any non-linear modelling. A possible solution to this drawback is through coupling between the BEM and nonlinear FEM as in [31].

Another advancement of the FEM occurred with the concept of isogeometric analysis (IGA) first proposed in [32] where element shapes match physical geometries exactly. B-spline functions, which are widely used in computer aided design, are introduced into the basis functions of elements in the interpolation, so the profiles of engineering structures can be exactly described by the assembly of elements. More importantly, shape functions of elements can be highly smooth by using the B-spline functions, which is much easier than by changing the element type in the FEM. This method can provide good accuracy in non-linear problems, e.g. damage [33], blood flow [34] and contact treatment [35]. However, manual operation is still unavoidable in the process of building up elements to match element shapes with the problem patterns, especially for complex geometries [36]. A recent review of the IGA is given in [37].

1.3 Meshless methods

Conventional numerical methods relying on meshes for the discretisation of a problem domain meet problems of high pre-processing time and remeshing issues. A class of meshless methods (MMs) has been developed to address these issues and are ideal for problems of large deformation, fracture, fragmentation and material damage as reviewed in [3–5]. Only nodal data are involved to approximate PDEs, for instance through a moving least squares process as in [2], and therefore remeshing is avoided. Each node is assigned to a weight function which controls the interaction with all its neighbours, and the influence domain of the weight function (known as "support") decides the number of neighbours. While MMs are designed to get rid of meshes, the use of elements is necessary in some MMs for either imposing essential boundary conditions or for integration. Therefore it is sometimes confusing how to distinguish MMs from mesh-based methods. A possible answer from the literature [38] is that a MM is defined as such if it can satisfy the following requirement, *"A predefined mesh is not necessary, at least in field variable interpolation."*

The most important features of MMs are listed below, which make MMs distinct from conventional numerical methods like the FEM.

- Absence of mesh. No mesh generation is required at the beginning of the calculation to determine the connectivity of nodes, so the issue of remeshing is avoided.
- Continuity of shape functions. It is easier to construct shape functions with any desired order of continuity in MMs than in the FEM.
- Convergence. The convergence rate for error in MMs can be much higher than that of the FEM as mentioned in [2].
- Adaptivity. Since no mesh is involved in the discretisation process, it is easy to generate node distributions with different densities, while transition elements are required to connect elements with different sizes in the FEM.

The standard FEM is challenged by volumetric locking for using C^0 continuous shape functions which somewhat overestimate the element stiffness and result in locking. This issue is relieved in MMs with large supports and high-order continuous shape functions as in [39, 40].

1.3.1 History and classification

A large number of MMs have been developed in recent decades, as reviewed in [5]. Here the history of MMs is introduced, and then a classification is provided according to their individual features.

One of the earliest MMs is the smoothed partial hydrodynamics (SPH) method proposed by Lucy [41] and by Gingold and Monaghan [42] in 1977. The SPH method is based on a Lagrangian formulation where the problem domain is represented by a set of moving particles with predefined masses and volumes. This makes it possible to model large deformation problems without considering accuracy degradation caused by mesh distortion. The method has been applied to a large variety of problems, e.g. shock simulation [43], fluid hydrodynamics [44, 45], impact [46] and metal forming [47]. However, the SPH method suffers from a number of problems such as spurious boundary effects [48] and tension instability [49]. Recent developments of the SPH method are given in [50, 51].

Another early MM is the diffuse element method (DEM) which was proposed in 1992 in [52], and it can provide better description of displacement gradients than the FEM. Here the FEM interpolation in elements is replaced by a local weighted least-squares fitting to neighbourhood nodes, known as the moving least squares (MLS) approximation [53]. While the DEM has accuracy issues due to using simplifications for the derivatives of displacement, it provided a foundation for the later element free Galerkin method (EFGM) [2, 54, 55]. In the EFGM, derivatives of shape functions are calculated correctly and the MLS approximation is incorporated into a Galerkin weak form of governing equations with Lagrange multipliers used to impose essential boundary conditions. It can provide better convergence properties than the FEM as mentioned in [2] and has been applied to a wide range of problems, e.g. linear and non-linear problems [56, 57], static and dynamic fractures [58–60], thin shell analysis [61], vibration [62, 63], biomechanics [64], electro-magnetics [65] and thermal problems [66, 67].

Other methods make the displacement approximation based on the theory of wavelets, from which the reproducing kernel particle method (RKPM) was developed in 1995 [68]. In the RKPM, displacements are represented by a group of wavelet functions describing the dilatation and translation of waves. While it starts from a different origin, similar

approximations are obtained in some cases matching with the MLS approximation, more precisely the RKPM can be seen as a continuous version of the MLS approximation. It has been shown that the RKPM can provide effective results for large deformation [69, 70], contact [71, 72], impact and fragment problems [73, 74].

At the same time, the *hp*-cloud method was developed [75], which provides easy implementation of h and p enrichment of the approximation functions. MLS approximations are enriched by adding additional degrees of freedom to build the partition of unity (PU) with higher order complete polynomials [76]. Compared with the EFGM and the RKPM which have discontinuities when p-adaptivity is attempted, the approximation space in the *hp*-cloud is smooth. This method was applied to the modelling of thick plates [77], where shear locking is controlled using *hp* cloud approximations with high order polynomial degrees and the results are the same as in the p-version FEM. The ideas in the *hp*-cloud method were extended to the FEM in [78], which combined the features of the two methods and exponential convergence was obtained. A recent development of the *hp*-cloud can be found in [79] for solving the Schrödinger equation in quantum mechanics.

MMs based on a global Galerkin weak form, e.g. the EFGM and the RKPM, require an integration over a problem domain and background cells are usually used (this is the issue referred to above in the discussion of truly MMs). An alternative which avoids the need for a grid for integration is the meshless local Petrov-Galerkin (MLPG) method [80], where a local weak form is employed. A local domain is selected to coincide with the support of weight functions, and background cells are not necessary, which makes the MLPG method truly meshless. The MLPG method has also been extended to a boundary integral technique in [81, 82], which is a simple and efficient alternative to the EFGM as mentioned in [82]. The MLPG method has been applied to problems such as acoustic analysis [83, 84], magneto-electro-elastic solids [85, 86], heat transfer [87–89], and a recent review is presented in [90].

The MMs mentioned above work from a Galerkin weak form of PDEs, but other methods based on the strong form have also been developed, termed point collocation methods. In this class of methods, a set of points in the problem domain are used to approximate displacements and their derivatives, and to select a solution which can satisfy the strong form governing equations at these collocation points. Although many related methods for

scattered data interpolation were developed for at least five decades earlier as reviewed in [91], the earliest applications to solve PDEs were in 1990 [92, 93]. A radial basis function (RBF), which is continuously differentiable and is capable to represent functions with deep gradients, was applied for spatial approximation and also for partial derivative estimates. The theoretical foundation of solving PDEs with the approximation of the RBF was established in [94], yielding the radial basis collocation method (RBCM), and the convergence of the RBCM was discussed in [95]. Since the RBF depends only on the distance between a pair of two points, no mesh is required in the approximation process. The RBCM has accuracy issues on derivatives of interpolating functions at boundaries, and one solution is using a Hermite type boundary collocation method as in [96] where Hermite polynomials were used for all nodes on boundaries. The RBCM has been applied to a wide range of problems, e.g. heat transfer [97, 98], fracture [99] and wave propagation [100–102]. In addition, approximations of the MLS or the RK can also be used in the collocation methods, as given in [103–105], and then the reproducing kernel collocation method (RKCM) is developed. While the RBCM suffers from issues of an ill-conditioning and fully dense system matrix, the RKCM uses locality property of the RK approximation which yields a sparse system matrix. The stability and convergence of the RKCM was discussed in [106], showing that the RKCM can provide algebraic convergence rate for the global error and be as stable as the FEM. The requirement of calculating second-order derivatives in PDEs is avoided by using a gradient RK approximation [107].

Despite the variety of names for MMs mentioned above, significant similarities can be found. These methods are classified according to their individual origins and viewpoints as given in Table 1.1.

1.3.2 Major issues

Despite the fact that MMs have been successfully applied in engineering analysis, some issues remain and hinder further development of MMs: these are imposition of boundary conditions, integration, complexity of calculating shape functions, convergence and error control.

Most MMs do not possess both the property of high-order continuous shape functions and satisfaction of the Kronecker delta property which means that the approximation at a node is equal to its nodal value. In those methods lacking the Kronecker delta property,

Table 1.1: Classification of meshless methods

Classification	Method	Approximation	Reference
strong form	SPH	smooth Kernel	[41]
	RBCM	RBF	[92, 93]
	RKCM	RK	[103]
weak form	DEM	MLS	[52]
	EFG	MLS	[2]
	RKPM	RK	[68]
	hp-clouds	enriched MLS	[75]
	MLPG	MLS	[80]

essential boundary conditions cannot be imposed directly to governing equations in the same way as in the FEM. A hybrid of MMs and the FEM is one solution, where boundaries are described by finite elements and the inner domain is modelled by MMs, as given in [108], but this combination brings many difficulties to the implementation. Alternatively, a number of techniques have been developed to address this issue by either modifying the weak form or using compliant shape functions. The former include Lagrange multipliers [2], penalty method [109] and Nitsche's method [110], while the latter can be achieved by using a singular weight function [111], or an improved meshless Shepard least squares approach [112]. A detailed description of these methods is included in Section 2 where the detailed derivation of the governing equations is covered.

Integration is a major issue for those MMs based on a weak form and is usually carried out using background cells or nodal integration. When Gaussian quadrature is performed over background cells [2, 54], a large number of integration points are necessary to obtain accurate results, and shape functions have to be evaluated at each integration point, thus affecting the efficiency of these MMs. Nodal integration is an alternative which is simpler and faster than complete Gaussian integration, and usually works with Voronoi cells [113, 114]. But this approach is less accurate and stable, and can become cumbersome for generating Voronoi cells when used for 3D problems. Other methods make use of the influence domain of particles, which are originally used to calculate shape functions, to evaluate all integrals and the need for a background mesh is eliminated, as in [115].

The calculation of shape functions in MMs is generally more time-consuming than in the FEM and this is a key computational cost. For MMs using the MLS or the RK approximation, the inversion of a matrix is inevitable for calculating shape functions, while in the FEM this is not required and shape functions can be obtained explicitly. In [54], orthogonal bases were introduced in the MLS approximation so the matrix becomes diagonal, but certain terms were omitted in the calculation of derivatives which can lead to large errors as mentioned in [116]. Since the size of the matrix to be inverted is usually small, e.g. 4×4 for a 3D problem with linear basis functions, it is also possible to figure out the explicit expression, and this was introduced to the MLS approximation in [117] and the RKPM in [118] to speed up the calculation of meshless shape functions.

Convergence and error control are common issues in all numerical methods. Efficiency and accuracy compete in that a finer node distribution can provide more accurate results but also lead to higher computational cost. These issues are addressed by developing an adaptive algorithm to handle node density so that the pre-described accuracy can be obtained with minimal computational cost. An *a posteriori* error estimator was proposed in the FEM in 1992, where exact solutions were approached by a patch recovery technique as in [119, 120]. This method was extended to MMs in [121] and then adaptive refinement for the EFGM was developed as in [122, 123]. A convergence study of the EFGM was carried out in [124], showing that the EFGM with discontinuous shape functions for non-convex domains is convergent. A later work on error control in the EFGM was presented in [125] demonstrating that approximations of the field compete with their derivatives, where the former require a smaller size of support while the latter show better accuracy with larger supports. However, the number of analytical studies on this issue to date is limited and more attention needs to be paid.

1.4 Fracture mechanics

With the development of numerical methods, a wider range of engineering problems have been solved and in particular, it has enabled computational fracture mechanics to take major steps forward [126]. Fracture is challenging because both non-linearity and discontinuity are involved. Traditional numerical methods based on continuum solid mechanics, e.g. the FEM, meet a dilemma when attempting to model discontinuity, and MMs are

more versatile to handle discontinuity and hence are ideal for computational fracture modelling, as mentioned in [3]. From another point of view, the study of fracture mechanics is in demand for the analysis of engineering structures. Cracks have a great impact on the loading capacity of materials, which therefore heavily affect the lifespan of engineering structures, such as aircraft bodies and engine components. Therefore, the topic of computational fracture mechanics is drawing more and more attention. Although this thesis is focused on crack modelling, the theory of fracture mechanics is also important and can promote future developments of computational fracture mechanics. Before introducing current numerical methods for fracture modelling, the history of fracture mechanics is firstly reviewed.

Fracture mechanics is the field of mechanics concerned with crack propagation and fracture of materials and structures. A fracture is defined as the separation of one material or object into two or more parts, while a crack is defined as a discontinuity without full separation. In fracture mechanics, theories of solid mechanics are used to study the mechanism of crack propagation and experiments are employed to characterise material resistance to fracture.

1.4.1 Griffith's theory

The study of cracks in engineering materials predates the birth of fracture mechanics. Inglis [127] studied the stress field around an elliptical cavity in a plate and obtained the analytical stress σ_f at the vertex,

$$\sigma_f = \sigma(1 + \frac{2a}{b}), \tag{1.1}$$

where σ is the tensile loading at the upper and lower edges of the plate, a and b are the two radiuses of the ellipse, as in Figure 1.1. If $a = b$ and the cavity becomes circular, the stress at the vertex becomes $\sigma_f = 3\sigma$ in agreement with the analytical solution for a circular hole in an infinite plate. To study the stress at the right vertex, b is replaced by r which is the radius of curvature at the vertex, with $r = b^2/a$. Then σ_f becomes

$$\sigma_f = \sigma(1 + 2\sqrt{\frac{a}{r}}). \tag{1.2}$$

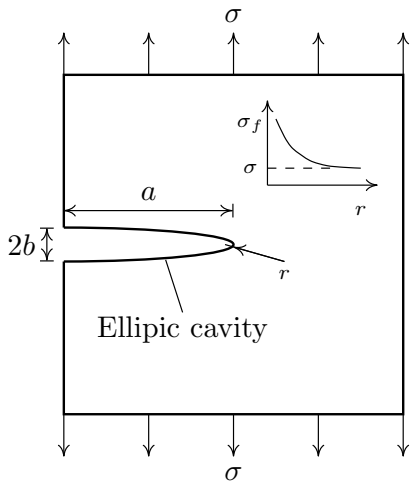

Figure 1.1: Stress at the vertex of an elliptic cavity.

From Equation (1.2), it can be seen that σ_f tends to increase as r decreases. If $r \to 0$, the cavity becomes a crack and $\sigma_c \approx \infty$, a result which is independent of the crack length a and the applied loading σ and clearly physically unreasonable. Although Inglis' research did not provide a qualitative explanation of the stress concentration at the crack tip, it laid a foundation for the start of fracture mechanics.

The development of modern fracture mechanics was motivated by the work of Griffith [128] during World War I. Griffith found two contradictory facts in his study on failure of brittle materials: The uniaxial tensile stress level leading to bulk glass fracture is around 100MPa whereas the theoretical stress to break the atomic bonds of glass is about 10000MPa. His experiments on glass fibres showed that the decrease of fibre diameter led to an increase of fracture stress. Thus, using the uniaxial tensile strength to predict material failure was not applicable for all materials, although this had been used extensively before Griffith. As suggested by Griffith, the reason was the presence of microscopic flaws in bulk materials which affected the macroscopic mechanical behaviour. To verify this hypothesis, Griffith carried out experiments on glass specimens each with a large artificial crack, the results showing that the square root of the crack length a times the critical stress at fracture σ_f is constant, i.e.

$$\sigma_f \sqrt{a} \approx C. \tag{1.3}$$

As outlined above, based on the linear elastic theory, the stress at the crack tip is

infinite which conflicts with Equation (1.3). A thermodynamic approach was proposed by Griffith, where it was assumed that the crack growth required an increase in the surface energy W_{surf} balanced by a reduction in the total strain energy U, i.e.

$$G = -\frac{\partial U}{\partial a} = \frac{\partial W_{\text{surf}}}{\partial a}, \tag{1.4}$$

where G is a quantity known as the strain energy release rate. Using Inglis' solution [127], the total strain energy released is

$$U = -\frac{\sigma^2 \pi a^2}{2E}, \tag{1.5}$$

here the thickness of the plane is taken to be unit and E is the Young's modulus. The surface energy W_{surf} associated with the crack is

$$W_{\text{surf}} = 2\gamma a, \tag{1.6}$$

where γ is the surface energy density (J/m^2), i.e. the energy needed to generate new surface, and the factor 2 is set because a pair of two crack surfaces are formed. Substituting Equations (1.5) and (1.6) back to Equation (1.4) yields

$$\sigma_f = \sqrt{\frac{2E\gamma}{\pi a}}, \tag{1.7}$$

and the constant in Equation (1.3) is $C = \sqrt{2E\gamma/\pi}$. The strain energy release rate G can be regarded as the driving force for crack propagation: if $G > 2\gamma$, then the crack can propagate; if $G < 2\gamma$, there is no crack propagation.

1.4.2 Stress intensity factors

Griffith's theory provides good agreement with experiments for brittle materials (e.g. glass), but not for ductile materials (e.g. steel). From experimental data on steel, the surface energy is usually much higher than assumed using Griffith's theory, although Equation (1.3) can still be satisfied. Irwin realized that plasticity can have an important influence on the fracture of ductile materials [129], something not considered by Griffith. For ductile materials, a plastic zone develops around the crack tip with the increase of

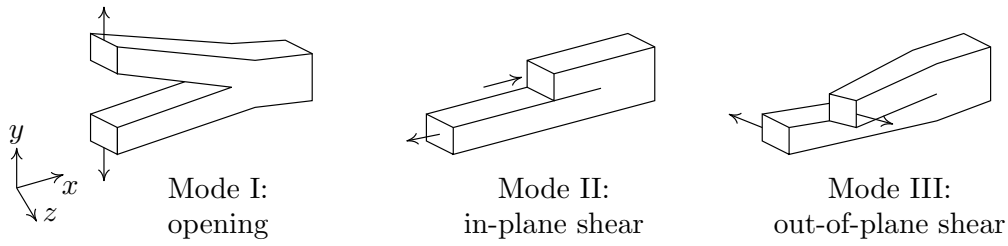

Figure 1.2: Three modes of crack deformation.

applied loading. When a crack grows, the strained material around the crack increment unloads. The plastic loading and unloading cycle leads to the dissipation of energy, which then becomes heat. So an energy term for the dissipation should be added in Equation (1.4) and the energy balance expression becomes

$$G = 2\gamma + G_p, \tag{1.8}$$

where G_p is the dissipation of the plastic energy U_p per unit crack surface area, $G_p = \frac{\partial U_P}{\partial a}$. The modified critical stress at the crack tip is

$$\sigma_f = \sqrt{\frac{E(2\gamma + G_p)}{\pi a}}. \tag{1.9}$$

For brittle materials, the surface energy dominates, e.g. for glass $G \approx 2\gamma = 2\text{J/m}^2$, while for ductile materials, the plastic dissipation dominates, e.g. for steel $G \approx G_p = 1000\text{J/m}^2$ [129].

Irwin found a method to measure the fracture energy in a linear elastic solid [130], in which the stress field around a crack front is asymptotic

$$\sigma_{ij} = \frac{K}{\sqrt{2\pi r}} f_{ij}(\theta), \quad i, j \in \{1, 2, 3\}, \tag{1.10}$$

where σ_{ij} are the Cauchy stress components, r and θ are local polar coordinates centred at the crack front and f_{ij} are dimensionless variables varying with external loadings and problem geometries. K is the stress intensity factor (SIF) with unit $\text{Pa}\cdot\text{m}^{1/2}$. There are three modes of deformation linked to a crack propagation as shown in Figure 1.2: mode I, a crack opens under a pair of tensile stresses normal to the crack surface; mode II, a crack forms by sliding due to a shear stress parallel to the crack surface and perpendicular to

the front; mode III, a crack is formed by tearing also under a shear stress parallel to the crack surface but parallel to the front leading to an out-of-plane deformation. All real crack behaviours can be represented by a combination of these three modes. The three SIFs are defined by

$$K_{\mathrm{I}} = \lim_{r\to 0} \sqrt{2\pi r}\sigma_{yy}(r,0), \tag{1.11a}$$

$$K_{\mathrm{II}} = \lim_{r\to 0} \sqrt{2\pi r}\sigma_{xy}(r,0), \tag{1.11b}$$

$$K_{\mathrm{III}} = \lim_{r\to 0} \sqrt{2\pi r}\sigma_{yz}(r,0). \tag{1.11c}$$

The relationship between G and the SIFs, with subscripts indicating the crack mode, is as follows

$$G_{\mathrm{I}} = \alpha K_{\mathrm{I}}^2, \quad G_{\mathrm{II}} = \alpha K_{\mathrm{II}}^2, \quad G_{\mathrm{III}} = \frac{K_{\mathrm{III}}^2}{2\mu}, \tag{1.12}$$

and

$$\alpha = \begin{cases} \frac{1}{E} & \text{plane strain,} \\ \frac{1-\nu^2}{E} & \text{plane stress,} \end{cases} \tag{1.13}$$

where ν is the Poisson's ratio, μ is the shear modulus and E is the Young's modulus. The total energy release rate is obtained by summing the three modes, as

$$G = G_{\mathrm{I}} + G_{\mathrm{II}} + G_{\mathrm{III}}. \tag{1.14}$$

1.4.3 Cohesive zone model

The cohesive zone model assumes there is a plastic zone ahead the crack tip, where cohesive tractions are applied to resist crack opening. The method was proposed by Dugdale (1960)[131] and Barenblatt (1962) [132] to trace the spread of plasticity from the front of a pre-existent crack. The cohesive tractions are determined by the value of material separation and a relation between the two is plotted as a traction-displacement curve, and although material properties of Young's modulus and Poisson's ratio are not involved, different curves can be applied according to the materials, e.g. three traction-displacement curves were included in [133] as depicted in Figure 1.3.

In a standard traction-displacement curve, the traction is the largest at the beginning,

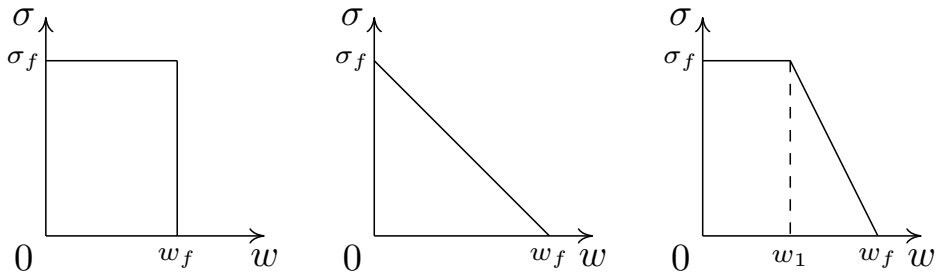

Figure 1.3: Three traction-displacement curves in the cohesive zone model.

and then reduces with the increase of separation and subsequently becomes zero which results in complete separation. The area under the curve is the energy required to separate the crack surface. The cohesive zone model maintains the continuity conditions mathematically and eliminates the singularity around the crack tip. The method has been applied to model cohesive crack growth in [134, 135] and to study rate-dependent elasto-plastic behaviour for dynamic crack propagation [136]. It can provide an effective methodology to study fracture problems in solids, as reviewed in [137, 138].

1.4.4 Fatigue fracture

Fatigue fracture is the weakening, damage and fracture of materials under repeated loading and unloading (also called cyclic loading). The maximum nominal stress causing damage can be much lower than the yield stress limit. Normally a fatigue fracture goes through three stages, as shown in Figure 1.4, where a is the crack length, N the number of loading cycles and ΔK is the range of the SIF, i.e. $\Delta K = K_{\max} - K_{\min}$. Stage I, when the loading is above a threshold, microscopic cracks are generated at stress concentrators, e.g. sharper corners, persistent slip bands and interfaces. With the progress of the cyclic loading in the second stage, microscopic cracks accumulate and grow steadily. Finally when a crack reaches a critical size, it propagates rapidly and leads to the full fracture of the material. For some materials such as steel and titanium, a fatigue fracture will not occur if the stress amplitude is set below a certain value, which is called the fatigue limit.

The history of fatigue fracture can be traced back to the 1900s, when Ewing and Humfrey [139] studied the fatigue behaviour of metals under repeated reversals of stress. It was found that metal specimens under cyclic loadings develop slip-bands, which gradually widen before the material fractures. A log-log relationship between the strain amplitude

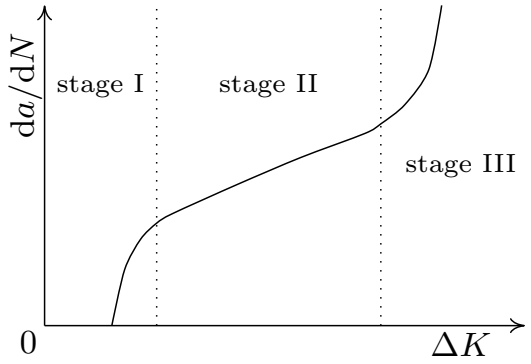

Figure 1.4: Crack growth rate with respect to the cyclic loading in the fatigue fracture.

and the number of cycles was presented in [140], also known as the S-N curves, through which the damage process of a material can be depicted easily. A formulation (the Paris' law) was proposed by Paris et al. in [141], by which a linear relationship between the crack growth rate and the range of SIF in stage II can be visualized in a log-log plot, Figure 1.4, as

$$\frac{\mathrm{d}a}{\mathrm{d}N} = C\Delta K^m, \tag{1.15}$$

where C and m are constants depending on materials and environments, and m is typically between 3 and 5 for metals. A fatigue fracture is usually caused by tensile loadings but it was found that compressive loadings can also lead to fatigue cracks [142]. During the progress of cyclic loading, it was noticed in an experiment that a fatigue crack can be completely or partially closed when the loading becomes zero [143], even when full tensile loading cycles are applied. The crack closure phenomenon is due to the incompatibility between the remaining and permanent tensile plastic deformations during the crack propagation. An extended cohesive law can handle crack closure [144], with a repulsive cohesive traction defined to prevent inter-penetration. Recent studies on the micro-structures of fatigue cracks can be found in [145–147] and a review of the fatigue life of metal structures is given in [148].

Several rules can be used to design against the fatigue failure, as follows.

- Keep stress below the fatigue limit so fatigue fracture is limited to stage I and can be avoided ideally.
- Plan a fixed lifetime for devices and components following a finite lifetime concept so they can be replaced before reaching stage III and becoming fatigue failure.

- Set up damage tolerance and replace the device with a crack exceeding the critical length, so the stage III of a fatigue fracture is avoided.

1.5 Numerical methods for fracture modelling

Purely theoretical studies meet dilemmas when attempting to explain fracture behaviour in general problems, because crack propagation is highly non-linear. Computational fracture modelling (i.e. approximate methods based on discretisation) provides the only serious approach for engineering analysis. The FEM, which was originally designed for continuum solids, has been tried for crack modelling, and crack discontinuities can be obtained by generating elements to lie along existing crack faces, as in [149–151]. However, a crack can only propagate along the interface of elements and remeshing to align element edges with crack growth is inevitable, which is computationally expensive especially for 3D cracks [152]. New methods are required to handle both the crack discontinuity and non-linearity for crack propagation in an efficient and effective way, which is also the object of this thesis.

1.5.1 The extended finite element method

The extended finite element method (XFEM) was developed in the last two decades [153–155], and is method in which cracks can propagate independently from elements. Crack discontinuities are included by introducing discontinuous enrichment functions into the displacement approximation, so remeshing is not required during the crack propagating process. The XFEM can also handle holes and inclusions [156], and meshing the interface boundaries is not required. The crack opening value can be obtained through these enrichment functions and a cohesive law was introduced in the XFEM in [157]. Frictional contact on two crack faces has also been considered in the XFEM, and the study of crack propagation under compressive loadings was carried out in [158]. This method can be improved to gain better convergence properties and more accurate description of curved cracks by using high order enrichment functions [159] or elements [160]. The XFEM has been applied to solve problems including crack branching and intersection [155] and non-planar 3D crack growth [161, 162]. Recent developments and applications of the XFEM are reviewed in [163].

In the standard FEM, the displacement $u(\mathbf{x})$ is approximated and interpolated by

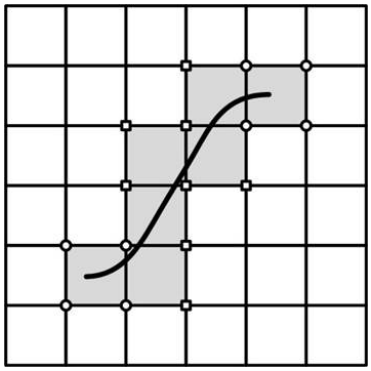

Figure 1.5: Enriched elements (in grey) in the XFEM to model a crack.

surrounding nodal values u_i,

$$u^h(\mathbf{x}) = \sum_i^n \phi_i(\mathbf{x}) u_i, \tag{1.16}$$

where n is the number of nodes, i is the index, $\mathbf{x}$ is the location vector, i.e. $\mathbf{x} = [x, y]$ in 2D and $\phi_i(\mathbf{x})$ are interpolation functions, also known as shape functions, which can be obtained through the Lagrangian interpolation functions. In the XFEM, elements cut by a crack are enriched, e.g. those shadowed in Figure 1.5. Crack discontinuities are introduced by adding discontinuous enrichment functions into the displacement approximation, as

$$u^h(\mathbf{x}) = \sum_i^n \phi_i(\mathbf{x}) u_i + \sum_j^{n_1} \phi_j(\mathbf{x}) H(\mathbf{x}) b_j + \sum_j^{n_c} \phi_j(\mathbf{x}) \Big(\sum_{k=1}^{4} R_k a_j^k \Big), \tag{1.17}$$

where $H(\mathbf{x})$ is the sign function with values +1 for nodes on one side of the crack surface and -1 on the other side. n_1 is a group of nodes belonging to elements totally cut by the crack, while n_c is the set of nodes belonging to elements containing the crack tip. b_j and a_j^k are nodal enriched unknowns and R_k are components of the near-tip enrichments $\boldsymbol{R}$, as

$$\boldsymbol{R}(r, \theta) = \left[\sqrt{r} \sin(\frac{\theta}{2}), \sqrt{r} \cos(\frac{\theta}{2}), \sqrt{r} \sin(\theta) \sin(\frac{\theta}{2}), \sqrt{r} \sin(\theta) \cos(\frac{\theta}{2}) \right], \tag{1.18}$$

where r and θ are local polar coordinates at the crack tip. The use of singular enrichment around a crack tip can also bring challenges for the numerical integration and can affect the calculation stability.

1.5.2 The phase-field method

The phase-field is a mathematical model to solve interface problems between various materials/phases [164]. The concept can be used to model cracks as interfaces of intact and broken material, and the transition zone is described by an order parameter, called the crack phase field. Crack propagation is handled by the phase field independently from a domain discretisation, e.g. a finite element mesh, and the complexity of tracking crack geometries is not required, although the calculation and the evolution of the phase field during crack propagation brings extra computational burden. Early application of the phase field to crack modelling can be found in [165], where mode I dynamic crack propagation was investigated. A continuum field theory for crack propagation was represented where an order parameter was introduced in the constitutive model between strain and stress controlling the degradation of materials due to cracks, and the method can capture crack initiation, crack branching and fracture instability. Borrowing ideas from the phase field for solidification [164], a modification of the phase field approach for fracture was proposed, where the momentum balance equation was included in the governing equations and three modes of fracture were studied [166, 167]. Apart from this material damage model, some phase field models for fracture have been developed on the basis of Griffith's theory. The surface energy of the crack has been included in the total energy and its minimisation with respect to both displacement field and crack field is used to yield the governing equations [168–170]. It was found that the phase field fracture approach is a special case of the gradient damage model [171]. The phase field has been applied to a variety of problems, e.g. ductile fracture [172], hydraulic fracture [173], fracture in lithium-ion battery [174] and fracture in biological tissues [175]. Recent developments of the phase field fracture approach can be seen in a review paper [176].

A brief introduction to the phase field is included here and interested readers are referred to [170, 177]. A discontinuity Γ (crack surface) is approximated by a smeared surface Γ_l. For one dimensional problems, an exponential function can be used, as in Figure 1.6,

$$d(x) = e^{-|x|/l}, \tag{1.19}$$

where l is a length scale parameter determining the area of the transition zone and $d(x)$

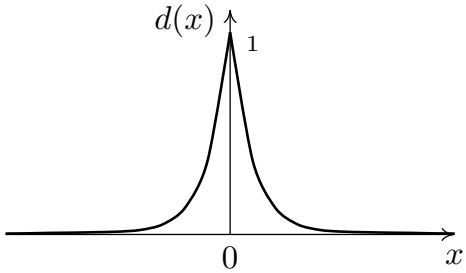

Figure 1.6: A phase field model to approximate a crack.

is the phase field: $d = 1$ indicating for fully broken material; $d = 0$ for intact material. Equation (1.19) is the solution to the equation

$$d - l^2 d_{,xx}(x) = 0, \tag{1.20}$$

where $d_{,xx}(x)$ is the second derivative of d with respect to x, and then using the weak form of this equation, Γ is approximated with Γ_l by integrating a Galerkin-type weak form of Equation (1.20),

$$\Gamma \approx \Gamma_l(d) = \int_\Omega \frac{1}{2l}\Big(d^2 + l^2 d_{,x}^2(x)\Big)\mathrm{d}\Omega, \tag{1.21}$$

where details can be found in [170] and $d_{,x}(x)$ is the first derivative of d with respect to x. The minimization of this function in Equation (1.21) gives the regularized crack topology in Figure 1.6. A crack surface for multi-dimensional problems can be obtained from the extension of the 1D case in Equation (1.21),

$$\Gamma_l(d) = \int_\Omega \gamma(d, \nabla d)\mathrm{d}\Omega, \tag{1.22}$$

and

$$\gamma(d, \nabla d) = \frac{1}{2l}d^2 + \frac{l}{2}(\nabla d)^2, \tag{1.23}$$

where $\gamma(d, \nabla d)$ is the crack surface density function. In the transition zone, materials become damaged using a degradation function of the phase field, e.g. a quadratic polynomial in [170] as

$$h(d) = (1 - d)^2, \tag{1.24}$$

and a very small positive value is defined where full degradation $d = 1$ is applied. The

total potential energy for the brittle fracture in a smeared formulation is

$$\Psi = \int_{\Omega} h(d)\Psi_e^+ + \Psi_e^- + G_c\gamma(d, \nabla d)\mathrm{d}\Omega, \tag{1.25}$$

where Ψ_e^+ and Ψ_e^- are the strain energy due to tension and compression respectively, and G_c is the critical surface energy dissipation per unit of crack surface. The minimisation of Equation (1.25) leads to the governing equation of the phase field,

$$h_{,d}(d)\Psi_e^+ + \frac{G_c}{l}(d - l^2\nabla^2 d) = 0. \tag{1.26}$$

This is a second order PDE specific to the phase field, which controls the evolution of cracks. Since the phase field and the displacement field can be discretised with the same set of nodes and elements in the FEM, the solution of Equation (1.26) can be obtained easily as in [170, 176]. The advantages of the phase field method for crack modelling exist in a simple algorithm for tracking crack geometries, which makes it easy to model crack propagation and coalescence of cracks, while the disadvantages come from high computational expense [170]. An extra PDE for the phase field is required, which increases the total number of degrees of freedom. In addition, the method requires fine elements in the cracked zone to ensure the accuracy of results. For instance, the element size should be below the half width of crack l as mentioned in [177], which leads to a large number of elements.

1.5.3 The element-free Galerkin method with level sets

The element-free Galerkin method (EFGM) [2] is a MM requiring no mesh in the problem discretisation, which makes it promising for crack modelling since no remeshing is needed if one is modelling crack propagation. It has been applied to solve static and dynamic crack problems in [58–60], where the description of crack geometries is still necessary by using either lines (2D) or surfaces (3D). The level set method, which is generally used to describe evolving surfaces, was introduced into the EFGM to model crack geometry in [178–180]. Since the level set method can provide accurate descriptions of surfaces, precise results can be obtained during the crack propagation process, especially for 3D fracture modelling [180].

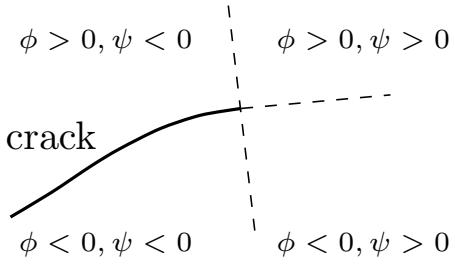

Figure 1.7: Level set functions to describe a crack.

Two level set functions are used to describe a crack surface: one measures the shortest distance normal to the crack surface and its extension, ϕ; the other level set ψ gives the shortest distance parallel to the crack surface and normal to the crack front. These two level set functions ϕ and ψ are signed functions as in Figure 1.7, and the crack geometries are given as $\phi = 0, \psi \leqslant 0$ is the crack surface and $\phi = 0, \psi = 0$ is the crack front. It is assumed that ϕ and ψ are orthogonal to each other,

$$\nabla\phi \cdot \nabla\psi = 0, \tag{1.27}$$

where the gradient operator is calculated by $\nabla = [\frac{\partial}{\partial x}, \frac{\partial}{\partial y}, \frac{\partial}{\partial z}]$. Details on the update of level set functions for the crack propagation can be found in [181]. The level set method has also been used in the XFEM [182, 183].

1.5.4 The numerical manifold method

The numerical manifold method (NMM) is based on the finite cover approximation where a number of discrete blocks (covers) are used to describe continuum bodies. For fractured bodies, those covers containing cracks are truncated and discontinuous. It can use a unified form to handle both continuum and fractured problems in solids and can model crack propagation without remeshing. The covers can be nonconforming to a problem domain, so the meshing task is simplified.

In the NMM, there are three components involved to build the displacement approximation: mathematical cover, physical cover and manifold element, as in Figure 1.8. The mathematical cover is predefined and can be of arbitrary shape, e.g. triangular or rectangular as in Figure 1.8 (a). Physical covers are the division of mathematical covers by the problem domain and physical features, e.g. cracks and interfaces, and those covers

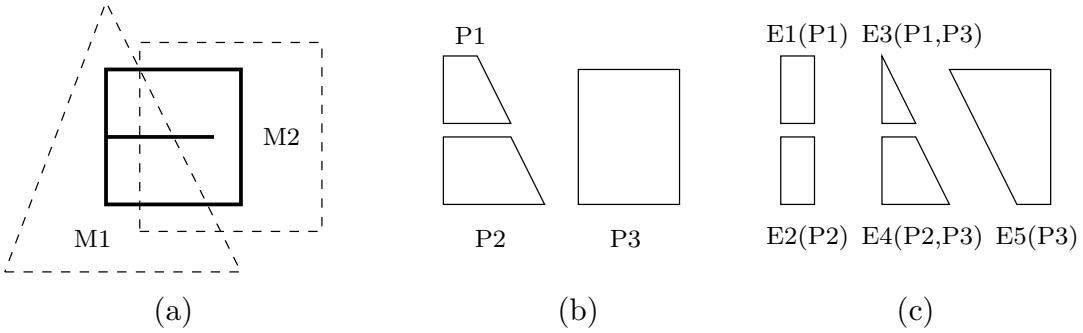

Figure 1.8: Three basic components in the NMM to model a crack: (a) mathematical cover; (b) physical cover; (c) manifold element.

partially cut by the crack are not divided. Manifold elements are defined as the intersection of several physical covers, e.g. in Figure 1.8 (c) five manifold elements are defined. A weight function is defined over each mathematical cover M_i following

$$\begin{aligned} \varphi_i(\mathbf{x}) &= 0, \quad \mathbf{x} \notin \mathrm{M}_i, \\ 0 \leqslant \varphi_i(\mathbf{x}) &\leqslant 1, \quad \mathbf{x} \in \mathrm{M}_i. \end{aligned} \tag{1.28}$$

An example of a weight function is defining it to be of value one at the centre of the cover and linearly declining to 0 at all edges. The weight functions for all physical covers including the location $\mathbf{x}$ satisfy the partition of unity, as

$$\sum_i \varphi_i(\mathbf{x}) = 1. \tag{1.29}$$

The displacement approximation $u^h(\mathbf{x})$ on an manifold element is

$$u^h(\mathbf{x}) = \sum_i^{n_p} \varphi_i(\mathbf{x}) u_i(\mathbf{x}), \tag{1.30}$$

where n_p is the number of physical covers sharing the element. The cover function $u(\mathbf{x})$ with respect to the physical cover i is defined as

$$u_i(\mathbf{x}) = \mathbf{p}^{\mathrm{T}}(\mathbf{x}) \cdot \mathbf{a}_i, \tag{1.31}$$

where $\mathbf{a}_i$ is a vector of unknowns and $\mathbf{p}^{\mathrm{T}}(\mathbf{x})$ is a matrix of polynomial basis, e.g. a linear

basis in 1D,

$$\mathbf{p}^{\mathrm{T}}(\mathbf{x}) = \begin{bmatrix} 1 & x & y \end{bmatrix}. \tag{1.32}$$

For instance, the displacements of elements E3 and E4 in Figure 1.8 (c) are respectively

$$u_3^h(\mathbf{x}) = \sum_i^{\{1,3\}} \varphi_i(\mathbf{x}) u_i(\mathbf{x}), \tag{1.33}$$

and

$$u_4^h(\mathbf{x}) = \sum_i^{\{2,3\}} \varphi_i(\mathbf{x}) u_i(\mathbf{x}), \tag{1.34}$$

and then the discontinuity is introduced on the common edge of elements E3 and E4, as $u_3^h(\mathbf{x}) \neq u_4^h(\mathbf{x})$. It is notable that in the NMM unknowns are associated with physical covers not nodes, which is the major difference with the FEM.

The NMM was first reported in [184, 185], indicating both the FEM and the discontinuous deformation analysis are special cases of the NMM. It has since been applied to model crack propagation problems, but the crack has to cut a cover totally and cannot be inside [186]. Crack tip enrichment functions were introduced in the NMM, so the crack can be arbitrary within a cover [187]. The NMM is usually based on finite elements to build covers and the MLS-based NMM (e.g. [188]) provides easier generation of covers cut by cracks. A high order NMM was proposed in [189], where a nine-node triangular mesh was used to build high-order approximations for covers. A review on the NMM can be found from [190], showing that the FEM is a special case of the NMM when cover functions are constant and external boundaries are conforming with manifold covers.

1.5.5 Peridynamics

Peridynamics is a MM designed for deformation problems involving discontinuities, particularly for fracture problems. In peridynamics, PDEs generally used in continuum solid mechanics are replaced with integral equations, so the calculation of partial derivatives can be avoided, which can simplify the handling of singularities at cracks and provide a uniform formulation to describe the deformation with or without discontinuities.

The method was first proposed by Silling in 2000 [191], where the original bond-based formulation of peridynamics was introduced. In this approach a "bond-force" is assumed

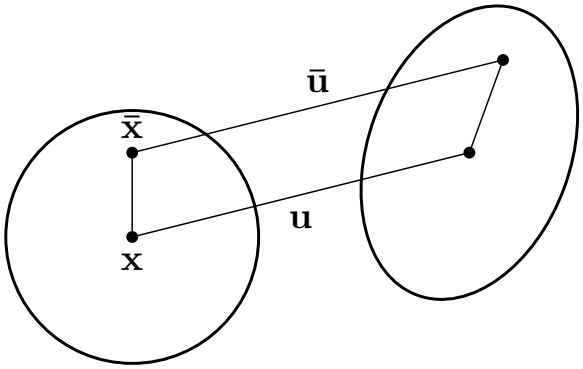

Figure 1.9: Deformation in peridynamics.

between each pair of two particles in a discretisation formed of a large number of particles, each bond working like a spring (in the case of application to elasticity for instance). When the stretch between these two particles exceeds a critical value, the bond becomes broken irreversibly and a crack occurs. The influence domain of a particle to its surrounding is called *horizon*. The method at this stage is called the bond-based peridynamics, and a meshfree method based on the peridynamic model was developed in [192]. The limitation of this method is that bond-based peridynamics only considers pairwise interactions between particles, so the effective Poisson's ratio is fixed to $\nu = 0.25$ for isotropic linear elastic materials [191]. A state-based formulation was developed in [193], in which general constitutive models were incorporated and materials with any Poisson's ratio can be considered. It has been shown that peridynamics for an elastic material can reproduce the classical elastic model in solid mechanics, when the stretch between particles declines to zero [194]. An introduction to the implementation of peridynamics based on a molecular dynamics code can be found in [195]. If nodal integration is used, the discretised equations of peridynamics and the SPH coincide [196]. Currently a uniform distribution of particles is defined in peridynamics, but non-uniformly distributed particles are required in an adaptive refinement approach to increase the computational efficiency. One attempt was made in [197], where particles were given different sizes of influence domain, and the interactions between particles were modified to ensure the balance of forces. Peridynamics has been applied to solve a variety of problems, e.g. crystal plasticity [198], crack branching [199] and multiscale modelling of cracks [200].

The governing equation of the bond-based peridynamics in a problem domain Ω can

be though of as a continuum version of molecular dynamics and is given by

$$\rho\ddot{\mathbf{u}} = \int_{\Omega} \mathbf{f}(\bar{\mathbf{u}} - \mathbf{u}, \bar{\mathbf{x}} - \mathbf{x}) \mathrm{d}\Omega + \mathbf{b}, \tag{1.35}$$

where ρ is the material density, $\ddot{\mathbf{u}}$ is the second order derivative of displacement to time, Ω is the problem domain, $\mathbf{x}$ and $\bar{\mathbf{x}}$ are the location vectors of two particles, $\mathbf{u}$ and $\bar{\mathbf{u}}$ are the displacement vectors respectively and $\mathbf{b}$ is the body force vector. Function $\mathbf{f}$ is the pairwise force function, which contains the constitutive relationship of materials and should satisfy the following restriction,

$$\mathbf{f}(\boldsymbol{\eta}, \boldsymbol{\xi}) + \mathbf{f}(-\boldsymbol{\eta}, -\boldsymbol{\xi}) = 0, \tag{1.36a}$$

$$(\boldsymbol{\eta} + \boldsymbol{\xi}) \times \mathbf{f}(\boldsymbol{\eta}, \boldsymbol{\xi}) = 0, \tag{1.36b}$$

where $\boldsymbol{\eta} = \bar{\mathbf{u}} - \mathbf{u}$ and $\boldsymbol{\xi} = \bar{\mathbf{x}} - \mathbf{x}$. An example of $\mathbf{f}$ for a prototype micro-elastic material is from [195],

$$\mathbf{f}(\boldsymbol{\eta}, \boldsymbol{\xi}) = \frac{c}{\|\boldsymbol{\xi}\|}(\|\boldsymbol{\eta} + \boldsymbol{\xi}\| - \|\boldsymbol{\xi}\|)\frac{\boldsymbol{\eta} + \boldsymbol{\xi}}{\|\boldsymbol{\eta} + \boldsymbol{\xi}\|}, \tag{1.37}$$

where $c/\|\boldsymbol{\xi}\|$ is the stiffness per unit volume and $\|\cdot\|$ is the L_2 norm of a vector, i.e. $\|[x, y]\| = \sqrt{(x^2 + y^2)}$.

Moving to the state-based peridynamics, the response at one material point due to external loadings depends on the collective deformation of all bonds connected to that point. Every particle can only interact with other particles within a finite distance (horizon). A force state is defined in a similar way to the stress tensor in classical continuum mechanics, so it can handle general materials with arbitrary Poisson's ratio. Governing equations are built by replacing the bond force term in Equation (1.35) with the force state term, i.e.

$$\rho\ddot{\mathbf{u}} = \int_{\Omega} \mathbf{T}(\boldsymbol{\xi}) - \mathbf{T}(-\boldsymbol{\xi}) \mathrm{d}\Omega + \mathbf{b}, \tag{1.38}$$

and the force state $\mathbf{T}(\boldsymbol{\xi})$ is

$$\mathbf{T}(\boldsymbol{\xi}) = w(\|\boldsymbol{\xi}\|)\mathbf{P}\mathbf{K}^{-1}\boldsymbol{\xi}, \tag{1.39}$$

where $w(\|\boldsymbol{\xi}\|)$ is a scalar influence function, e.g. $w(\|\boldsymbol{\xi}\|) = e^{-\|\boldsymbol{\xi}\|^2/d^2}$ from [201] with d the radius of a circular horizon. $\mathbf{P}$ is the first Piola-Kirchhoff stress tensor from a conventional

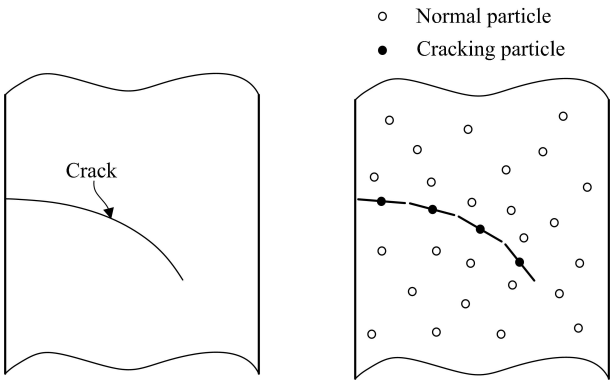

Figure 1.10: A crack path approximated by a set of segments in the CPM.

constitutive model and $\mathbf{K}$ is a symmetric shape tensor,

$$\mathbf{K} = \int_{\Omega} w(\|\boldsymbol{\xi}\|)\boldsymbol{\xi} \times \boldsymbol{\xi} \mathrm{d}\Omega. \tag{1.40}$$

The implementation of peridynamics can be made from a molecular dynamics code as in [195]. In peridynamics, crack behaviours are modelled by removing the force between particles, which reduces the complexity for tracking crack patterns, and crack coalescence and branching are natural outcomes of the method [193]. However, a fine distribution of particles are required to get accurate results, which leads to low efficiency for calculation.

1.5.6 The cracking particle method

The cracking particle method (CPM) is a MM, where continuous crack paths are described by a set of discontinuous segments centred at cracking particles, as in Figure 1.10. These segments cut the supports of weight functions, which are used to define the connection of a particle to its surrounding in MMs like the EFGM, and discontinuities at cracks are therefore introduced. Since the locations and orientations of these discontinuous segments are arbitrary, this method is suitable for complex fracture problems. The research work in this thesis is based on the CPM so details of the method will be demonstrated in following chapters and a literature review is included below.

The original CPM was proposed by Rabczuk in 2004 [202] to model 2D cracks where problems including crack branching in a plate and fragment of a cylinder under dynamic loadings were studied. The method was later extended to 3D cracks and to large deformation problems as in [203, 204]. Although the CPM originally used enrichments to describe

crack surfaces which is similar to some enrichment-type methods for fracture modelling as given in [205–208], it has been shown that extra unknowns caused by enrichments can be removed by splitting cracking particles with divided supports as in [204]. A number of papers have appeared recently applying the CPM to problems including dynamic fracture [209], shear bands [210] and ductile fracture [211, 212]. In [213], a stabilized nodal integration method was introduced to the CPM, by which both computational efficiency and stability are maintained. There are also a few publications using cracking-particle-type methods for fracture modelling, like the use of cohesive zone element in [214] and cohesive links in [215].

1.6 Outline of the thesis

Even though several computational methods have been developed and successfully applied for fracture modelling in recent decades, there are still some issues remaining before further applications in engineering analysis. Due to the properties of enrichment functions in the XFEM, it is problematic to be applied for crack initiation, e.g. when a crack is totally within an element in the XFEM, crack tip enrichments produce no discontinuity in this element. Besides, the XFEM is based on the FEM and there will be issues for large deformation problems. The approximation is obtained through the interpolation of nodes in an element, but when the element is cut by a crack and the nodes at two sides of the crack are far away after deformation, the interpolation between these nodes is unreasonable. In the phase field method for fracture modelling, the solution of an extra PDE for the phase field is required, leading to an increase of computational expense [170]. The EFGM with level sets can provide accurate description of crack geometry, but it meets a dilemma for multiple crack problems. Each crack needs two level set functions, so the computational cost increases with the number of cracks [179]. The NMM makes use of finite cover approximation and is suitable for multiple crack simulation, but the generation of covers and their truncation by cracks is still bothersome [216]. Peridynamics defines “bonds” between particles to describe the deformation of the problem and crack discontinuities are introduced by breaking the connection between particles. This method is suitable for complex crack problems but the accuracy of the crack geometry is only guaranteed by using a very fine distribution of particles which is costly. The CPM has

shown its ability to handle multiple cracks and dynamic fracture but spurious crack results have been found in [204, 213]. Currently a robust method for computational fracture modelling is still needed and is the motivation of this thesis. The CPM is employed and modified to handle complex crack problems in 2D and 3D and to address issues of spurious cracking results, where the calculation efficiency is maintained by using an adaptive approach and this is the goal of this thesis. The contents of each chapter are listed as below.

Chapter 2 demonstrates basic formulations and main features of the EFGM. Although the thesis is focused on fracture modelling, the EFGM for continuum solids is firstly demonstrated, because the CPM is based on the EFGM by introducing crack discontinuities into the displacement approximation. It starts from setting up the governing equations of the EFGM, and then the strong form and weak form are introduced. Three techniques of integration required in the weak form are included: nodal integration, integration with background meshes and integration over supports. Since essential boundary conditions cannot be imposed to the weak form directly in the EFGM, four methods including Lagrange multipliers, penalty method, Nitsche's method and coupling with the FEM are discussed. An example is used to demonstrate the differences between the EFGM and the FEM.

In Chapter 3, an adaptive CPM is developed for 2D cracks. The development of the CPM is reviewed and issues of the method are discussed. A key contribution of this research is the use of a set of bilinear discontinuous segments centred at particle to approximate a continuous crack path instead of straight discontinuous segments in early CPMs. Cracking angles can be recorded by changing the orientation of those segments, so problems of spurious crack results can be relieved. An adaptive approach is introduced to the CPM to handle the stress gradients around the crack tip, by which particle refinements are added automatically, and different error estimators for adaptivity are included. Several methods to calculate SIFs are mentioned, including an contour integration and a domain interaction integration.

Chapter 4 applies the method developed in Chapter 3 to problems with multiple crack. Different methods to model crack branches and intersections are mentioned, which are through enrichments in basis functions or weight functions. A multi-cracked particle

method is developed which can achieve discontinuities at crack branches in an easier way than through enrichments. Several example with complex crack geometries are used to test the ability of the proposed method.

Chapter 5 contains a discussion of different crack propagation criteria. A review on the maximum principal stress criterion, the minimum strain energy density criterion and the maximum strain energy release rate criterion are included. The theory configurational force for fracture modelling is presented here and its implementation in MMs is also mentioned. A comparison between the use of propagation criteria based on the J-integral and the configurational force is carried out and demonstrated with several crack problems.

In Chapter 6, the modified CPM is extended from 2D to 3D cracks. Conventional methods of level sets and triangular meshes to describe 3D crack surfaces are reviewed. The CPM in 3D is combined with triangular facets, where the cracking changes are recorded by modifying the orientation of triangular meshes. Calculation of SIFs in 3D is through an interaction integration method in a local coordinate system decided by triangular meshes. Cracking angle is determined by the maximum principal stress criterion while the crack increment length along a crack front is decided by the Paris' law. Examples with planar or curved 3D crack surfaces are tested and a comparison between the proposed method and the original CPM is included.

Chapter 7 demonstrates a further development of the proposed method for modelling thermoelastic crack problems. Governing equations of the heat flux are introduced and the implementation of the weak form is included. Two types of cracks under thermal loadings are mentioned: an adiabatic crack and an isothermal crack. An adaptive approach is introduced so enrichment functions can be avoided which are commonly used in current numerical methods. Due to the effect of thermal stress, the interaction integral method needs modification to make it compliant with the assumptions of thermal fracture mechanics.

The thesis finishes with Chapter 8 summarizing all the research work mentioned above and providing an outlook of future directions in terms of MMs and computational fracture mechanics.

Chapter 2

Formulation of the element free Galerkin method

2.1 Introduction

In this chapter, fundamental formulations of the EFGM are demonstrated before introducing the CPM, since the CPM is based on the EFGM and is specific to crack problems. It starts from the moving least squares approximation, which is used to approximate the displacement field with a set of nodes, while elements are not involved to discretise the problem domain. Then the basic theory of solid mechanics is introduced, precisely the equilibrium of solids under static or quasi-static external loadings. These equilibrium equations are not solved directly but are converted to the weak form, which provides numerical benefit of reduced order differentiation of the governing equations. Major issues in meshless methods of integration and imposing essential boundary conditions are discussed and several approaches are provided to address these issues. Finally, an example is used to demonstrate the difference between the FEM and the EFGM.

2.2 Moving least squares approximation

In the EFGM, a set of nodes are used to discretise the problem domain with on elements, and the approximation between these nodes is carried out by the moving least squares (MLS) approximation in the EFGM. The MLS approximation was first proposed in [53] for curve and surface fitting. Then this approach was introduced to the problem discretisation

process as in [2, 52] without using any element, triggering the development of MMs.

Displacements are approximated by polynomial interpolation, and the displacement approximation u^h is

$$u^h(\mathbf{x}) = \mathbf{p}^{\mathrm{T}}(\mathbf{x})\mathbf{a}(\mathbf{x}), \tag{2.1}$$

where $\mathbf{x}$ is a vector of location (for instance $\mathbf{x} = [x, y, z]^{\mathrm{T}}$ in 3D), $\mathbf{p}(\mathbf{x})$ is a basis function, e.g. linear basis function in 3D is $\mathbf{p}(\mathbf{x}) = [1, x, y, z]^{\mathrm{T}}$, and $\mathbf{a}(\mathbf{x})$ is a vector of unknown coefficients at $\mathbf{x}$. An error term is formed being the difference between unknown nodal values and the approximation, as

$$J = \sum_{i}^{n} w_i(\mathbf{x})\Big(\mathbf{p}^{\mathrm{T}}(\mathbf{x}_i)\mathbf{a}(\mathbf{x}) - u_i\Big)^2, \tag{2.2}$$

where i is the node index, n is the number of nodes with influence domain covering $\mathbf{x}$, $\mathbf{x}_i$ is the location vector of node i, u_i is the nodal value of u at $\mathbf{x} = \mathbf{x}_i$ and $w_i(\mathbf{x})$ is a weight function. The requirements for a weight function are: non-negativity, monotonically decreasing, continuous and differentiable. The first two requirements ensure a weight function which will lead to stable results in the approximation and to have a localized property, and the latter guarantees a smooth approximation with high order consistency in basis functions. Each node is defined with an influence domain (also named as "support") which is normally rectangular or circular in 2D and cuboidal or spherical in 3D, and the weight function becomes zero outside the support. There are many options for the weight function as in [2, 58, 217, 218], e.g.

$$w(r) = \begin{cases} 1 - 6r^2 + 8r^3 - 3r^4 & \text{if } r \leq 1, \\ 0 & \text{if } r > 1, \end{cases} \tag{2.3}$$

where $r = \|\mathbf{x} - \mathbf{x}_i\|/r_0$ with r_0 the radius of a circular support and $w(\|\mathbf{x} - \mathbf{x}_i\|/r_0)$ is written as $w_i(\mathbf{x})$ for short. The support size r_0 is typically 2-4 times larger than the average distance to neighbouring nodes [55]. The unknown $\mathbf{a}$ is determined by minimizing the error term, i.e. $\partial J/\partial a_j = 0$ where a_j is the jth component of $\mathbf{a}$, then we have

$$\mathbf{a} = \mathbf{A}^{-1}(\mathbf{x}) \cdot \mathbf{B}(\mathbf{x})\mathbf{u}, \tag{2.4}$$

where

$$\mathbf{A}(\mathbf{x}) = \sum_{i}^{n} w_i(\mathbf{x})\mathbf{p}^{\mathrm{T}}(\mathbf{x}_i) \cdot \mathbf{p}(\mathbf{x}_i), \tag{2.5}$$

$$\mathbf{B}(\mathbf{x}) = [w_1(\mathbf{x})\mathbf{p}(\mathbf{x}_1), w_2(\mathbf{x})\mathbf{p}(\mathbf{x}_2), ..., w_n(\mathbf{x})\mathbf{p}(\mathbf{x}_n)], \tag{2.6}$$

$$\mathbf{u} = [u_1, u_2, ..., u_n]^{\mathrm{T}}, \tag{2.7}$$

where $\mathbf{u}$ is the displacement vector for n nodes. Substituting the above into Equation (2.1), the displacement approximation $u^h(\mathbf{x})$ is obtained by a linear combination of shape functions $\Phi_i(\mathbf{x})$ and nodal values u_i as

$$u^h(\mathbf{x}) = \sum_{i=1}^{n} \Phi_i(\mathbf{x})u_i = \mathbf{\Phi}^{\mathrm{T}}\mathbf{u}\,, \tag{2.8}$$

where i is the node index with coordinate $\mathbf{x}_i$ and n is the number of nodes with influence domain covering $\mathbf{x}$. The shape functions $\Phi_i(\mathbf{x})$ are defined by basis vectors $\mathbf{p}(\mathbf{x}_i)$ and weight functions $w_i(\mathbf{x})$,

$$\mathbf{\Phi}(\mathbf{x}) = \mathbf{p}^{\mathrm{T}}(\mathbf{x})\mathbf{A}^{-1}(\mathbf{x})\mathbf{B}(\mathbf{x}). \tag{2.9}$$

The partial derivatives of shape functions $\mathbf{\Phi}(\mathbf{x})$ are required to solve the PDEs and can be calculated by

$$\frac{\partial \mathbf{\Phi}(\mathbf{x})}{\partial x_j} = \frac{\partial \mathbf{p}^{\mathrm{T}}(\mathbf{x})}{\partial x_j}\mathbf{A}^{-1}(\mathbf{x})\mathbf{B}(\mathbf{x}) + \mathbf{p}^{\mathrm{T}}(\mathbf{x})\left[\frac{\partial \mathbf{A}^{-1}(\mathbf{x})}{\partial x_j}\mathbf{B}(\mathbf{x}) + \mathbf{A}^{-1}(\mathbf{x})\frac{\partial \mathbf{B}(\mathbf{x})}{\partial x_j}\right]. \tag{2.10}$$

Note that in the diffuse element method [52], the terms containing partial variation of $\mathbf{A}(\mathbf{x})$ and $\mathbf{B}(\mathbf{x})$ are neglected, where results are greatly detracted from the accurate value as in [2]. If the zero-order basis function is used, i.e. $\mathbf{p}(\mathbf{x}) = [1]$, the well-known Shephard's functions can be obtained,

$$\Phi_i(\mathbf{x}) = \frac{w_i(\mathbf{x})}{\sum_{i=1}^{n} w_i(\mathbf{x})}. \tag{2.11}$$

Because they use the MLS approximation, MMs can provide continuous results without using post-processing approaches, which are required in the FEM. While the FEM is interpolatory, MMs based on the MLS approximation are not and hence do not possess the Kronecker delta property. Extra techniques are therefore needed to impose essential

boundary conditions, which will be discussed in Section 2.6.

2.3 Equilibrium equation

Consider a problem domain Ω as in Figure 2.1, which is under external tractions $\bar{\mathbf{t}}$ on Γ_t and displacement boundary conditions $\bar{\mathbf{u}}$ on Γ_u. Here $\bar{\mathbf{t}}$ and $\bar{\mathbf{u}}$ are vectors, e.g. $\bar{\mathbf{t}} = [\bar{t}_x, \bar{t}_y, \bar{t}_z]^{\mathrm{T}}$ and $\bar{\mathbf{u}} = [\bar{u}_x, \bar{u}_y, \bar{u}_z]^{\mathrm{T}}$ in 3D, where over bars are used for constraints on boundaries. Subscripts x, y and z are components of $\bar{\mathbf{t}}$ and $\bar{\mathbf{u}}$ with their corresponding directions in the global Cartesian coordinate system and sometimes are described by x_1, x_2 and x_3 with subscripts 1, 2 and 3 in the tensorial form. In continuum mechanics, *stress* is a physical quantity representing the internal force between neighbouring particles in a continuous material. Choosing an arbitrary infinitesimal cube inside the body, the nine stress components are shown in Figure 2.2, where the two subscripts indicate the face and the direction respectively. The Cauchy stress tensor is

$$[\boldsymbol{\sigma}] = \begin{bmatrix} \sigma_{xx} & \sigma_{xy} & \sigma_{xz} \\ \sigma_{yx} & \sigma_{yy} & \sigma_{yz} \\ \sigma_{zx} & \sigma_{zy} & \sigma_{zz} \end{bmatrix} = \begin{bmatrix} \sigma_{11} & \sigma_{12} & \sigma_{13} \\ \sigma_{21} & \sigma_{22} & \sigma_{23} \\ \sigma_{31} & \sigma_{32} & \sigma_{33} \end{bmatrix}. \tag{2.12}$$

Due to the balance of shear stresses between neighbouring surfaces, only six stress components are independent, i.e.

$$\sigma_{xy} = \sigma_{yx}, \quad \sigma_{yz} = \sigma_{zy}, \quad \sigma_{xz} = \sigma_{zx}. \tag{2.13}$$

The stress tensor is also written in a vector format named as the Voigt notation, i.e.

$$\boldsymbol{\sigma} = [\sigma_{xx}, \sigma_{yy}, \sigma_{zz}, \sigma_{xy}, \sigma_{yz}, \sigma_{xz}]^{\mathrm{T}}. \tag{2.14}$$

For clarity in the thesis, the tensor format is written in square bracket, e.g. $[\boldsymbol{\sigma}]$, while the vector format in the Voigt notation is just bold, e.g. $\boldsymbol{\sigma}$. The equilibrium equations for

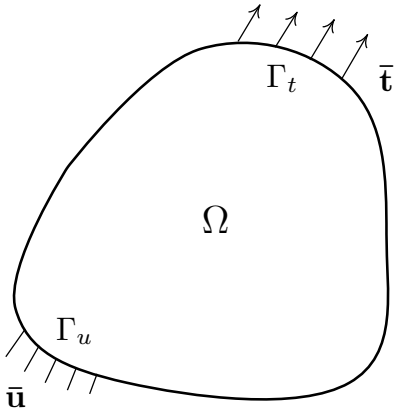

Figure 2.1: A problem domain with essential boundary conditions and external loadings.

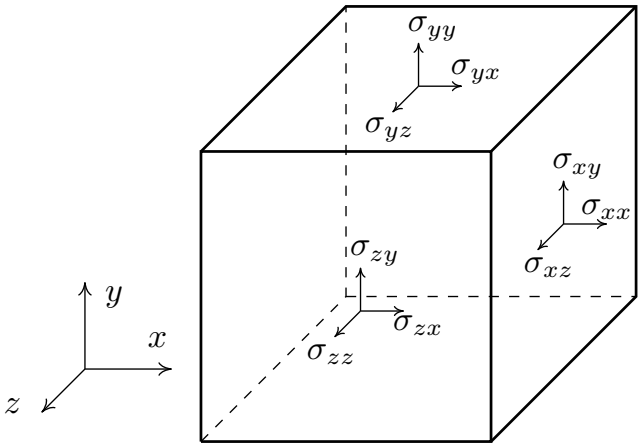

Figure 2.2: Stress components in an infinitesimal cube.

static problems require the force balance of the infinitesimal cube, i.e.

$$\begin{cases} \frac{\partial \sigma_{xx}}{\partial x} + \frac{\partial \sigma_{yx}}{\partial y} + \frac{\partial \sigma_{zx}}{\partial z} + b_x = 0, \\ \frac{\partial \sigma_{xy}}{\partial x} + \frac{\partial \sigma_{yy}}{\partial y} + \frac{\partial \sigma_{zy}}{\partial z} + b_y = 0, \\ \frac{\partial \sigma_{xz}}{\partial x} + \frac{\partial \sigma_{yz}}{\partial y} + \frac{\partial \sigma_{zz}}{\partial z} + b_z = 0, \end{cases} \tag{2.15}$$

where $\mathbf{b} = [b_x, b_y, b_z]^{\mathrm{T}}$ is the body force per unit volume. A tensorial form of equilibrium equations can be written as

$$\nabla \cdot [\boldsymbol{\sigma}] + \mathbf{b} = \mathbf{0} \qquad \text{in } \Omega, \tag{2.16}$$

or

$$\frac{\partial \sigma_{ij}}{\partial x_j} + b_i = 0, \quad i, j \in \{1, 2, 3\}, \tag{2.17}$$

in which the subscripts x, y and z are replaced by x_1, x_2 and x_3 respectively and $\partial \sigma_{ij}/\partial x_j$ uses Einstein summation. The solution of equilibrium equations should satisfy both essential boundary conditions and external loadings,

$$[\boldsymbol{\sigma}] \cdot \mathbf{n} = \bar{\mathbf{t}} \qquad \text{on } \Gamma_t, \tag{2.18}$$

$$\mathbf{u} = \bar{\mathbf{u}} \qquad \text{on } \Gamma_u, \tag{2.19}$$

where $\mathbf{n}$ is the outer normal of boundaries Γ, i.e. $\mathbf{n} = [n_x, n_y, n_z]^{\mathrm{T}}$ and $\boldsymbol{u}$ is the displacement vector for one node, $\boldsymbol{u} = [u_x, u_y, u_z]^{\mathrm{T}}$. If the stress $\boldsymbol{\sigma}$ uses the Voigt notation of Equation (2.14), Equation (2.18) becomes $[\mathbf{n}]^{\mathrm{T}} \cdot \boldsymbol{\sigma} = \bar{\mathbf{t}}$ where $[\mathbf{n}]^{\mathrm{T}}$ is written as

$$[\mathbf{n}]^{\mathrm{T}} = \begin{bmatrix} n_x & 0 & 0 & n_y & 0 & n_z \\ 0 & n_y & 0 & n_x & n_z & 0 \\ 0 & 0 & n_z & 0 & n_y & n_x \end{bmatrix}. \tag{2.20}$$

To solve the equilibrium equations, the relationship between stress $\boldsymbol{\sigma}$ and displacement $\mathbf{u}$ should be specified. In solid mechanics, *strain* is defined as a geometrical measurement representing the relative deformation between neighbouring particles in a continuous material. Similar to the stress expression, strain in matrix is defined as

$$[\boldsymbol{\varepsilon}] = \begin{bmatrix} \varepsilon_{xx} & \varepsilon_{xy} & \varepsilon_{xz} \\ \varepsilon_{yx} & \varepsilon_{yy} & \varepsilon_{yz} \\ \varepsilon_{zx} & \varepsilon_{zy} & \varepsilon_{zz} \end{bmatrix} = \begin{bmatrix} \varepsilon_{11} & \varepsilon_{12} & \varepsilon_{13} \\ \varepsilon_{21} & \varepsilon_{22} & \varepsilon_{23} \\ \varepsilon_{31} & \varepsilon_{32} & \varepsilon_{33} \end{bmatrix}, \tag{2.21}$$

and strain in the Voigt notation is

$$\boldsymbol{\varepsilon} = [\varepsilon_{xx}, \varepsilon_{yy}, \varepsilon_{zz}, \gamma_{xy}, \gamma_{yz}, \gamma_{xz}]^{\mathrm{T}}, \tag{2.22}$$

where engineering shear strains are used, $\gamma_{xy} = 2\varepsilon_{xy}$, $\gamma_{yz} = 2\varepsilon_{yz}$, $\gamma_{xz} = 2\varepsilon_{xz}$. The relation between stress and strain is called the *constitutive model*, and the standard form for

isotropic elastic materials is

$$\varepsilon_{ij} = \frac{1}{E}[(1+\nu)\sigma_{ij} - \nu\sigma_{kk}\delta_{ij}], \tag{2.23}$$

where δ_{ij} is the Kronecker delta function, i.e.

$$\delta_{ij} = \begin{cases} 0 & \text{if } i \neq j, \\ 1 & \text{if } i = j. \end{cases} \tag{2.24}$$

Also, stresses can be written in terms of strains as

$$\sigma_{ij} = \frac{2\mu\nu}{1-2\nu}\delta_{ij}\varepsilon_{kk} + 2\mu\varepsilon_{ij}, \tag{2.25}$$

where E and ν are Young's modulus and Poisson's ratio respectively, μ is the shear modulus of the material and has the relationship with other material properties,

$$\mu = \frac{E}{2(1+\nu)}. \tag{2.26}$$

Equation (2.23) can be written in matrix form, as

$$\boldsymbol{\sigma} = \mathbf{D} \cdot \boldsymbol{\varepsilon}, \tag{2.27}$$

where $\mathbf{D}$ is the constitutive matrix, e.g. for an isotropic linear elastic material in 3D,

$$\mathbf{D} = \frac{E}{(1+\nu)(1-2\nu)} \begin{bmatrix} 1-\nu & \nu & \nu & 0 & 0 & 0 \\ \nu & 1-\nu & \nu & 0 & 0 & 0 \\ \nu & \nu & 1-\nu & 0 & 0 & 0 \\ 0 & 0 & 0 & \frac{1-2\nu}{2} & 0 & 0 \\ 0 & 0 & 0 & 0 & \frac{1-2\nu}{2} & 0 \\ 0 & 0 & 0 & 0 & 0 & \frac{1-2\nu}{2} \end{bmatrix}. \tag{2.28}$$

The linear elasticity theory can be converted to 2D with the assumptions of plane stress or plane strain. The former assumes all stress components in the z direction are zero for problems with small dimension in that direction, i.e. $\sigma_{zz} = \sigma_{yz} = \sigma_{xz} = 0$. In contrast, the

plane strain approximation assumes all strain components to be zero in the z direction, i.e. $\varepsilon_{zz} = \varepsilon_{yz} = \varepsilon_{xz} = 0$, and is suitable for problems which are thick in the z direction. With these assumptions, the 2D constitutive matrix $\mathbf{D}$ can be written as

$$\mathbf{D} = \frac{\bar{E}}{1-\bar{\nu}} \begin{bmatrix} 1 & \bar{\nu} & 0 \\ \bar{\nu} & 1 & 0 \\ 0 & 0 & \frac{1-\bar{\nu}}{2} \end{bmatrix}, \tag{2.29}$$

where

$$\bar{E} = \begin{cases} E & \text{plane stress,} \\ \frac{E}{1-\nu^2} & \text{plane strain,} \end{cases} \qquad \bar{\nu} = \begin{cases} \nu & \text{plane stress,} \\ \frac{\nu}{1-\nu} & \text{plane strain.} \end{cases} \tag{2.30}$$

The relation between displacement and strain follows the *compatibility* condition, e.g. for small strain,

$$\varepsilon_{ij} = \frac{1}{2}\left(\frac{\partial u_i}{\partial x_j} + \frac{\partial u_j}{\partial x_i}\right). \tag{2.31}$$

Equation (2.31) can be written in tensorial form as

$$\boldsymbol{\varepsilon} = \mathbf{L}\mathbf{u}, \tag{2.32}$$

where $\mathbf{u}$ is the displacement vector for one node and $\mathbf{L}$ is a differential operator, e.g. for 3D cases,

$$\mathbf{L} = \begin{bmatrix} \frac{\partial}{\partial x} & 0 & 0 & \frac{\partial}{\partial y} & 0 & \frac{\partial}{\partial z} \\ 0 & \frac{\partial}{\partial y} & 0 & \frac{\partial}{\partial x} & \frac{\partial}{\partial z} & 0 \\ 0 & 0 & \frac{\partial}{\partial z} & 0 & \frac{\partial}{\partial y} & \frac{\partial}{\partial x} \end{bmatrix}^{\mathrm{T}}, \tag{2.33}$$

and in 2D,

$$\mathbf{L} = \begin{bmatrix} \frac{\partial}{\partial x} & 0 & \frac{\partial}{\partial y} \\ 0 & \frac{\partial}{\partial y} & \frac{\partial}{\partial x} \end{bmatrix}^{\mathrm{T}}. \tag{2.34}$$

2.4 Weak form

Governing equations in Equation (2.16) are in the strong form and usually difficult to solve in all but trivial cases. The difficulties lie in the requirement of second-order consistency over the entire problem domain. Alternatively, the weak form of the governing equations

is widely used in numerical methods in that only the first order consistency is required for a second order PDE. The weak form is built on the basis of Hamilton's principle. In continuum mechanics, the system energy L consists of kinetic energy T, internal energy U and external work W_f, as

$$L = T - U + W_f. \tag{2.35}$$

For static problems, T is zero and the external work is

$$W_f = \int_\Omega \mathbf{u}^{\mathrm{T}} \mathbf{b} \mathrm{d}\Omega + \int_{\Gamma_t} \mathbf{u}^{\mathrm{T}} \bar{\mathbf{t}} \mathrm{d}\Gamma_t. \tag{2.36}$$

Assuming the material is linear elastic, the internal energy U is

$$U = \frac{1}{2} \int_\Omega \boldsymbol{\varepsilon}^{\mathrm{T}} \boldsymbol{\sigma} \mathrm{d}\Omega. \tag{2.37}$$

The variational form of Equation (2.35) satisfies all possible states while the actual solution makes the function L a minimum, i.e. $\delta L = 0$ where δ indicates the virtual status. The weak form of governing equations can be obtained as

$$\int_{\Gamma_t} \delta \mathbf{u}^{\mathrm{T}} \bar{\mathbf{t}} \, \mathrm{d}\Gamma_t + \int_\Omega \delta \mathbf{u}^{\mathrm{T}} \mathbf{b} \mathrm{d}\Omega - \int_\Omega \delta \boldsymbol{\varepsilon}^{\mathrm{T}} \boldsymbol{\sigma} \mathrm{d}\Omega = 0. \tag{2.38}$$

Equation (2.38) can also be regarded as the principle of virtual work, i.e. the virtual work by external forces and internal forces are equal.

Considering the constitutive model in Equation (2.27) and the compatibility in Equation (2.32), the weak form becomes

$$\int_\Omega \delta(\mathbf{L}\mathbf{u})^{\mathrm{T}} \mathbf{D} (\mathbf{L}\mathbf{u}) \mathrm{d}\Omega = \int_{\Gamma_t} \delta \mathbf{u}^{\mathrm{T}} \bar{\mathbf{t}} \, \mathrm{d}\Gamma_t + \int_\Omega \delta \mathbf{u}^{\mathrm{T}} \mathbf{b} \mathrm{d}\Omega. \tag{2.39}$$

The discretisation of the weak form is obtained using Equation (2.8), which yields

$$\mathbf{K}\mathbf{u} = \mathbf{f}, \tag{2.40}$$

where

$$\mathbf{K}_{ij} = \int_\Omega \mathbf{B}_i^{\mathrm{T}} \mathbf{D} \mathbf{B}_j \mathrm{d}\Omega, \tag{2.41a}$$

$$\mathbf{f}_i = \int_{\Gamma_t} \Phi_i \bar{\mathbf{t}} \, \mathrm{d}\Gamma_t + \int_{\Omega} \Phi_i \mathbf{b} \mathrm{d}\Omega, \tag{2.41b}$$

$$\mathbf{B}_i = \begin{bmatrix} \Phi_{i,x} & 0 \\ 0 & \Phi_{i,y} \\ \Phi_{i,y} & \Phi_{i,x} \end{bmatrix}. \tag{2.41c}$$

Here the subscripts in the bold variable $\mathbf{K}_{ij}$ do not mean the components of a matrix but stand for the stiffness between the nodes i and j.

2.5 Integration

The weak form Equation (2.40) involves integration over the entire problem domain. In the conventional FEM, Gaussian quadrature is used on each element and then the results are summed together. This idea is borrowed in some meshless methods and background meshes are used for integration. Comparing with the FEM using element vertexes as nodes, background meshes in meshless methods can be independent of nodes. To pursue truly meshless methods, other integration approaches have been developed, either by nodal integration or by integration over supports, which are both introduced below.

2.5.1 Gaussian quadrature

Gaussian quadrature of a function or integral is an approximation of the definite integral and is usually stated as a weighted summation of function values at some specified points within the integration domain. The domain of integration is conventionally taken as [-1,1] and arbitrary ranges can be converted to this conventional range, e.g. for a function $f(x)$ with integration range [a,b],

$$\int_a^b f(x)\mathrm{d}x = \frac{b-a}{2} \int_{-1}^{1} f(\frac{b-a}{2}x + \frac{b+a}{2})\mathrm{d}x. \tag{2.42}$$

The Gaussian quadrature can be written as

$$\int_{-1}^{1} f(x)\mathrm{d}x = \sum_{i=1}^{n} w_i f(x_i), \tag{2.43}$$

where n is the number of Gauss points, i is the index, and x_i and w_i are the location and weight respectively of a point i. The determination of w_i and x_i can be found in many

Table 2.1: Weights and points in Gaussian quadrature.

n	x_i	w_i
2	± 0.57735	1
3	0	0.88889
	± 0.77460	0.55556
4	± 0.33998	0.65215
	± 0.86114	0.34785
5	0	0.56889
	± 0.53847	0.47863
	± 0.90618	0.23693
6	± 0.66121	0.36076
	± 0.23862	0.46791
	± 0.93247	0.17132

n	x_i	w_i
7	0	0.41796
	± 0.40585	0.38183
	± 0.74153	0.27971
	± 0.94911	0.12948
8	± 0.18343	0.36268
	± 0.52553	0.31371
	± 0.79667	0.22238
	± 0.96029	0.10123

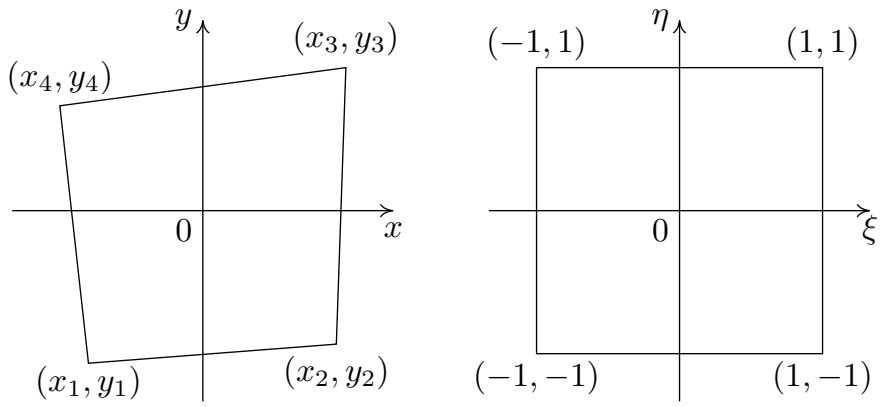

Figure 2.3: Gaussian quadrature from global coordinates to local coordinates.

mathematical references e.g. [219] and the values are given directly in Table 2.1.

The extension of the Gaussian quadrature from 1D to high-order dimensions is straightforward. For instance, if integration is required over a quadrilateral element in 2D global coordinates as in Figure 2.3 (a), the integration is first given over a standard element in local coordinates, i.e.

$$\int_{-1}^{1}\int_{-1}^{1} f(\xi,\eta)\mathrm{d}\xi\mathrm{d}\eta = \sum_{i}^{n}\sum_{j}^{n} w_i w_j f(\xi_i,\eta_j), \tag{2.44}$$

where n is the order of Gaussian quadrature and w_i, w_j, ξ_i and η_j can be selected from Table 2.1. The transformation between global coordinates and local coordinates is obtained using the chain rule,

$$\begin{bmatrix} \mathrm{d}x \\ \mathrm{d}y \end{bmatrix} = \begin{bmatrix} \frac{\partial x}{\partial \xi} & \frac{\partial x}{\partial \eta} \\ \frac{\partial y}{\partial \xi} & \frac{\partial y}{\partial \eta} \end{bmatrix} \begin{bmatrix} \mathrm{d}\xi \\ \mathrm{d}\eta \end{bmatrix} = \boldsymbol{J}^{\mathrm{T}} \begin{bmatrix} \mathrm{d}\xi \\ \mathrm{d}\eta \end{bmatrix}, \tag{2.45}$$

where $\boldsymbol{J}$ is the Jacobian matrix, and the scalar symbol J is the determinant of $\boldsymbol{J}$, i.e. $J = \det(\boldsymbol{J})$. The area of an infinitesimal element can be written as

$$\mathrm{d}\Omega = \|\mathrm{d}\vec{x} \times \mathrm{d}\vec{y}\| = \|(\frac{\partial x}{\partial \xi}\mathrm{d}\vec{\xi} + \frac{\partial x}{\partial \eta}\mathrm{d}\vec{\eta}) \times (\frac{\partial y}{\partial \xi}\mathrm{d}\vec{\xi} + \frac{\partial y}{\partial \eta}\mathrm{d}\vec{\eta})\| = J\|\mathrm{d}\vec{\xi} \times \mathrm{d}\vec{\eta}\|. \tag{2.46}$$

The integration over an arbitrary quadrilateral element is then given as

$$\int_{\Omega} f(x,y)\mathrm{d}\Omega = \int_{-1}^{1}\int_{-1}^{1} f\Big(x(\xi), y(\eta)\Big) J \mathrm{d}\xi \mathrm{d}\eta = \sum_{i}^{n}\sum_{j}^{n} w_i w_j J f\Big(x(\xi_i), y(\eta_j)\Big). \tag{2.47}$$

Gauss points in global coordinates are located by ξ_i and η_j in local coordinates following the mapping law between the two coordinate systems, i.e.

$$x = \sum_{k=1}^{4} N_k(\xi,\eta) x_k, \qquad y = \sum_{k=1}^{4} N_k(\xi,\eta) y_k, \tag{2.48}$$

where $N_k(\xi,\eta)$ are shape functions in Gaussian quadrature, i.e. for a linear quad,

$$\begin{aligned} N_1 &= \frac{(1-\xi)(1-\eta)}{4}, \quad N_2 = \frac{(1+\xi)(1-\eta)}{4}, \\ N_3 &= \frac{(1+\xi)(1+\eta)}{4}, \quad N_4 = \frac{(1-\xi)(1+\eta)}{4}. \end{aligned} \tag{2.49}$$

The Jacobian matrix is determined as

$$\boldsymbol{J} = \begin{bmatrix} \sum_{k=1}^{4} \frac{\partial N_k}{\partial \xi} x_k & \sum_{k=1}^{4} \frac{\partial N_k}{\partial \xi} y_k \\ \sum_{k=1}^{4} \frac{\partial N_k}{\partial \eta} x_k & \sum_{k=1}^{4} \frac{\partial N_k}{\partial \eta} y_k \end{bmatrix}. \tag{2.50}$$

2.5.2 Direct nodal integration

Nodal integration is a method for calculating a spatial integration by sampling the integrand only at nodes, which can be regarded as the order-one Gaussian quadrature,

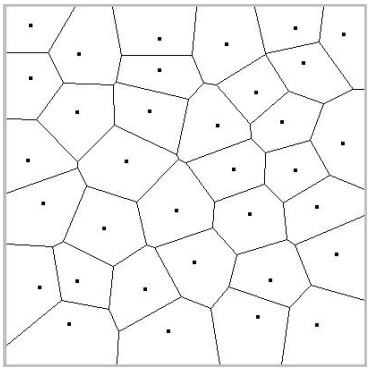

Figure 2.4: Voronoi cells for nodal integration.

and no background mesh is required so the resulting scheme is truly meshless. A spatial integration can be written as

$$\int_{\Omega} f(x,y)\mathrm{d}\Omega = \sum_{i=1}^{n} q_i f(x_i, y_i), \tag{2.51}$$

where i is the index of nodes and a node i has a location of (x_i, y_i) and weight q_i is a fraction of the total area Ω. There are several methods to choose the weight, e.g. in [113],

$$q_i = \frac{a_i r_i^2}{\sum_{i=1}^{n} a_i r_i^2} A_{\Omega}, \tag{2.52}$$

where A_{Ω} is the integral area of Ω, r_i is the support size associated with node i and a_i is the fraction of the support according to the location of node i, e.g. for interior nodes $a_i = 1$; for nodes at edges $a_i = 0.5$; for nodes at corners $a_i = 0.25$.

An alternative to define the weight q_i in Equation (2.51) is through Voronoi cells [114, 202, 220], as in Figure 2.4. The area of a Voronoi cell A_i is the weight for a node i, i.e. $q_i = A_i$. Since the nodal integration is like order-one Gaussian integration, it is more efficient than higher order Gaussian quadrature but suffers however from serious stability issues linked to rank deficiency when integration points cannot collect sufficient information. Some stress points are added between nodes as additional quadrature points but are not used in the problem discretisation [202].

2.5.3 Integration over supports

Except for the integration methods mentioned above, the integration can be calculated over the support of each node rather than using background cells, which is ideal for

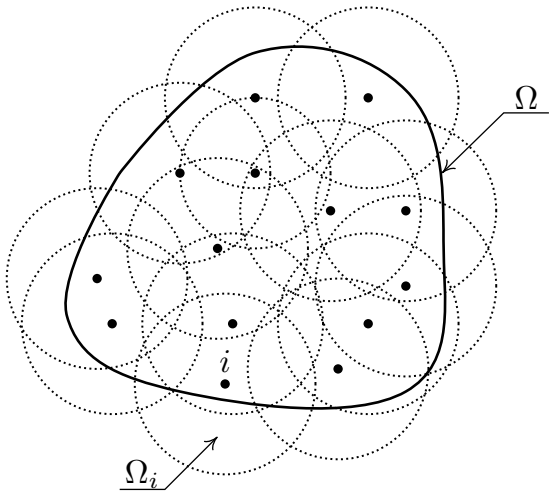

Figure 2.5: Computational model for integration over supports.

methods based on a *local* weak form such as the MLPG and can also be used for other Galerkin MMs as in [115, 221, 222]. Dividing the intersections of supports has been tried in [221] and applied in adaptive calculations, but these intersections form complex geometries which are usually too complicated for practical applications. The partition of unity quadrature is more promising where no division is required [115, 222]. An integration for function $f(x, y)$ over a domain Ω can be written as

$$\int_{\Omega} f(x,y)\mathrm{d}\Omega = \int_{\Omega} f(x,y) H \sum_{i=1}^{n} w_i \mathrm{d}\Omega = \sum_{i=1}^{n} \int_{\Omega_i} f(x,y) H w_i \mathrm{d}\Omega, \tag{2.53}$$

where n is the number of nodes, i is the index of a node i with support Ω_i and weight function w_i, as in Figure 2.5, $\Omega \subseteq \bigcup_{i=1}^{n} \Omega_i$. All weight functions follow the partition of unity, i.e. $\sum_{i=1}^{n} w_i(x, y) = 1$, and $w_i(x, y) = 0$ if $(x, y) \notin \Omega_i$. w_i can be chosen to coincide with MLS shape functions or through Shephard's functions in Equation (2.11). H is the function indicating whether a point is inside the domain Ω,

$$H(x,y) = \begin{cases} 1 & \text{if } (x,y) \in \Omega, \\ 0 & \text{if } (x,y) \notin \Omega. \end{cases} \tag{2.54}$$

Overall, nodal integration and integration over supports are faster than Gauss integration and no background meshes are required, which is desired to achieve truly meshless methods, however, the speed of these two methods comes with a sacrifice of accuracy, as

mentioned in [114, 115]. For fracture modelling, there are high stress gradients around the crack tip, and crack propagation is sensitive to numerical errors in the problem approximation. Therefore, Gaussian integration is used in this thesis, to guarantee the integration accuracy for modelling crack problems.

2.6 Imposition of boundary conditions

One disadvantage of the MLS approximation is lack of the Kronecker delta property, due to which essential boundary conditions cannot be imposed directly as in the FEM. A number of techniques have been developed to solve this problem by modifying the weak form [2, 54, 109, 110] or by employing shape function with the Kronecker delta property [111, 112]. The most common approaches are Lagrange multipliers, penalty and Nitsche's methods.

2.6.1 Lagrange multipliers

In the Lagrange multiplier method, essential boundary conditions are incorporated into the Hamilton Equation (2.35) with a vector of unknown Lagrange multipliers $\boldsymbol{\lambda}$, i.e.

$$[L] = L + \int_{\Gamma_u} \boldsymbol{\lambda}^{\mathrm{T}}(\mathbf{u} - \bar{\mathbf{u}})\,\mathrm{d}\Gamma_u. \tag{2.55}$$

Equation (2.55) ensure satisfaction of the displacement boundary condition, although trial functions do not satisfy Equation (2.19). The weak form equation in Equation (2.38) is modified to

$$\int_{\Omega} \delta\boldsymbol{\varepsilon}^{\mathrm{T}}\boldsymbol{\sigma}\,\mathrm{d}\Omega - \int_{\Gamma_u} \delta\boldsymbol{\lambda}^{\mathrm{T}}(\mathbf{u} - \bar{\mathbf{u}})\,\mathrm{d}\Gamma_u - \int_{\Gamma_u} \delta\mathbf{u}^{\mathrm{T}}\boldsymbol{\lambda}\,\mathrm{d}\Gamma_u = \int_{\Omega} \delta\mathbf{u}^{\mathrm{T}}\mathbf{b}\,\mathrm{d}\Omega + \int_{\Gamma_t} \delta\mathbf{u}^{\mathrm{T}}\bar{\mathbf{t}}\,\mathrm{d}\Gamma_t. \tag{2.56}$$

The physical meaning of Lagrange multipliers $\boldsymbol{\lambda}$ is the traction along essential boundary Γ_u as mentioned in [54]. The Lagrange multipliers $\boldsymbol{\lambda}$ are expressed by arc length s along the boundary and shape functions $N_i(s)$,

$$\boldsymbol{\lambda}(\mathbf{x}) = \sum_{i=1}^{k} N_i(s)\lambda_i, \quad \mathbf{x} \in \Gamma_u\,, \tag{2.57}$$

$$\delta\boldsymbol{\lambda}(\mathbf{x}) = \sum_{i=1}^{k} N_i(s)\delta\lambda_i, \quad \mathbf{x} \in \Gamma_u\,, \tag{2.58}$$

where k is the total number of constraints at essential boundaries, λ_i are nodal values of Lagrange multipliers and $\delta\lambda_i$ are the virtual status. The determination of $N_i(s)$ can be through the same shape functions for displacement approximation or be constructed by the Lagrangian interpolation,

$$N_i(s) = \frac{(s-s_1)\cdots(s-s_{i-1})(s-s_{i+1})\cdots(s-s_k)}{(s_i-s_1)\cdots(s_i-s_{i-1})(s_i-s_{i+1})\cdots(s_i-s_k)}. \tag{2.59}$$

With Lagrange multipliers, Equation (2.40) is modified to

$$\begin{bmatrix} \mathbf{K} & \mathbf{G} \\ \mathbf{G}^{\mathrm{T}} & \mathbf{0} \end{bmatrix} \begin{Bmatrix} \mathbf{u} \\ \boldsymbol{\lambda} \end{Bmatrix} = \begin{Bmatrix} \mathbf{f} \\ \mathbf{q} \end{Bmatrix}, \tag{2.60}$$

where $\mathbf{K}$ and $\mathbf{f}$ are obtained by Equation (2.41) and

$$\mathbf{G}_{ik} = -\int_{\Gamma_u} \Phi_i N_k \mathrm{d}\Gamma_u, \tag{2.61a}$$

$$\mathbf{q}_k = -\int_{\Gamma_u} N_k \bar{\mathbf{u}} \mathrm{d}\Gamma_u. \tag{2.61b}$$

Although the number of system unknowns increases and the system stiffness matrix is not definite positive any more, essential boundary conditions are rigorously enforced in the weak form equations, therefore accurate results can be achieved [2, 3]. The Lagrange multipliers can be replaced by their physical counterpart at the outset, so that the modified weak form results in a positive definite and sparse matrix [54]. However, the accuracy is somewhat reduced as in [108], and more nodes are required in the approximation.

2.6.2 The penalty method

Similar to Lagrange multipliers, the Hamilton equations can also be modified by introducing a penalty factor β [109],

$$L = L - \frac{1}{2}\int_{\Gamma_u} \beta(\mathbf{u}-\bar{\mathbf{u}})^{\mathrm{T}}(\mathbf{u}-\bar{\mathbf{u}})\,\mathrm{d}\Gamma_u. \tag{2.62}$$

Then the weak form of Equation (2.38) becomes

$$\int_{\Omega} \delta\boldsymbol{\varepsilon}^{\mathrm{T}}\boldsymbol{\sigma}\,\mathrm{d}\Omega + \int_{\Gamma_u} \beta\delta\mathbf{u}^{\mathrm{T}}(\mathbf{u}-\bar{\mathbf{u}})\,\mathrm{d}\Gamma_u = \int_{\Omega} \delta\mathbf{u}^{\mathrm{T}}\mathbf{b}\,\mathrm{d}\Omega + \int_{\Gamma_t} \delta\mathbf{u}^{\mathrm{T}}\bar{\mathbf{t}}\,\mathrm{d}\Gamma_t. \tag{2.63}$$

The discrete weak form of Equation (2.40) is changed to

$$(\mathbf{K}+\beta\mathbf{K}^u)\mathbf{u} = \mathbf{f}+\beta\mathbf{f}^u, \tag{2.64}$$

where

$$\mathbf{K}^u_{ij} = \int_{\Gamma_u} \Phi_i\Phi_j \mathrm{d}\Gamma_u, \tag{2.65a}$$

$$\mathbf{f}^u_i = \int_{\Gamma_u} \Phi_i\bar{\mathbf{u}}\mathrm{d}\Gamma_u. \tag{2.65b}$$

Since β is a predefined constant factor ($\beta \gg 1$, e.g. $\beta = 10^5 E$ in [223]), there are no extra unknowns compared with the Lagrange multiplier method, and the system stiffness matrix remains positive definite. However, a very large penalty factor β will lead to the system becoming ill-conditioned, and how to define suitable values of β is still problematic [109].

2.6.3 Nitsche's method

Nitsche's method is considered an improvement on the penalty method which is achieved by adding a number of terms to the weak form of system equations rather than introducing only one penalty term [110], i.e.

$$L = L - \frac{1}{2}\int_{\Gamma_u} \beta(\mathbf{u}-\bar{\mathbf{u}})^{\mathrm{T}}(\mathbf{u}-\bar{\mathbf{u}})\,\mathrm{d}\Gamma_u + \int_{\Gamma_u} \mathbf{t}^{\mathrm{T}}(\mathbf{u}-\bar{\mathbf{u}})\,\mathrm{d}\Gamma_u\,, \tag{2.66}$$

where $\mathbf{t}$ is the reaction force at the displacement boundary Γ_u and is obtained from the stress field as $\mathbf{t} = [\boldsymbol{\sigma}]\cdot\mathbf{n}$. The governing equation of Equation (2.38) becomes

$$\begin{aligned} &\int_{\Omega} \delta\boldsymbol{\varepsilon}^{\mathrm{T}}\boldsymbol{\sigma}\,\mathrm{d}\Omega - \int_{\Gamma_u} \delta\mathbf{t}^{\mathrm{T}}(\mathbf{u}-\bar{\mathbf{u}})\,\mathrm{d}\Gamma_u - \int_{\Gamma_u} \mathbf{t}^{\mathrm{T}}\delta\mathbf{u}\,\mathrm{d}\Gamma_u + \\ &\int_{\Gamma_u} \beta(\mathbf{u}-\bar{\mathbf{u}})^{\mathrm{T}}\delta\mathbf{u}\,\mathrm{d}\Gamma_u = \int_{\Omega} \delta\mathbf{u}^{\mathrm{T}}\mathbf{b}\,\mathrm{d}\Omega + \int_{\Gamma_t} \delta\mathbf{u}^{\mathrm{T}}\bar{\mathbf{t}}\,\mathrm{d}\Gamma_t. \end{aligned} \tag{2.67}$$

The discrete weak form is

$$(\mathbf{K} + \beta\mathbf{K}^u - \mathbf{K}^t)\mathbf{u} = \mathbf{f} + \beta\mathbf{f}^u - \mathbf{f}^t, \tag{2.68}$$

where $\mathbf{K}$, $\mathbf{K}^u$ and $\mathbf{f}^u$ are the same as above. $\mathbf{K}^t$ and $\mathbf{f}^t$ are defined by

$$\mathbf{K}^t_{ij} = \int_{\Gamma_u} \Phi_i^{\mathrm{T}}[\mathbf{n}]^{\mathrm{T}}\mathbf{D}\mathbf{B}_j \mathrm{d}\Gamma_u + \int_{\Gamma_u} \mathbf{B}_i^{\mathrm{T}}\mathbf{D}\cdot[\mathbf{n}]\Phi_j \mathrm{d}\Gamma_u, \tag{2.69a}$$

$$\mathbf{f}^t_i = \int_{\Gamma_u} \mathbf{B}_i^{\mathrm{T}}\mathbf{D}\cdot[\mathbf{n}]\bar{\mathbf{u}}\mathrm{d}\Gamma_u. \tag{2.69b}$$

Nitsche's method combines the advantages of the Lagrange multiplier method and the penalty method, by which a considerably smaller β can be chosen to avoid ill-conditioning, and is therefore superior than these two methods [110].

2.6.4 Coupling with finite elements

Since the FEM possesses the Kronecker delta property, essential boundary conditions can be imposed by the combination of finite elements and meshless approximations. This idea was proposed in [108, 224], where a string of elements were used along the essential boundaries, and FEM and EFGM shape functions are coupled with modified consistency conditions, as in [224]. The merits of both the FEM and the EFGM can be used, and the procedure has been applied to both linear and non-linear problems [225]. The advantage of this approach is the easy imposition of essential boundary conditions due to the use of finite elements. However, transition elements or interface elements have to be generated, and the coupling process usually leads to a complicated code structure.

Overall, essential boundary conditions can be imposed to the weak form in the EFGM by Lagrange multiplier method, penalty method, Nitsche's method or coupling with the FEM. Both penalty and Nitsche's methods use penalty terms to constrain displacement at essential boundaries and bring no extra unknown, but a larger penalty factor makes the global stiffness matrix more ill-conditioned. Coupling the FEM and the EFGM has an issue of complex code structure for the communication between the two methods, although displacement constraints can be obtained directly by using finite elements. The Lagrange multiplier method brings extra unknowns and leads to zero terms in the diagonal of the stiffness matrix, but displacement constraints are rigorously ensured. Hence, the Lagrange

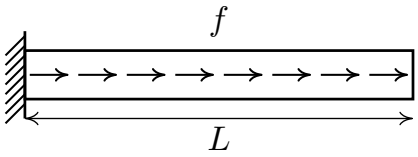

Figure 2.6: 1D bar under body force.

multiplier method is used in this thesis for imposing essential boundary conditions.

2.7 Example

An example of a 1D bar is now used to demonstrate the differences between the FEM and the EFGM. The configuration of the problem is depicted in Figure 2.6. The length of the bar $L = 1$ and the section area $A = 1$. The left side is fixed and it is under a body force $f = 1$. The material is assumed linear elastic with Young's modulus $E = 1$ in compatible units. The governing equations are

$$EA\frac{\mathrm{d}^2 u}{\mathrm{d}x^2} + f = 0, \tag{2.70a}$$

$$u|_{x=0} = 0, \quad \sigma|_{x=L} = 0, \tag{2.70b}$$

where the strain-displacement relationship $\varepsilon(x) = \partial u(x)/\partial x$ and the constitutive law $\sigma(x) = E\varepsilon(x)$ are used. The exact solutions of displacement and stress are

$$u(x) = \frac{fL}{EA}\Big(x - 0.5\frac{x^2}{L}\Big), \tag{2.71a}$$

$$\sigma(x) = \frac{fL}{A}(1 - \frac{x}{L}). \tag{2.71b}$$

The 1D bar is discretised initially with 11 nodes and 10 elements in both the FEM and the EFGM. The support size in the EFGM is set as

$$r_0 = d_s\, l_0, \tag{2.72}$$

where l_0 is the average distance between nodes and $d_s = 2.2$. In the FEM, these elements are used to build shape functions, while in the EFGM they are only used for integration. A comparison of shape functions and derivatives between the FEM and the EFGM can be seen in Figure 2.7. For the EFGM, both shape functions and derivatives are smooth,

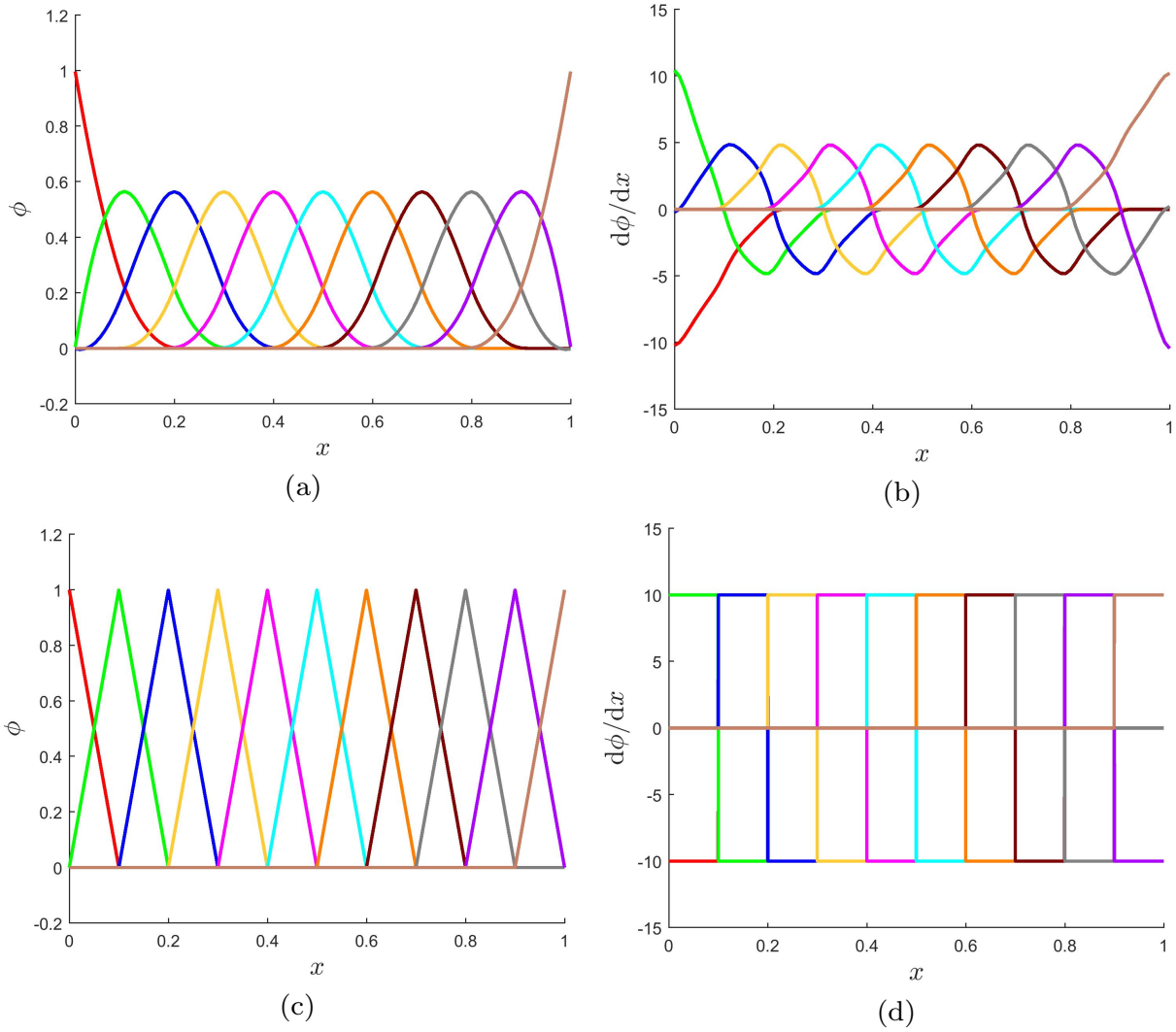

Figure 2.7: Comparison of shape functions between the FEM and the EFGM: (a-b) EFGM shape functions and their derivatives; (c-d) FEM shape functions and their derivatives.

but shape functions cannot satisfy the Kronecker delta property in Equation (2.24) as shown in Figure 2.7 (a), although the node at the left end seems not to be influenced by other nodes. In contrast shape functions are linear in the FEM, and their derivatives are constant within an element but discontinuous between two elements. Shape functions in the FEM can satisfy the Kronecker delta property, as shown in Figure 2.7 (c).

Results of displacements and stresses are presented in Figure 2.8. Displacements by both methods match with the theoretical solution in Equation (2.71). However, stresses obtained by the FEM are inaccurate while those obtained using the EFGM are much more accurate. Due to the derivatives of shape functions in the FEM are constant within one element, the stresses are also constant in the element and decrease gradually along

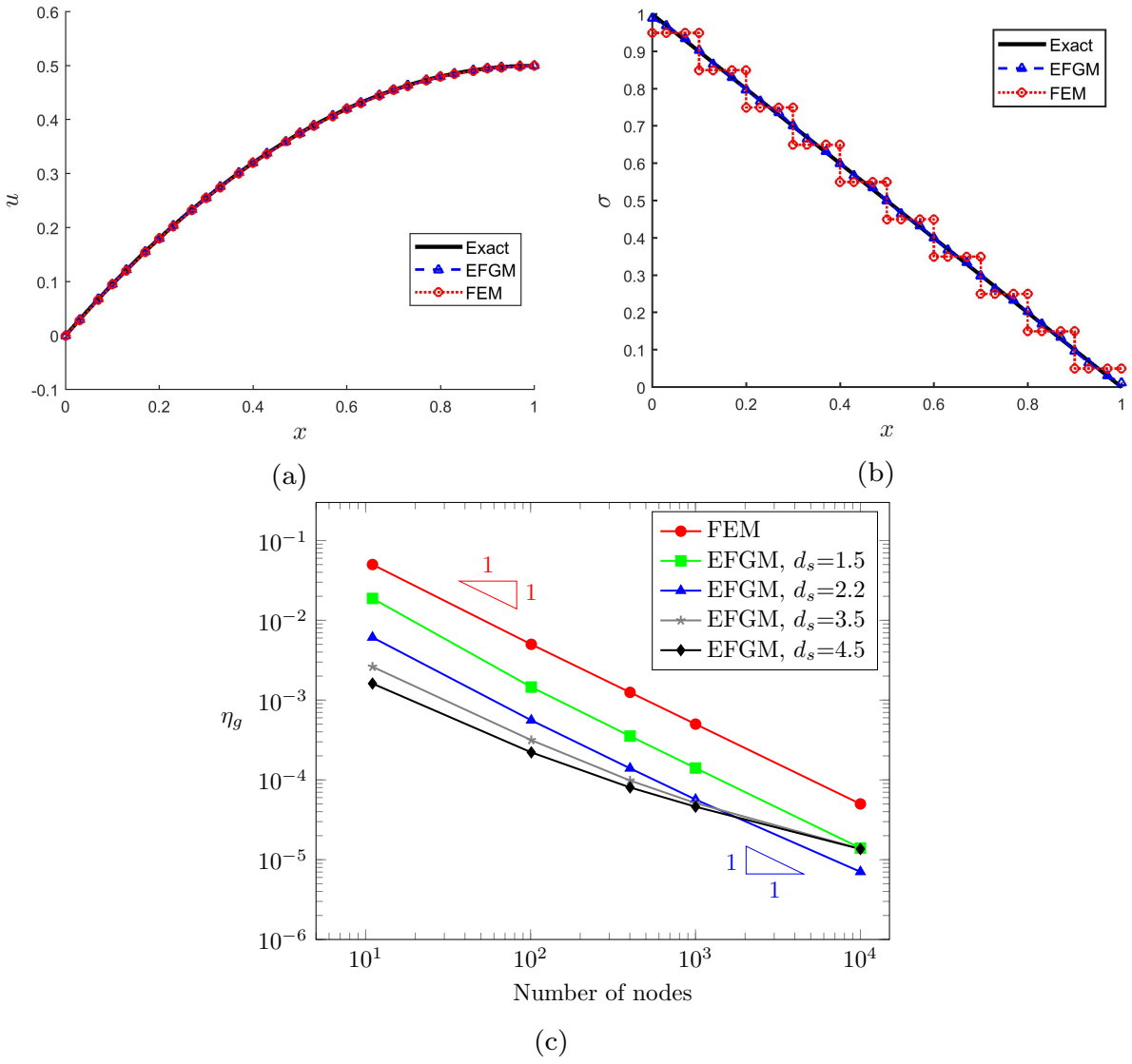

Figure 2.8: Comparison of results for the 1D bar problem between the FEM and the EFGM: (a) displacement; (b) stress; (c) convergence rate.

the bar as in Figure 2.8 (b). A study of convergence for both methods has been carried out, and the global error η_g is determined by the difference between the calculated stress σ^h and the exact stress σ from Equation (2.71), as

$$\eta_g = \frac{\|E_g\|}{\|U\|}, \tag{2.73a}$$

$$\|E_g\| = \left\{ \int_\Omega \frac{1}{2E} (\sigma^h - \sigma)^2 \mathrm{d}\Omega \right\}^{1/2}, \tag{2.73b}$$

$$\|U\| = \left\{ \int_\Omega \frac{\sigma^2}{2E} \mathrm{d}\Omega \right\}^{1/2}. \tag{2.73c}$$

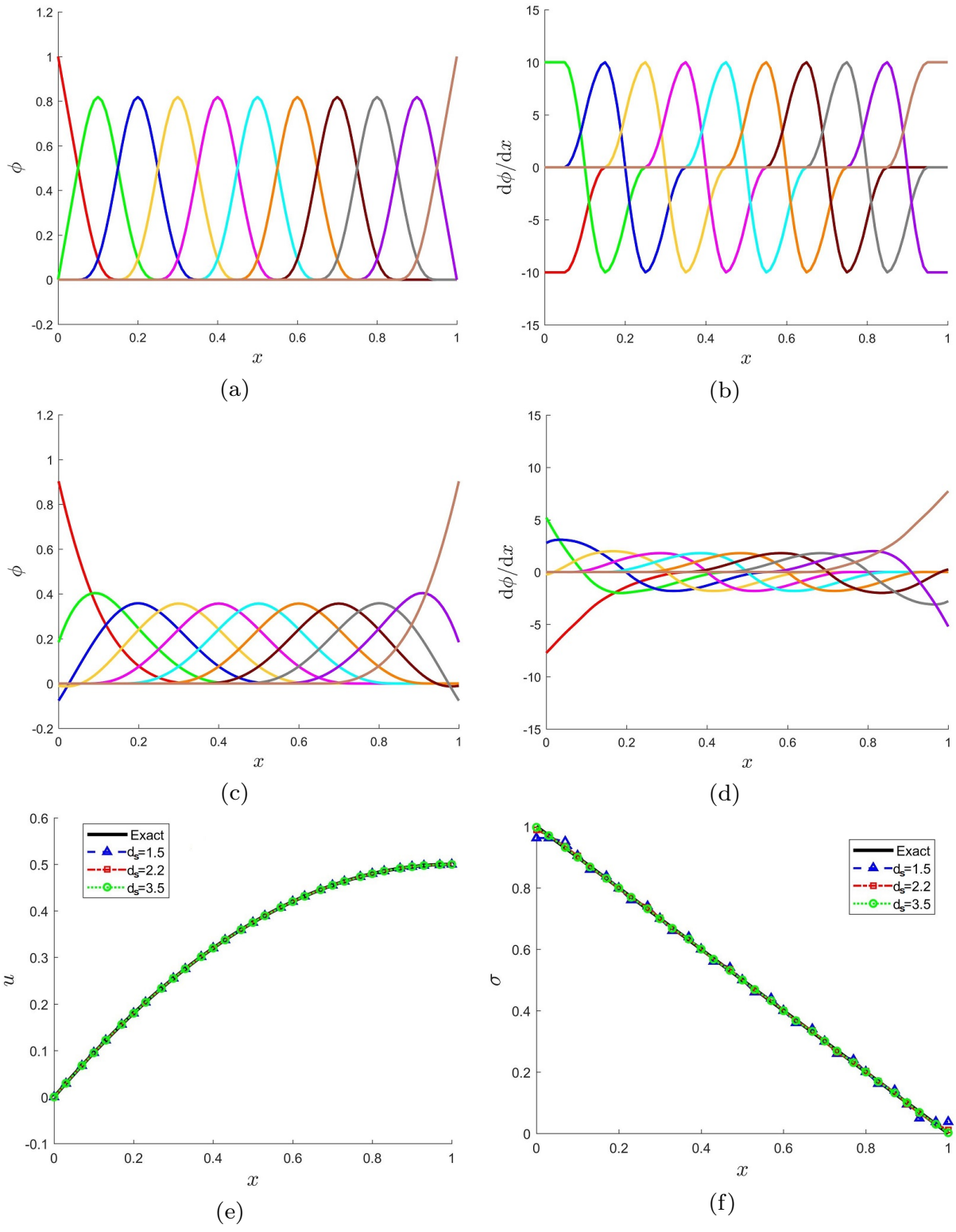

Figure 2.9: Comparison of results for the 1D bar problem for the EFGM with different support sizes: (a-b) shape functions and derivatives for $d_s = 1.5$; (c-d) shape functions and derivatives for $d_s = 3.5$; (e) displacement; (f) stress.

As in Figure 2.8 (c), the convergence rates for the results from both methods are around 1 using linear basis functions except for the EFGM with large support (d_s =3.5 and 4.5), but the EFGM generally shows better accuracy than the FEM. For the EFGM, increasing the support size can improve the accuracy of results, but this improvement is not effective when the number of nodes becomes large, e.g. 10^4 nodes in this 1D bar problem. The degradation of convergence rate for the EFGM with larger support size can be attributed to the reduce of local characteristics in the problem approximation, as mentioned in [125].

Results from a study of support size in the EFGM is also included in Figure 2.9. Three different support sizes are considered, $d_s = 1.5, 2.2$ and 3.5, where d_s is as defined in Equation (2.72). Shape functions and their derivatives in the EFGM with different support sizes are given in Figures 2.7 (a-b) and 2.9 (a-d). When smaller supports are used, less nodes are involved in the MLS process at a location, and the peak values of shape functions are larger. Displacements in all three cases are accurate compared with the exact solutions, while for stresses, results of $d_s = 1.5$ show oscillations especially at boundaries, as shown in Figure 2.9 (f). The approximation with large supports (d_s = 2.2 or 3.5) provides good accuracy for both displacement and stress, Figure 2.9 (e-f). Thus, large enough supports of nodes are required to contain sufficient information in the approximation of the FEGM, but if too large supports are applied, it will be difficult to capture the local properties in the approximation [125]. A sound support size is within the range $2 < d_s < 4$ as suggested in [55].

2.8 Summary

In this chapter, the governing equations of the EFGM for static problems are introduced, and implementation issues including integration and imposition of boundary conditions are discussed. The integration methods include Gaussian quadrature, nodal integration and integration over supports. Since the EFGM makes use of the MLS approximation to discretise the problem, essential boundary conditions cannot be imposed directly but through Lagrange multipliers, the penalty method, Nitsche's method or coupling with finite elements. In an example of a 1D bar, the EFGM shows better accuracy than the FEM because of smoother shape functions.

Chapter 3

An adaptive cracking particle method for fracture modelling in 2D

3.1 Introduction

Since elements are not involved in the discretisation process of the EFGM, it can handle crack propagation problems with one arrangement of nodes, while the standard FEM for fracture modelling requires remeshing (to match element edges with crack paths). In [179, 180], the EFGM is combined with the level set method for crack problems in 2D and 3D, however updating level set functions for crack propagation increases the computational cost, especially for multiple cracks [181]. Based on the EFGM, the cracking particle method (CPM) was proposed by Rabczuk et al. [202–204], where a set of discontinuous segments centred at particles are used to approximate a crack path. The locations and orientations of these segments are easily modified making the method suitable for problems with complex cracks. But the method faces issues of spurious cracking [204] and the need for a large number of particles, leading to high computational expense to achieve good accuracy as mentioned in Section 1.5.6.

An adaptive CPM is developed in this chapter and a new type of cracking particle is proposed, which avoids spurious crack results and incorporates an adaptivity approach to control the number of particles. In this chapter, the development of the CPM is firstly reviewed, and the strategy of cracking particles with bilinear discontinuous segments is proposed, by which these segments are aligned to provide a finer crack path prediction

than by the original CPM. Then the adaptivity approach is introduced which includes a review of different error estimators and refinement strategies. After that, the J-integral and different methods to calculate SIFs are included. Finally, some 2D crack problems are used to demonstrate the performance of the proposed methodology.

3.2 Crack modelling by the CPM

Crack discontinuities are introduced into the CPM either by extrinsic enrichment or intrinsic enrichment. In the former, discontinuous terms are added in the basis functions similar to the XFEM (Section 1.5.1), while the latter is through modifying the support of weight functions.

3.2.1 The visibility criterion and the diffraction criterion

Before introducing the CPM, previous strategies in the EFGM for crack modelling are firstly explained, which are also used in many other MMs. In the EFGM, for nodes adjacent to a crack, supports are adjusted to avoid them having influence on the opposite side of the crack, by which the displacement jump at cracks is obtained. Two methods have been widely used: the visibility criterion [2] and the diffraction criterion [226].

The visibility criterion comes from the idea of discontinuity opaqueness. The support of a node i is modified to the area receiving "light" from the centre, and the "shadow" area caused by the discontinuity is excluded, as shown in Figure 3.1. An issue of this approach is that an artificial discontinuity is introduced into the weight function so the resulting shape function is not even C^0 continuous, although convergence can still be reached [124]. Significant errors and oscillations can occur around the crack tip especially when large supports are used [226]. Due to the simplicity of the visibility criterion, this approach is applied to all numerical examples in this thesis.

By contrast in the diffraction method, a small part of the support around the crack tip is included following the law of "ray diffraction". A more moderate truncation can be applied and oscillations around the tip are therefore reduced. The input parameter $r = \|\mathbf{x} - \mathbf{x}_i\|/r_0$ for the weight function $w(r)$ of the node i is modified correspondingly as

$$r = \left(\frac{\|\mathbf{x} - \mathbf{x}_i\| + \|\mathbf{x}_c - \mathbf{x}_i\|}{\|\mathbf{x} - \mathbf{x}_i\|} \right)^{\gamma} \|\mathbf{x} - \mathbf{x}_i\|/r_0, \tag{3.1}$$

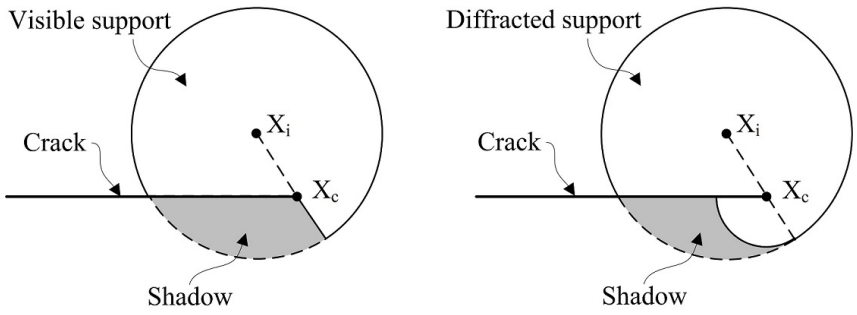

Figure 3.1: Visibility and diffraction criterion.

where $\mathbf{x}_c$ is the crack tip coordinate, r_0 is the support size and γ is a constant which is 1 or 2 as suggested in [226]. The diffraction method provides better accuracy than the visibility criterion, but cannot avoid high computational complexity, especially when used for either non-planar cracks in 3D or multiple cracks in 2D and 3D.

3.2.2 A new strategy of cracking particles

A literature review of the CPM was included in Section 1.5.6. The CPM provides an approximation of a crack path by using a set of discontinuous segments centred at particles, so updating the crack pattern is easily achieved by editing cracking particles. The development of the method is described below.

In the original CPM proposed by Rabczuk et al. (2004) [202, 203], the discontinuity in displacements at cracks is obtained by using discontinuous extrinsic enrichment functions. All particles are divided into two groups, namely normal particles $\mathcal{N}$ and cracking particles $\mathcal{N}_c$. The displacement in the problem domain is approximated by

$$u^h(\mathbf{x}) = \sum_{i\in\mathcal{N}} \Phi_i(\mathbf{x})u_i + \sum_{j\in\mathcal{N}_c} \Psi_j(\mathbf{x})H(\mathbf{x})b_j, \tag{3.2}$$

where $H(\mathbf{x})$ is the sign function with value 1 on one side of the crack and -1 on the other side, and b_j are extra unknowns. Shape functions including the normal part Φ_i and the enrichment part Ψ_j are evaluated by the MLS approximation but with different support sizes, where the support sizes for calculating shape functions in the enrichments are usually larger than for the normal part. A crack path is approximated by a group of discontinuous segments as in Figure 3.2 (a), and the orientations of these segments control the values of the sign function and therefore the crack discontinuity. Crack opening, described by the

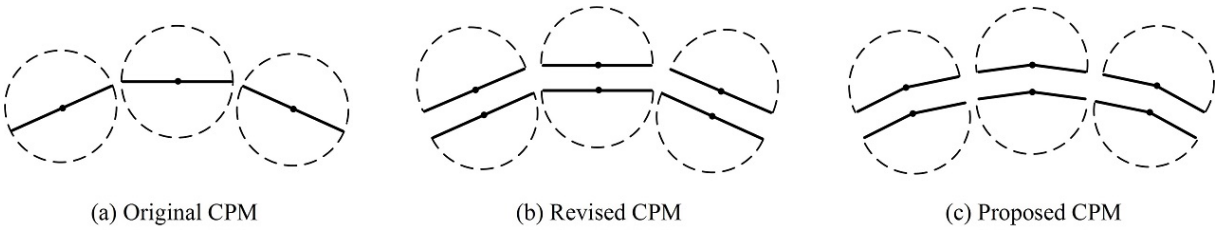

Figure 3.2: The development of the CPM.

operator $[\![\cdot]\!]$, can be obtained by the enrichment functions, as

$$[\![u(\mathbf{x})]\!] = \|u(\mathbf{x}^{\mathcal{S}^+}) - u(\mathbf{x}^{\mathcal{S}^-})\| = 2\sum_{j\in\mathcal{N}_c}\Psi_j(\mathbf{x})b_j, \tag{3.3}$$

where $\mathcal{S}^+$ and $\mathcal{S}^-$ are two opposite sides of crack paths. However, additional unknowns b_j are introduced to the variational formulation and bring extra cost to solve the weak form equations. An alternative presented by Rabczuk et al. (2010) [204] is by splitting cracking particles into two subparts belonging to the two sides of the crack, Figure 3.2 (b). No additional terms are required in the displacement approximation, and crack opening is obtained by the relative displacements of cracking particles on the two sides of the crack, i.e.

$$[\![u(\mathbf{x})]\!] = \sum_{i\in\mathcal{S}^+}\Phi_i(\mathbf{x}^+)u_i - \sum_{i\in\mathcal{S}^-}\Phi_i(\mathbf{x}^-)u_i \tag{3.4}$$

The CPM in Figure 3.2 (a-b) suffers from spurious crack results as mentioned in [204, 213], when these crack segments do not align well especially for curved cracks. A new strategy to define the influence domain of cracking particles is proposed in this thesis (and as published in [227]), where bilinear segments are used instead of straight segments to cut the support as shown in Figure 3.2 (c). The orientations of crack segments are modified according to surrounding cracking particles, by which these segments are aligned to continuous crack paths. The support of a given cracking particle i is split into two sectors complying with the crack pattern, and the two segment arms are directed by angles θ_1^i, θ_2^i where the angle should satisfy $\theta \in (-\pi, \pi]$, as

$$\theta_1^i = \arctan(\frac{y_{i+1}-y_i}{x_{i+1}-x_i}), \quad \theta_2^i = \arctan(\frac{y_{i-1}-y_i}{x_{i-1}-x_i}), \quad i \in \mathcal{N}_c. \tag{3.5}$$

The relationship is depicted in Figure 3.3 (here arctan should be atan2 in MATLAB or

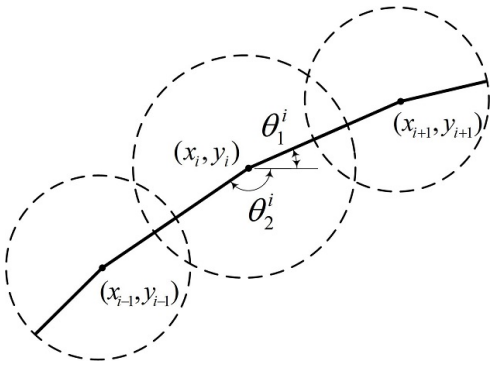

Figure 3.3: The two segment arm directions of a cracking particle.

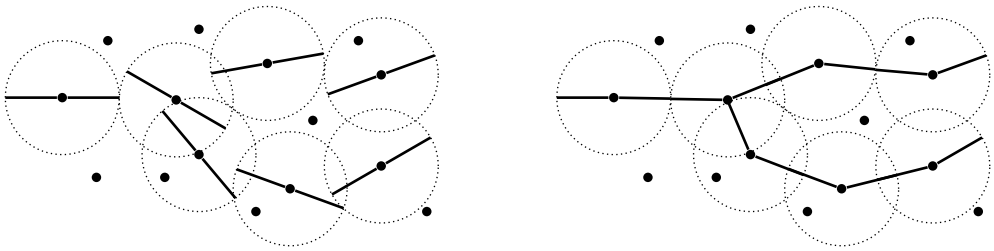

Figure 3.4: Comparison between the original and the modified CPM: (a) original CPM; (b) modified CPM.

equivalent). The crack tip particle has influence on both sides of the crack path and is not itself split.

One advantage of the proposed CPM over the original method is illustrated in Figure 3.4. In the original CPM, cracking particles are defined as each carrying a straight discontinuous segment of the crack face, splitting the supports as in Figure 3.4 (a). If there is a "bad" overlap between those segments, spurious cracking occurs. In the modified CPM proposed for the first time here [227], this problem is solved by using bilinear segments where the crack path can change its direction at each cracked particle. All discontinuous segments are aligned and "good" overlaps are obtained, as shown in Figure 3.4 (b).

3.3 Adaptivity

One drawback of the original CPM is the requirement for fine node/particle arrangements to obtain accurate descriptions of complex crack patterns, since the length of crack segments is linked to nodal distances [211]. Therefore the original CPM is usually computationally expensive, but this issue can be alleviated by using an adaptive approach, as in [203, 228]. Outside the CPM, the major challenge in linear elastic fracture mechanics

is the issue of stress singularity at a crack tip for computational fracture modelling. To capture the high gradients of stress around the crack tip, a large number of particles or high order basis functions (or both) are required to obtain accurate results in either the FEM or a meshless method. But away from the crack tip, the need for particle refinement level is much lower. The task to set up particle arrangements reasonably to obtain a given level of accuracy is still challenging, especially for crack problems with propagation, and an adaptive procedure is demanded to maintain efficiency.

A posteriori adaptive finite element methods, which are composed of an error estimation step and a refinement to the discretisation of the problem domain, have a long history with a comprehensive mathematical basis being available for the FEM. In this class of adaptive approaches, there are two main categories for error estimators: recovery-based [225, 229–231] or residual-based [220, 232, 233]. Reviews on different error estimators can be found in [234, 235]. Methods to amend the discretisation of the problem include: h-adaptivity, mesh refinement and adding more particles; p-adaptivity, increasing the polynomial degree of the shape functions; hp-adaptivity, the combination of the above two; r-adaptivity, moving particles to adjust the local density of particle distribution. All these approaches have been developed in MMs for decades, e.g. [2, 229, 236–238], but at present no firm mathematical basis for error estimators has been built for MMs. Recent research indicates that it can be problematic if FEM-based adaptive approaches are applied to meshless methods directly. For instance in [125], it is shown that in meshless methods errors from discretisation and those caused by using a particular basis cannot be decoupled, and the support size has an opposite influence on error indicators of displacement and its derivatives. Error estimators specific for meshless methods are therefore still under development.

3.3.1 Error estimator

As stated above two types error estimators are involved in the adaptive approaches, namely residual-based and recovery-based error estimators. In the former, the error is defined as in [220, 232, 233] by

$$u^h(\mathbf{x}) - u(\mathbf{x}) = \sum_{i=1}^{n} \Phi_i(\mathbf{x}) u_i - u(\mathbf{x}) \,, \tag{3.6}$$

where $u^h(\mathbf{x})$ is the approximated displacement, $u(\mathbf{x})$ is the exact displacement, u_i is the displacement of particle i and $\Phi_i(\mathbf{x})$ is the shape function of particle i. Expanding $u(\mathbf{x})$ through a set of Taylor series, the nodal values can be expressed as

$$u(\mathbf{x}_i) = \sum_{m=0}^{s_c} \frac{1}{m!} \left((\mathbf{x}_i - \mathbf{x}) \frac{\partial}{\partial \mathbf{x}} \right)^m u(\mathbf{x}) + R_{s_c+1}\,, \tag{3.7}$$

with the residual

$$R_{s_c+1} = \frac{1}{(s_c+1)!} \left((\mathbf{x}_i - \mathbf{x})^{\mathrm{T}} \frac{\partial}{\partial \mathbf{x}} \right)^{s_c+1} u(\bar{\mathbf{x}}), \quad \bar{\mathbf{x}} = (1-v)\mathbf{x} + v\mathbf{x}_i, \quad 0 < v < 1, \tag{3.8}$$

where s_c is the complete order of shape functions, e.g. for linear complete shape functions, $s_c = 1$. Combining the two equations above yields

$$\begin{aligned} u^h(\mathbf{x}) - u(\mathbf{x}) = \sum_{i=1}^{n} \Big(\Phi_i(\mathbf{x}) - 1 \Big) u(\mathbf{x}) + \sum_{m=1}^{s_c} \frac{1}{m!} \sum_{i=1}^{n} \Phi_i(\mathbf{x}) \left((\mathbf{x}_i - \mathbf{x}) \frac{\partial}{\partial \mathbf{x}} \right)^m u(\mathbf{x}) \\ + \sum_{i=1}^{n} \Phi_i(\mathbf{x}) R_{s_c+1} = \sum_{i=1}^{n} \Phi_i(\mathbf{x}) R_{s_c+1}. \end{aligned} \tag{3.9}$$

Considering $|\Phi(\mathbf{x})| \leq c$ and $|\mathbf{x}_i - \mathbf{x}| \leq h$, where c and h are bounded constants, the error estimator in the L_2 norm becomes

$$\left\| u^h(\mathbf{x}) - u(\mathbf{x}) \right\|_{L_2(\Omega)} = c h^{s_c+1} \left\| \frac{1}{(s_c+1)!} \mathcal{D}^{s_c+1} u(\mathbf{x}) \right\|_{L_2(\Omega)}, \tag{3.10}$$

where $\mathcal{D} = \frac{\partial}{\partial x} + \frac{\partial}{\partial y}$ for 2D problems. The term $\mathcal{D}^{s_c+1} u(\mathbf{x})$ in Equation (3.10) for a representative nodal domain Ω_j can be approximated by

$$\mathcal{D}^{s_c+1} u(\mathbf{x}) = \frac{1}{a_j} \int_{\Omega_j} \sum_{i=1}^{n} \mathcal{D}^{s_c+1} \Phi_i(\mathbf{x}) u_i \mathrm{d}\Omega_j, \tag{3.11}$$

where a_j is the area of Ω_j and n is the number of particles affecting the location $\mathbf{x}$. The approximation error for the displacement derivatives can be obtained in a similar way with considering the derivatives of shape functions are bounded by $|\nabla \Phi(\mathbf{x})| \leq c/h$, e.g.

the first derivative error is

$$\left\| \frac{\partial u^h(\mathbf{x})}{\partial \mathbf{x}} - \frac{\partial u(\mathbf{x})}{\partial \mathbf{x}} \right\|_{L_2(\Omega)} = ch^{s_c} \left\| \frac{1}{(s_c+1)!} \mathcal{D}^{s_c+1} u(\mathbf{x}) \right\|_{L_2(\Omega)}. \tag{3.12}$$

By contrast, recovery-based error estimators are computed in a convenient energy norm depending on the difference between the exact stress $\boldsymbol{\sigma}$ and the calculated stress $\boldsymbol{\sigma}^h$ as in [225, 229–231] by

$$\|E_g\| = \left\{ \frac{1}{2} \int_\Omega (\boldsymbol{\sigma} - \boldsymbol{\sigma}^h)^{\mathrm{T}} \mathbf{D}^{-1} (\boldsymbol{\sigma} - \boldsymbol{\sigma}^h) \mathrm{d}\Omega \right\}^{\frac{1}{2}}, \tag{3.13}$$

where $\mathbf{D}$ is defined in Equation (2.29). The exact stress is unknown for most problems, and this issue is solved for MMs in [121], where a simple way to approximate the error in meshless methods was proposed by replacing the exact stress with the "projected" stress $\boldsymbol{\sigma}^p$, as

$$\|E_g\| \approx \left\|E_g^p\right\| = \left\{ \frac{1}{2} \int_\Omega (\boldsymbol{\sigma}^p - \boldsymbol{\sigma}^h)^{\mathrm{T}} \mathbf{D}^{-1} (\boldsymbol{\sigma}^p - \boldsymbol{\sigma}^h) \mathrm{d}\Omega \right\}^{\frac{1}{2}}. \tag{3.14}$$

The "projected" stress $\boldsymbol{\sigma}^p$ is evaluated by using an approximation combining stresses at surrounding particles inside a smaller support as below

$$\boldsymbol{\sigma}^p = \sum_{k=1}^{m} \Psi_k(\mathbf{x}) \boldsymbol{\sigma}^h(\mathbf{x}_k), \tag{3.15}$$

where m is the number of surrounding particles and $\Psi_k(\mathbf{x})$ is the shape function calculated by the MLS approximation with this smaller support. The global error η_{g} of the problem domain is evaluated by

$$\eta_{\mathrm{g}} = \frac{\|E_{\mathrm{g}}\|}{\|U\|}, \tag{3.16}$$

with

$$\|U\| = \left\{ \frac{1}{2} \int_\Omega (\boldsymbol{\sigma}^h)^{\mathrm{T}} \mathbf{D}^{-1} \boldsymbol{\sigma}^h \mathrm{d}\Omega \right\}^{1/2}. \tag{3.17}$$

When the global error is larger than the user predefined target error η_{t}, i.e. $\eta_{\mathrm{g}} > \eta_{\mathrm{t}}$, the adaptivity process is applied. The local error of a cell Ω_i is estimated by

$$\|E_i\| = \left\{ \frac{1}{2} \int_{\Omega_i} (\boldsymbol{\sigma}^p - \boldsymbol{\sigma}^h)^{\mathrm{T}} \mathbf{D}^{-1} (\boldsymbol{\sigma}^p - \boldsymbol{\sigma}^h) \mathrm{d}\Omega_i \right\}^{1/2}. \tag{3.18}$$

To take the global error into account, the relative local error is used instead,

$$\eta_i = \frac{\|E_i\|}{\|U\| / \sqrt{n_{\text{cell}}}}, \tag{3.19}$$

where n_{cell} is the total number of background cells. In the adaptive procedure, those background cells with large errors are refined while those with small errors are coarsened, which is governed by the refinement and coarsening procedures respectively, and the following rules are used

$$\begin{cases} \eta_i > L_{\text{fin}} & \text{to be refined}, \\ \eta_i < L_{\text{rec}} & \text{to be coarsened}, \end{cases} \tag{3.20}$$

where L_{fin} is the refinement trigger and L_{rec} is for coarsening. These two parameters are determined by a relationship with the target global error η_{t} as below

$$L_{\text{fin}} = 2\eta_t, \quad L_{\text{rec}} = 0.5\eta_t. \tag{3.21}$$

The target global error η_t is user defined and can affect the adaptivity process. A smaller η_t allows more background cells to be refined and more particles are added, which is suitable for problems requiring high level accuracy. Using a large η_t increases the threshold for refinement and can improve the convergence rate of global errors for results but can lead to issues of no cells to be refined. The range of η_t between 0.01 and 0.1 is suggested for 2D problems in this chapter.

This procedure is inexpensive since there is no need for matrix solution which is however needed in most of other error estimation procedure as in [122, 123]. Recovery-based error estimators are accurate, robust and in most cases can provide more accurate estimation than residual-based methods [234] and is applied in the adaptive procedure in this thesis.

3.3.2 Refinement strategy

The refinement strategy here is based on h-adaptivity because of the complexity of p-adaptivity. For methods employing Voronoi cells for nodal integration, refinement in h-adaptivity is by adding particles on the edges of cells and updating the surrounding Voronoi cells, details of which are referred to [220, 239]. Since integration cells are used in the EFGM to integrate the domain stiffness matrix, it is convenient to build the adaptive

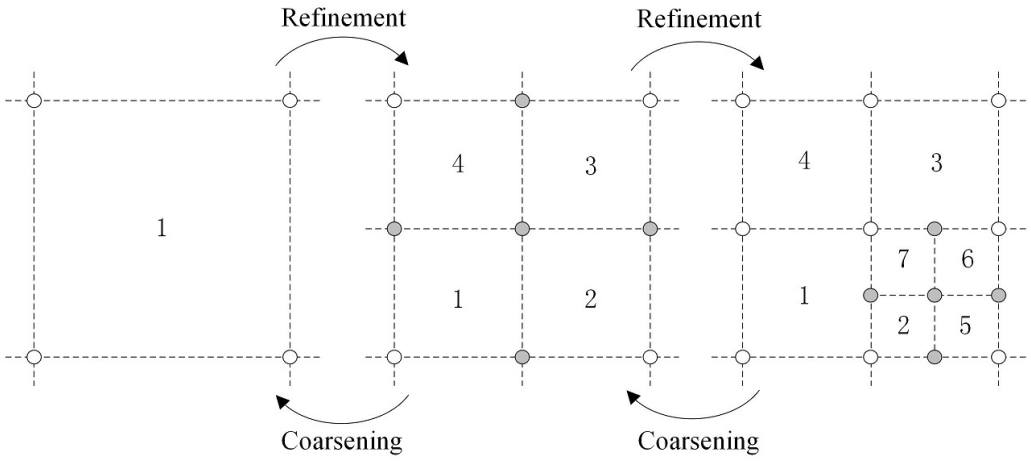

Figure 3.5: The strategy of refinement and coarsening

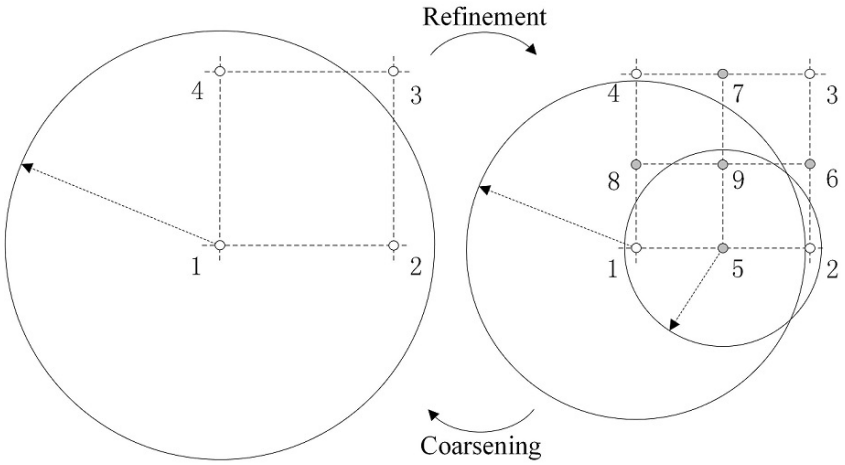

Figure 3.6: Support size change in refinement and coarsening

procedure on dividing background cells and adding particles at vertices of grid cells. A background cell for Gaussian quadrature is divided into four small cells with five particles added, the same as in many references [225, 229, 231, 233]. The adaptive strategy is depicted in Figure 3.5. For the refinement, cell 1 is divided into four small cells 1, 2, 3 and 4 with five particles added, and cell 2 is divided further into cells 2, 5, 6 and 7. When the errors measured in four cells 2, 5, 6 and 7 are small, they are combined by the coarsening procedure back to the "mother" cell 2 and five particles are deleted, same with cells 1, 2, 3 and 4 to cell 1.

When the cells are divided into small cells, particle density is changed and nodal support sizes should be modified accordingly for a good balance between accuracy and efficiency, as illustrated in Figure 3.6. If a cell described by four particles 1, 2, 3 and 4 with

refinement level l_r is refined, five particles are added all with support size $r_i = r_0 \cdot 0.5^{l_r+1}$. A modification is made to the support of the four particles by $r_i = r_i \cdot \sqrt[4]{0.5}$, i=1, 2, 3 and 4. When four cells around particle 1 are all divided, its support becomes the same as that of the added particles 5, 6, 7, 8 and 9. The coarsening is the reverse of the refinement process, and when four small cells are combined, supports of four particles become $r_i = r_i/\sqrt[4]{0.5}$, i=1, 2, 3 and 4. The particles in the group of 5, 6, 7, 8 and 9, which do not belong to other cells, are deleted. In the initial configuration, the problem domain is discretised with a uniformly distributed particles with the same support r_0, and the refinement level of all background cells are $l_r = 0$. The whole adaptivity process is illustrated in Figure 3.7.

3.4 Calculation of SIFs

SIFs are important parameters in fracture analysis, which are used to judge whether a crack can propagate and to determine the crack growth rate and direction. Although SIFs are governed by the stress and strain around the crack tip, far field results from the crack tip are usually used in methods to calculate SIFs, e.g. the J-integral, since the stress field around the crack tip is very complex and singular.

3.4.1 The J-integral

The J-integral was proposed by Rice [240] and is a method to calculate the strain energy release rate. The J-integral in 2D is defined as

$$J = \int_\Gamma \left(W \, \mathrm{d}x_2 - T_k \frac{\partial u_k}{\partial x_1} \mathrm{d}s \right), \quad k \in \{1, 2\}, \tag{3.22}$$

where the path Γ is a curve surrounding the crack tip, x_1 and x_2 are the coordinates, s is the arc length along Γ, strain energy density is $W = \frac{1}{2}\sigma_{ij}u_{i,j}$, traction is $T_i = \sigma_{ij}n_j$ defined according to the outward normal $\mathbf{n}$ along Γ and i, j are used with the Einstein summation, $i, j \in \{1, 2\}$. The terms $u_{i,j}$ are the derivatives of u_i to x_j, and n_j are the components of the vector $\mathbf{n}$. The relationship between the J-integral and the SIFs is

$$J = \alpha(K_\mathrm{I}^2 + K_\mathrm{II}^2), \tag{3.23}$$

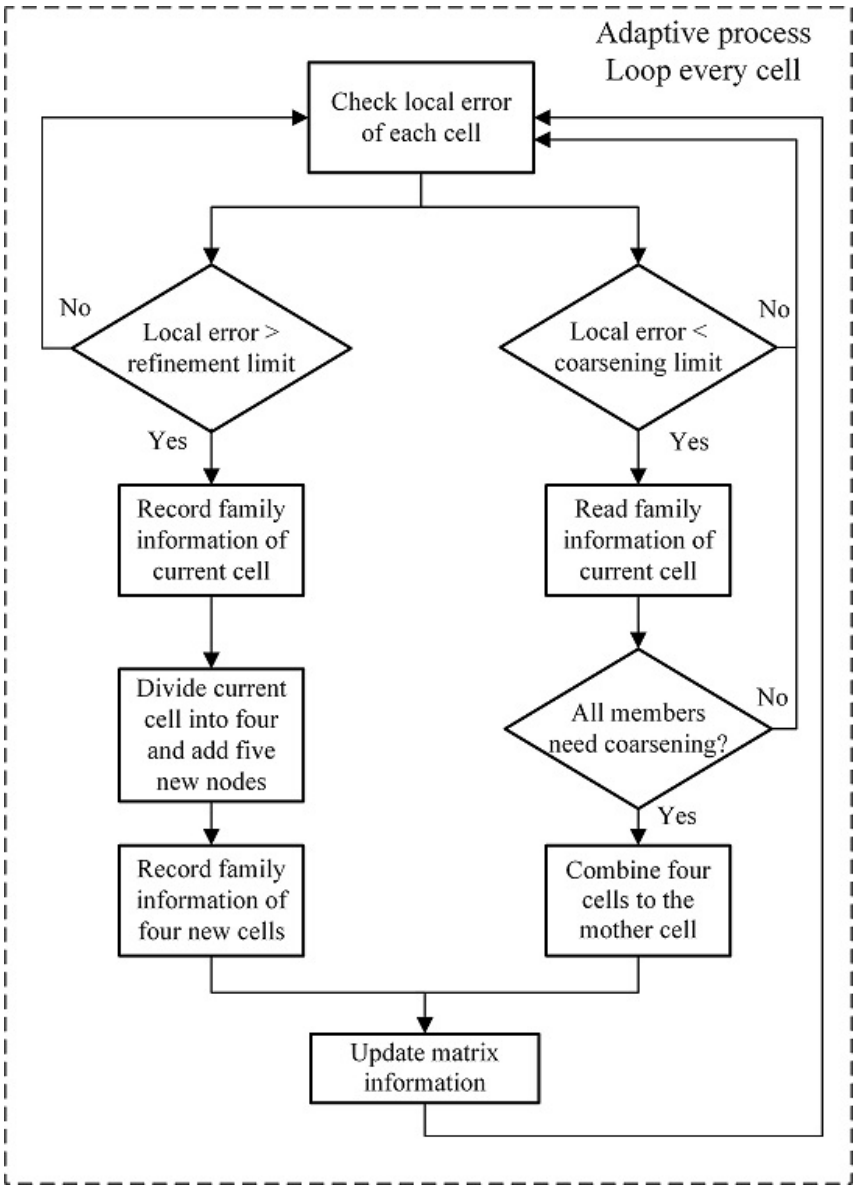

Figure 3.7: The flow chart of the adaptive process

$$\alpha = \begin{cases} (1-\nu^2)/E & \text{for plane strain,} \\ 1/E & \text{for plane stress,} \end{cases} \tag{3.24}$$

with the Young's modulus E and the Poisson's ratio ν.

Rice [240] showed that the J-integral is zero over a closed path when the integral contour encloses a simply connected region which contains no elastic inhomogeneity, e.g. voids and cracks. Based on this character, it is easy to prove that the J-integral is path-independent if the crack surfaces are traction free, as described in Appendix B.

3.4.2 Contour integration

One way to calculate the J-integral is through a contour integral according to the definition in Equation (3.22). Normally, the integral path is calculated by following a circle [241] or a square [242] around the crack tip as in Figure 3.8. The latter has a simpler implementation since on each edge one differential part of the J-integral becomes zero in the local Cartesian coordinates. The SIFs for a mixed-mode problem can be obtained by decomposing the elastic field around the crack tip into its respective symmetric and antisymmetric mode components [241]. Consider a pair of points $P(x_1, x_2)$ and $P'(x_1, -x_2)$ which are symmetric to the crack line relative to the tip. The decomposition in the elastic field for 2D problems follows

$$\left\{ \begin{array}{c} \sigma_{11}^{\mathrm{I}} \\ \sigma_{22}^{\mathrm{I}} \\ \sigma_{12}^{\mathrm{I}} \end{array} \right\} = \frac{1}{2} \left\{ \begin{array}{c} \sigma_{11} + \sigma'_{11} \\ \sigma_{22} + \sigma'_{22} \\ \sigma_{12} - \sigma'_{12} \end{array} \right\}, \quad \left\{ \begin{array}{c} \sigma_{11}^{\mathrm{II}} \\ \sigma_{22}^{\mathrm{II}} \\ \sigma_{12}^{\mathrm{II}} \end{array} \right\} = \frac{1}{2} \left\{ \begin{array}{c} \sigma_{11} - \sigma'_{11} \\ \sigma_{22} - \sigma'_{22} \\ \sigma_{12} - \sigma'_{12} \end{array} \right\}, \tag{3.25}$$

$$\left\{ \begin{array}{c} u_1^{\mathrm{I}} \\ u_2^{\mathrm{I}} \end{array} \right\} = \frac{1}{2} \left\{ \begin{array}{c} u_1 + u'_1 \\ u_2 + u'_2 \end{array} \right\}, \quad \left\{ \begin{array}{c} u_1^{\mathrm{II}} \\ u_2^{\mathrm{II}} \end{array} \right\} = \frac{1}{2} \left\{ \begin{array}{c} u_1 - u'_1 \\ u_2 + u'_2 \end{array} \right\}, \tag{3.26}$$

where dashed terms are associated with point $P'(x_1, -x_2)$. Then the J-integral is decomposed into two components:

$$J^m = \int_\Gamma (W^m n_1 - T_j^m u_{j,1}^m)\, \mathrm{d}\Gamma, \quad m \in [\mathrm{I}, \mathrm{II}], \quad j \in [1, 2]. \tag{3.27}$$

Finally, the SIFs can be obtained by

$$J^{\mathrm{I}} = \alpha K_{\mathrm{I}}^2, \; J^{\mathrm{II}} = \alpha K_{\mathrm{II}}^2 \,. \tag{3.28}$$

3.4.3 Interaction integration

SIFs can also be calculated by a domain integration, through applying the divergence theorem and converting the contour integral into a domain form, e.g. over an area in 2D

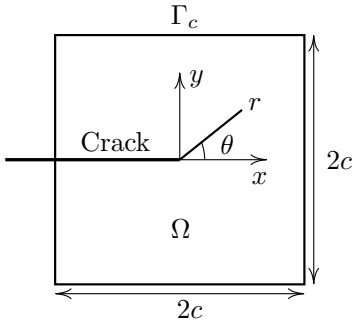

Figure 3.8: Integration contour and domain for the J-integral

or a volume in 3D. The domain is the area Ω enclosed by the contour Γ as shown in Figure 3.8 and is assumed under two independent equilibrium states as in [243]: real state u and auxiliary state u^{aux}, where the superscript "aux" indicates parameters from the auxiliary state, the definition of which is included in Appendix C. The interaction integral I of the two states is

$$I = \int_A (\sigma_{ij}^{\text{aux}} u_{j,1} + \sigma_{ij} u_{j,1}^{\text{aux}} - \sigma_{jk}^{\text{aux}} \varepsilon_{jk} \delta_{1i}) q_{,i} \, \mathrm{d}A, \quad i,j \in \{1,2\}\,, \tag{3.29}$$

where q is a weight function, e.g. $q = (1 - |x_1/c|)(1 - |x_2/c|)$ and the index cnotation is used with the Einstein summation. The relationship between the SIFs and the interaction integral is

$$I = 2\alpha(K_{\text{I}} K_{\text{I}}^{\text{aux}} + K_{\text{II}} K_{\text{II}}^{\text{aux}}), \tag{3.30}$$

where $K_{\text{I}}^{\text{aux}}$ and $K_{\text{II}}^{\text{aux}}$ are the SIFs associated with the auxiliary state. Mixed mode K_{I} and K_{II} are obtained by choosing the specific auxiliary state, e.g. if $K_{\text{I}}^{\text{aux}} = 1$ and $K_{\text{II}}^{\text{aux}} = 0$, mode I SIF is $K_{\text{I}} = I/(2\alpha)$. This approach provides a general form of integral near the crack tip and is applicable to both linear and non-linear problems [244]. Hence, the interaction integral is used for calculating SIFs in this thesis.

3.4.4 Crack propagation

A crack propagation procedure comprises two steps: deciding the propagating angle and advancing the crack front. For the former, a review on different crack propagation criteria can be found in [245], where the maximum principal stress criterion was shown to maintain both efficiency and reasonable accuracy. Following this criterion, a crack propagates towards the direction of angle θ in a local polar coordinate system where the shear stress

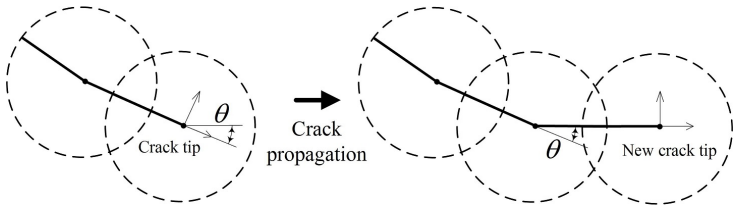

Figure 3.9: Crack propagation and new cracking particles.

$\sigma_{r\theta}$ becomes zero,

$$\sigma_{r\theta} = \frac{1}{2\pi r}\cos\frac{\theta}{2}\Big[\frac{1}{2}K_{\mathrm{I}}\sin(\theta) + \frac{1}{2}K_{\mathrm{II}}(3\cos(\theta) - 1)\Big] = 0. \tag{3.31}$$

The solution is

$$\theta = 2\arctan\Big(\frac{K_{\mathrm{I}} - \sqrt{K_{\mathrm{I}}^2 + 8K_{\mathrm{II}}^2}}{4K_{\mathrm{II}}}\Big). \tag{3.32}$$

This has been covered in many references [153, 227, 245] for modelling crack propagation in linear elastic fracture mechanics.

When the crack growth angle θ is obtained, an increment of crack extension is applied along θ in the local polar coordinate system, as presented in Figure 3.9. The value of the crack increment Δa is predefined and proportional to the initial crack length a, where $\Delta a \in [0.1a, 0.5a]$ is used in this thesis to control the speed of crack propagation. If the crack direction has a large change when $|\theta| > \pi/36$, the crack increment length is set to $0.5\Delta a$. If there is a particle at the position of the new tip, that particle becomes a cracking particle, otherwise a new cracking particle is introduced. The old crack tip particle is split into two particles, both with two cracking branches, one inherits the angle of the old crack tip segment and another records the propagating angular change θ. The new crack tip is not split but defined with a cracking line directed back to the old crack tip. Crack propagation is achieved by repeating the two steps mentioned above. Since the new crack tip is always aligned with one cracking branch of the old tip during crack propagating, a nearly continuous crack path can be obtained.

3.5 Update of the stiffness matrix

A large number of quadrature points are normally required to get accurate results in meshless methods, therefore the integration of the system stiffness $\mathbf{K}$ is computationally costly. The calculation of $\mathbf{K}$ is demanded for each adaptivity or crack propagation step,

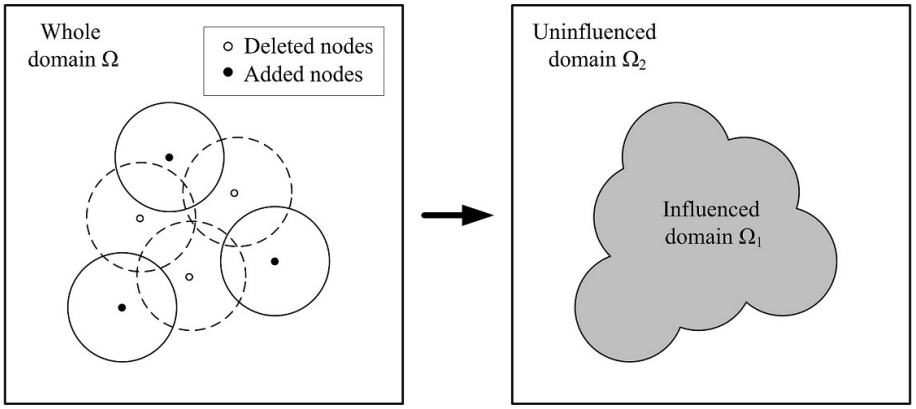

Figure 3.10: Influenced domain due to the adaptivity.

which makes the whole process potentially time-consuming. However, the integration over the whole domain is not necessary for every step, because the change caused by either adaptivity or crack propagation usually occurs in a small zone around the crack tip.

Here, a strategy to amend the stiffness matrix is proposed to reduce the cost of calculating $\mathbf{K}$. The integral of $\mathbf{K}$ is divided into two subparts, one from the influenced subdomain Ω_1 due to adaptivity or crack propagation and another from the uninfluenced subdomain Ω_2,

$$\mathbf{K} = \int_{\Omega_1} \mathbf{B}^{\mathrm{T}}\mathbf{D}\mathbf{B}\mathrm{d}\Omega_1 + \int_{\Omega_2} \mathbf{B}^{\mathrm{T}}\mathbf{D}\mathbf{B}\mathrm{d}\Omega_2. \tag{3.33}$$

The update of the $\mathbf{K}$ matrix is through modifying the contribution from Ω_1, and the integration over Ω_2 is not required. Since Ω_1 is usually much smaller than the problem domain at each step of either adaptivity or crack propagation, the calculating expense related to updating $\mathbf{K}$ is decreased. Two issues remain to implement this approach, which are obtaining the influenced domain Ω_1 and saving the contribution from Ω_2.

The former is solved by tracking the change of the problem discretisation. After one adaptive step, the influenced domain is obtained by summing up the supports of added and deleted particles as in Figure 3.10, and particles with support changes are considered in the two groups. The situation is similar for a crack propagation step and the change is due to the generated new crack segment, which cuts the supports of some particles around the crack tip, Figure 3.11. The area Ω_1 comes from the combination of all shadow areas and is usually with complex geometries, as shown in Figure 3.11. Alternatively, a larger "possible" domain containing all possible areas is used, where the integration of $\mathbf{K}$ is recalculated.

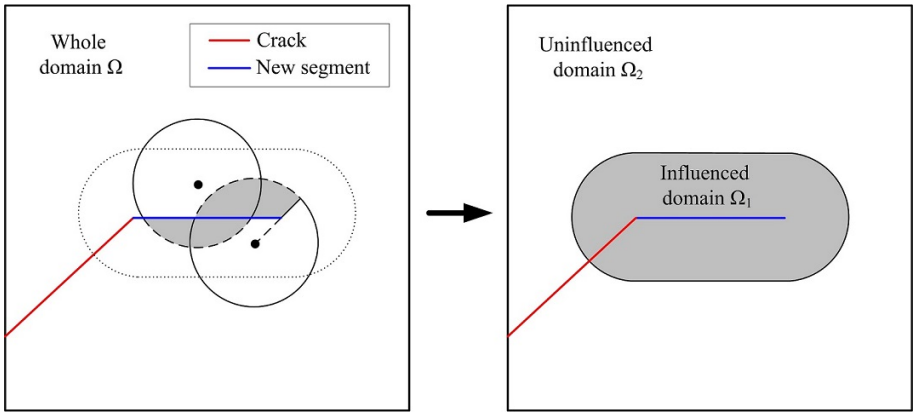

Figure 3.11: Influenced domain due to crack propagation.

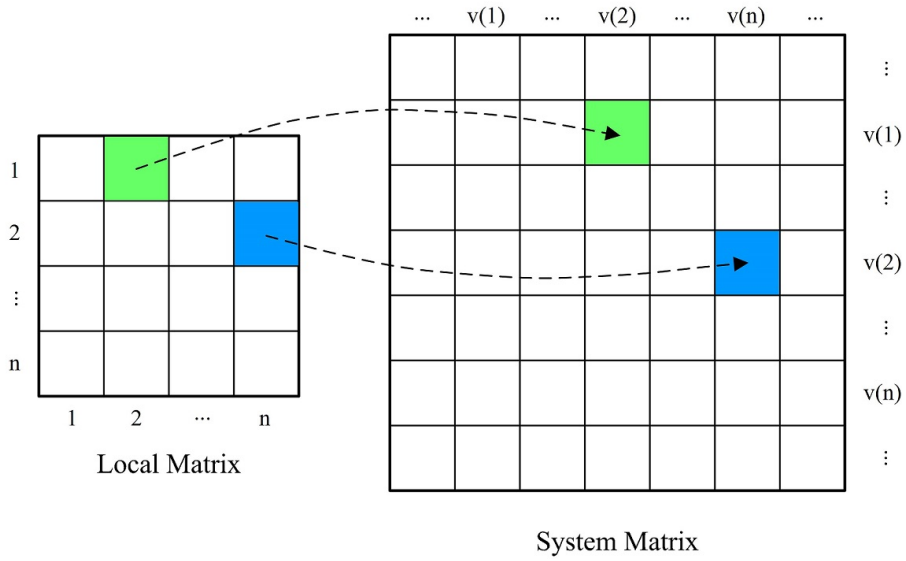

Figure 3.12: Transfer function from local stiffness matrix to global stiffness matrix.

The storage of the system stiffness matrix $\mathbf{K}$ is problematic in that the size of $\mathbf{K}$ is usually very large. The strategy of a local stiffness matrix [246] is therefore introduced here, by which the contribution of each background cell to the sparse matrix $\mathbf{K}$ can be stored in a local and dense matrix $\mathbf{k}$ with a smaller size. The storage requirement is much reduced, and there is no need to reform a large matrix frequently. The local matrix is achieved by integrating over each cell with Gauss quadrature. The relationship between the local matrix $\mathbf{k}$ and the global stiffness $\mathbf{K}$ is described by a mapping function $\mathcal{T}$, which transfers the local index i to the system index $\mathrm{v}(i)$ with $i = 1, 2, \ldots n$ where n is the number of particles associated with the local matrix, as in Figure 3.12. When particles are deleted or added during either the adaptivity or crack propagation process, the vector

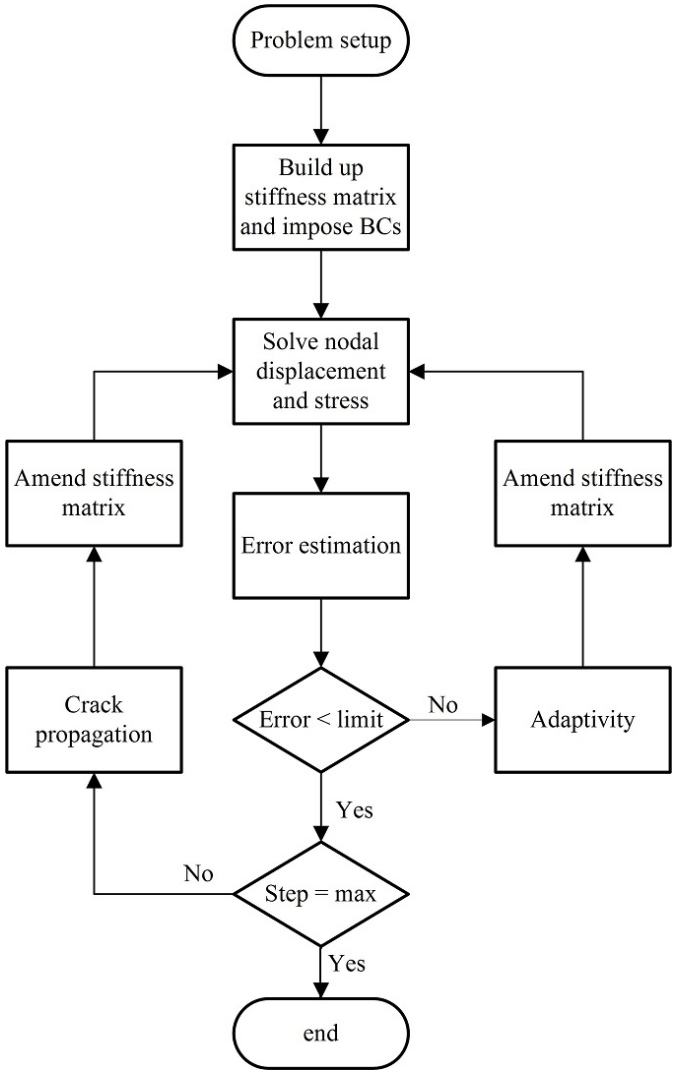

Figure 3.13: The flow chart of whole analysis process.

v(i) is amended accordingly. Then the update of $\mathbf{K}$ is obtained by

$$\mathbf{K} = \int_{\Omega_1} \mathbf{B}^{\mathrm{T}}\mathbf{D}\mathbf{B}\mathrm{d}\Omega_1 + \sum_{i\in\Omega_2} \mathcal{T}\left(\mathbf{k}_i\right), \tag{3.34}$$

where the subscript i indicates the local matrix $\mathbf{k}$ of cell i.

The whole analysis process is demonstrated in the flow chart of Figure 3.13. The problem is discretised with coarse particles initially and then adaptive steps are used to adjust nodal arrangements and to improve the accuracy. After the global error is reduced to a lower level than the target, the next crack propagation step starts, and the particle density is amended by another group of adaptivity steps until the maximum propagation step (the final terminal condition) is reached.

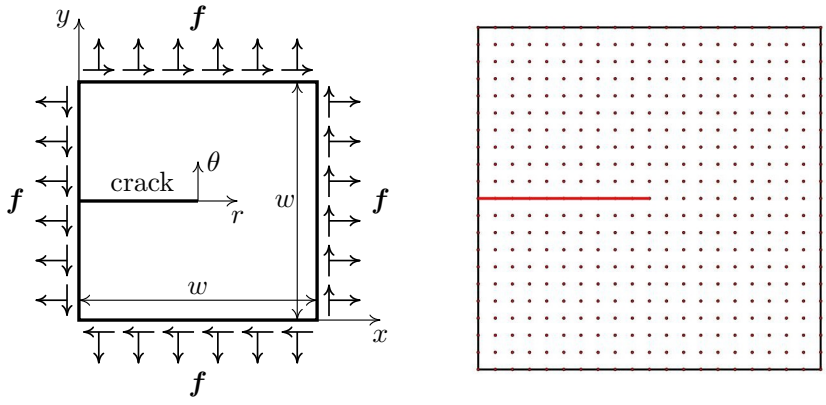

Figure 3.14: Half central crack under a stress field inducing mixed mode fracture: (a) configuration; (b) initial particles.

3.6 Numerical examples

Several numerical examples of 2D crack problems are used to demonstrate the performance of the proposed CPM. All the examples are subject to quasi-static loading, and both static and propagating cracks are studied where the critical SIF is set a low value, e.g. $K_{\mathrm{IC}} = 100\mathrm{N/mm}^{3/2}$. A linear basis function is applied to build shape functions and 4×4 Gauss points are used for the integration over each background cell. The initial support size is $r_0 = 2l_0$, where l_0 is the average distance between particles at the start, and the factor 2 is chosen from the range 2.0-4.0 as suggested in [55, 125]. In contrast, smaller support size should be used for the stress projection to avoid the overestimation of stress [121], and the value is 0.6 times of the support of particle i, i.e. $r = 0.6r_i$ is chosen. All problems are assumed to be under plane stress conditions and with elastic material properties unless stated otherwise. SIFs are normalised by

$$K'_{\mathrm{I}} = K_{\mathrm{I}}/(\sigma\sqrt{\pi a}), \quad K'_{\mathrm{II}} = K_{\mathrm{II}}/(\tau\sqrt{\pi a}), \tag{3.35}$$

where a is the crack length, σ and τ are external loadings.

3.6.1 Half central crack under mixed mode loading

A half central crack under a stress field inducing mixed mode fracture is studied here. The half central crack is of length $a = 0.5w$, where w is the length of a square plate,

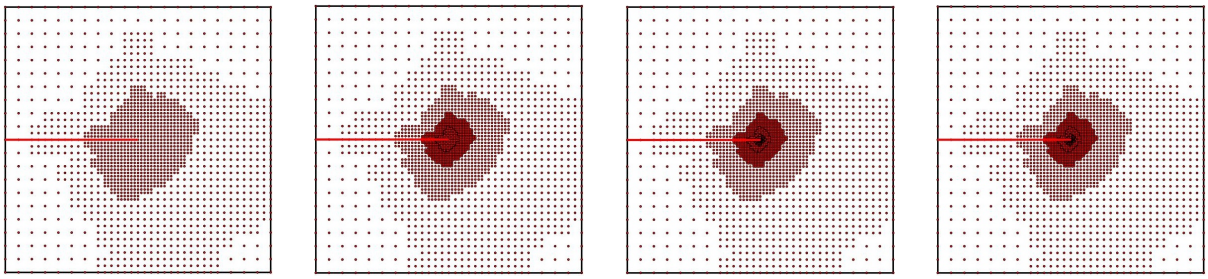

(a) (b) (c) (d)

Figure 3.15: Adaptive particle distributions for the half central crack in mixed mode fracture: (a) step 2; (b) step 4; (c) step 7; (d) step 9.

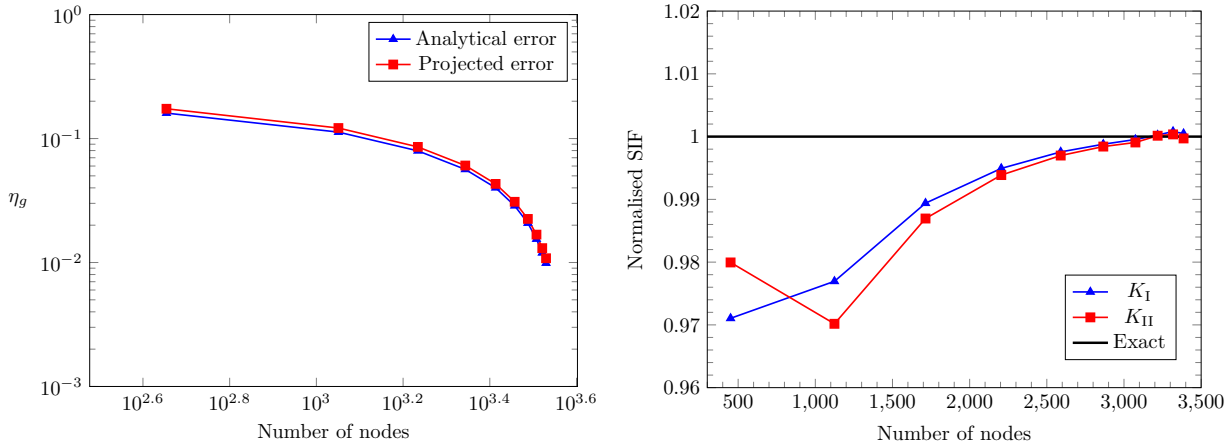

a b

Figure 3.16: Adaptive results for the half central crack in mixed mode fracture: (a) error estimation; (b) SIFs.

$w = 100$mm as depicted in Figure 3.14. This example is extracted from the problem of an infinite plate with a central crack (length=$2a$) under biaxial tension $\sigma = 100$MPa and shear $\tau = 100$MPa, and the analytical SIFs are $K_{\mathrm{I}} = \sigma\sqrt{\pi a}$ and $K_{\mathrm{II}} = \tau\sqrt{\pi a}$. The target error to execute adaptive steps is $\eta_{\mathrm{t}} = 0.02$. The analytical stress and displacement fields for this problem are from Westergaard [247], as

$$\sigma_{xx} = \frac{K_{\mathrm{I}}}{\sqrt{2\pi r}}\cos(\frac{\theta}{2})[1-\sin(\frac{\theta}{2})\sin(\frac{3\theta}{2})] - \frac{K_{\mathrm{II}}}{\sqrt{2\pi r}}\sin(\frac{\theta}{2})[2+\cos(\frac{\theta}{2})\cos(\frac{3\theta}{2})], \tag{3.36a}$$

$$\sigma_{yy} = \frac{K_{\mathrm{I}}}{\sqrt{2\pi r}}\cos(\frac{\theta}{2})[1+\sin(\frac{\theta}{2})\sin(\frac{3\theta}{2})] + \frac{K_{\mathrm{II}}}{\sqrt{2\pi r}}\sin(\frac{\theta}{2})\cos(\frac{\theta}{2})\cos(\frac{3\theta}{2}), \tag{3.36b}$$

$$\sigma_{xy} = \frac{K_{\mathrm{I}}}{\sqrt{2\pi r}}\cos(\frac{\theta}{2})\sin(\frac{\theta}{2})\cos(\frac{3\theta}{2}) + \frac{K_{\mathrm{II}}}{\sqrt{2\pi r}}\cos(\frac{\theta}{2})[1-\sin(\frac{\theta}{2})\sin(\frac{3\theta}{2})], \tag{3.36c}$$

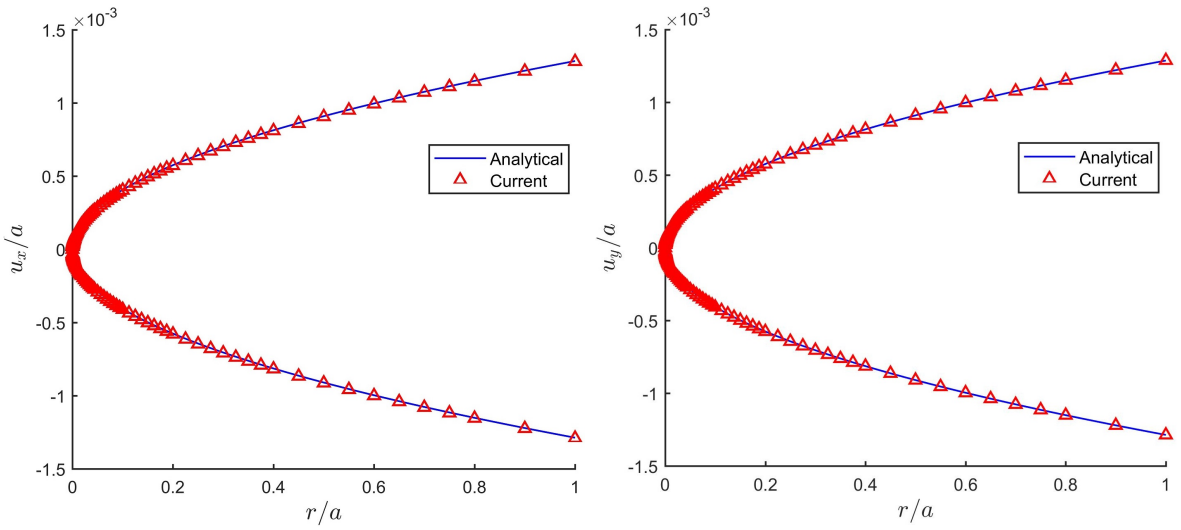

Figure 3.17: Final displacement for the half central crack in mixed mode fracture: (a) u_x; (b) u_y.

$$u_x = \frac{K_{\mathrm{I}}}{2\mu}\sqrt{\frac{r}{2\pi}}\cos(\frac{\theta}{2})[\kappa - 1 + 2\sin^2(\frac{\theta}{2})] + \frac{K_{\mathrm{II}}}{2\mu}\sqrt{\frac{r}{2\pi}}\sin(\frac{\theta}{2})[\kappa + 1 + 2\cos^2(\frac{\theta}{2})], \quad (3.36d)$$

$$u_y = \frac{K_{\mathrm{I}}}{2\mu}\sqrt{\frac{r}{2\pi}}\sin(\frac{\theta}{2})[\kappa + 1 - 2\cos^2(\frac{\theta}{2})] - \frac{K_{\mathrm{II}}}{2\mu}\sqrt{\frac{r}{2\pi}}\cos(\frac{\theta}{2})[\kappa - 1 - 2\sin^2(\frac{\theta}{2})], \quad (3.36e)$$

where μ is the shear modulus and κ is a material constant, as in Equation (C.3). The analytical stresses from Equation (3.36) are applied as external loading as

$$\boldsymbol{f} = [\boldsymbol{\sigma}] \cdot \mathbf{n} = [\sigma_{xx}n_x + \sigma_{xy}n_y,\ \sigma_{xy}n_x + \sigma_{yy}n_y]^{\mathrm{T}}, \quad (3.37)$$

where $\mathbf{n} = [n_x, n_y]^{\mathrm{T}}$ is the outer normal of each edge. The rigid body movement of the plate is constrained by using the following essential boundary conditions,

$$u_x = 0, u_y = 0 \quad \text{at } x = w/2, y = w/2, \quad (3.38a)$$

$$u_y^{\mathcal{S}^+} + u_y^{\mathcal{S}^-} = 0 \quad \text{at } x = 0, y = w/2, \quad (3.38b)$$

where superscripts $\mathcal{S}^+$ and $\mathcal{S}^-$ indicate the two sides of the crack the same as Equation (3.4).

The initial particle arrangement is given in Figure 3.14 (b) and the subsequent particle distributions during adaptive steps are shown in Figure 3.15. In Figure 3.16 (a) it is shown

Table 3.1: Comparison between adaptivity and uniform refinement for the half central crack in mixed mode fracture.

	Adaptive	Uniform refinement				
Particles	initial 20×20	20×20	60×60	100×100	200×200	300×300
Time/t_0	28.539	1.000	4.755	12.890	68.773	224.550
Analytical error	0.00989	0.16039	0.09185	0.07103	0.05017	0.04095
Projected error	0.01083	0.17385	0.09886	0.07633	0.05385	0.04393
Error (K_{I})	0.00048	0.02895	0.01216	0.00775	0.00399	0.00262
Error (K_{II})	0.00029	0.02005	0.01446	0.00932	0.00481	0.00314

that projected errors calculated with the projected stresses in Equation (3.13) are similar with the errors obtained by using analytical stresses from Equation (3.36). The SIFs of two modes during adaptive steps can be seen in Figure 3.16 (b) and can approach the exact values. The final deformation of two crack surfaces are in Figure 3.17, where both u_x and u_y can match the analytical solution from Equation (3.36). The performance of the adaptivity and uniform refinement is compared as in Table 3.1, from which it shows that the adaptivity approach can provide better accuracy by using fewer particles and therefore has a higher computational efficiency than uniform refinement, although the adaptivity approach requires an overhead for adaptive steps to achieve the final particle arrangement. The calculating time is normalised by time/t_0 where t_0 is the time for the initial particle arrangement and $t_0 = 18.123$s for running with MATLAB on a PC (i7 4790, 16GB RAM).

3.6.2 Edge crack under tensile loading

The second example is an edge crack under tensile loading and it is pure mode I fracture, for which there are analytical solutions [248] for validation, as

$$K_{\mathrm{I}} = \sigma\sqrt{\pi a}\left[1.122 - 0.231(\frac{a}{b}) + 10.550(\frac{a}{b})^2 - 21.710(\frac{a}{b})^3 + 30.382(\frac{a}{b})^4\right] . \tag{3.39}$$

The geometries of the problem is depicted in Figure 3.18 where the plate is with height $2h = 200$mm, width $b = 100$mm and crack length $a = 0.2b$. A pair of uniform tensile loadings $\sigma = 100$MPa is applied on the upper and lower edges of the plate. The material

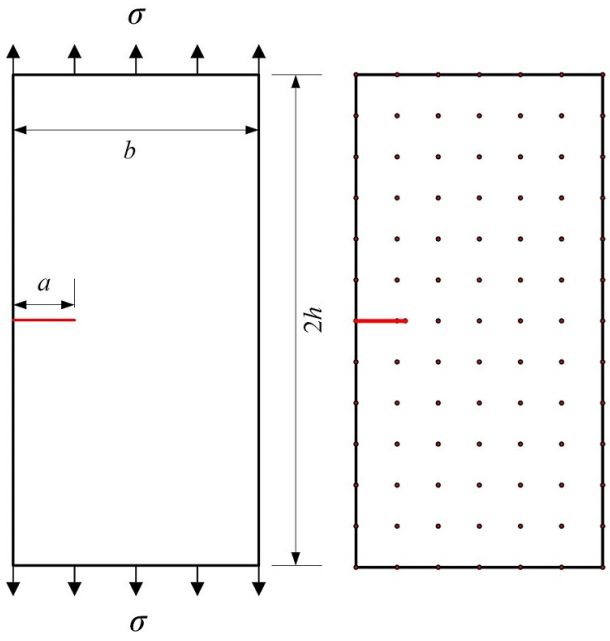

Figure 3.18: Configuration and initial particles of an edge crack problem under uniaxial tensile loading.

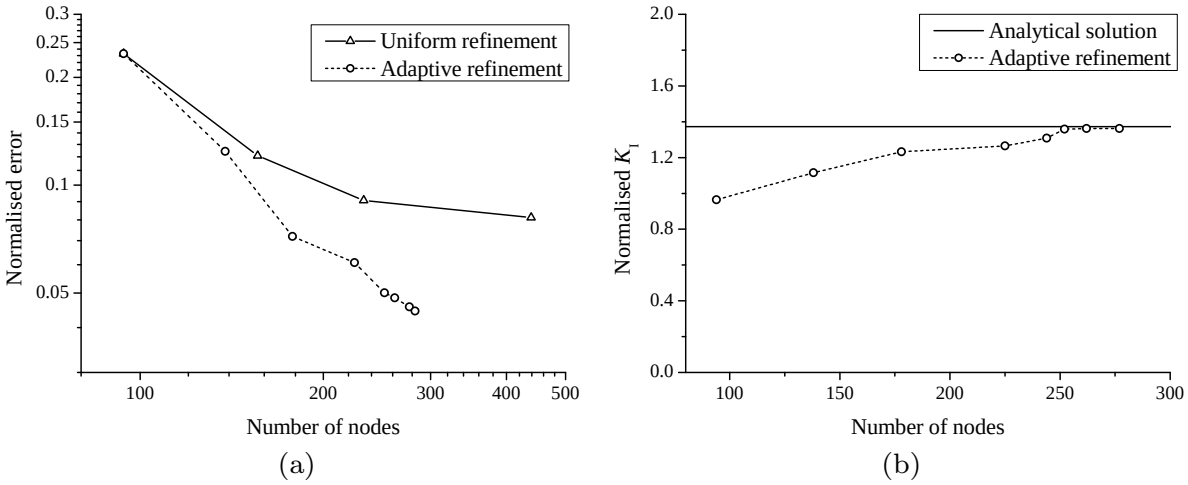

Figure 3.19: Adaptive results for the edge crack under uniaxial tensile loading with initial length: (a) convergence; (b) K_{I}.

properties are $E = 74\mathrm{GPa}$ and $\nu = 0.3$. The midpoint of the right edge is fixed to lock the rigid body movement of the plate. The target error during adaptive steps is set to $\eta_t = 0.05$ and the maximum refinement level is 6 which allows the smallest distance between particles $2^{-6}r_0 = r_0/64$, where r_0 is the initial support size of particles.

Adaptive results for the edge crack problem with the initial crack length are presented in Figure 3.19, from which it is shown that the convergence rate by the adaptivity ap-

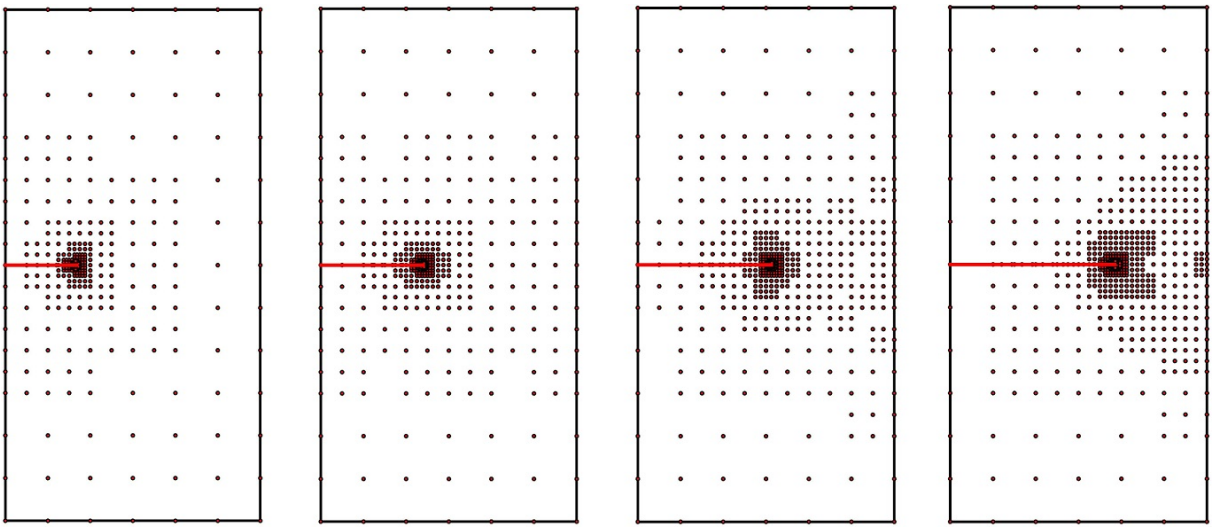

Figure 3.20: Crack propagation (steps 3, 6, 9, 12) and corresponding particle arrangements for the edge crack under uniaxial tensile loading.

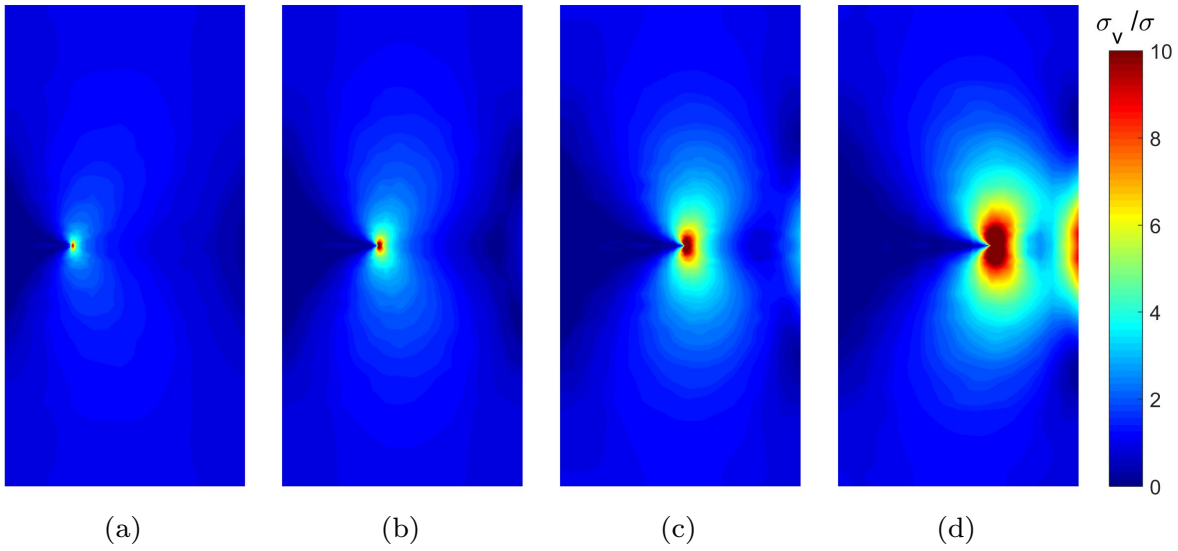

Figure 3.21: Von Mises stress contours for the edge crack under uniaxial tensile loading during crack propagation: (a) steps 3; (b) step 6; (c) step 9; (d) step 12.

proach is higher than that of uniform refinement. The calculated K_{I} becomes close to the theoretical solution after five adaptive steps, as in Figure 3.19 (b). Then crack propagation is considered and this process is seen in Figure 3.20. The crack propagates horizontally with no change of cracking angle because of the symmetry of the problem, and a "mass" of particles generates around the crack tip and moves with the propagating crack which is controlled by the adaptivity approach where the *refinement* function adds particles around the crack tip and the *coarsening* function deletes particles near to old crack tips

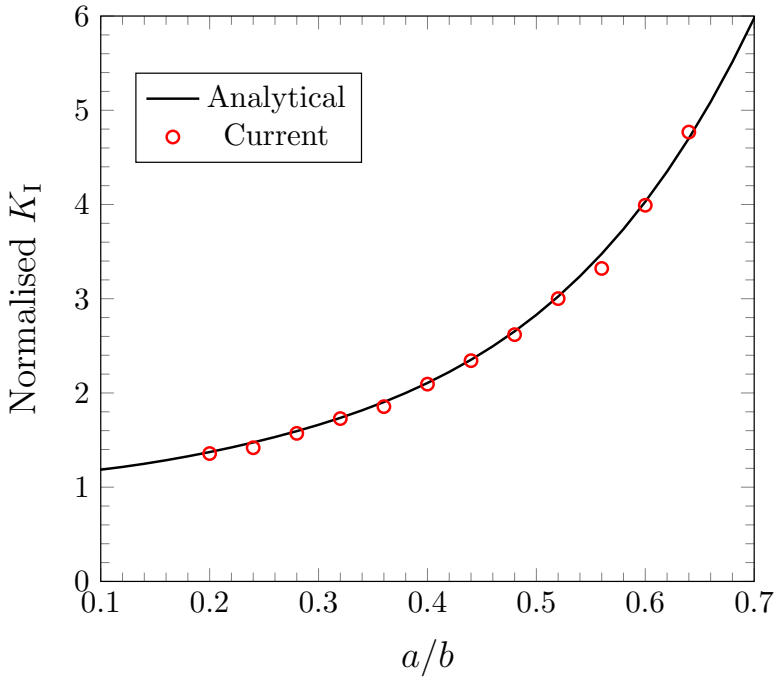

Figure 3.22: Comparison between calculated K_{I} with theoretic solutions for the edge crack under uniaxial tensile loading.

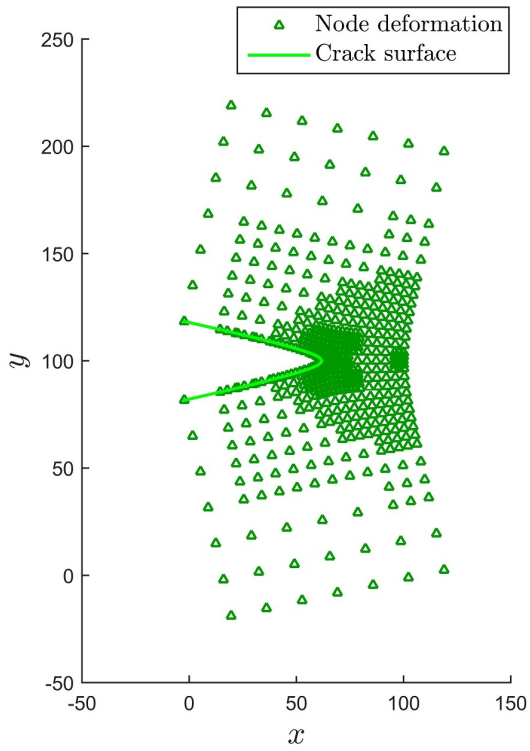

Figure 3.23: Deformation of the edge crack problem under tensile loading enlarged by 10 times

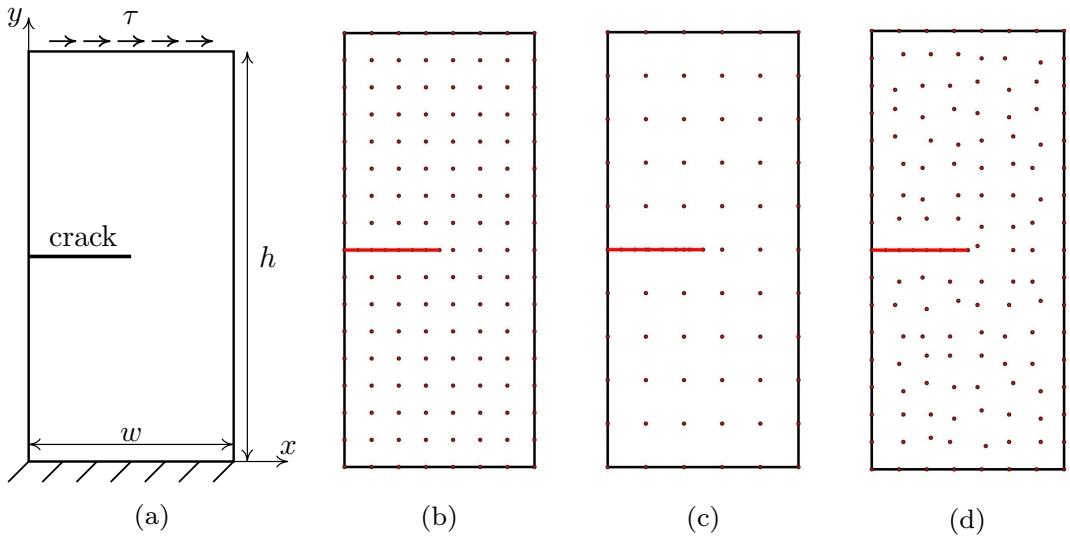

Figure 3.24: An edge crack in a plate under shear loading on the top with different particle arrangements: (a) configuration; (b) case 1; (c) case 2; (d) case 3.

in previous steps. The number of particles is initially 94 and increases to the maximum of 719. The von Mises stress contours of the plate during crack propagation steps are presented in Figure 3.21, where the Von Mises stress σ_v is defined as

$$\sigma_v = \sqrt{\sigma_{11}^2 - \sigma_{11}\sigma_{22} + \sigma_{22}^2 + 3\sigma_{12}^2} \quad \text{for plane stress,} \tag{3.40}$$

and is normalised by the external tensile loading with σ_v/σ. High stresses can be found around the crack tip, and when the crack tip becomes close to the left edge, there are also high stresses around the midpoint of the left edge. The mode I SIF K_{I} is extracted through the interaction integration and is compared with exact values from Equation (3.39), as shown in Figure 3.22. Good results are achieved and particle arrangements are adjusted automatically to maintain both efficiency and accuracy during the crack propagation process. The deformation of the problem in the final crack propagation step is given in Figure 3.23 where a linear crack opening shape can be found in terms of the zoom out response.

3.6.3 Edge crack under shear loading

The third example comes from the geometry of the second problem but a shear loading is used instead, so a pure mode II fracture at the beginning is studied here. The geometry

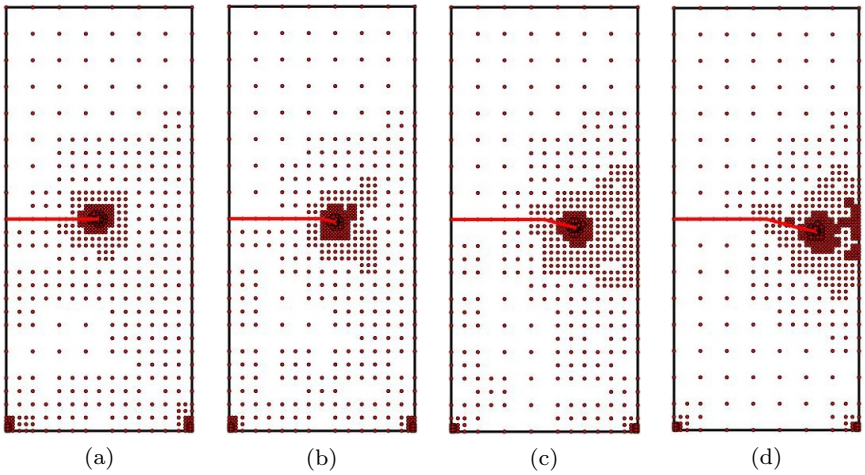

Figure 3.25: Crack propagation steps of the edge crack problem under shear loading for case 1: (a) step 1; (b) step 4; (c) step 8; (d) step 12.

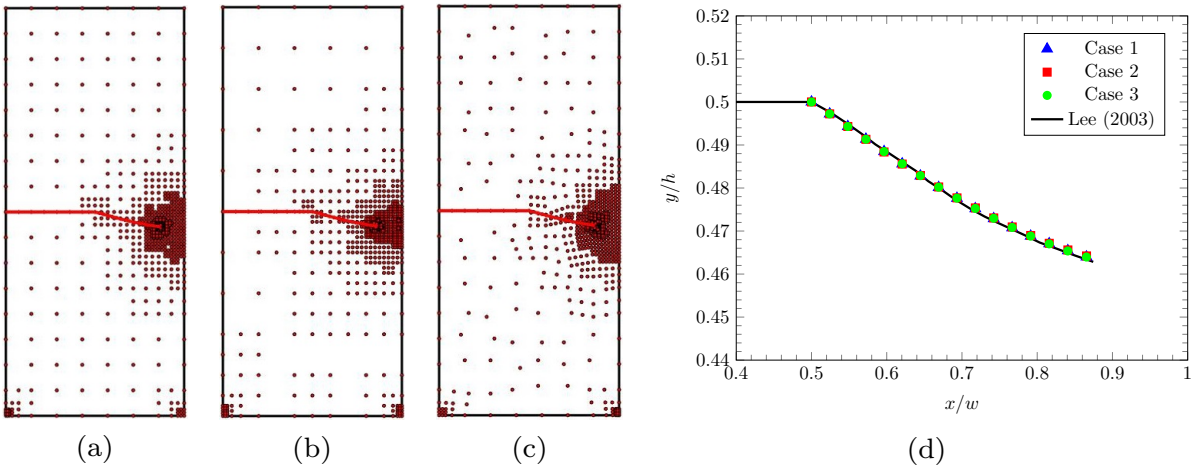

Figure 3.26: Crack growth of an edge crack under shear loading predicted by different initial particle arrangements: (a) case 1; (b) case 2; (c) case 3; (d) comparison.

is illustrated in Figure 3.24 and crack growth predictions by three different initial particle arrangements are compared. Figures 3.24 (b-c) have uniform distribution but different particle densities, while a set of non-uniform distributed particles is defined in Figure 3.24 (d). The plate has height $h = 160$mm, width $w = 70$mm, crack length $a = 0.5w$, material properties $E = 206.8$GPa and $\nu = 0.25$, the same as [229]. The plate is fixed at the bottom and under a shear loading $\tau = 100$MPa at the top, and plane strain conditions are assumed. The target error for adaptive steps is $\eta_{\mathrm{t}} = 0.05$.

Adaptive particle arrangements during the crack propagation process are illustrated in Figure 3.25, where a "mass" of particles travels with the propagating crack tip, which is controlled by the adaptivity approach. The predicted crack growth of all three cases can

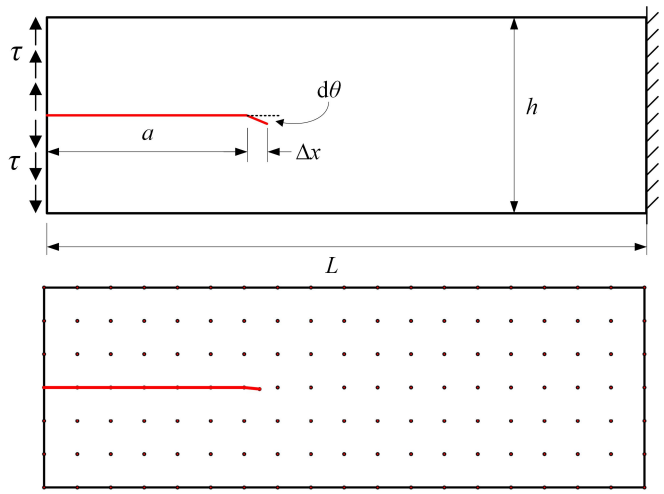

Figure 3.27: Configuration and initial particle arrangement of a double cantilever beam.

be seen in Figure 3.26, from which it is shown that the difference of crack propagation path through different initial particle arrangements is negligible, and the crack paths of the three match the results in [229].

3.6.4 Double cantilever beam

The last example presented here is a double cantilever beam with a horizontal crack at one end and loaded such that mixed mode fracture is considered, as in Figure 3.27. The beam has height $h = 10$cm, length $L = 3h$, crack length $a = h$ and material properties $E = 206.8$GPa and $\nu = 0.3$, the same values as in [229]. A perturbation at the crack tip is defined to control the direction of crack propagation, $\Delta x = 0.76$cm and $\mathrm{d}\theta = 0.1$. The target error during adaptive steps is set to $\eta_t = 0.06$, and the maximum iteration step for the adaptivity process is 6. The beam is fixed at the right and under a pair of tractions $\tau = 1.75$MPa at the left edge.

Crack propagation steps are shown in Figure 3.28 where the crack changes its direction from horizontal to vertical due to the predefined perturbation, and particle arrangements are adjusted automatically around the propagating crack tip by the adaptivity approach. Note that since the crack path is approximated by discrete segments, which are decided by particle densities, fine particles are required where there is a sudden change in the direction of the crack path and these refinements will not be coarsened, as seen in Figure 3.28. The maximum number of particles is 982 while the initial number is 141. Good agreement with the result from [229] can be seen in Figure 3.29, and the deformation of

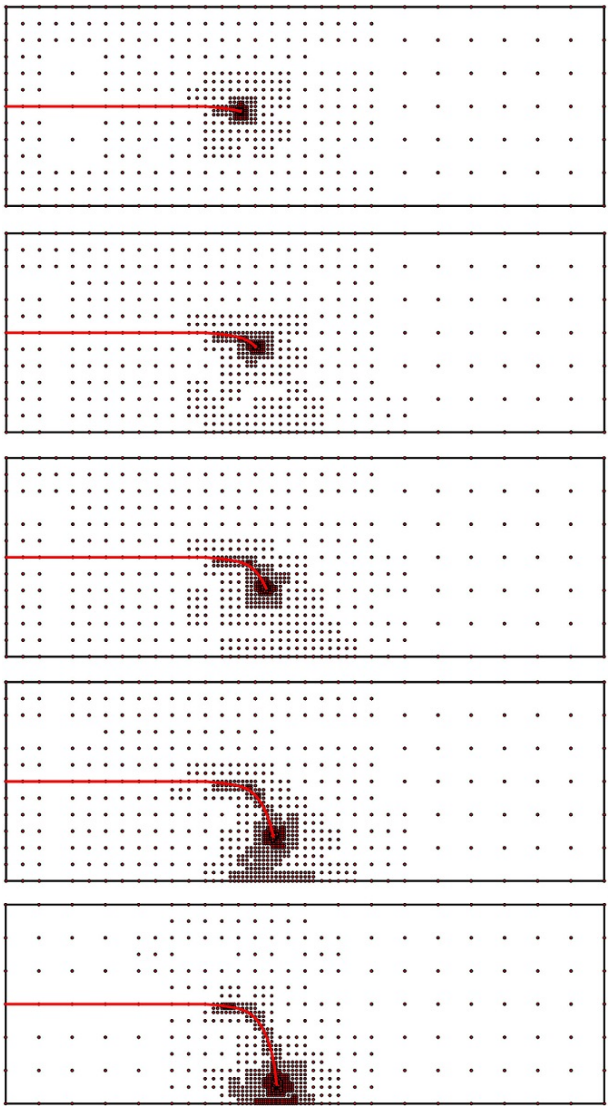

Figure 3.28: Adaptive steps for the crack propagation process for the double cantilever beam (steps 5, 10, 15, 20 and 25).

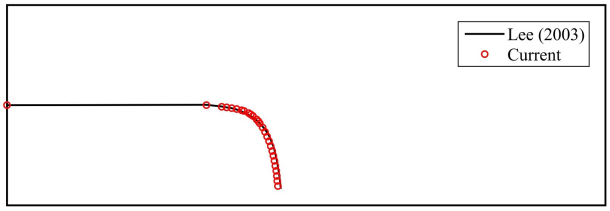

Figure 3.29: Comparison between crack growth prediction and previous results for the double cantilever beam.

the double cantilever beam at the final crack propagation step is shown in Figure 3.30. A comparison between the original and the modified CPM is demonstrated in Figure 3.31, where there is no adaptivity in the original CPM and a fine group of particles are applied

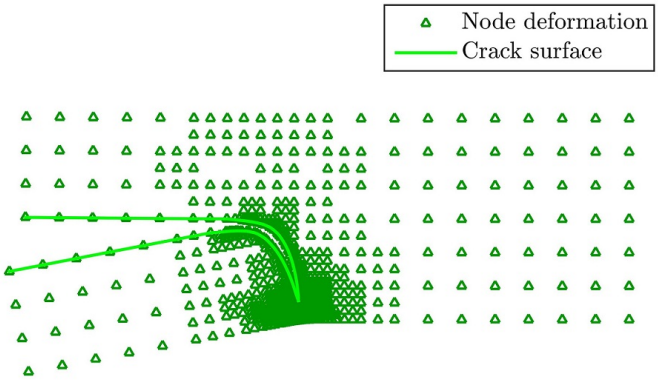

Figure 3.30: Deformation (enlarged by 50 times) of the double cantilever beam.

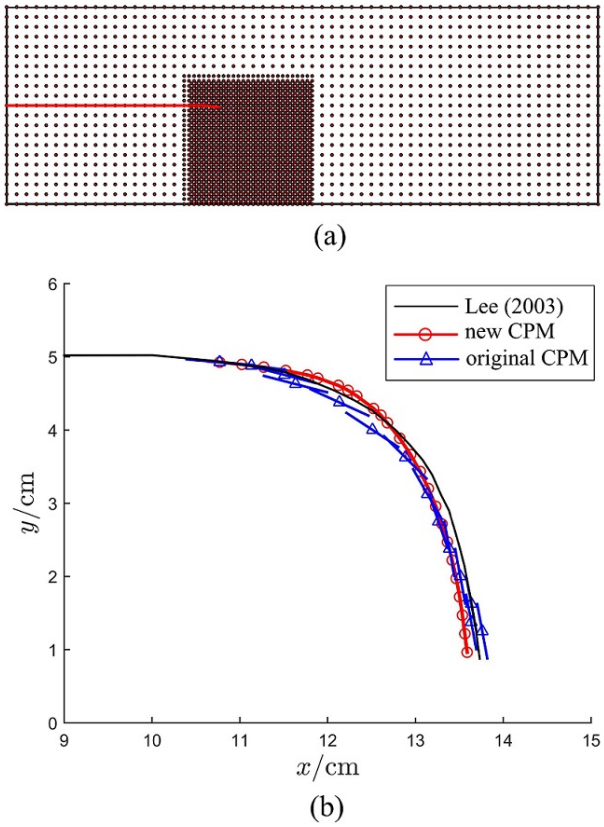

Figure 3.31: Comparison of results between new CPM and original CPM for the double cantilever beam: (a) nodal arrangements for original CPM; (b) crack path description.

at the possible crack propagating zone. The results of the crack growth for two methods are both close to the reference curve, while the modified CPM provides a smoother crack path than the original CPM. The modified CPM also shows better efficiency by using the adaptivity approach, as the maximum number of particles in the modified CPM is 982, much lower than 2479 in the original CPM. Normally, the original CPM requires the number of particles at the level of 10^4 to achieve good accuracy as in [202, 211].

3.7 Summary

An adaptive CPM has been developed in this chapter for 2D crack propagation analysis under quasi-static loading. A continuous crack path is described by a set of discrete segments centred at particles, so updating the crack pattern is made easy by adding and deleting cracking particles, which makes this methodology a simpler alternative to crack description using, for instance, the level set method and is suitable for multiple-crack problems. These discrete segments are located by cracking particles with bilinear segments by which the angular change of crack paths is recorded, so they do not cross each other and therefore no spurious cracking occurs. The densities of particles are controlled by an adaptivity approach, which adds and removes nodes/particles and adjusts support sizes, to make the whole analysis accurate and efficient. The adaptivity approach makes use of a recovery-based error estimator and the h-adaptive strategy to decide where and how to refine the particle density. A novel approach is used to revise the stiffness matrix in an efficient way and information relating to the system stiffness matrix is stored in a local matrix at cell level. In this way, the integration of the system stiffness is only required over the small domain which is changed by either the adaptivity or crack propagation, while the remainder can be read from the storage directly. Since the changed domain is usually smaller than the problem domain, the whole calculating time is much reduced. This approach can be applied to other methods using adaptive procedures as a kind of acceleration. SIFs are calculated by the interaction integral around the crack tip, which is a domain quadrature type of the J-integral. Essential boundary conditions are imposed into governing equations by Lagrange multipliers. Several numerical examples demonstrate the performance of the proposed methodology and all show good agreement. The feature of using discrete segments to approximate continuous crack path makes this methodology suitable to describe nonsmooth cracks and multiple cracks, which will be covered in the following chapter.

Chapter 4

A multiple-cracked particle method for complex crack modelling

4.1 Introduction

Fracture behaviour in nature is usually characterised by complex crack patterns composed of multiple and branching cracks, while conventional numerical methods are mainly focused on fracture problems involving a single crack somewhat far from these real situations. The simulation of complex cracks with multiple tips and complicated geometries brings many challenges to current numerical methods. For instance in the XFEM, enrichment functions are introduced into the displacement approximation to capture the discontinuities at cracks as in Section 1.5.1 and this becomes mathematically complicated for multiple cracks. A multiple-cracked particle method is developed here to address this issue and is based on the CPM in Chapter 3. The particle at a crack branch point is split into several subparticles complying with the crack patterns, and crack opening is captured by the relative displacement of these subparticles, not through enrichment functions. A crack with a complex geometry can therefore be decomposed and modelled by a set of crack segments, and is then handled by the visibility criterion using a similar algorithm for single cracks.

This chapter is focused on the modelling of multiple cracks. The issues in problems of multiple cracks are firstly reviewed, including the modelling of multiple crack tips and crack branches. Then the strategy of multi-split cracking particles is presented, and the

implementation is included. Finally, several numerical examples are used to demonstrate the performance of the proposed methodology for crack problems with complex geometries.

4.2 Issues in the modelling of multiple cracks

When multiple crack problems (i.e. where there are more than one crack tips in a fracture pattern) are studied, the interaction between cracks must be considered, which leads to some issues in modelling. The issues exist in two places: when multiple crack tips become close to each other and in the modelling of discontinuities at crack branches, as will be discussed below.

4.2.1 Modified weight function for multiple crack tips

The visibility criterion and the diffraction criterion are two widely used methods to capture the discontinuities at cracks in meshless methods, as mentioned in Section 3.2.1. In many situations [59, 179, 217], they are applied for single crack problems, but their application to multiple cracks is rare.

For the visibility criterion, the connectivity between two nodes is defined by checking whether the straight line connecting the two nodes is sheltered by crack paths. The algorithm for a single crack can still be applied for multiple cracks, and the difference is that this algorithm should be executed for every crack. One example of its use in the literature is by Rabczuk et al. [204] in the cracking particle method (Section 3.2), where crack discontinuities are obtained by checking the visibility between particles in a set of discontinuous segments for modelling multiple crack branches.

The situation for the diffraction criterion is more complicated, since crack tip coordinates are involved to modify the supports of particles, e.g. the two cracks in Figure 4.1. The weight function $w(r)$ for a node $\mathbf{x}_i$ is defined by Equation (2.3) with the input parameter $r = \|\mathbf{x} - \mathbf{x}_i\|/r_0$, and the diffraction criterion for a single crack is Equation (3.1). In [249] the diffraction criterion is modified for multiple cracks to

$$r = (\frac{s_1 + s_2}{s_0})^{\gamma} s_0, \tag{4.1}$$

where $s_0 = \|\mathbf{x} - \mathbf{x}_i\|$, γ is the same as in Equation (3.1), s_1 and s_2 are modified distances

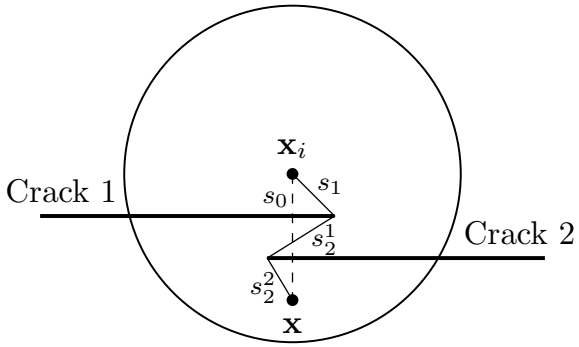

Figure 4.1: Modified diffraction criterion for multiple cracks.

defined as

$$s_1 = \|\mathbf{x}_c^1 - \mathbf{x}_i\|, \tag{4.2a}$$

$$s_2 = \sum_j^n s_2^j, \tag{4.2b}$$

where

$$s_2^j = \|\mathbf{x}_c^{j+1} - \mathbf{x}_c^j\|, \quad j = 1, 2 \ldots n-1, \tag{4.2c}$$

and

$$s_2^n = \|\mathbf{x} - \mathbf{x}_c^n\|, \tag{4.2d}$$

and n is the total number of cracks cutting the straight line between $\mathbf{x}$ and $\mathbf{x}_i$, and $\mathbf{x}_c^j$ is the location of the jth crack tip. This modified version has been shown to be sufficient to characterise multiple cracks in the influence domain of a node as in [249].

Apart from the two methods mentioned above, discontinuities of multiple cracks can also be modelled by modifying the weight function with an intrinsic enrichment function $h(\mathbf{x})$, as in [250, 251]. The evaluation of $h(\mathbf{x})$ is given in detail in [250, 251], while the features of the method are described below. The parameter $h(\mathbf{x})$ is a scalar distance function with a range from 1 on the side of the crack containing the node $\mathbf{x}_i$ to 0 on the other side, and provides a smooth angular transition between the two sides around the crack tip. This approach has been applied to the RKPM for multiple cracks and kinked cracks [250, 251] and is also applicable to other meshless methods. The resulting weight function of a node is modified by multiplying the enrichment functions of all cracks, as

$$h(\mathbf{x}) = \prod_{i=1}^{n} h_i(\mathbf{x}), \tag{4.3}$$

where $h_i(\mathbf{x})$ is the enrichment function for the ith crack and n is the number of cracks. This approach provides a simple way to handle the discontinuities associated with multiple cracks, however the evaluation of $h_i(\mathbf{x})$ requires the distance to each ith crack tip, which is not computationally cheap for multiple cracks

In addition, those methods using tip enriched basis functions have to be amended when multiple crack tips are involved, e.g. in [252]. The enriched basis function in the EFGM for a single crack is

$$\mathbf{p}^{\mathrm{T}}(\mathbf{x}) = [1, x, y, \sqrt{r}\cos(\frac{\theta}{2}), \sqrt{r}\sin(\frac{\theta}{2}), \sqrt{r}\sin(\frac{\theta}{2})\sin(\theta), \sqrt{r}\cos(\frac{\theta}{2})\sin(\theta)], \tag{4.4}$$

where r and θ are the local polar coordinates originating at the crack tip. When there are n crack tips in the node influence domain, the coordinates (r, θ) are chosen by the minimum normalised distance to the crack tip, i.e. $\min r_i/a_i,\ i \in \{1, 2, \ldots, n\}$, where r_i and a_i are the distance to the tip and the crack length of the ith crack respectively. This modified approach can work well for multiple cracks with similar lengths in the domain.

4.2.2 Enrichment functions for crack branches

The XFEM, a popular method for fracture modelling, makes use of enrichment functions in the displacement approximation to obtain the discontinuities at cracks, so that a crack can propagate arbitrarily within elements and remeshing is not required [253]. However, the XFEM meets a dilemma when applied to problems of multiple cracks and crack branches.

The displacement in the XFEM for a single crack is modelled by Equation (1.17) as mentioned in Section 1.5.1. When two or more intersecting cracks are considered [155, 253, 254], e.g. a cross crack in Figure 4.2, the displacement becomes

$$\begin{aligned} u^h(\mathbf{x}) = &\sum_i^n \Phi_i(\mathbf{x})u_i + \sum_i^{n_1} \Phi_i(\mathbf{x})H_1(\mathbf{x})b_{1i} + \sum_i^{n_2} \Phi_i(\mathbf{x})H_2(\mathbf{x})b_{2i} \\ &+ \sum_i^{n_3} \Phi_i(\mathbf{x})H_3(\mathbf{x})b_{3i} + \sum_i^{n_{1,2}} \Phi_i(\mathbf{x})J_{1,2}(\mathbf{x})c_i + \\ &\sum_i^{n_{1,3}} \Phi_i(\mathbf{x})J_{1,3}(\mathbf{x})d_i + \sum_i^{n_c} \Phi_i(\mathbf{x}) \left(\sum_{k=1}^{4} R_k a_i^k \right), \end{aligned} \tag{4.5}$$

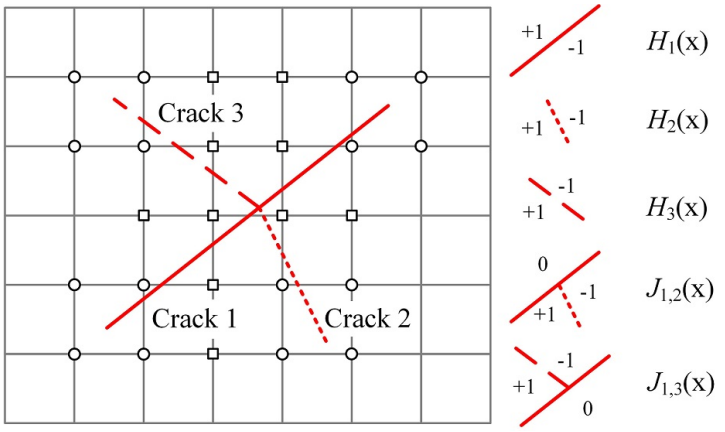

Figure 4.2: Enrichment functions in the XFEM for modelling crack branches.

where the subscripts of $H(\mathbf{x})$ and n indicate the crack index, and $n_{1,2}$ is a group of nodes with influence domains covering the junction of cracks 1 and 2, the same as $n_{1,3}$ for cracks 1 and 3. $J_{1,2}(\mathbf{x})$ and $J_{1,3}(\mathbf{x})$ are two modified Heaviside functions, where an extra value of 0 for the crack junctions is included, as shown in Figure 4.2. b_{1i}, b_{2i}, b_{3i}, c_i, d_i and a_i are extra unknowns in the enrichment functions. With the more cracks, more terms are included in the enrichment functions and hence the computational cost rises.

For numerical methods using the level set approach to describe crack patterns, e.g. in the XFEM [161, 183] and the EFGM [179, 180], a crack requires two level set functions to describe its geometry, and the problem becomes more complex as the number of cracks increases. Although in [254] it is claimed that the numerical manifold method provides a simpler way for the displacement approximation in problems with complex crack patterns, the expense of generating physical covers in this method still impedes its further application, as mentioned in [216].

4.3 Multiple split cracking particles

A simple approach to model multiple cracks and crack branches can be achieved via a modified CPM [202–204, 227]. In the CPM, continuous crack paths are approximated by a set of discontinuous segments centred at cracking particles, which reduces the cost of tracking multiple cracks. Discontinuities at crack branches are modelled by modifying the influence domain of particles, so that complex enrichment functions in the XFEM mentioned above are avoided and the algorithm for a single crack can still be applied to multiple cracks without major amendments, which is the crux of this chapter. A

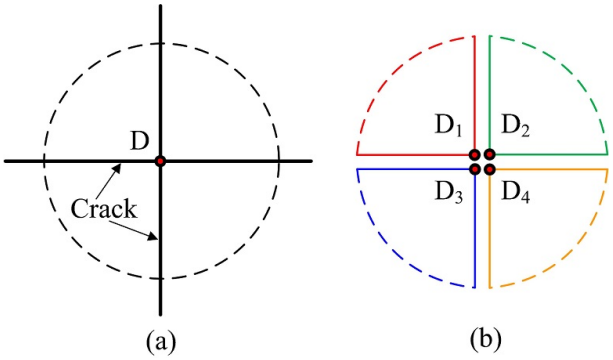

Figure 4.3: Multiple-split cracking particle for a cross crack: (a) particle at the junction; (b) four subparticles.

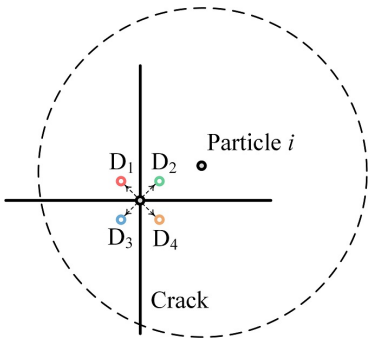

Figure 4.4: Strategy to distinguish cracking particles at the same location.

multi-cracked particle method is developed here, which is based on the CPM in [227] and material contained in previous chapters of this thesis.

Considering a cross crack as in Figure 4.2 again, the particle D at the junction in Figure 4.3 (a) is split into four subparticles, D_1, D_2, D_3 and D_4, and the support is also divided into four subparts, as in Figure 4.3 (b). These four subparticles are not connected to each other, and the crack opening at this junction point is obtained by the relative displacements of those four subparticles, i.e.

$$[\![u(\mathbf{x})]\!] = \sum_{i\in\mathcal{S}^+} \Phi_i(\mathbf{x}^+)u_i + \sum_{i\in\mathcal{S}^-} \Phi_i(\mathbf{x}^-)u_i, \tag{4.6}$$

where $\mathbf{x}^+$ and $\mathbf{x}^-$ are two sets of particles located on the opposite sides of crack surfaces $\mathcal{S}^+$ and $\mathcal{S}^-$ respectively. The visibility criterion (following the algorithm in [255]) is applied to check the connectivity between those particles. For cracking particles which are multiply split, a simply strategy is used to distinguish between these subparticles at the same location. Each subparticle i is given a tiny shift at the bisector direction θ_i of

its sector support following the Equation (4.7), and then the standard visibility algorithm is applied.

$$\begin{cases} x_i' = x_i + 0.0001 r_i \cos(\theta_i), \\ y_i' = y_i + 0.0001 r_i \sin(\theta_i), \end{cases} \tag{4.7}$$

where r_i and (x_i, y_i) are the support size and the location of particle i respectively, and (x_i', y_i') is the shifted location. With this strategy, four subparticles in Figure 4.3 (b) at the same location of the original particle D are moved away in different directions, as seen in Figure 4.4. Then it is easy to assess the visibility between particle i and D_1 while the other three subparticles are invisible to particle i. It is notable that the shift is only applied to the visibility algorithm and the location of particles is not actually changed in other calculations. The whole process is demonstrated in Algorithm 4.1

Algorithm 4.1 Check the visibility between particles i and j

Input: Node information of nodes i and j
Output: *status*: 0 – invisible; 1 – visible

```
status ← 1
if node j is outside the support of node i then
    status ← 0
else
    if node i is a cracking particle then
        shift the location of node i by Equation (4.7)
    end if
    if node j is a cracking particle then
        shift the location of node j by Equation (4.7)
    end if
    status ← standard visibility criterion
end if
return status
```

4.4 Numerical examples

In this section, some numerical examples with multiple crack tips are studied, where the crack branch and the propagation of multiple cracks are considered, however the situation when many crack tips become very close is not included, since this causes issues in calculating the J integral. A linear basis function and fourth order Gaussian quadrature are used. The adaptivity process developed in Section 3.3 is used here, where the error target is $\eta_t = 0.06$, and the maximum adaptive steps for one propagation step is 6.

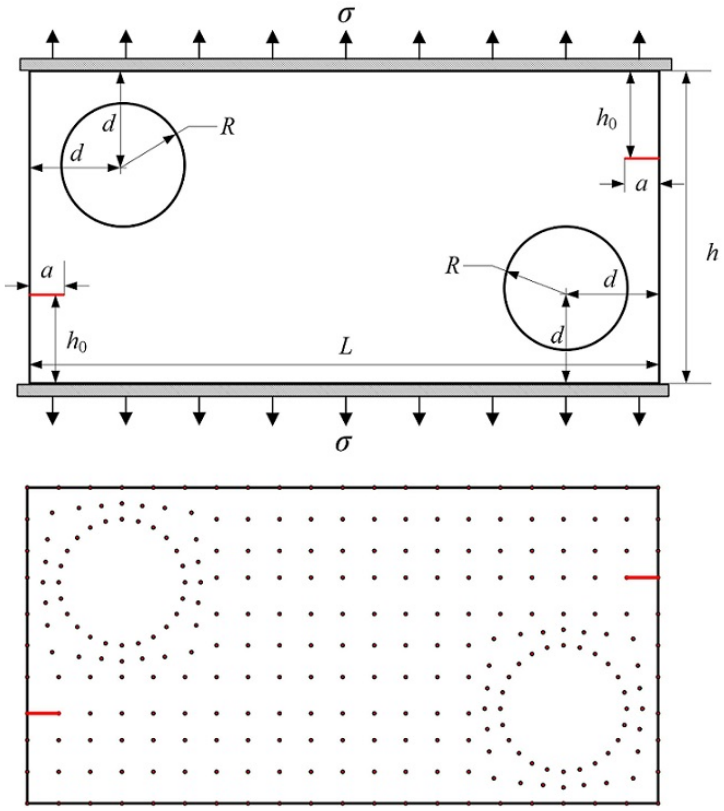

Figure 4.5: Two cracks in a plate with two holes: configuration and initial nodes.

Plane stress conditions and linear elastic materials are assumed for all problems with $E = 200\text{GPa}$ and $\nu = 0.3$, unless stated otherwise. SIFs are calculated by the interaction integral and in all examples are normalised as

$$K'_n = K_n/(\sigma\sqrt{\pi a}), \quad n \in \{\text{I, II}\}. \tag{4.8}$$

4.4.1 Two cracks in a plate with two holes

The first example includes two straight edge cracks in a plate with two holes, (see Figure 4.5), and the propagation of both two cracks are executed simultaneously. The configuration of this problem is the same as in references [256, 257], where $L = 20\text{mm}$, $h = 0.5L$, $a = 0.1h$, $h_0 = 2.85\text{mm}$, $R = 2\text{mm}$ and $d = 3\text{mm}$. The upper and lower edges are kept straight and loaded by a pair of tensile forces, the magnitude of which is not mentioned in [256]. The loading condition is approximated by fixing the bottom and shifting the upper edge vertically by $0.02h$.

Adaptive particle arrangements during the crack propagation process are shown in

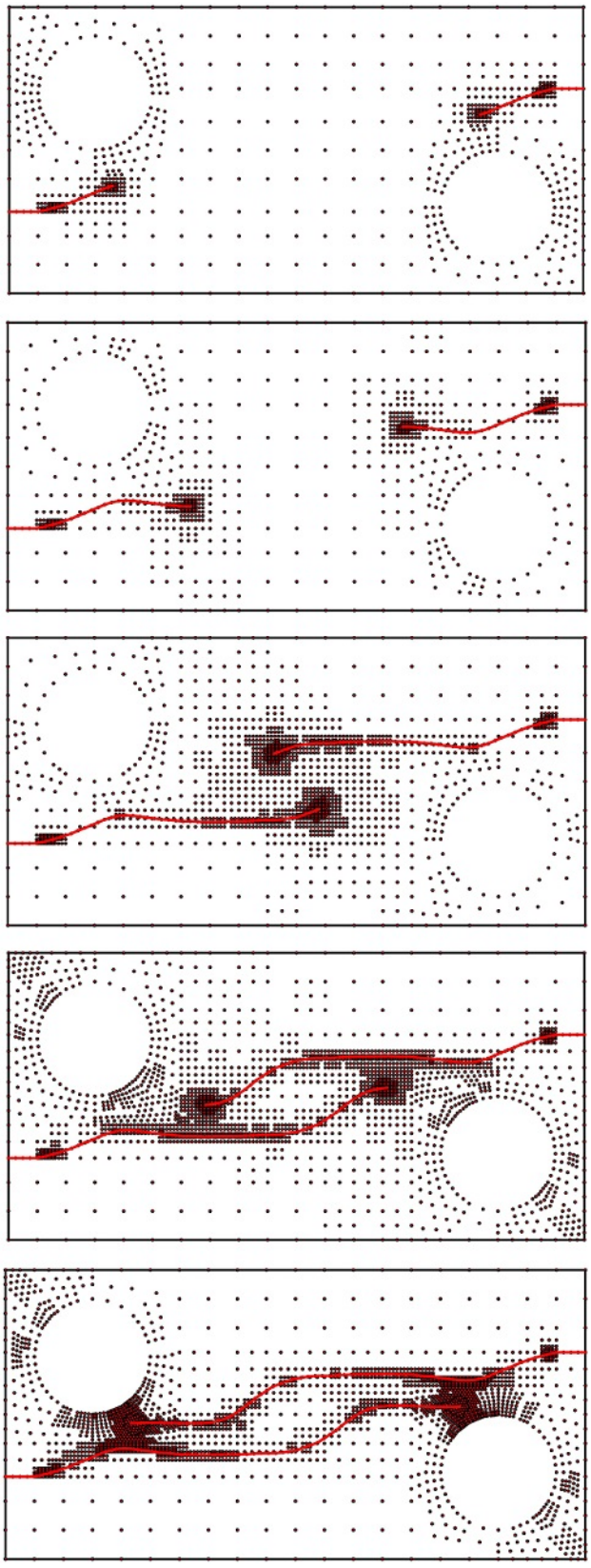

Figure 4.6: Crack propagation of two cracks and particle arrangements: steps 8, 16, 26, 34 and 39.

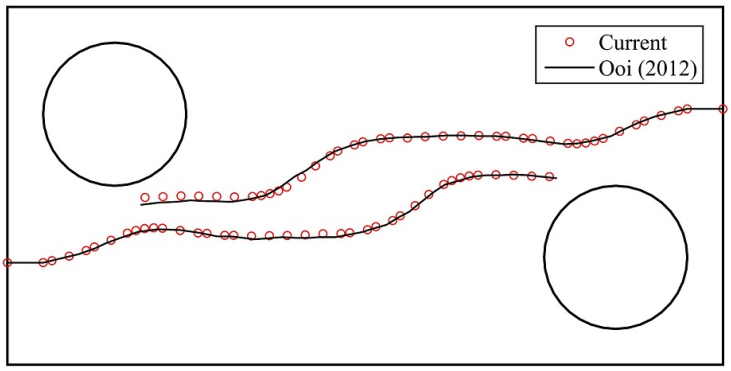

Figure 4.7: Comparison between predicted crack path and previous result for the two-crack problem.

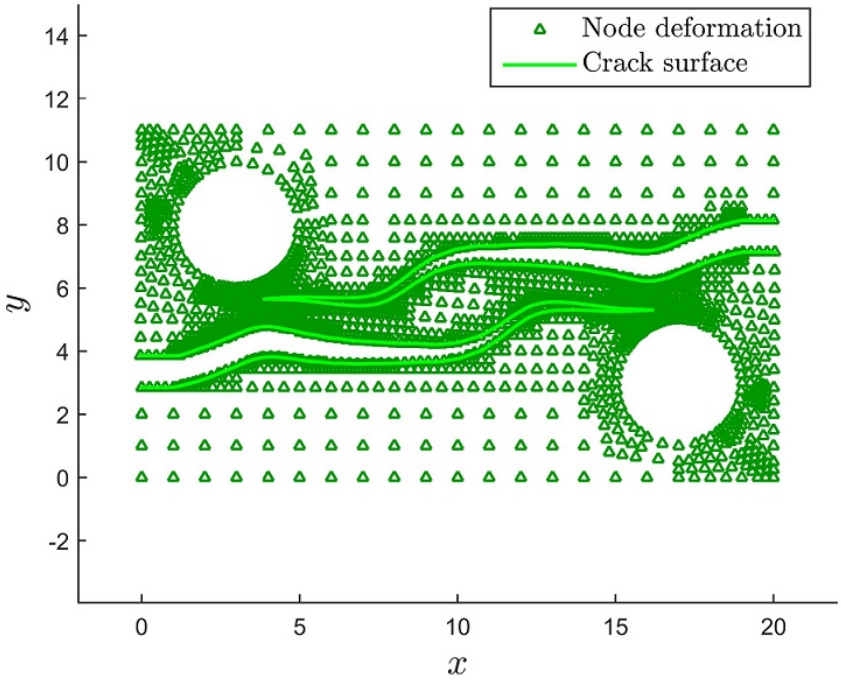

Figure 4.8: Final deformation enlarged by 5 times for the two-crack problem.

Figure 4.6, where there are two "masses" of particles generated automatically around each crack tip and they move with the two crack tips. The two cracks firstly travel towards their nearest hole, then advance horizontally until they are close to each other at the centre of the plate. Finally, the two crack tips are each attracted by the hole on their opposite side of the plate and move towards it. The adaptivity approach controls the particle arrangements during the crack propagation and increases the number of particles from 279 up to 3152. The calculated crack growth is compared with previous results from [256] and good agreement is obtained as given in Figure 4.7. The deformation of the final

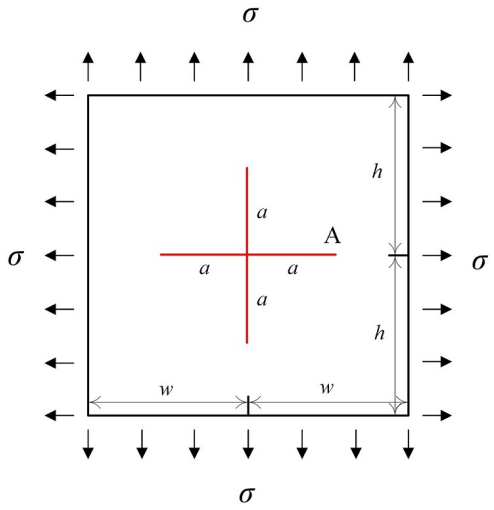

Figure 4.9: Configuration of the cross crack.

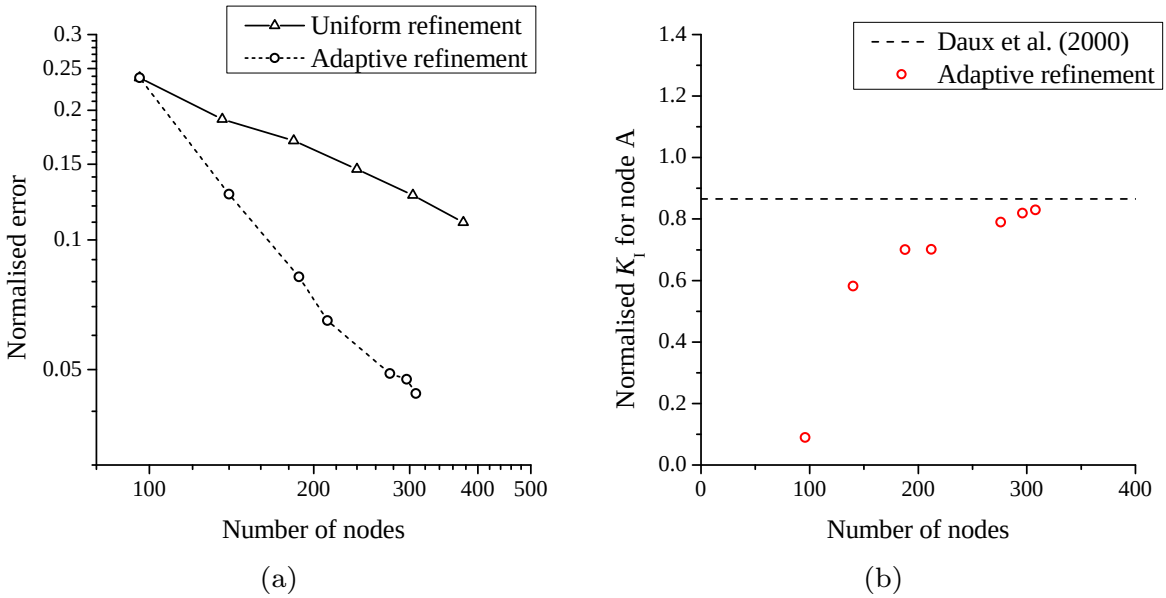

Figure 4.10: Adaptive results for the cross crack with the initial length: (a) error estimation; (b) normalised K_{I} for tip A.

propagation step is shown in Figure 4.8. It is notable that non-uniform background cells are used around the two holes, indicating that the adaptivity process can work well with non-uniformly distributed particles.

4.4.2 Cross crack

In the second example, the deformation of a square plate with a cross crack loaded by biaxial tensile loading is studied. The configuration is given in Figure 4.9 where $w =$ 20mm, $w/h = 1$ and $a/w = 0.1$. The biaxial tensile traction is set with $\sigma = 100$MPa

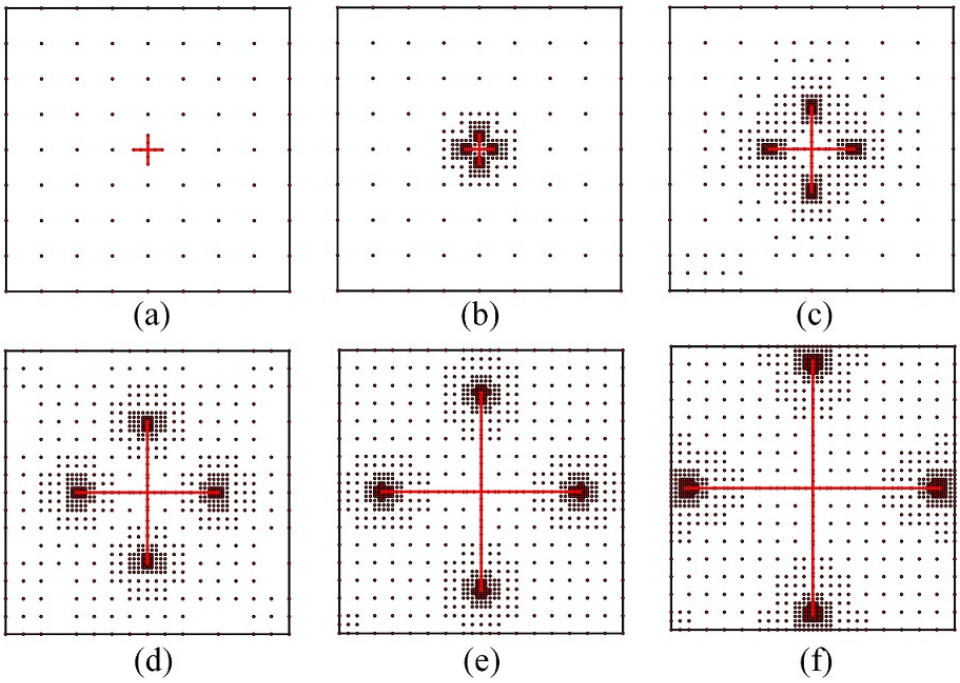

Figure 4.11: Adaptive particle arrangements for the cross crack during the crack propagation: (a) initial nodes; (b) step 1; (c) step 3; (d) step 5; (e) step 7; (f) step 9.

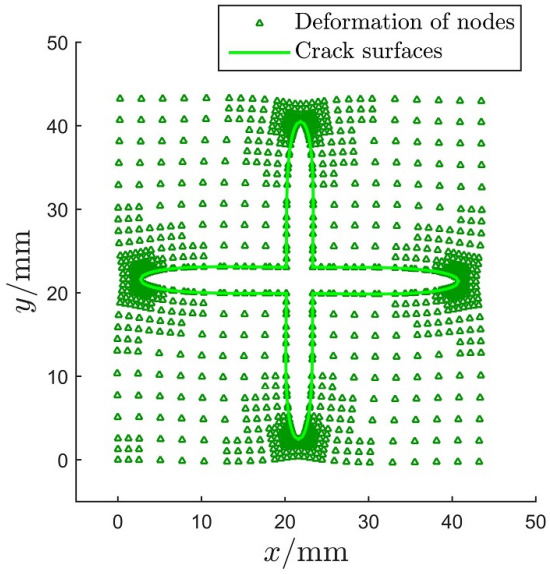

Figure 4.12: Final deformation enlarged by 50 times of the cross crack problem at the final propagation step.

and the plate is fixed by locking the movement of the left bottom corner. Due to the symmetry of this problem, SIFs are nearly the same at all four crack tips and are under mode I fracture, while mode II SIFs at four tips are zero.

The global errors during adaptive steps for the initial crack length are given in Figure

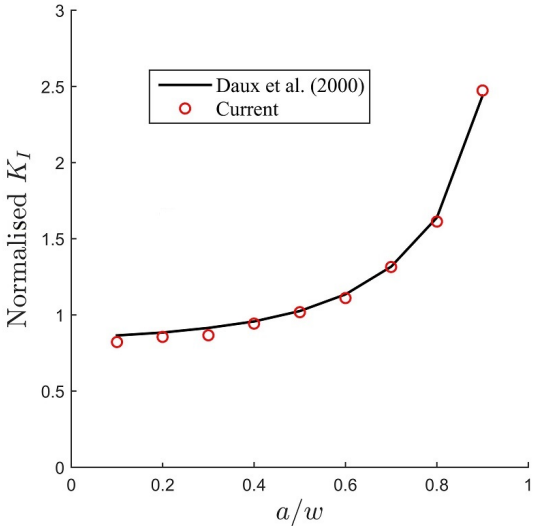

Figure 4.13: SIF K_{I} at the tip A for the cross crack with different lengths.

4.10 (a), with an initial particle arrangement of Figure 4.11 (a). This shows that the adaptivity approach has a higher convergence rate than that obtained with uniform refinement, and a converged K_{I} for the right crack tip (marked as the tip A) can be achieved as in Figure 4.10 (b). Adaptive particle arrangements during the crack propagation can be seen in Figure 4.11, where four "masses" of particles travel with the crack tips as in the previous example, and the number of nodes ascends from 112 to 1851. The deformation of the problem at the final propagation step is shown in Figure 4.12, where similar particle arrangements can be seen at four cracks because of the symmetry. Results of Mode I SIF at the tip A for different crack lengths are given in Figure 4.13, which indicates good agreement with results from Daux et al. [155].

4.4.3 Star-shaped crack

The star-shaped crack is the third example under consideration, which is more complex than the second example with an increase of crack tips from 4 to 6. The geometries are $w = 20$mm and $w/h = 1$ as in Figure 4.14. The crack geometry consists of length $a/w = 0.1$ at the beginning and propagates to $a/w = 0.9$ after eight steps. The plate is under a biaxial tensile loading $\sigma = 100$MPa, and similar boundary conditions to the second example are applied. For this problem, two cases are considered: firstly the six crack branches propagate straightly without changing their direction to make a comparison with the results from Daux et al. [155], where SIFs of this problem with different crack lengths

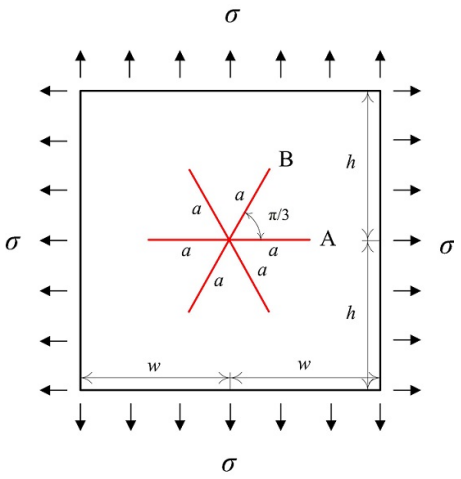

Figure 4.14: Configuration of the star-shaped crack.

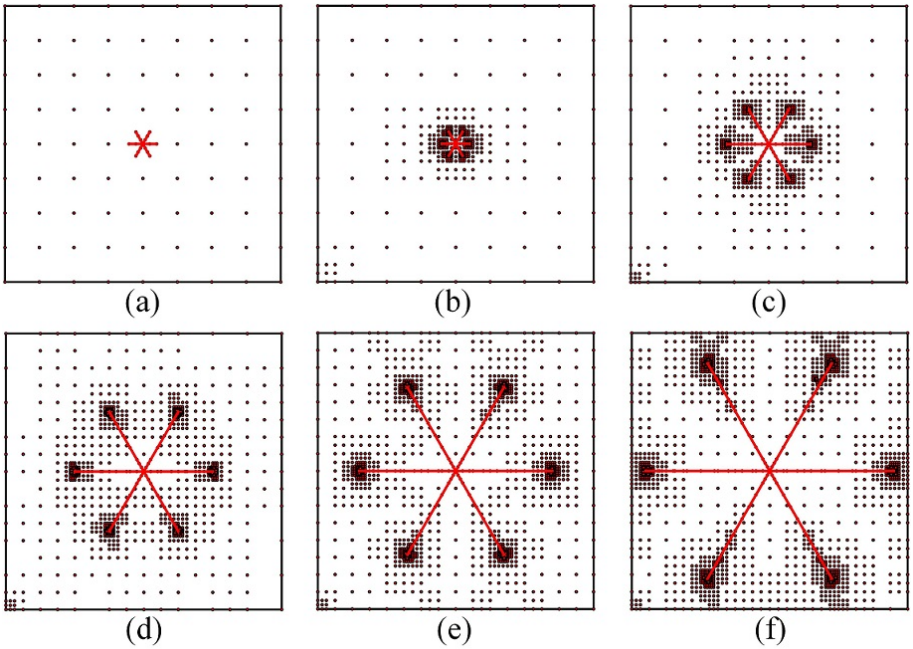

Figure 4.15: Adaptive steps for star-shaped crack propagation without angular change: (a) initial particles; (b) step 1; (c) step 3; (d) step 5; (e) step 7; (f) step 9.

are calculated and there is no propagation; then in the second analysis this constraint is removed and it is used to show that with propagation very little deviation from its original direction can occur anyway.

This problem is discretised with the initial particles in Figure 4.15 (a). In the first case, adaptive particle arrangements can be seen in Figure 4.15, where six groups of particles are generated around six crack tips and move with these crack tips during the propagation. The maximum number of particles in this calculation is 2158, which starts from 112 in the

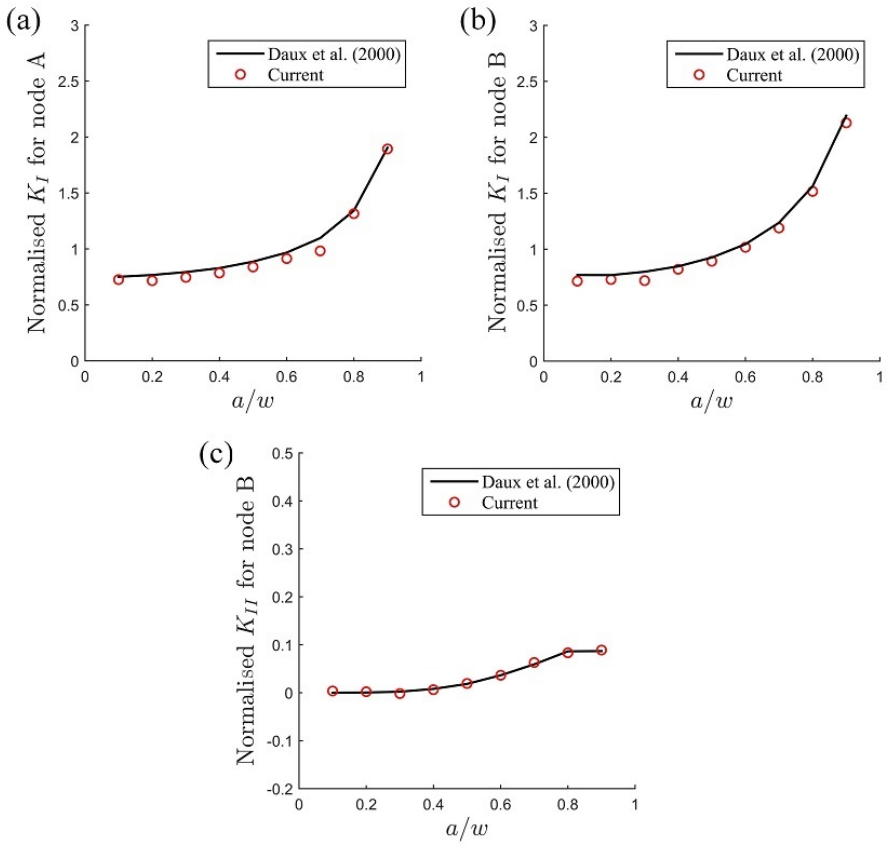

Figure 4.16: Validation of SIFs for the star-shaped crack: (a) K_{I} at crack tip A; (b) K_{I} at crack tip B; (c) K_{II} at crack tip B.

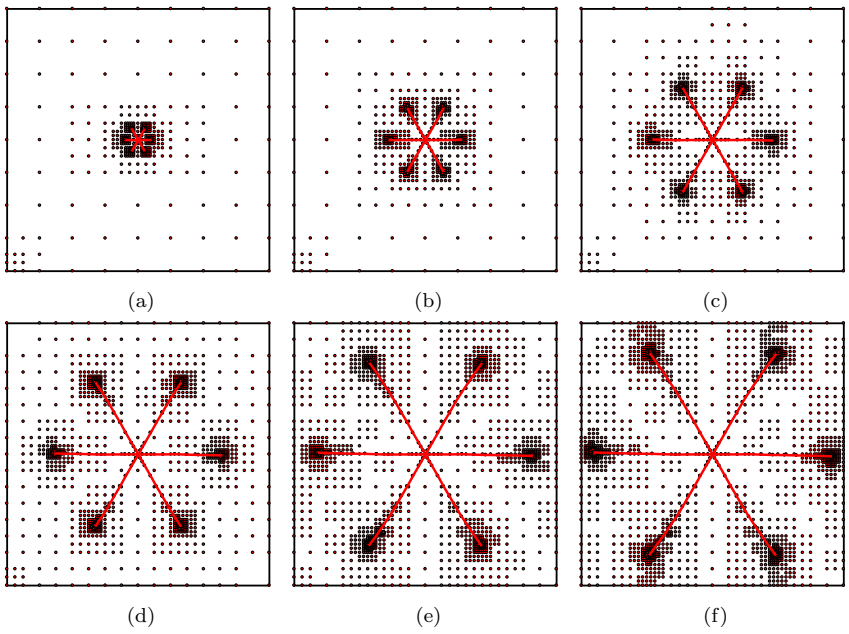

Figure 4.17: Adaptive steps for star-shaped crack propagation with angular change: (a) step 1; (b) step 3; (c) step 5; (d) step 7; (e) step 9; (f) step 10.

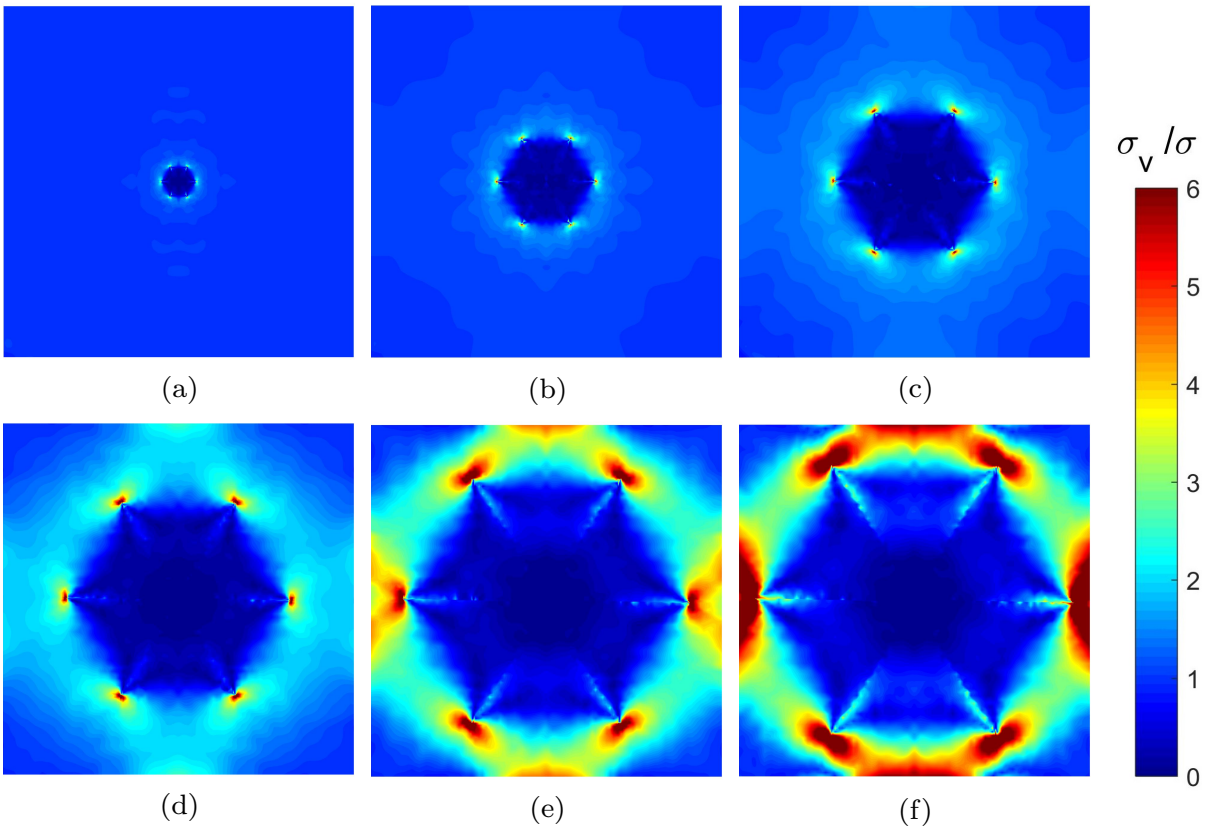

Figure 4.18: Von Mises stress distribution for star-shaped crack propagation steps with angular change: (a) step 1; (b) step 3; (c) step 5; (d) step 7; (e) step 9; (f) step 10.

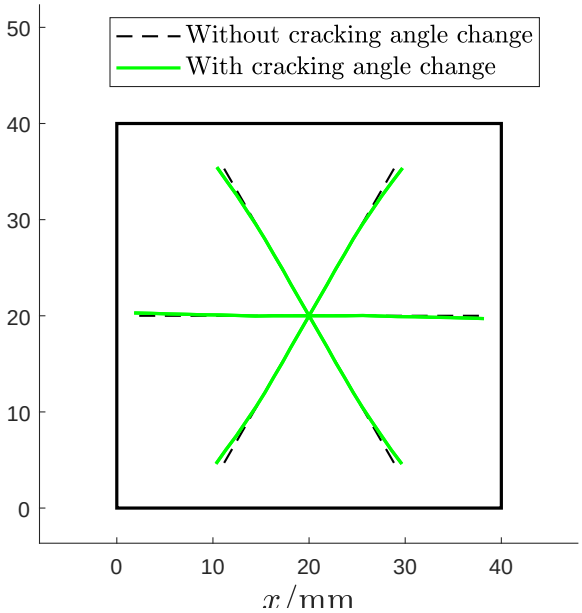

Figure 4.19: Comparison of crack path between with and without cracking angle change for the star-shaped crack.

initial particle arrangement. Particle arrangements are symmetric at the two horizontal crack tips and different at the others, although the difference is small. SIFs at the crack tips A and B are given in Figure 4.16 which match well with the results from Daux et al. [155].

Secondly, the propagating direction is not locked and crack paths are not kept straight during crack propagation steps. Adaptive particle arrangements for the propagation process are presented in Figure 4.17, which shows that particle distributions are not symmetric any more at the two horizontal crack tips, and the maximum particle number becomes 2606. This asymmetry comes from the imposition of boundary conditions where the left bottom corner of the plate is fixed. The Von Mises distributions during crack propagation steps are presented in Figure 4.18, where the Von Mises stress is normalised by Equation (3.40) and high stress gradients can be found around six crack tips. The crack growths of both cases are compared in Figure 4.19, where it can be seen that the propagating direction of all crack branches are constant at the majority of steps and change a little at the end. This can be explained from the SIFs of all crack tips in Figure 4.16, where K_{II} at crack tips A and B are much lower than K_{I}, and all crack branches are dominated by the mode I type fracture so the changes of crack directions are small.

4.4.4 Tree-shaped crack

The final problem is the most complicated where a tree-shaped crack with up to ten crack tips is included. The configuration of the problem is in Figure 4.20 where $w = 6$mm, $h = w$, $a = b = 2c = 1$mm, $\alpha = 45°$ and $\beta = 90°$, the same as in [258]. A biaxial tensile loading $\sigma = 100$MPa is applied at four edges of the plate, and an initial particle arrangement is set as in Figure 4.21 (a).

Adaptive particle arrangements are shown in Figures 4.21 (b-d), and the number of particles goes up to 848 from 262. Fine particles are generated around the four crack tips on the left and right sides while the requirement of refinements for the other six is low. Calculating the SIFs at four crack tips A, B, C and D marked in Figure 4.20, converged results can be obtained after adaptive steps, Figure 4.22, where the superscripts indicate the crack tip, and the results are consistent with the results from Ma et al. [258], although minor differences for K_{II} at crack tip A are found. In this calculation, K_{II} at crack tip A is nearly zero and its deformation is dominated by the mode I fracture. Both modes I

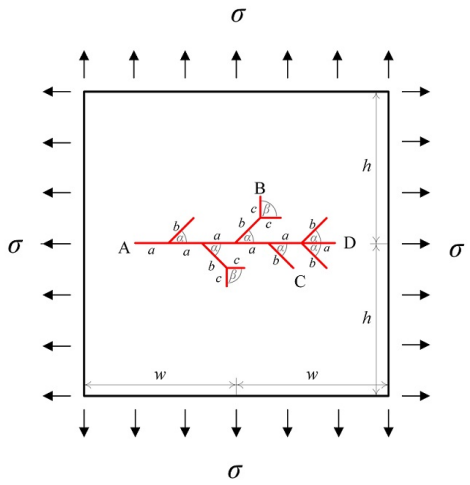

Figure 4.20: Configuration of the tree-shaped crack in a square plate.

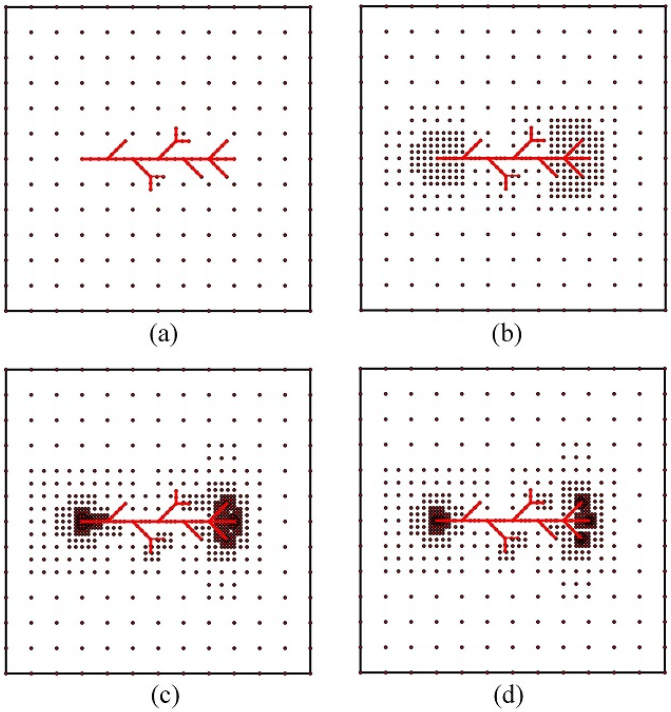

Figure 4.21: Adaptive steps for the tree-shaped crack problem: (a) initial particles; (b) step 2; (c) step 4; (d) step 6.

and II SIFs at crack tips B and C are much smaller than at crack tips A and D, which explains why the refinement level at crack tips B and C is much lower than at crack tips A and D. The deformation of this problem is presented in Figure 4.23, from which it can be seen that some cracks are opening and some are closing. There are some non-physical results for the closing cracks as shown in Figure 4.23 (b), because the current algorithm

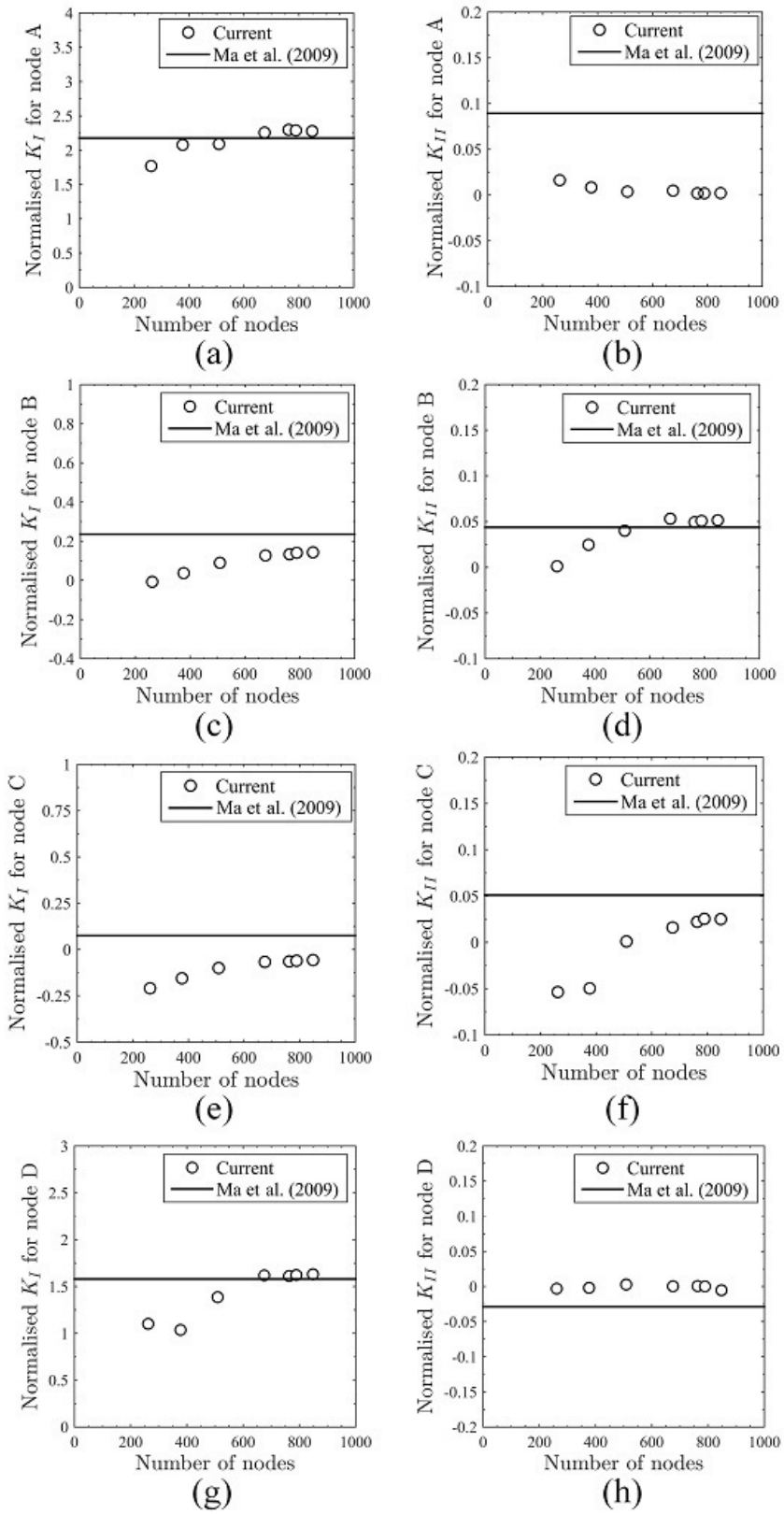

Figure 4.22: Validation of calculated SIFs for the tree-shaped crack problem: (a) $K_{\mathrm{I}}^{\mathrm{A}}$; (b) $K_{\mathrm{II}}^{\mathrm{A}}$ (c) $K_{\mathrm{I}}^{\mathrm{B}}$; (d) $K_{\mathrm{II}}^{\mathrm{B}}$; (e) $K_{\mathrm{I}}^{\mathrm{C}}$; (f) $K_{\mathrm{II}}^{\mathrm{C}}$; (g) $K_{\mathrm{I}}^{\mathrm{D}}$; (h) $K_{\mathrm{II}}^{\mathrm{D}}$.

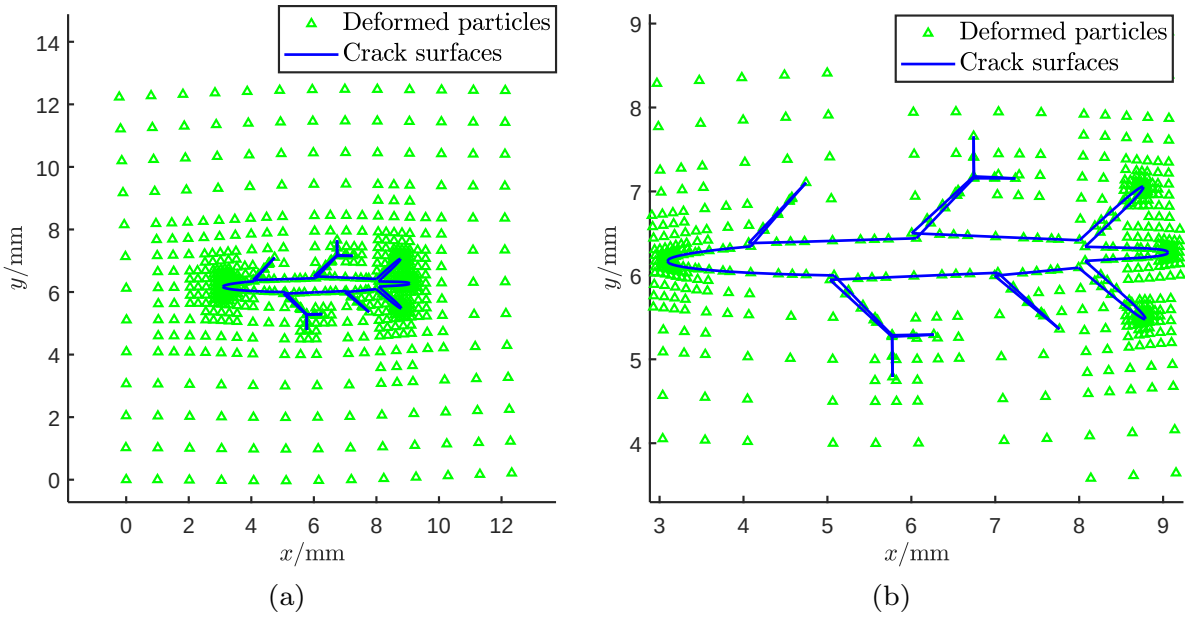

Figure 4.23: Displacement enlarged by 50 times for the tree-shaped crack problem: (a) displacement; (b) enlarged view.

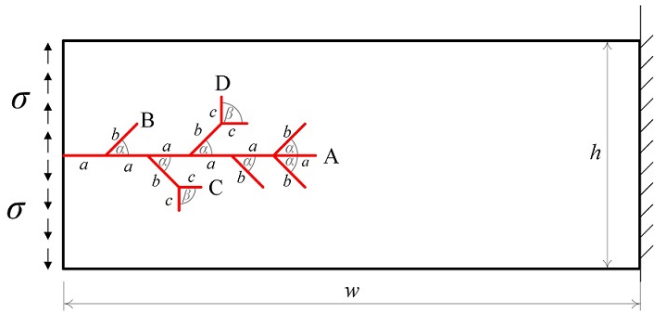

Figure 4.24: Configuration of tree-shaped crack in a double cantilever beam.

does not cover contacts between two surfaces.

It is a more challenging problem for the tree-shaped crack to start from the edge, e.g. in a double cantilever beam as in Figure 4.24. The configuration of the beam is $w = 24$mm and $w/h = 3$, and the crack pattern is kept the same as above. The beam is fixed at the right side and is loaded under a pair of tractions $\sigma = 100$MPa at the left edge.

Adaptive particle arrangements are presented in Figure 4.25, where fine particles are generated automatically around all ten crack tips while no refinement occurs on the right part of the beam. The final number of particles increases to 3359 from 283, which is about 11 times larger than the initial number. The final deformation is illustrated in Figure 4.26, including an enlarged view of the rectangular zone. A clear crack opening

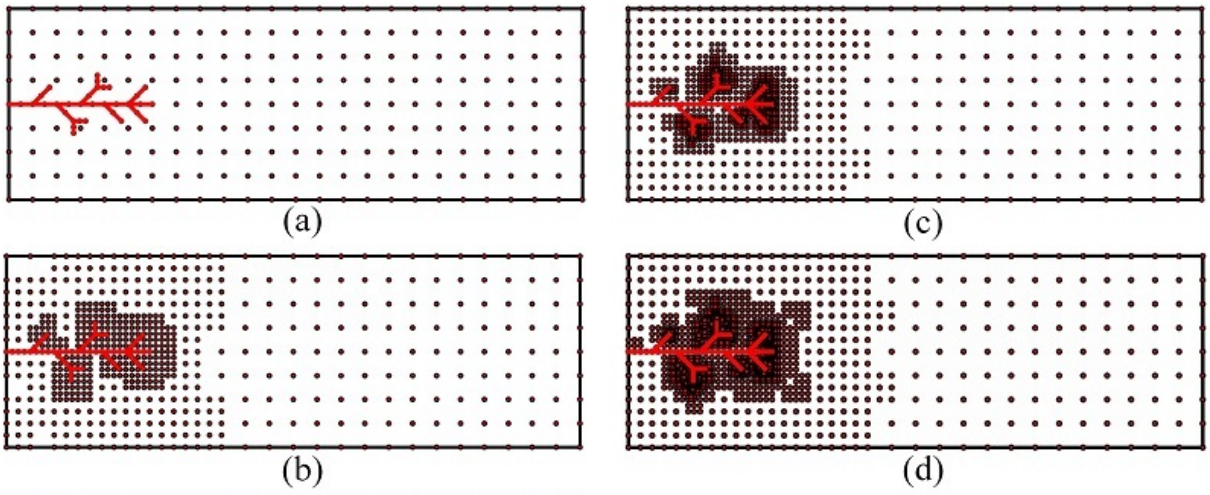

Figure 4.25: Adaptive steps for tree-shaped crack in a double cantilever beam: (a) initial particles; (b) step 2; (c) step 4; (d) step 6.

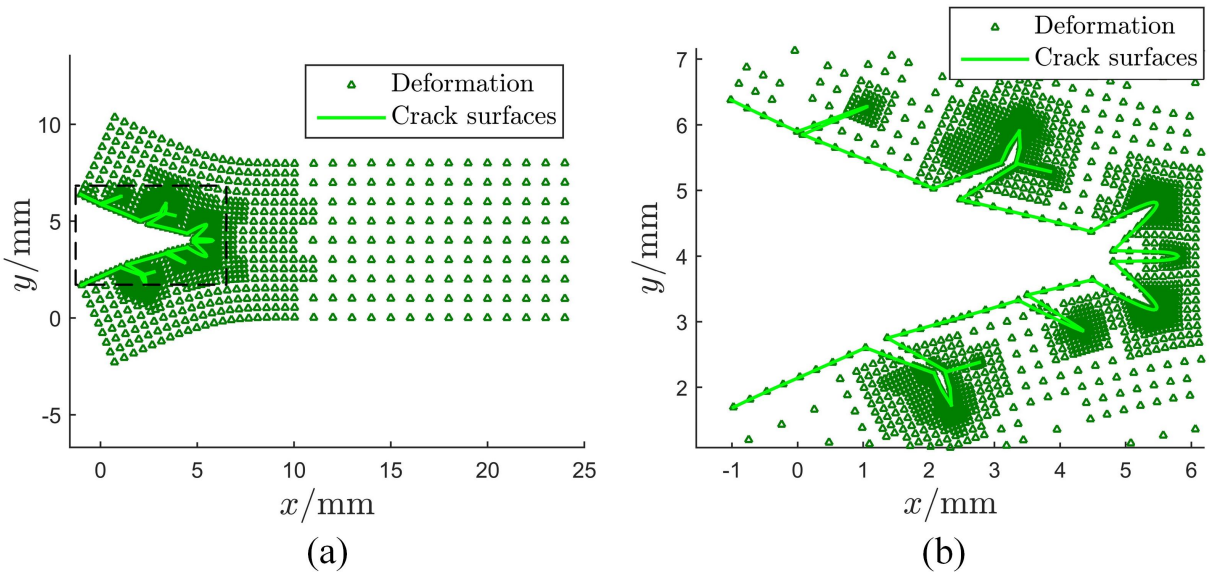

Figure 4.26: Crack opening for the tree-shaped crack in a double cantilever beam enlarged by 20 times: (a) overall deformation; (b) partial enlarged view.

can be seen at the three crack branches on the right; while for the two branched cracks, only one part is opened; and for two single cracks small crack openings are detected. Extracting the SIFs at crack tips A, B, C and D, converged values are obtained as given in Figure 4.27. It can be seen that K_{I}^{A} and K_{I}^{D} are almost three times larger that K_{I}^{B}, while K_{I}^{C} is much smaller, which explains why the crack opening is large at crack tips A and D and why the deformation at crack tip C is negligible. K_{II}^{A} is nearly zero, and K_{II}^{B} and K_{II}^{D} are much lower than K_{I}^{B} and K_{I}^{D}, indicating the deformations at crack tips A,

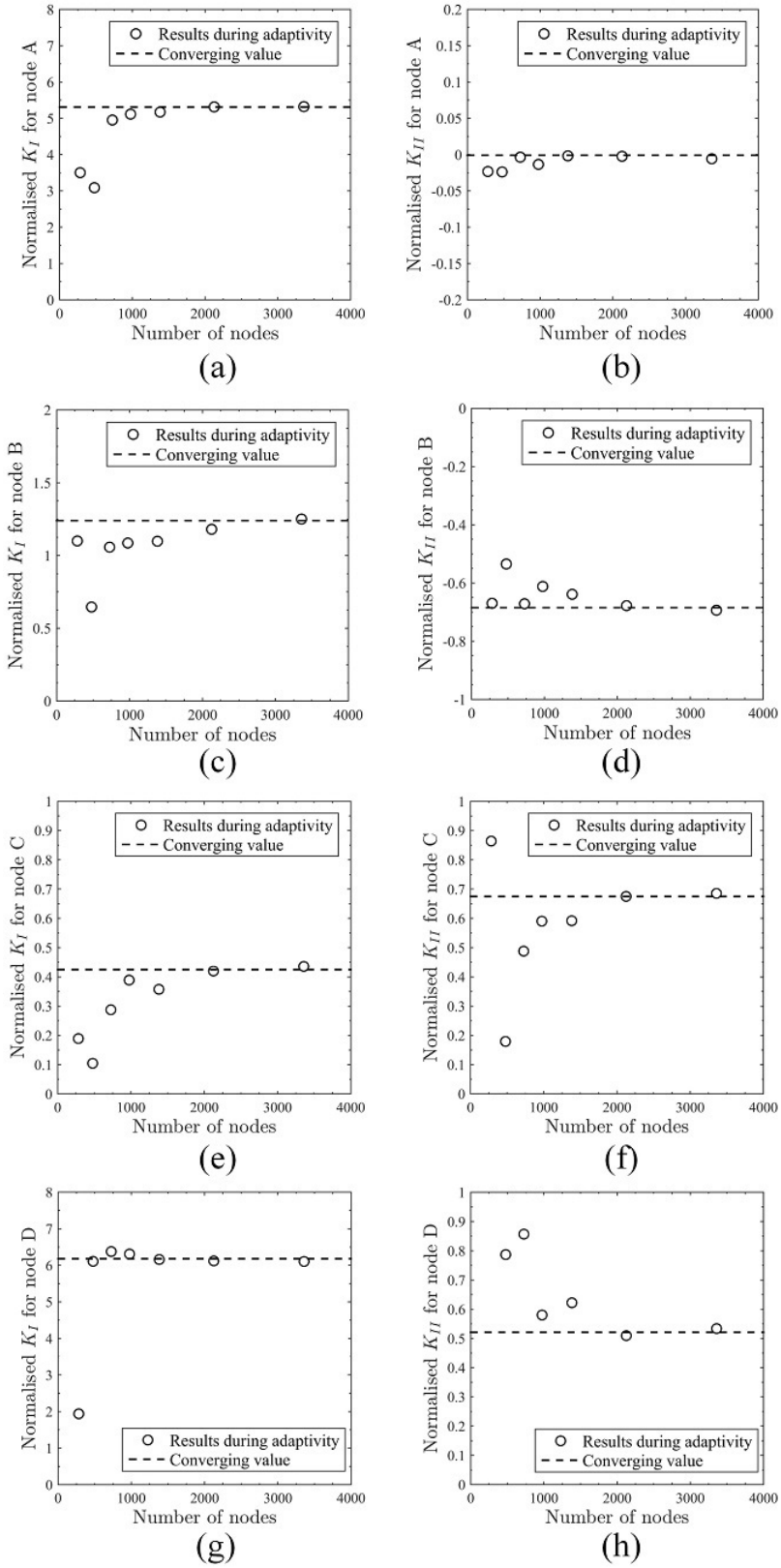

Figure 4.27: Calculated SIFs for the tree-shaped crack in a double cantilever beam: (a) $K_{\mathrm{I}}^{\mathrm{A}}$; (b) $K_{\mathrm{II}}^{\mathrm{A}}$ (c) $K_{\mathrm{I}}^{\mathrm{B}}$; (d) $K_{\mathrm{II}}^{\mathrm{B}}$; (e) $K_{\mathrm{I}}^{\mathrm{C}}$; (f) $K_{\mathrm{II}}^{\mathrm{C}}$; (g) $K_{\mathrm{I}}^{\mathrm{D}}$; (h) $K_{\mathrm{II}}^{\mathrm{D}}$

B and D are dominated by the mode I type fracture. No reference has been found till now to the author's knowledge so the accuracy regarding the final SIFs cannot be fully assessed, however this example has shown the ability of the modified CPM to handle a complex crack problem.

It is notable that the proposed methodology is able to handle the simulation of crack coalescence, e.g. one crack propagating into and splitting another, by adding one particle at the intersection position and subsequently splitting it according to the crack patterns. But in this type of situation, there will be issues in the calculation of the J-integral when two crack tips are in close proximity, which is not covered in this chapter.

4.5 Summary

A multi-split particle method is proposed for the simulation of complex cracks and multiple cracks in 2D. In this methodology, discontinuities at cracks are achieved by the modification of the influence domain of particles, and the displacement approximation involves no enrichment function and therefore is kept simple. The cracking particle at a crack branch point is multiply split into several subparticles, and the influence domain of this particle is also divided. The crack opening at the crack branch point is obtained by the relative displacements of these subparticles. Crack geometries are described by a set of crack segments rather than using level set functions, so the computational cost for modelling multiple cracks is controlled. An adaptivity strategy developed in Section 3.3 is introduced here to amend the density of particle distribution, by which the calculation efficiency is improved. Finally, several examples of multiple cracks including two independent cracks, a cross crack, a star-shaped crack and a tree-shaped crack are used to demonstrate the ability of the proposed methodology, where good agreement with previous results has been obtained.

Chapter 5

Configurational-force-driven cracking particle method for 2D problems

5.1 Introduction

In Chapters 3 and 4, crack propagation was determined by the maximum circumferential stress criterion, however there are other options developed for controlling the behaviour of crack growth. This chapter comprises a discussion and study of different criteria for crack propagation in the numerical modelling of fracture. The problem of crack initiation is not included, in that a new crack induces a severe topological change rarely supported by current numerical methods.

Accurate determination of the mechanism of crack propagation in mixed-mode situations is of great importance in fracture mechanics, since the correctness of a crack propagation criterion is directly linked to the accuracy of crack growth prediction. A crack propagation criterion must provide answers to the following two questions: whether a crack is going to propagate and in which direction? These two questions are checked at each time of load step for a successive crack propagation process. Some crack propagation criteria are based on the local stress and displacement field at the crack tip, e.g. the maximum circumferential stress criterion [259] and the minimum strain energy density criterion [260], while others follow a global approach accounting for the energy distribution throughout the cracked part, e.g. the maximum strain energy release rate criterion [261]. In addition, the concept of the configurational force (CF) has been used

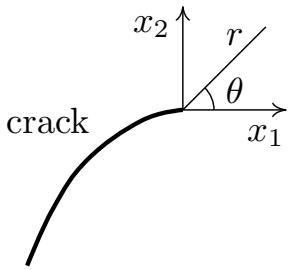

Figure 5.1: Local polar coordinate system at a crack tip.

in modelling the behaviour of brittle fracture [262–264], which is an alternative to more traditional computational fracture mechanics based on stress intensity factors and the J-integral. The CF is a vectorial force-like quantity conjugated to the topological change due to crack propagation and is consistent with the crack propagating direction. This approach requires no decomposition of the stress and displacement about the crack tip for mixed-mode fracture, which is needed in many other methods using the J-integral [179, 241]. The CF approach has been applied to the finite element method (FEM) to solve crack problems including brittle cracks [263, 264], elastoplasticity [265], 3D cracks [266] and a review of recent advances for the CF approach in elasto-plastic fracture can be found in [267], although the application to meshless methods to date is limited. Here, a configurational-force-driven cracking particle method (CFCPM) is developed for fracture modelling in 2D, and a comparison with the crack modelling using a criterion based on the conventional J-integral is carried out.

5.2 Crack propagation criteria

Micro failure and inclusions induce stress concentrations in materials under external loading which can develop into large cracks and finally fractures. The angular change θ in Figure 5.1 during a crack propagation process is determined by the local stress and displacement field at the vicinity of the crack tip, and some crack propagation criteria have been developed using measures of these quantities, e.g. the maximum circumferential stress criterion, the minimum strain energy density criterion and the maximum strain energy release rate criterion. In all three criteria, there is a limit for the angular change of crack direction, $\theta \in [-70.54°, 70.54°]$ as in [245], where angular change beyond this range is not allowed. These three criteria are now introduced in more detail.

5.2.1 The maximum circumferential stress criterion

In the maximum circumferential stress criterion (MCSC) [259], a crack propagates when the circumferential stress exceeds the critical stress (defined as the stress when a material fails under external loadings), and the propagation direction is towards the location of maximum circumferential stress. This approach is however mesh-dependent when applied to the FEM, since the number of elements connected to the crack tip affects the approximation of stresses and displacements and therefore has a knock-on influence on the crack growth predicted. An alternative uses the relationship between the circumferential stress and stress intensity factors as described in Section 3.4.4, so that the stress and displacement fields of the local zone around the crack tip are used with the J-integral, which makes the technique mesh-independent. Although the implementation of the latter is generally more complicated, it can provide more accurate results in that this criterion is based on the stresses away from the crack tip.

5.2.2 The minimum strain energy density criterion

The minimum strain energy density criterion (MSEDC) [260] assumes that high values of strain energy (W) prevent a crack from propagating and the crack grows towards the direction where this energy is minimum. The so-called strain energy density factor is defined as $S = r\mathrm{d}W/\mathrm{d}V$ where V is the volume of strain energy and r is the distance to the crack tip. W is singular at the crack tip varying with $1/r$, so S remains bounded. In this approach, a crack propagates when the minimum S falls below a designated critical value S_{cr}. An analytical formulation for S representing the intensity of the local energy field from [245] is

$$S = r\big(\frac{1+\nu}{2E}\big)[\sigma_{11}^2 + \sigma_{22}^2 + \sigma_{33}^2 - \frac{\nu}{1+\nu}(\sigma_{11}+\sigma_{22}+\sigma_{33})^2 + 2\sigma_{12}^2]. \tag{5.1}$$

The angular change of the crack direction is obtained by

$$\frac{\partial S}{\partial \theta} = 0, \quad \frac{\partial^2 S}{\partial^2 \theta} \geq 0. \tag{5.2}$$

This criterion is not considered a global approach since the calculation of the strain energy density is based on local stresses. The computational accuracy for S in the FEM is linked

to the number of elements around the crack tip, as mentioned in [245].

5.2.3 The maximum strain energy release rate criterion

The strain energy release rate G is defined in Section 1.4.1, and represents the energy required to create new crack surfaces by one unit. The maximum strain energy release rate criterion (MSERRC) assumes that, among all situations of virtual and kinematically admissible crack increments, the real crack propagation is that with the maximum strain energy release rate. The angular change of crack propagation is obtained by

$$\frac{\partial G}{\partial \theta} = 0, \quad \frac{\partial^2 G}{\partial^2 \theta} \geq 0. \tag{5.3}$$

One way to calculate G is through the J-integral [240] as in Equation (3.22). Since the J-integral is path-independent, accurate results can be obtained using an integration over a path far from the crack tip, then this criterion becomes a global approach.

A comparison between the three criteria for fracture modelling is given by Bouchard et al. [245] using the FEM. It is shown that the MSEDC is less accurate than the other two criteria which are almost equivalent in terms of accuracy and efficiency. The MCSC is the easiest to implement in the FEM but requires a fine mesh around the crack tip. In contrast the MSERRC is the most complicated, however it provides good results and the accuracy becomes mesh-independent. Comparison between these three criteria in meshless methods is limited, which requires more attention by other researchers.

5.3 Configurational force

Apart from the three crack propagation criteria mentioned above, the configurational force (CF) approach is another option where the crack propagation is determined by the configurational force at the crack tip. Compared with the J-integral in classical fracture mechanics in Section 3.4.1, the CF approach requires no projection of stress terms from integration points to the integration line/surface. The advantage of the CF approach is no requirement to decompose the stress and displacement fields for mixed-mode crack problems, which is however required in the interaction integral approach described in Section 3.4.3.

5.3.1 Theoretical background to the configuration force

The classical theory of elasticity had issues with the concept of forces acting on a singularity (crack or concave corner) until the development of the CF theory by Eshelby [268]. The CF is defined as the negative gradient of the total potential energy with respect to the position of a singularity and provides a useful description of energy changes in solids with singularities undergoing deformation. It is a fictitious force and is distinct from the normal surface and body forces acting on a material. Similar to the equilibrium equations in classical solid mechanics, as in Equation (2.16), the Eshelby stress $\boldsymbol{\Sigma}$ is also self-equilibrating in the absence of body forces as

$$\nabla \cdot \boldsymbol{\Sigma} = \mathbf{0} \quad \text{in}\, \Omega, \tag{5.4}$$

and the Eshelby stress tensor $\boldsymbol{\Sigma}$ is defined as

$$\boldsymbol{\Sigma} = W\boldsymbol{I} - \boldsymbol{H}^{\mathrm{T}} \cdot [\boldsymbol{\sigma}], \tag{5.5}$$

where $\boldsymbol{I}$ is an identity matrix, $\boldsymbol{H}$ is the displacement gradient tensor, the components of which are $H_{ij} = \partial u_i / \partial x_j$, $i, j \in \{1, 2\}$ for 2D and W is the strain energy, as defined in Equation (3.22). $[\boldsymbol{\sigma}]$ is the Cauchy stress tensor as in Equation (2.16). For a simply connected domain with boundary Γ, the resultant CF (material force) for the Eshelby stress along Γ must vanish considering Equation (5.4), which yields

$$\oint_{\Gamma} \boldsymbol{\Sigma} \cdot \mathbf{n} \, \mathrm{d}\Gamma = \mathbf{0}, \tag{5.6}$$

where $\mathbf{n}$ is the outward normal to Γ and $\mathbf{0}$ is a zero vector. When a crack is considered as in Figure 5.2, the material force $\boldsymbol{F}_{\mathrm{mat}}$ is not balanced,

$$\boldsymbol{F}_{\mathrm{mat}} = \int_{C_s} \boldsymbol{\Sigma} \cdot \mathbf{n} \, \mathrm{d}\Gamma \neq 0, \tag{5.7}$$

where C_S is a contour from the lower crack surface to the upper crack surface as shown in Figure 5.2. The CF $\boldsymbol{g}$ for a crack is defined by shrinking the contour to infinitesimal

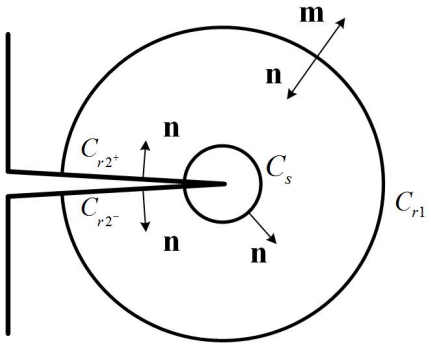

Figure 5.2: Integration path around the crack tip.

at the crack tip, as in [263, 264]

$$\boldsymbol{g} = \lim_{|C_s|\to 0} \int_{C_s} \boldsymbol{\Sigma} \cdot \mathbf{n} \, \mathrm{d}\Gamma, \tag{5.8}$$

The resultant vector direction of $\boldsymbol{g}$ represents the crack propagation direction and a crack propagates when $\|\boldsymbol{g}\|$ (the L_2 norm of $\boldsymbol{g}$) exceeds g_c, which is defined as the critical energy release per unit area of the crack.

5.3.2 Application to the CPM

Here the CF is now introduced to the CPM for crack modelling. Since it is difficult to guarantee high accuracy for the approximation around the crack tip where there are high gradients of stresses, Equation (5.8) is amended to integrate over a contour away from the crack tip, as

$$\int_{C_s} \boldsymbol{\Sigma} \cdot \mathbf{n} \mathrm{d}\Gamma = \oint_{C} \boldsymbol{\Sigma} \cdot \mathbf{n} \mathrm{d}\Gamma - \int_{C_{r2}} \boldsymbol{\Sigma} \cdot \mathbf{n} \mathrm{d}\Gamma - \int_{C_{r1}} \boldsymbol{\Sigma} \cdot \mathbf{n} \mathrm{d}\Gamma, \tag{5.9}$$

where $C = C_s + C_{r1} + C_{r2}$, which is a closed contour, and $C_{r2} = C_{r2^-} + C_{r2^+}$ as shown in Figure 5.2. The first term on the right hand side (*r.h.s.*) of Equation (5.9) becomes zero using Equation (5.6). Neglecting the integral over crack surfaces (as will be discussed later), the configurational force becomes

$$\boldsymbol{g} = -\int_{C_{r1}} \boldsymbol{\Sigma} \cdot \mathbf{n} \mathrm{d}\Gamma. \tag{5.10}$$

Alternatively, the CF can be calculated through a domain integration. The first step is to build an integral over a closed contour and Equation (5.8) is modified to

$$\int_{C_s} \boldsymbol{\Sigma} \cdot \mathbf{n} \mathrm{d}\Gamma = \oint_C \boldsymbol{\Sigma} \cdot \mathbf{n} \cdot q(\mathbf{x}) \mathrm{d}\Gamma - \int_{C_{r2}} \boldsymbol{\Sigma} \cdot \mathbf{n} \cdot q(\mathbf{x}) \mathrm{d}\Gamma, \tag{5.11}$$

where $q(\mathbf{x})$ is a weight function defined as

$$q(\mathbf{x}) = \begin{cases} 1 & \text{on } C_s \\ 0 & \text{on } C_{r1} \\ \text{arbitrary} & \text{within } \Omega\,, \end{cases} \tag{5.12}$$

The first term on the *r.h.s.* of Equation (5.11) is transferred to a domain integration using Green's theorem (2D version of divergence theorem), as

$$\oint_C \boldsymbol{\Sigma} \cdot \mathbf{n} \cdot q(\mathbf{x}) \mathrm{d}\Gamma = -\oint_C \boldsymbol{\Sigma} \cdot \mathbf{m} \cdot q(\mathbf{x}) \mathrm{d}\Gamma = -\int_\Omega \nabla\Big(\boldsymbol{\Sigma} \cdot q(\mathbf{x})\Big) \mathrm{d}\Omega, \tag{5.13}$$

where $\mathbf{m}$ is the outward normal to C_{r1} and Ω is the domain inside the contour C. When $\lim C_s \to 0$ and C_{r2} approaches the crack surfaces, Ω can be considered as the domain inside C_{r1}. Substituting Equation (5.4) into Equation (5.13) yields

$$-\int_\Omega \nabla\big(\boldsymbol{\Sigma} \cdot q(\mathbf{x})\big) \mathrm{d}\Omega = -\int_\Omega \boldsymbol{\Sigma} \cdot \nabla q(\mathbf{x}) \mathrm{d}\Omega. \tag{5.14}$$

The second term on the *r.h.s.* of Equation (5.11) is not involved in the calculation of the CF by Miehe et al. [263, 264], while it is claimed that this term cannot be neglected in [262]. A discussion on this issue, i.e. the contribution from the crack surface integration to the CF, will be included later. Without considering the integration term over crack surfaces, the final expression for the CF becomes

$$\boldsymbol{g} = -\int_\Omega \boldsymbol{\Sigma} \cdot \nabla q(\mathbf{x}) \mathrm{d}\Omega. \tag{5.15}$$

It is notable that the integration in Equation (5.15) is path-independent so that it can be calculated using the stress and displacement fields away from the crack tip. After a solution of stresses and displacements is obtained by the CPM in this chapter, Equation

(5.15) is used through a post-processing procedure and calculated using Gaussian integration over a square domain Ω centred at the crack tip, and then the resulting CF is used in the crack propagation process. The *r.h.s.* of Equation (5.15) becomes the same form as Miehe's equation [263, 264] for the CF approach in the FEM, when the integration domain Ω is calculated over the elements connected to the crack tip and the weight function $q(\mathbf{x})$ is replaced by the shape functions of the crack tip in these elements, i.e. $q(\mathbf{x}) = N(\mathbf{x})$.

5.3.3 Relationship with the J-integral

The J-integral is the projection of the CF in the direction of the crack extension $\boldsymbol{e}$, as

$$J = \boldsymbol{e} \cdot \boldsymbol{g} = -\lim_{|C_s| \to 0} \int_{C_s} \boldsymbol{e} \cdot \boldsymbol{\Sigma} \cdot \mathbf{n} \mathrm{d}\Gamma. \tag{5.16}$$

Considering the relationship between the J-integral and the stress intensity factors (SIFs) K_{I} and K_{II} in Equation (3.23), the calculated CF should satisfy

$$g_1 = J = \alpha({K_{\mathrm{I}}}^2 + {K_{\mathrm{II}}}^2), \tag{5.17a}$$

$$g_2 = -2\alpha K_{\mathrm{I}} K_{\mathrm{II}}, \tag{5.17b}$$

as mentioned in [269] where g_1 is the first component of $\boldsymbol{g}$ (and g_2 is the second component) and α is a constant as in Equation (3.24).

5.4 The configurational force vs the J-integral

A comparison between the CF approach and the MCSC using the J-integral for crack modelling is now demonstrated with four crack problems in 2D. All problems are performed with plane stress assumptions and linear elastic materials unless otherwise stated. A square domain centred at the crack tip with dimensions of $2c \times 2c$ is used to evaluate Equation (5.15) as shown in Figure 3.8, and c is defined according to crack length a, e.g. $c = 0.01a$. The weight function of $q(\mathbf{x})$ is defined as

$$q(\mathbf{x}) = (1 - \frac{x}{c})(1 - \frac{y}{c}), \tag{5.18}$$

where x and y are local coordinates at the crack tip, with the x-axis along the crack and the y-axis normal to the crack. This domain is divided into 4×4 background cells and

10×10 Gauss points are used in each cell. The evaluation of the J-integral is achieved via the interaction integral as in Section 3.4.3. For ease of comparison, the CF and the SIFs are normalised as

$$J' = \frac{J}{\alpha\sigma^2\pi a}, \quad \boldsymbol{g}' = \frac{\boldsymbol{g}}{\alpha\sigma^2\pi a}, \tag{5.19a}$$

$$K'_{\mathrm{I}} = \frac{K_{\mathrm{I}}}{\sigma\sqrt{\pi a}}, \quad K'_{\mathrm{II}} = \frac{K_{\mathrm{II}}}{\sigma\sqrt{\pi a}}, \tag{5.19b}$$

where σ is the external loading and a is the initial crack length.

5.4.1 Half central crack

The half central crack from Section 3.6.1 is used here again, where two situations, a pure mode I and a mixed mode fracture, are considered. The former is obtained by using the stresses in the case of $K'_{\mathrm{I}} = 1$, $K'_{\mathrm{II}} = 0$ as the external loading, while in the latter $K'_{\mathrm{I}} = 1$, $K'_{\mathrm{II}} = 1$. These two situations are included to check the contribution of integration from crack surfaces to the CF, considering that the deformation of the pure mode I fracture is symmetric and the mixed-mode fracture is not. All geometries are kept the same as in Section 3.6.1, and the analytical stress and displacement fields in Equation (3.36) are used. The relationship between the CF and SIFs is given in Equation (5.17). The CF is calculated either by line integration as in Equation (5.10) or domain integration as in Equation (5.15), while SIFs are calculated through the interaction integration. The contribution from crack surfaces to the CF is obtained using the second term on the *r.h.s.* of Equation (5.11) when the domain integration is used. Various sizes of contours and domains are used to calculate the integrations, e.g. $c/a = 0.001, 0.01, 0.1, 0.5$. The error target for the adaptivity approach is $\eta_t = 0.02$.

Table 5.1: Mode I fracture for the half central crack (exact values $K'_{\mathrm{I}} = 1$, $K'_{\mathrm{II}} = 0$)

	Configurational force						J-integral		
	line integration		domain integration		crack surface part				
c/a	g'_1	g'_2	g'_1	g'_2	g'_1	g'_2	K'_{I}	K'_{II}	J'
0.5	1.0038	0.0000	1.0017	0.0000	0.0000	0.0000	1.0011	0.0000	1.0011
0.1	0.9992	0.0000	1.0040	0.0000	0.0000	0.0000	1.0026	0.0000	1.0026
0.01	1.0025	0.0000	0.9812	0.0000	0.0000	0.0000	0.9901	0.0000	0.9901
0.001	0.9837	0.0000	0.8496	0.0000	0.0000	0.0000	0.9091	0.0000	0.9091

Table 5.2: Mixed mode fracture for the half central crack (exact values $K'_{\mathrm{I}} = 1$, $K'_{\mathrm{II}} = 1$)

	Configurational force						J-integral		
	line integration		domain integration		crack surface part				
c/a	g'_1	g'_2	g'_1	g'_2	g'_1	g'_2	K'_{I}	K'_{II}	J'
0.5	1.9940	-1.9963	1.9994	-2.0003	0.0000	-0.0178	0.9999	1.0001	2.0001
0.1	2.0033	-2.0033	1.9987	-2.0019	0.0000	-0.0211	0.9999	0.9999	1.9995
0.01	2.0076	-2.0026	1.9910	-1.9999	0.0000	-0.1710	0.9973	0.9986	1.9918
0.001	2.0043	-1.9873	1.9883	-1.9927	0.0000	0.1256	0.9947	0.9994	1.9882

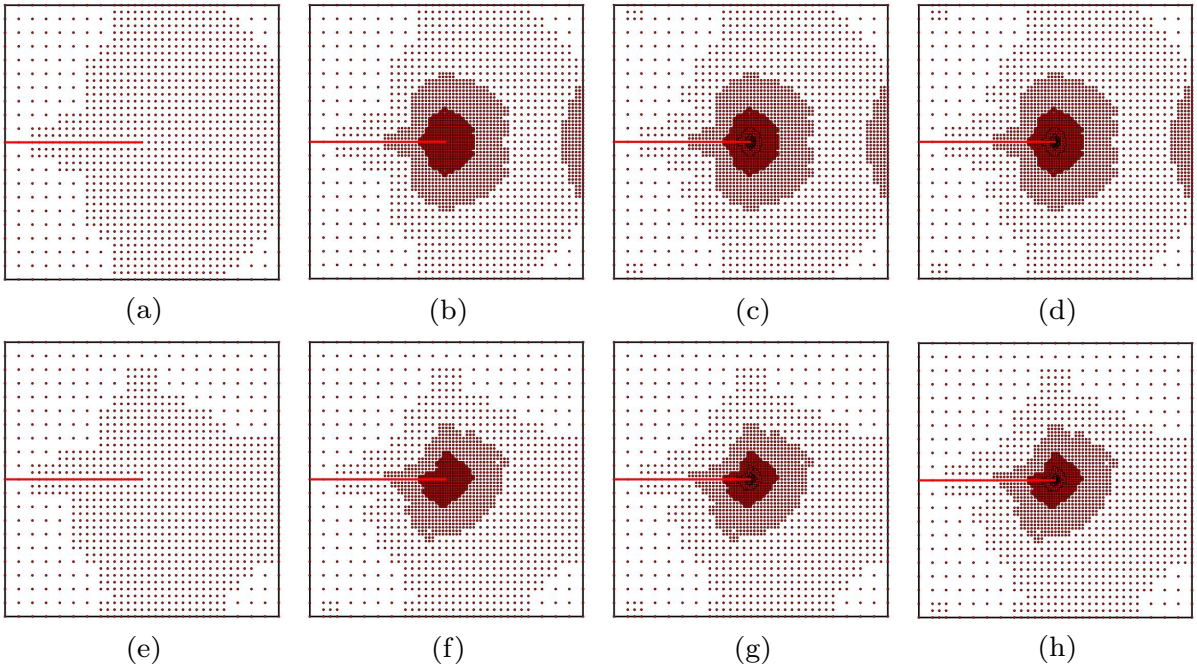

Figure 5.3: Adaptive particle arrangements for the half central crack problem: (a) mode I; (b) mixed mode.

Adaptive particle arrangements are shown in Figure 5.3, where particle refinements are symmetric and asymmetric in Figure 5.3 (a) and (b) respectively. Results for the two situations are given in Tables 5.1 and 5.2, where all numerical results match the exact values obtained by Equation (3.36). It is also clear that the integration of both the CF and the J-integral are path-independent. The integration over a larger domain provides better accuracy, and the domain integration generally outweighs the line integration. From Table 5.1, the contribution from crack surfaces to the CF is zero, while for the second case it is not zero but much smaller than the result from the domain integration when larger domains are used. Using small domains $c/a = 0.01$ and 0.001, the results of

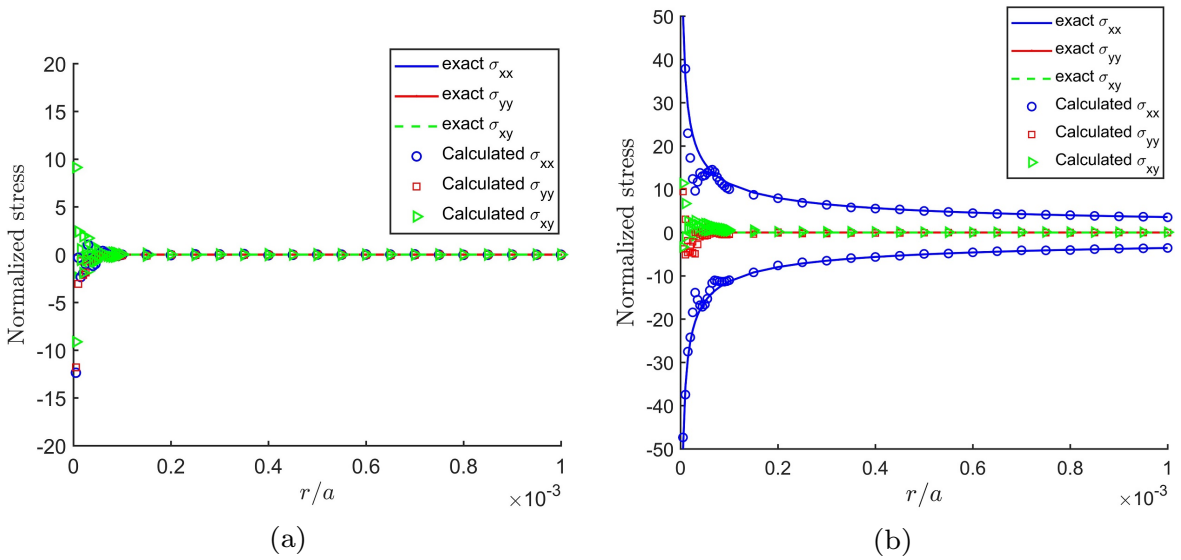

Figure 5.4: Stresses along the half central crack: (a) mode I; (b) mixed mode.

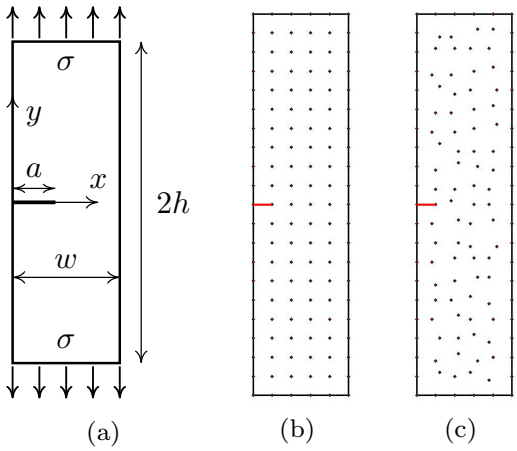

Figure 5.5: Single edge crack in a slender plate under tensile loading: (a) configuration; (b) case 1; (c) case 2.

the integration over crack surfaces appear unreasonable, and are caused by oscillations around the crack tip (for example, see the stresses along the crack surfaces in Figure 5.4). Even with very fine particle distributions around the crack tip, the accuracy for stresses within $r/a < 10^{-4}$ cannot be ensured, which is due to the singularity at the crack tip in linear elastic fracture mechanics, although in the range $r/a > 10^{-4}$ good results are achieved.

5.4.2 Single edge crack under tensile loading

The second example is a single edge crack under tensile loading (Figure 5.5), and two cases including uniformly and non-uniformly distributed particles are used as shown in Figures

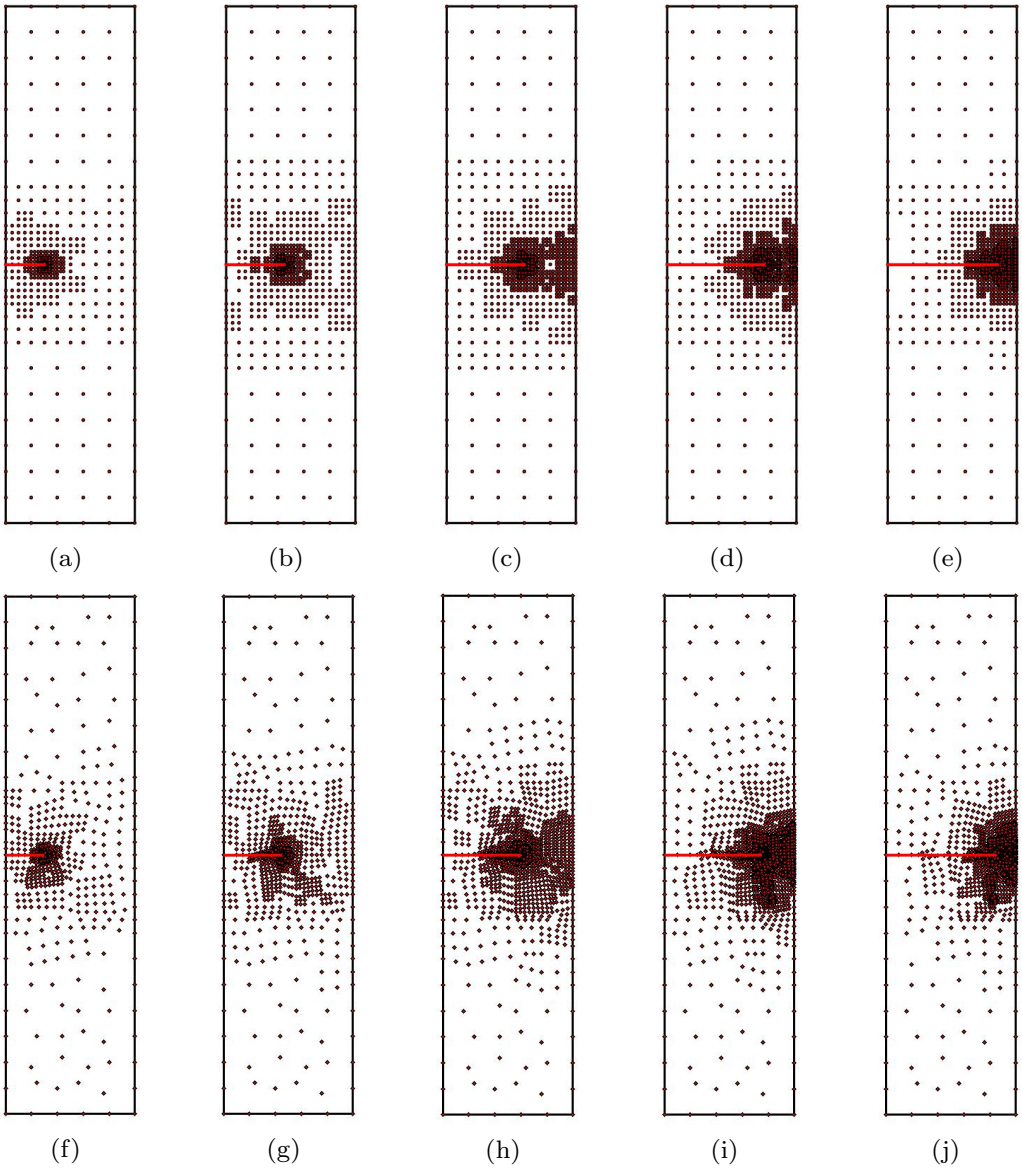

Figure 5.6: Adaptive particle arrangements for the edge crack under uniaxial tension during propagation steps=3, 6, 9, 12, 14 with different initial particle distributions: (a-e) case 1, (f-j) case 2.

5.5 (b-c), to study the effect of particle distribution on the results. The configuration is $a = 0.1$m, $b = 5a$, $h = 10a$, and the tensile loading is $\sigma = 10$MPa acting on the upper and lower edges of the plate. The plate is under plane strain condition with shear modulus $\mu = 80$GPa and Poisson's ratio $\nu = 0.3$, and is fixed by setting the average displacements and rotations to zero as in [270]. The analytical mode I SIF for the problem from Tada [248] is

$$K_{\mathrm{I}}/K_0 = 0.265(1 - a/b)^4 + \frac{0.857 + 0.265a/b}{(1 - a/b)^{3/2}}, \tag{5.20}$$

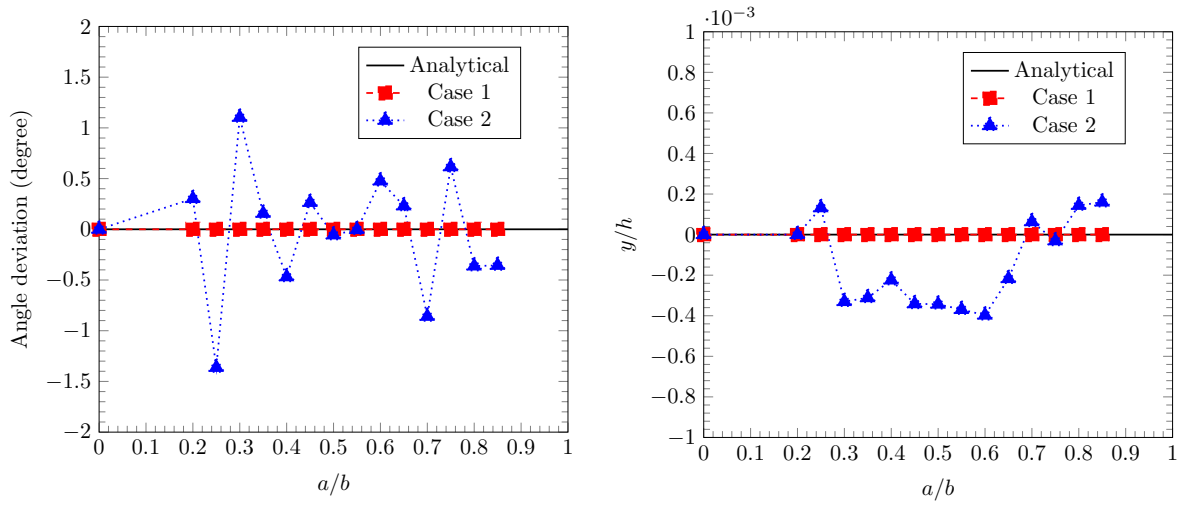

(a) (b)

Figure 5.7: Deviations for the edge crack propagation under uniaxial tension modelled by the configurational force: (a) angle; (b) vertical location.

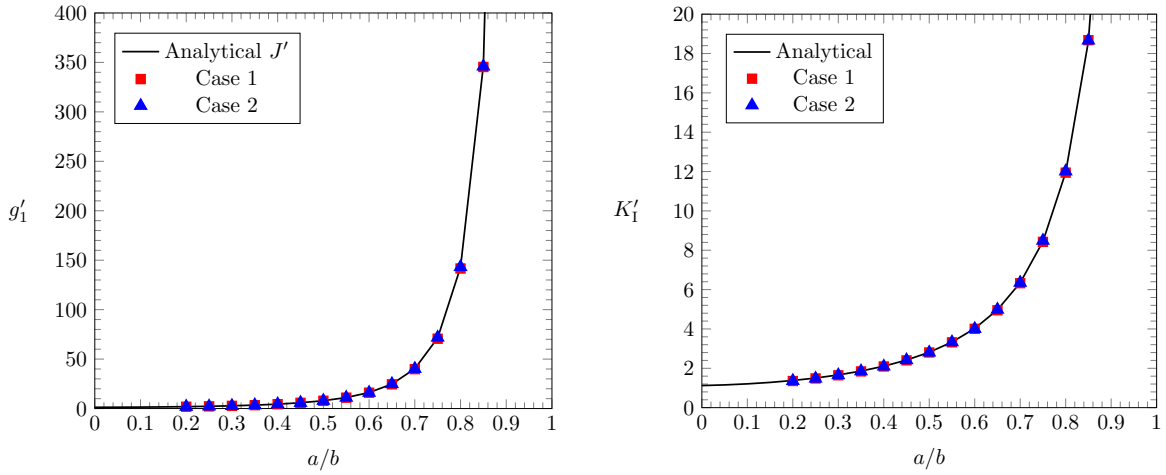

(a) (b)

Figure 5.8: Validation of results for the edge crack under uniaxial tension during crack propagation steps: (a) g_1'; (b) K_I'.

where $K_0 = \sigma\sqrt{\pi a}$. The error target for the adaptivity approach is $\eta_t = 0.02$.

A "mass" of particles is generated around the crack tip and travels with the crack propagation, as shown in Figures 5.6. Due to the asymmetry of initial particle distribution in case 2, the resulting particle refinements are asymmetric as in Figures 5.6 (f-j) and some deviations of the crack growth are found in Figure 5.7, although there is no deviation in the results of case 1. Calculating the mode I SIF for these crack propagation steps, results from both cases agree well with the analytical values from Equation (5.20) as given in

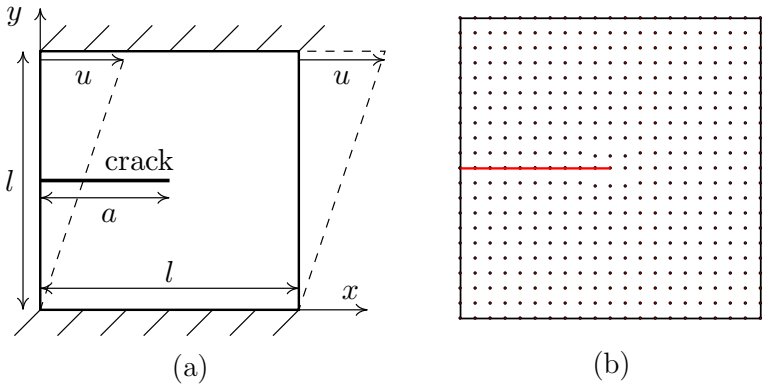

Figure 5.9: Single edge crack under shear loading: (a) configuration; (b) initial particle distribution.

Figure 5.8, where the relationship between g_1' and J' in Equation (5.17) is validated.

5.4.3 Single edge crack under shear

The next example is a square plate with an edge crack, as shown in Figure 5.9, where the crack growths predicted by the CF approach and the MCSC combined with the J-integral are compared. The dimensions of the plate are $l = 1$m and $a = 0.5l$. The plate has a shear modulus $\mu = 8.0$GPa and a Poisson's ratio $\nu = 0.3$. The shear loading is applied by horizontally shifting the upper edge of the plate towards the left side with $u = 0.02l$. The error target for the adaptivity approach is $\eta_t = 0.04$. A geometric imperfection is applied by slight deviation of particles around the crack tip, so that the crack propagation is downwards.

Adaptive results for the crack propagation steps are depicted in Figure 5.10. The crack changes its direction smoothly in Figures 5.10 (a-b) and then propagates linearly towards the lower left corner, while there is a rapid change of the crack path in Figures 5.10 (e-f) and the refinement level at this kinking position in Figure 5.10 (h) is much higher than in Figure 5.10 (d). The CF approach cannot model a sudden change of the crack direction but provides a smooth transition, while the MCSC can achieve a large kink of the crack path, similar to the results in Miehe et al. [263]. Comparing the crack paths obtained by the two approaches in Figure 5.11, the main difference occurs a few crack propagation steps at the beginning. For the initial crack, the deformation is pure mode II and $K_{\mathrm{I}} = 0$ and $K_{\mathrm{II}} \neq 0$. Using the MCSC and Equation (3.32) the crack propagation angle is $\theta = 70.5°$, while the CF is $g_1 \neq 0$ and $g_2 = 0$ following Equation

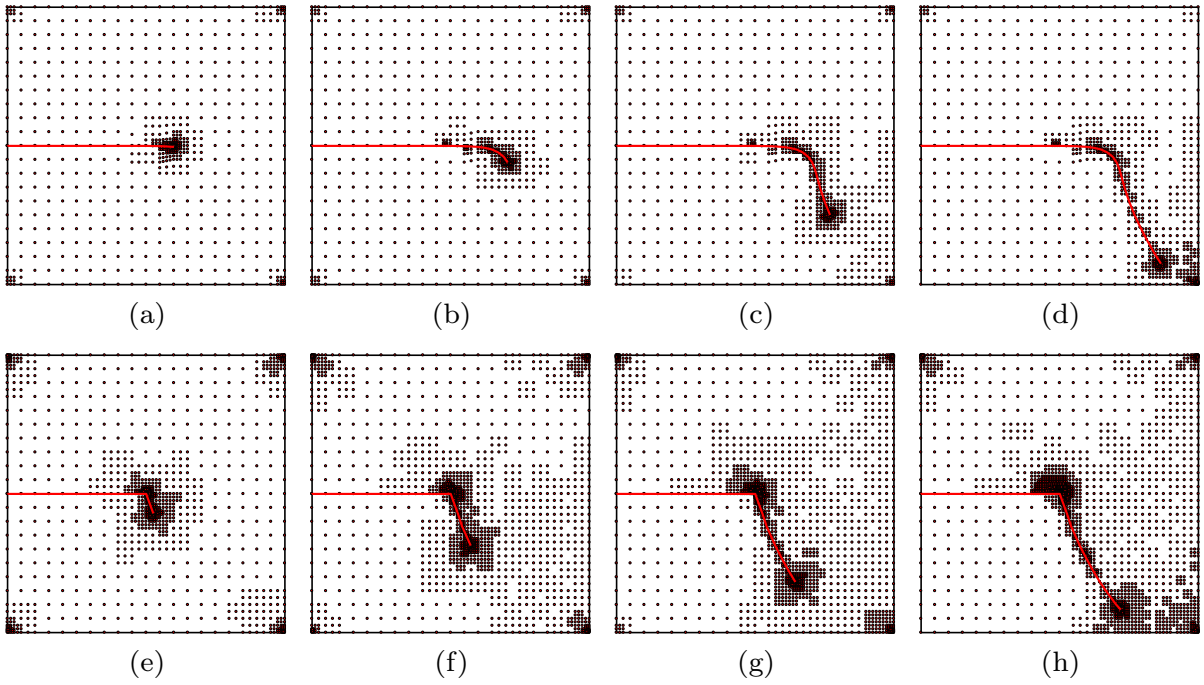

Figure 5.10: Adaptive particle arrangements for the edge crack under shear loading during crack propagation steps: (a-d) steps=5, 10 ,15, 19 by configuration force; (e-h) steps=3, 6, 9, 12 by maximum circumferential stress criterion

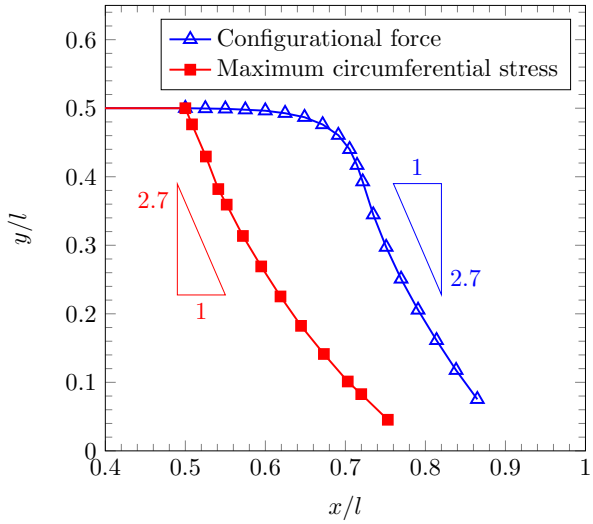

Figure 5.11: A comparison of crack growth predictions under shear loading between by configurational force and by the maximum circumferential stress criterion.

(5.17) which leads to horizontal crack propagation. The initial problem is antisymmetric and it is physically reasonable for the CF method to have horizontal crack growth for the beginning steps, although these results indicate that the CF method may not be suitable for modelling nonsmooth crack kinking. The final slope of two crack growths are not far

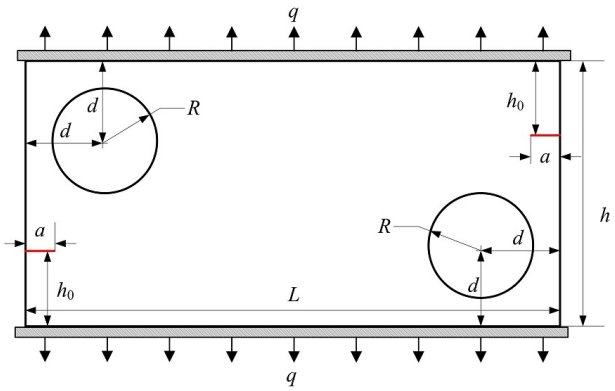

Figure 5.12: Two cracks in a plate with two holes.

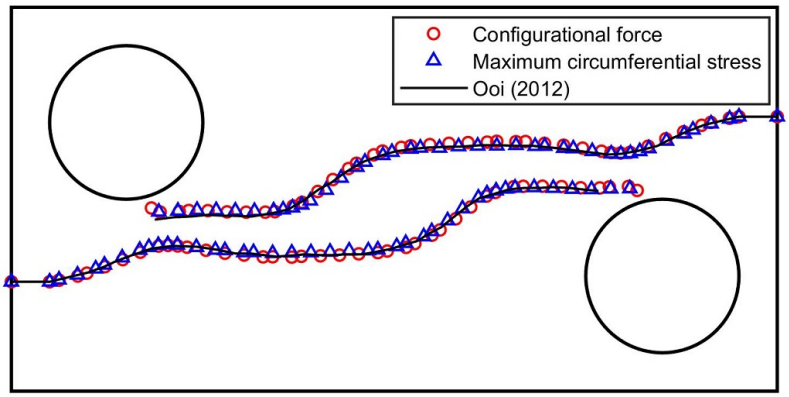

Figure 5.13: Predicted crack propagation of two cracks driven by the configurational force and the maximum circumferential stress criterion.

from the experimental results in Erdogan and Sih [259], where a kinking angle about 70° was obtained ($\tan 70° \approx 2.7$).

5.4.4 Two cracks in a plate with two holes

In the final example, the CF approach combined with the CPM is applied to model the propagation of two cracks, and the problem in Section 4.4.1 is used again. The configuration of this problem is not changed ($L = 20$, $h = 10$, $a = 1$, $h_0 = 2.85$, $R = 2$ and $d = 3$ all with dimensions in mm. Material properties are Young's modulus $E = 200$GPa and Poisson's ratio $\nu = 0.3$.). The bottom of the plate is fixed, and the top edge is moved upwards by $0.02h$. The error target for the adaptivity approach is $\eta_t = 0.06$. A domain integration with size $c = 0.1$mm is used to calculate the configurational force.

From Figure 5.13, the simulated crack path agrees well with both results from the polygon scaled boundary finite element method [256] and results obtained by the CPM

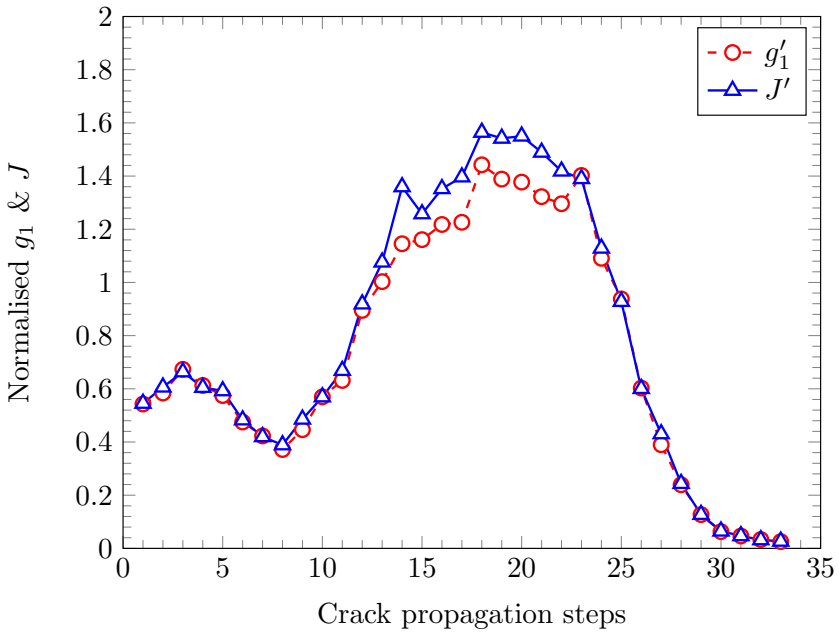

Figure 5.14: Energy release rate during crack propagation steps for the two-crack problem.

with the MCSC [227]. Equations (5.19) are used to normalise g_1 and J using $\sigma \approx 0.02E$. Comparing g_1 and J during crack propagation steps, results from the configurational force and the J-integral show the same trend as given in Figure 5.14. The major differences occur in steps 12-23, where crack paths by the two methods don't match very well but the difference is small.

5.5 Summary

This chapter includes a study of different crack propagation criteria and a methodology of the CFCPM which can take the advantages of both the CF approach and the CPM. It is shown that the MCSC can maintain both efficiency and accuracy and therefore surpasses the MSEDC and the MSERRC. The CF approach is compared with the MCSC through crack modelling based on the CPM. The advantages of the CF approach consist mainly of no decomposition of stresses and displacements with respect to the crack path for mixed-mode fracture problems, so it is easier to implement and faster than the MCSC. The calculation of the CF is via either a contour integration or a domain integration, and the results show that both methods are path-independent, where the domain integration is generally more accurate than the contour integration. The contribution from crack surfaces to the CF is much smaller than the contribution from domain integration and is

affected by the error in the approximation around the crack tip. This error still exists even with a very fine particle distribution. For crack propagation modelling, the CF approach usually leads to smooth crack growth, while the MCSC allows a sudden change of crack direction. Both the CF approach and the MCSC can provide a good prediction of crack propagation as shown in the example with two cracks in Section 5.4.4.

Chapter 6

A framework for 3D cracks with the CPM

6.1 Introduction

A crack in 3D usually has an arbitrary shape, a complex geometry and therefore brings many difficulties to current numerical methods for fracture modelling. The standard finite element method has been tried to use element faces to model 3D crack surfaces, and the remeshing work is found to be more burdensome than aligning element edges to 2D crack paths [152]. The issue of remeshing is addressed in the extended finite element method (XFEM) [153, 155] and the group of meshless methods [2, 58], where crack discontinuities are introduced by either discontinuous enrichment functions or modifying influence domain of nodes (for meshless methods) so the dependence on elements for crack modelling is removed. However, both the XFEM and these meshless methods require a specific approach for describing 3D crack geometries, e.g. through level set functions [161, 180], triangular meshes [251, 271–273] or a hybrid of the two approaches [274]. Triangular meshes can provide explicit crack descriptions of 3D crack patterns but cannot guarantee smooth results, while crack modelling by level sets is more accurate, but updating level set functions is computationally time-consuming for 3D problems [180, 181, 183]. The numerical manifold method (NMM) [187, 258] is an alternative as described in Section 1.5.4, but its application to 3D cracks still relies on the use of triangular cells [275, 276]. Peridynamics [192] requires no specific algorithm for describing crack geometries (Section

1.5.5) and the application to 3D cracks is straightforward [277], although much work is necessary to improve its efficiency and accuracy of crack predictions. The application of the phase field to 3D cracks is not difficult [170], but the high computational expense for the evolution of the phase field is still problematic as mentioned in Section 1.5.2. The cracking particle methods (CPM) has been shown its ability for crack modelling in both 2D and 3D [203, 204, 212, 278], although some early CPMs [204, 213] faced issues of spurious crack results. A modified CPM has been proposed in Chapter 3 of this thesis (also in [227]) which allows crack kinks and branches at particles and addresses the issues of spurious crack results. Here, this approach is extended to 3D crack problems, where a framework providing explicit crack description is developed.

6.2 Description of 3D crack surfaces

Describing the geometries of 3D cracks is one of the major challenges in computational fracture mechanics, and in the literature to date is mostly achieved through either triangular meshes [251, 271–273] or level sets [161, 180], where so-called "ghost" nodes are required for capturing crack geometries in either the XFEM or the EFGM. Here, a new approach using the modified CPM [227] is proposed, which is related to previous uses of triangular facets but where crack surfaces are defined by cracking particles and which is capable of handling both static and propagating cracks.

6.2.1 Issues in the modelling of 3D problems

Moving from 2D to 3D is challenging, because of both an increasing calculation burden for one more degree of freedom per node and the increased complexity of crack shape. A contribution to the former arises from the requirement of inverting a larger matrix for calculating shape functions at every integration point. For instance when a linear basis function is used, the size of the moment matrix $\mathbf{A}$, required in Equation (2.9) in the moving least squares process, is 3×3 for 2D problems but in 3D becomes 4×4, as mentioned in [2]. For high order bases, this increase in matrix size is more obvious.

Considering the latter source of complexity, cracks in 2D are composed of lines and crack tips are points, however 3D cracks consist of surfaces, and crack "fronts" are curves, so it should be no surprise that aspect of the formulation becomes considerably more complicated, e.g. the visibility criterion. For 2D problems, this criterion involves locating

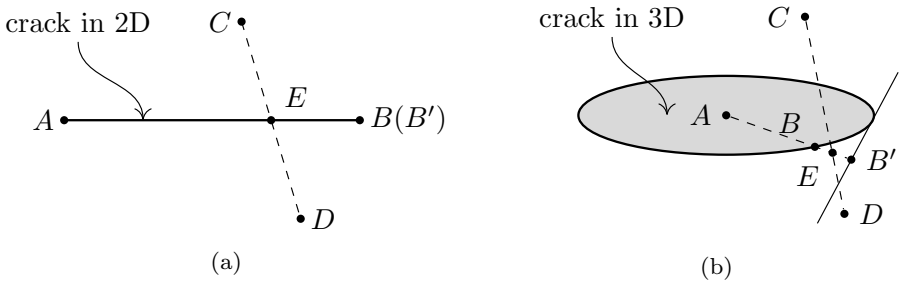

Figure 6.1: The visibility criterion: (a) 2D crack; (b) 3D crack

the intersection point E between the straight line connecting two particles C and D and a crack path AB as shown in Figure 6.1 (a). When E is within the segment AB, particles C and D are invisible to each other and are not influenced mutually. However, the situation for 3D cracks is different, as presented in Figure 6.1 (b). For a crack in 3D with a curved front, the line for checking the visibility is AB shorter than AB'. Particles C and D are visible in that the intersection E is outside of the line AB.

The adaptivity approach in Section 3.3 for 2D cracks is also modified here to be applicable to 3D problems. The same error estimator of Equation (3.13) is used, while the refinement strategy is different where the division of background cells is changed from a quad-tree structure in 2D [227, 231] to an octree structure in 3D [225]. For instance, a background cell is divided into eight subparts and 19 new particles are added, a much larger number than the 5 new particles in 2D.

6.2.2 Cracking particles in 3D

In the original CPM for 3D crack problems [203, 204], each particle is defined with a discontinuous circular plane in its support and the weight function is modified as shown in Figure 6.2 (a). Using these circular planes to describe nonplanar 3D crack surfaces can however give rise to issues of spurious cracking as mentioned in Section 3.2.2. The idea of the modified CPM in 2D (in Chapter 3) is here extended to 3D and an approach using nonplanar discontinuous segments is now presented as given in Figures 6.2 (b-d). Crack surfaces are described through a set of cracking particles as before but fully represented by a triangular mesh connecting these particles (Figure 6.3), where vertices of these triangular elements are the cracking particles. The orientations of these discontinuous "segments" (the triangular facets) are defined according to the locations of the cracking particles:

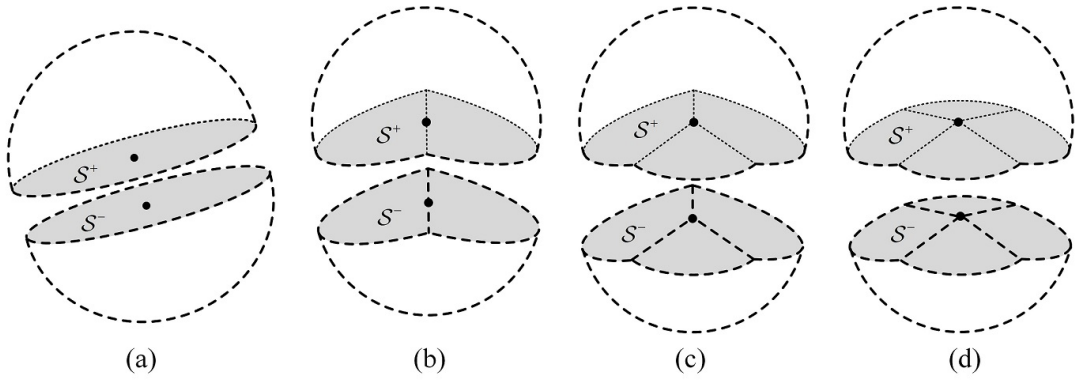

Figure 6.2: The support of cracking particles in 3D: (a) the original CPM; (b-d) proposed CPM with different segment numbers: 2, 3 and 4.

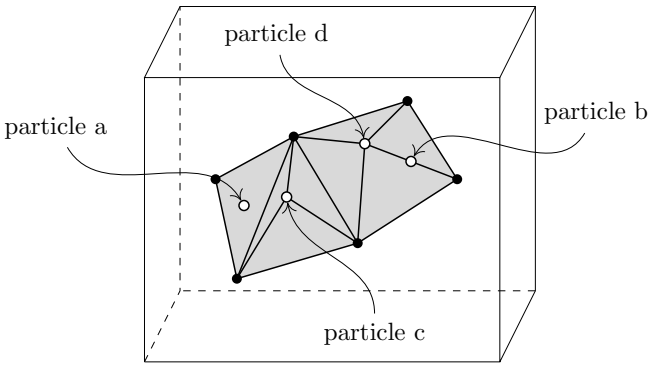

Figure 6.3: Crack surfaces presented by triangular meshes in a cube problem domain.

particle a located within a triangular element has a support as in Figure 6.2 (a); particle b on an edge in the mesh is defined with a support in Figure 6.2 (b); supports of particles c and d on the vertices are depicted in Figure 6.2 (c-d). The information of all triangular facets connected to one cracking particle is recorded in a matrix. The maximum number of facets which can be connected to any particle is limited and set to eight for the sake of simplicity. Those particles in black in Figure 6.3 belong to the crack front particles and are not themselves split because the crack front has influence on both sides of the crack. For a cracking particle near to the crack front, its influence domain is fully truncated, although the crack does not necessarily cross the entire influence domain. This is because the cracking particle does not affect the other side of the crack, when the visibility criterion is used to check the connectivity between particles. A pair of cracking particles sharing the same location cannot be distinguished from each other directly, and this is addressed by giving these cracking particles tiny shifts (e.g. 0.001 of their support sizes) to the two sides of the crack and then applying the standard algorithm for the visibility criterion.

This modification is only applied for checking the connectivity between particles, while the original locations of cracking particles are used to calculate shape functions. It is notable that the description of crack surfaces can be obtained through other shapes of meshes, especially for cracks with simple geometries. For instance, a circular cell (the initial crack itself) can be used to represent the penny-shaped crack and the crack propagation can be described by a triangular mesh, as will be shown later.

For simplicity, only linear problems with a single crack in 3D are considered here, although non-linear fracture problems with crack branching and crack coalescence have been studied by the CPM in [202–204]. The proposed CPM can cover problems of branched cracks [279], but crack branching itself, as a feature of dynamic crack propagation, is not contained in this implementation which uses an implicit quasi-static code. Whether a crack branches and how many branches generated are subject to the physics of the problem and are not method dependent, and an additional criterion is required to model this phenomenon. The extension of the proposed CPM to dynamic fracture will be included in future research work.

6.3 Crack propagation

Crack propagation in 3D is comprised of two steps, advancing the crack front and generating new crack surfaces. In the proposed method, the position of new crack front is obtained by giving the particles on the old crack front an increment following the maximum circumferential stress criterion, as in Section 5.2.1, and new crack surfaces are created by connecting the two groups of particles on the old and new crack fronts with triangular facets.

6.3.1 Calculation of SIFs in 3D

Similar to the situation in 2D crack propagation, stress intensity factors (SIFs) at crack fronts are used to determine the orientation of the propagation increment instead of directly using the stresses at the crack front. After a solution for the governing equations is obtained, SIFs are extracted via either the J-integral [240] over a contour path, or the interaction integral [243] over a domain in 2D or 3D. For the former in 3D, the SIFs of three modes are decomposed by using symmetric and antisymmetric stresses specific to the crack surface as in [180, 280], but extra terms for the energy contribution from the normal

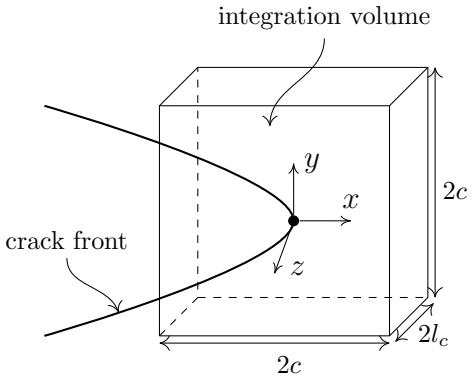

Figure 6.4: A volume for the interaction integration at a crack front particle.

direction of the contour plane are included, which contain the derivatives of stresses [281]. These derivative terms can be avoided by using a domain integration instead, and the interaction integral is used to calculate SIFs in this chapter. The interaction integral in 3D at one crack front particle is evaluated as

$$I = \frac{1}{l_c}\int_V (\sigma_{ij}^{\text{aux}} u_{j,1} + \sigma_{ij} u_{j,1}^{\text{aux}} - \sigma_{jk}^{\text{aux}} \varepsilon_{jk} \delta_{1i}) q_{,i}\, \mathrm{d}V, \quad i,j,k \in \{1,2,3\}\,, \tag{6.1}$$

and it has a relationship with SIFs as

$$I = 2\frac{(1-\nu^2)}{E}(K_{\text{I}} K_{\text{I}}^{\text{aux}} + K_{\text{II}} K_{\text{II}}^{\text{aux}}) + \mu K_{\text{III}} K_{\text{III}}^{\text{aux}}, \tag{6.2}$$

where q is a weight function e.g. $q = (1 - \frac{|x|}{c})(1 - \frac{|y|}{c})(1 - \frac{|z|}{l_c})$, c and l_c are sizes of the volume as in Figure 6.4. The superscript "aux" indicates the auxiliary state, and the auxiliary field is predefined as in Appendix C and is used to calculate the SIFs of three modes. For instance, if $K_{\text{I}}^{\text{aux}} = 1$, $K_{\text{II}}^{\text{aux}} = 0$ and $K_{\text{III}}^{\text{aux}} = 0$ then $I = 2\frac{(1-\nu^2)}{E} K_{\text{I}}$. This integration is evaluated under a local coordinate system originated at the crack front particle as in Figure 6.4. Although a curvilinear coordinate system was applied in [282] for 3D cracks with curved and non-planar surfaces, the integration here is evaluated over a cube with a Cartesian coordinate system for the sake of simplicity, as in many other references [161, 272, 273, 283].

The local Cartesian coordinate system for a particle on the crack front is built using

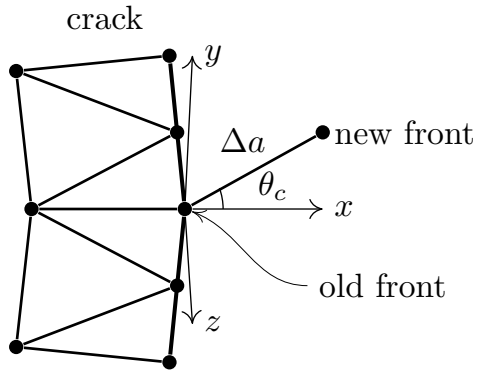

Figure 6.5: Local coordinates at crack fronts in 3D.

the geometries of the triangular facets as shown in Figure 6.5, as

$$\vec{x} = \frac{\sum_i^m \vec{l_i}}{\sum_i^m l_i}, \quad \vec{y} = \frac{\sum_i^n A_i \vec{n}_i}{\sum_i^n A_i}, \quad \vec{z} = \vec{x} \times \vec{y}, \tag{6.3}$$

where $\vec{x}$ and $\vec{z}$ are the extension and tangent vectors of the crack front respectively, and $\vec{y}$ is the normal of the crack surface. l_i are the lengths of lines connected to the particle and $\vec{l_i}$ are the vectors. A_i are the areas of triangular facets connected to the particle and $\vec{n}_i$ are the normals. m and n are the number of lines and triangular elements connected to the particle respectively. $\vec{x}$ and $\vec{y}$ obtained by Equation (6.3) are mostly not orthogonal, and in that case the projection of $\vec{y}$ on $\vec{x}$ needs to be removed and $\vec{y}$ is renormalised.

6.3.2 Advancing the crack front

Two parameters are involved to advance the crack front within the current algorithm, namely increment angle and length. The crack propagating angle can be determined by one of the three crack propagation criteria, including the maximum circumferential stress criterion, the minimum strain energy density criterion and the maximum strain energy release rate criterion as discussed in Section 5.2. Comparisons of all three criteria are given in [245] for 2D cracks and in [284] for 3D cracks. Here it is assumed that the deformation of mode III fracture does not affect the propagation angle, for simplicity [273]. The increment angle θ_c is determined by the maximum circumferential stress criterion and is defined with respect to the x axis within the xy plane under the local coordinate system in Figure 6.5, as in Equation (3.32).

The magnitudes of increments along the crack front are set following the Paris' law.

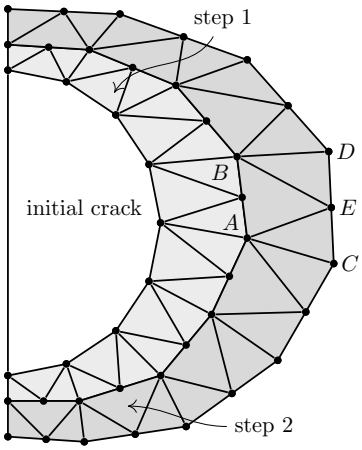

Figure 6.6: Crack propagation steps in 3D with new crack surfaces described by triangular facets.

Although the Paris' law is originally used for fatigue fracture as mentioned in Section 1.4.4, it is used here for 3D cracks under a quasi-static loading, since it provides a relationship between the crack incremental length and the SIF at the crack front, e.g. examples in [180, 273]. For mixed-mode fracture in 3D, the SIF K in Equation (1.15) is replaced with the "equivalent" SIF measuring the magnitude of all SIFs of three modes , as

$$K_{\text{eq}}^2 = \left(K_{\text{I}} \cos^3 \frac{\theta_c}{2} - 3K_{\text{II}} \cos^2 \frac{\theta_c}{2} \sin \frac{\theta_c}{2} \right)^2 + \frac{E}{(1-\nu^2)2\mu} K_{\text{III}}^2. \tag{6.4}$$

The particle on the crack front with the maximum K_{eq} is defined with a given incremental length $\Delta a_{\max}$, then the other particle i on the crack front is defined with

$$\Delta a_i = \Delta a_{\max} \left(\frac{\Delta K_{\text{eq}}}{\Delta K_{\text{eq}}^{\max}} \right)^m. \tag{6.5}$$

After both the incremental lengths and angles along the crack front are obtained, the locations of the new crack front can be easily determined. Looping over all particles on the crack front, a particle i is given an increment which yields the location of the new crack front, as

$$\mathbf{x}_i^{\text{new}} = \mathbf{x}_i + \Delta a_i Q^{-1} \cdot [\cos(\theta_c), \sin(\theta_c), 0]^{\text{T}}, \tag{6.6}$$

where $\mathbf{x}_i$ and $\mathbf{x}_i^{\text{new}}$ are positions of the crack front before and after crack propagation respectively, and Q is the rotation matrix from the global coordinates to the local coordinates. If no particle is located at $\mathbf{x}_i^{\text{new}}$, a new particle is created, otherwise the existing

particle at $\mathbf{x}_i^{\text{new}}$ becomes cracked. For crack propagation step 1 to 2 as shown in Figure 6.6, for instance, particles C and D on the new crack front are determined by Equation (6.6) from particles A and B on the old crack front respectively. The new crack surface, the quadrangle $ACDB$, can be nonplanar and is decomposed into three planar triangular facets, where the particle E is the midpoint of the segment CD. The particle E is not propagated in the current algorithm for simplicity, although crack propagation can be executed for the particle E when the crack front segments cannot provide good approximation of curvature. The strategy here is similar to Duflot (2006) [273], and the differences exist in division of the supports of particles in the proposed method while these triangular cells were only used for describing the crack geometries in [273]. The two steps are duplicated to make successive crack propagation steps, and the adaptivity method mentioned above is executed for every crack propagation step so that the particle density around the crack front is adjusted to improve the efficiency. The whole process of crack propagation is demonstrated in Algorithm 6.1.

Algorithm 6.1 Crack propagation for a 3D crack

```
Achieve SIFs of all front particles by Equations (6.1, 6.2)
Determine incremental angle θ_c by Equation (3.32)
Calculate equivalent SIF by Equation (6.4)
Find the maximum K_eq
for i=1:n_c % loop over all crack front particles
    Set incremental magnitude Δa_i by Equation (6.5)
    Obtain the position of new crack front by Equation (6.6)
    if there is no particle at the new position then
        Create new cracking particle
    else
        The particle at the new position becomes cracked
    end if
end for
Update the information of old front particles
Create new triangular meshes connecting old and new front particles
```

6.4 Numerical examples

The performance of the proposed methodology for modelling 3D cracks is demonstrated using the following three numerical examples. The first is a penny-shaped crack located inside a cube under uniaxial tensile loading, and the theoretical solution of which is used to check the accuracy of the calculation. The second example is obtained by giving the crack a rotation but keeping the same boundary conditions as the first example, which produces a mixed mode crack problem, and additionally crack propagation is considered. The final example contains a lens-shaped crack, which is used to test the abilities of the proposed method for modelling curved crack surfaces. A cube domain with side length $2w = 200$mm is used in all three examples and is initially discretised with a regular distribution of $15 \times 15 \times 15$ particles from which adaptive refinement proceeds. The integration over the cube is performed using $14 \times 14 \times 14$ cells each with $4 \times 4 \times 4$ Gauss points, and the surface integration for external loadings is calculated by using 14×14 cells with 8×8 Gauss points for each. Based on the conservation of momentum, the average movement and rotation of the cube are all zero, as

$$\int_V u_x \mathrm{d}V = 0, \int_V u_y \mathrm{d}V = 0, \int_V u_z \mathrm{d}V = 0, \tag{6.7}$$

$$\int_V \frac{\partial u_x}{\partial y} - \frac{\partial u_y}{\partial x} \mathrm{d}V = 0, \int_V \frac{\partial u_x}{\partial z} - \frac{\partial u_z}{\partial x} \mathrm{d}V = 0, \int_V \frac{\partial u_y}{\partial z} - \frac{\partial u_z}{\partial y} \mathrm{d}V = 0, \tag{6.8}$$

and Lagrange multipliers are used to impose these displacement boundary conditions. This approach has been applied to 2D crack problems [270] for the imposition of essential boundary conditions and is applicable for both symmetric and asymmetric problems. It leads to exactly symmetric results for Example 1 and provides simpler implementation of displacement boundaries for Examples 2 and 3 than by fixing some parts of the cube in [180]. It is not a burden for calculating these integrations in that they are obtained when the system stiffness matrix is assembled, and requires only six Lagrange multipliers for 3D problems. For crack propagation in 3D, the constant in Equation (6.5) is defined as $m = 3.32$ for all three examples, taking the value from [273]. The error in SIFs for all

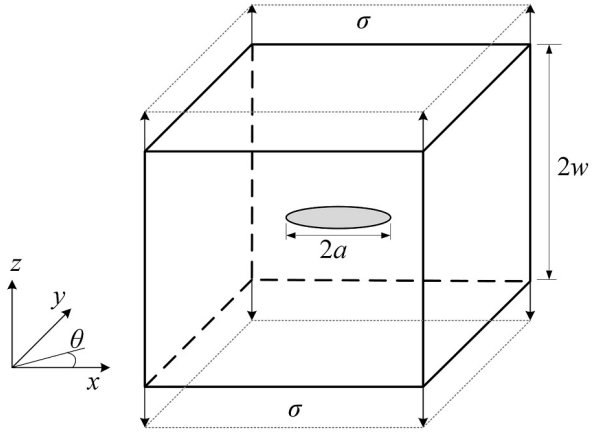

Figure 6.7: A penny-shaped crack in a cube, subjected to uniaxial tensile loading.

particles at the crack front is measured by

$$e_{K_n} = \frac{\sum_{k=1}^{n_c} |K_n^k - K_n^0|}{n_c K_n^0}, \quad n \in \{\text{I, II, III}\} \tag{6.9}$$

where n_c is the number of particles at the crack front, k is the index, K_n are calculated SIFs and K_n^0 are the exact values.

6.4.1 Penny-shaped crack

The deformation of the penny-shaped crack under uniaxial tensile loading is mode I fracture. The configuration is shown in Figure 6.7, where the crack has a radius $a = w/10$ and linear elastic material properties are applied with Young's modulus $E = 100$GPa and Poisson's ratio $\nu = 0.3$. The external loading is $\sigma = 100$MPa at both the upper and lower faces of the cube. An adaptivity approach is used to control particle densities around the crack front with the target global error $\eta_t = 0.008$. For this crack problem with a simple shape, a circular cell (the penny-shaped crack itself) is used directly instead of triangular facets for checking the connectivity between particles. A theoretical solution for both crack opening shapes and mode I SIF K_I is given by Tada [248], as

$$u = \frac{4(1-\nu^2)}{\pi E}\sigma\sqrt{a^2 - r^2}, \tag{6.10a}$$

$$K_\text{I} = \frac{2}{\pi}\sigma\sqrt{\pi a}. \tag{6.10b}$$

For the sake of results analysis, K_I is normalised to $K_\text{I}' = \frac{K_\text{I}}{2\sigma}\sqrt{\pi/a}$.

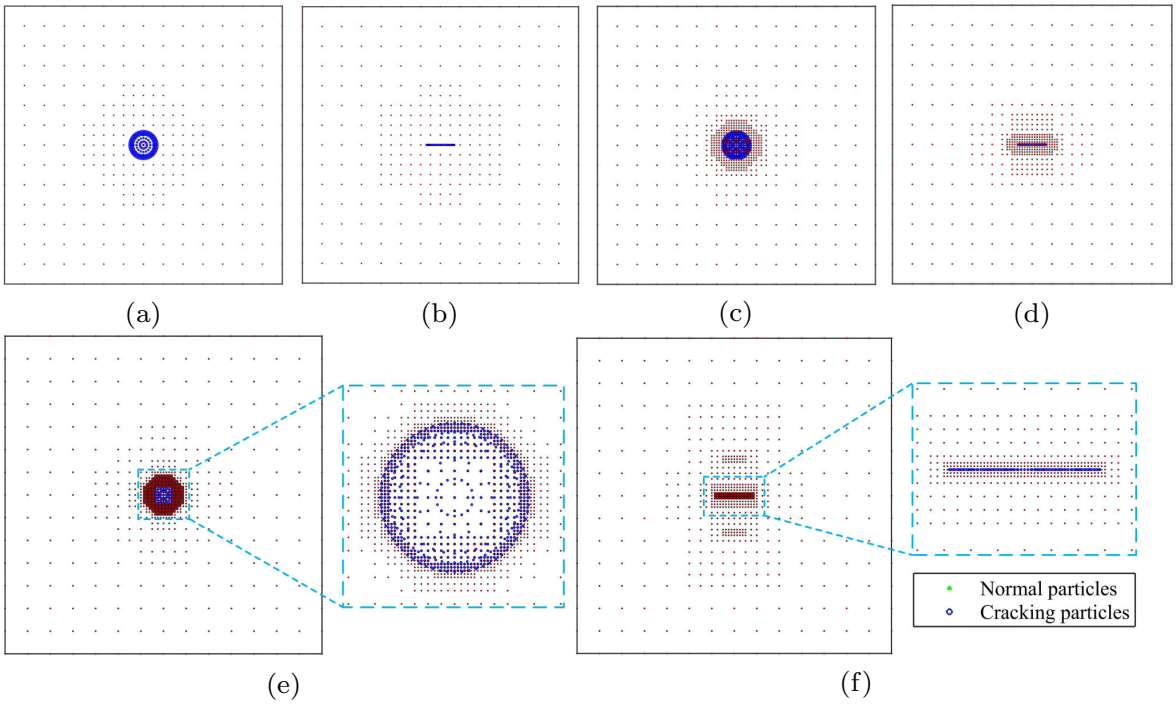

Figure 6.8: Adaptive steps of particle arrangements for the penny-shaped crack problem: (a) xy view for step 1; (b) xz view for step 1; (c) xy view for step 3; (d) xz view for step 3; (e) xy view for step 5; (f) xz view for step 5.

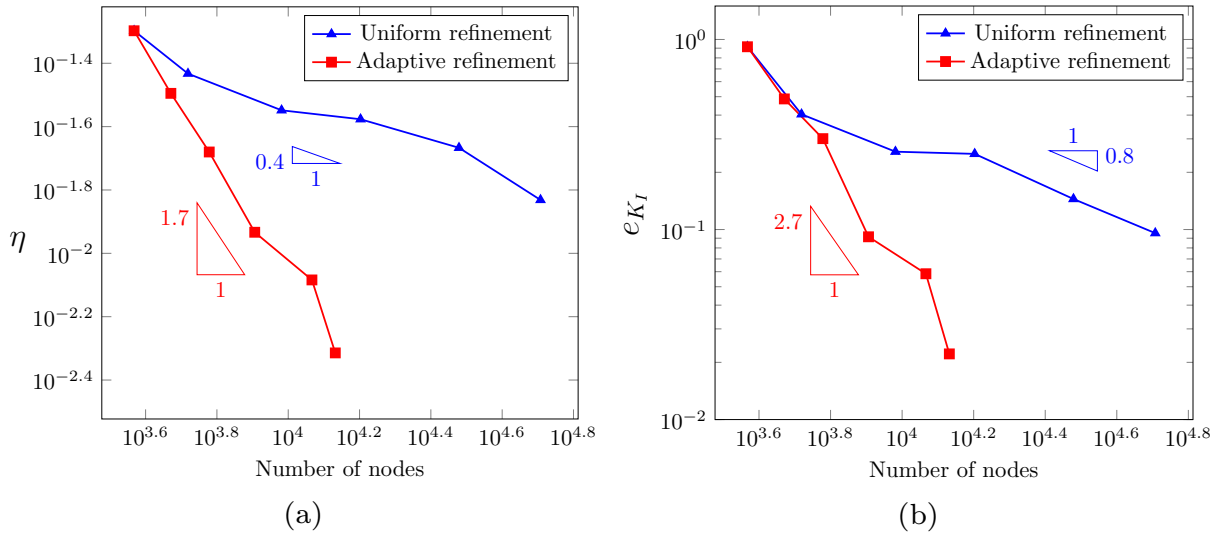

Figure 6.9: Results of the adaptivity in the penny-shaped crack problem: (a) convergence rate; (b) error in K_{I}.

Particle arrangements and densities are adjusted by the adaptivity approach mentioned above, as given in Figure 6.8, where the refinement occurs mainly around the crack front. From Figure 6.9, the convergence rate of error reduction by adaptive steps is higher

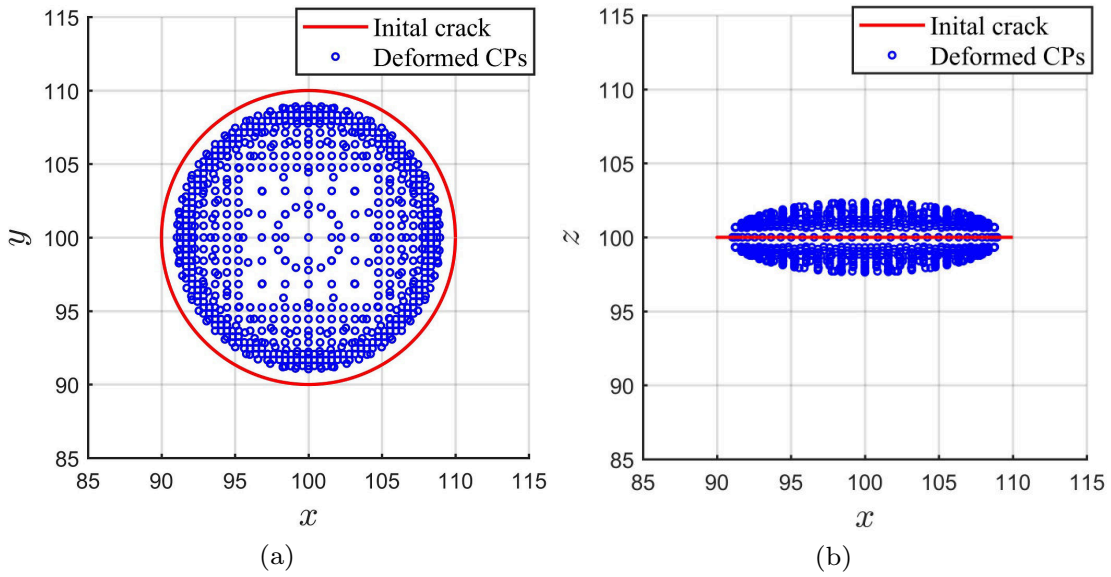

Figure 6.10: Deformation enlarged by 200 times of the penny-shaped crack under uniaxial tensile (unit mm): (a) xy view; (b) xz view.

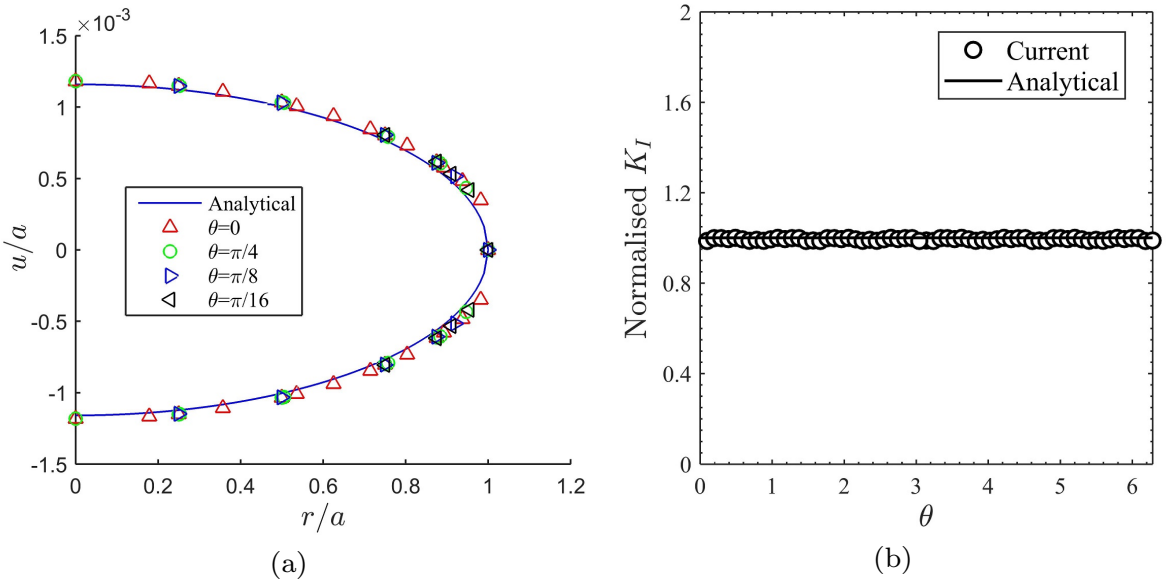

Figure 6.11: Validation of the results for the penny-shaped crack problem: (a) crack opening shape; (b) normalised K_{I}

than the result by uniform refinement, and more accurate SIFs are obtained through the adaptive approach using the same number of particles. It is also shown that using uniform refinement for 3D crack problems is impractical in that the size of crack is much smaller than the cube. Figure 6.10 shows the final deformation of the crack, where an elliptical crack opening shape for the xz view is obvious as shown in Figure 6.10 (b). The crack opening magnitude and mode I SIF for particles at the crack front are obtained

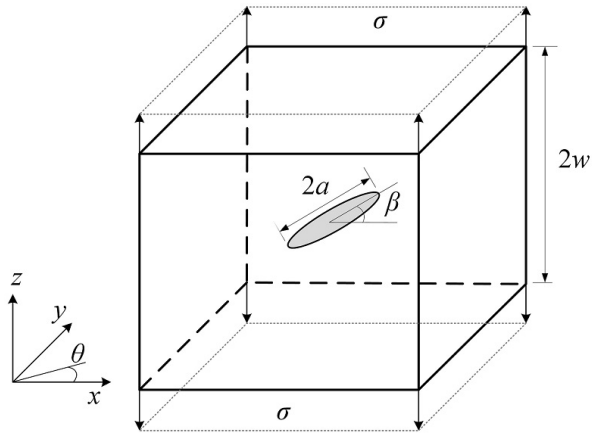

Figure 6.12: An inclined penny-shaped crack under uniaxial tensile loading.

and given in Figure 6.11, where θ is defined as the angle from the x axis and within the xy plane as depicted in Figure 6.7 and r is the distance to the centre of the crack. Figure 6.11 (a) depicts the displacements obtained by the proposed method for cracking particles at four different directions from the centre of the circle which match well with the analytical solution in Equation (6.10). Although a uniform distribution of particles is used initially to model the crack with a curved front, the adaptivity approach can adjust particle densities around the crack front and maintains the accuracy of the calculation. SIFs from the calculation also agree with analytical results from Equation (6.10), as shown in Figure 6.11 (b).

6.4.2 Inclined penny-shaped crack

A mixed-mode fracture is studied by giving the penny-shaped crack in the first example a rotation and keeping the other aspects, as given in Figure 6.12, where the crack has a larger radius $a = w/5$ and the rotation angle is $\beta = \pi/6$ from the x axis within the xz plane. The same material properties and boundary conditions as the first example are used, and Equation (6.8) is still applicable although the problem is not symmetric to the xy plane at the centre of the cube. Here the crack is represented by a circular cell which is the penny-shaped crack itself, while new crack surfaces after crack propagation are described by a triangular mesh. The target error for the adaptivity approach is defined a little higher to $\eta_t = 0.02$, because it is hard to ensure high accuracy after the crack propagates to a complex shape.

For the initial crack, the deformation under uniaxial tensile loading is given in Figure

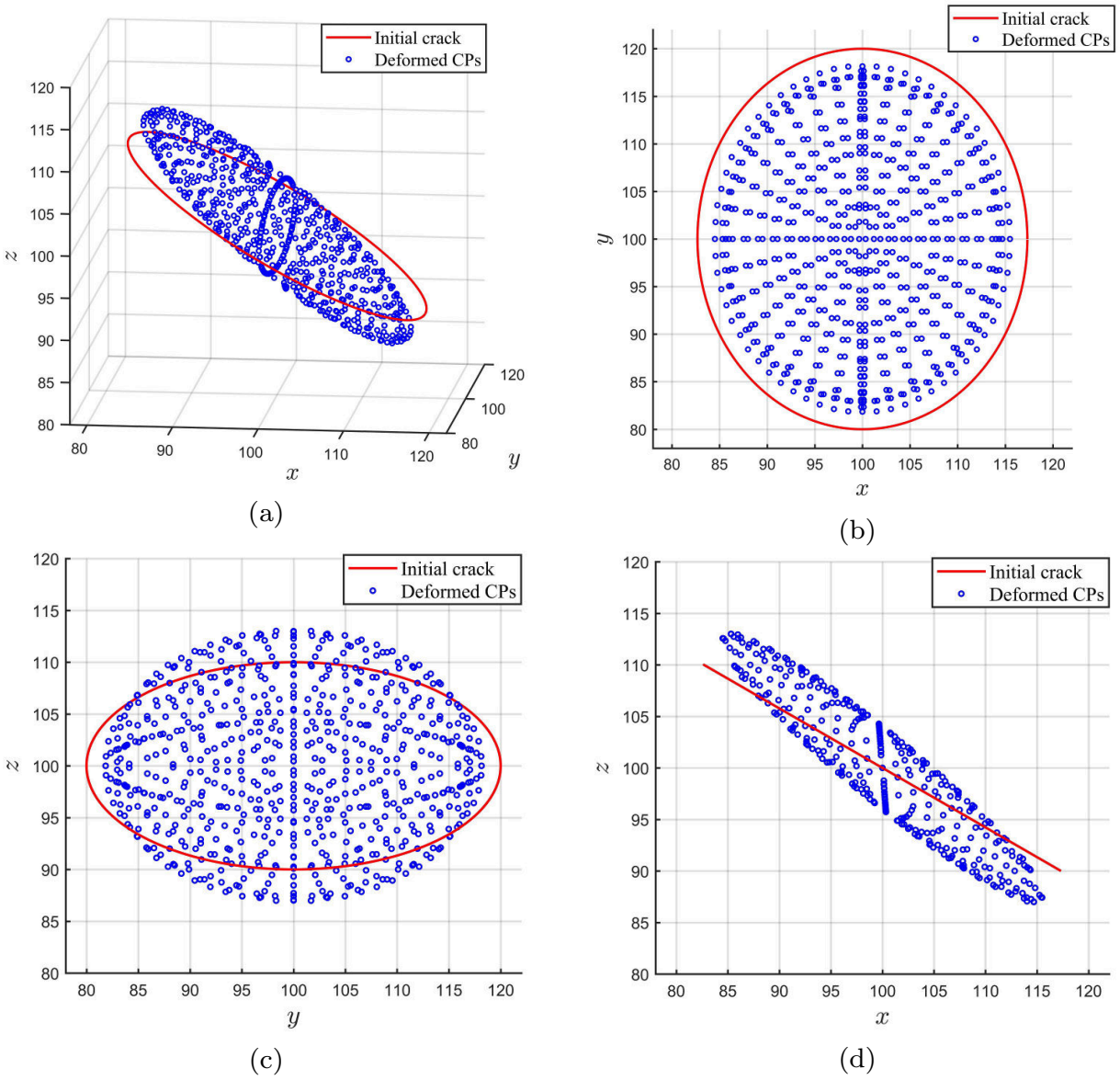

Figure 6.13: Deformation (unit mm) enlarged by 200 times of an inclined penny-shaped crack under uniaxial tension: (a) xyz view; (b) xy view; (c) yz view; (d) xz view.

6.13, where a small rotation of the crack relative to the original location is found. SIFs along the crack front are obtained and compared with analytical results from Tada [248] as in Equations (6.11 a-c), and good agreement is achieved as shown in Figure 6.14, where θ is defined the same as the first example.

$$K_{\mathrm{I}} = 2\sigma \cos^2 \beta \sqrt{\frac{a}{\pi}}, \tag{6.11a}$$

$$K_{\mathrm{II}} = -\frac{4\sigma}{2-\nu} \sin \beta \cos \beta \sqrt{\frac{a}{\pi}} \cos \theta, \tag{6.11b}$$

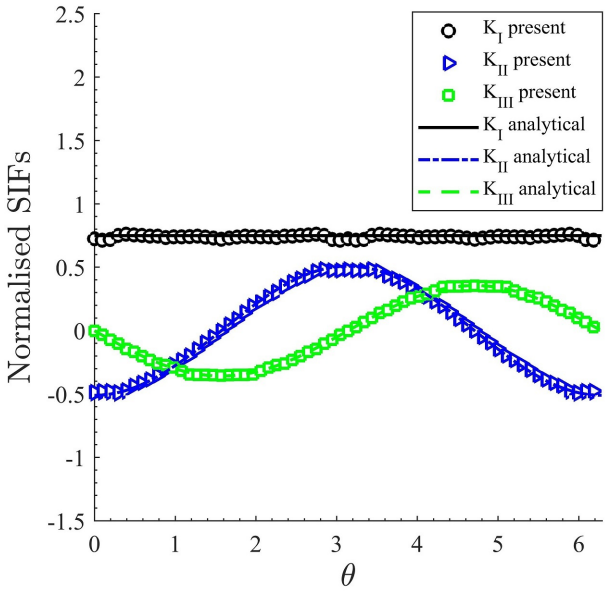

Figure 6.14: SIFs along the crack front for the inclined penny-shaped crack problem.

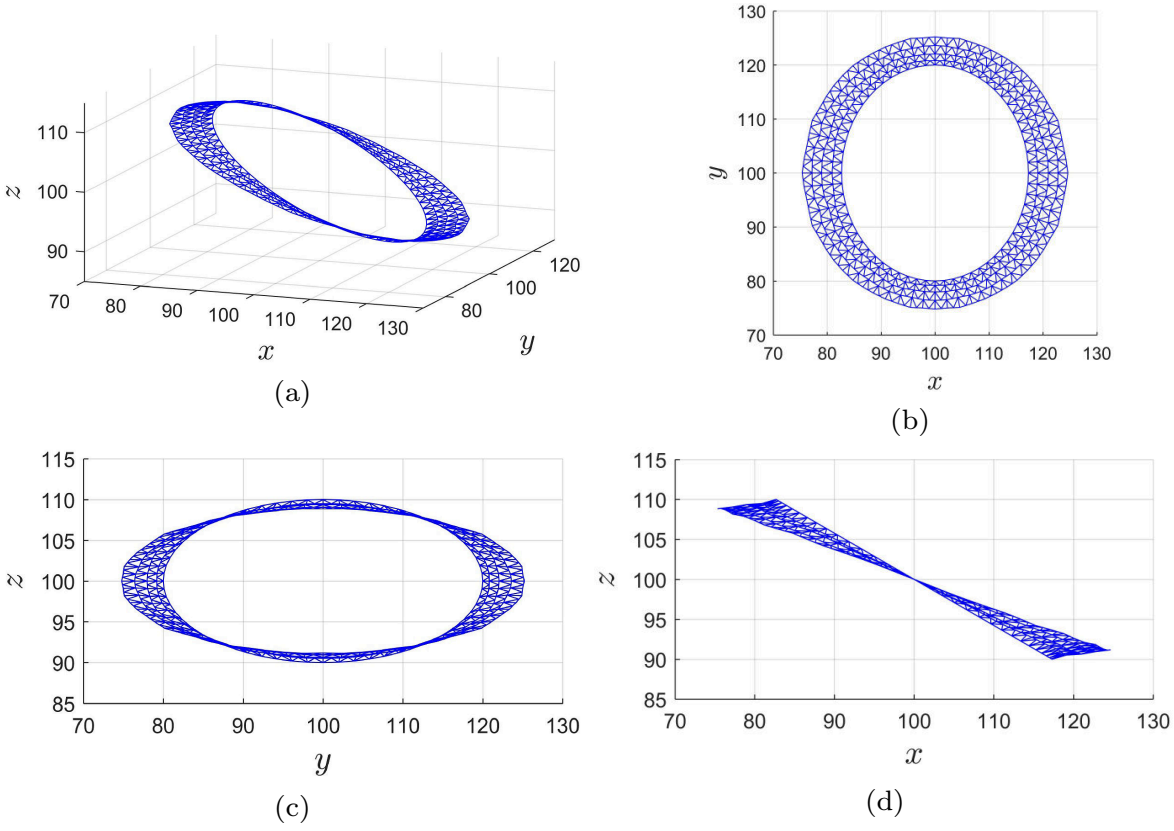

Figure 6.15: Crack propagation (unit mm) of the incline penny-shaped crack under uniaxial tension: (a) xyz view; (b) xy view; (c) yz view; (d) xz view.

$$K_{\mathrm{III}} = -\frac{4(1-\nu)\sigma}{2-\nu}\sin\beta\cos\beta\sqrt{\frac{a}{\pi}}\sin\theta. \tag{6.11c}$$

It is also shown that the adaptivity approach can ensure the accuracy along a curved crack

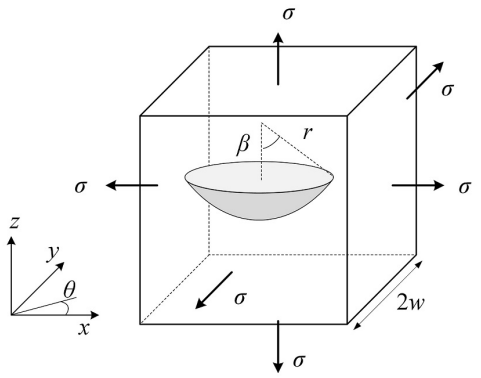

Figure 6.16: A lens-shaped crack in a cube under hydrostatic tensile loading.

front for mixed-mode fracture problems using a regular distribution of particles. There are, however, two deviations in the numerical results noticeably at $\theta = 0$ and $\theta = \pi$. This is explained by the fact that Equations (6.11) are predictions for a crack in an infinite volume while here the cube size is finite and SIFs are affected by boundary effects, similar results of which can be found in [180, 251]. Both Figure 6.13 and Figure 6.14 show that the deformation of fracture at $\theta = 0$ is predominantly mode I and II where $K_{\mathrm{III}} = 0$, while it is predominantly mode I and III at $\theta = \pi/2$ where $K_{\mathrm{II}} = 0$. After crack propagation, new crack surfaces are generated and described by a triangular mesh, as shown in Figure 6.15. There are two "kinks" in the crack shape at $\theta = \pi/2$ and $\theta = 3\pi/2$ caused by mode III fracture, which is consistent with the deformation pattern.

6.4.3 Lens-shaped crack

The final example is a lens-shaped crack in a cube as shown in Figure 6.16, where a comparison between the original CPM and the proposed method for modelling nonplanar cracks is demonstrated. The configuration of the crack consists of $r = w/5$, $\beta = \pi/4$, and linear elastic material properties are applied ($E = 68.9$GPa and $\nu = 0.22$), taking the values from [282]. The target global error for the adaptivity is $\eta_t = 0.008$. The cube is under tensile loading $\sigma = 100$MPa at all six faces. Three modes SIFs are calculated and normalised as

$$K'_n = \frac{K_n}{2\sigma}\sqrt{\frac{\pi}{r\sin\beta}}, \quad n \in \{\mathrm{I}, \mathrm{II}, \mathrm{III}\}, \tag{6.12}$$

and then the results are compared with the reference values $K'_{\mathrm{I}} = 0.874$, $K'_{\mathrm{II}} = 0.225$ and $K'_{\mathrm{III}} = 0$ from [282].

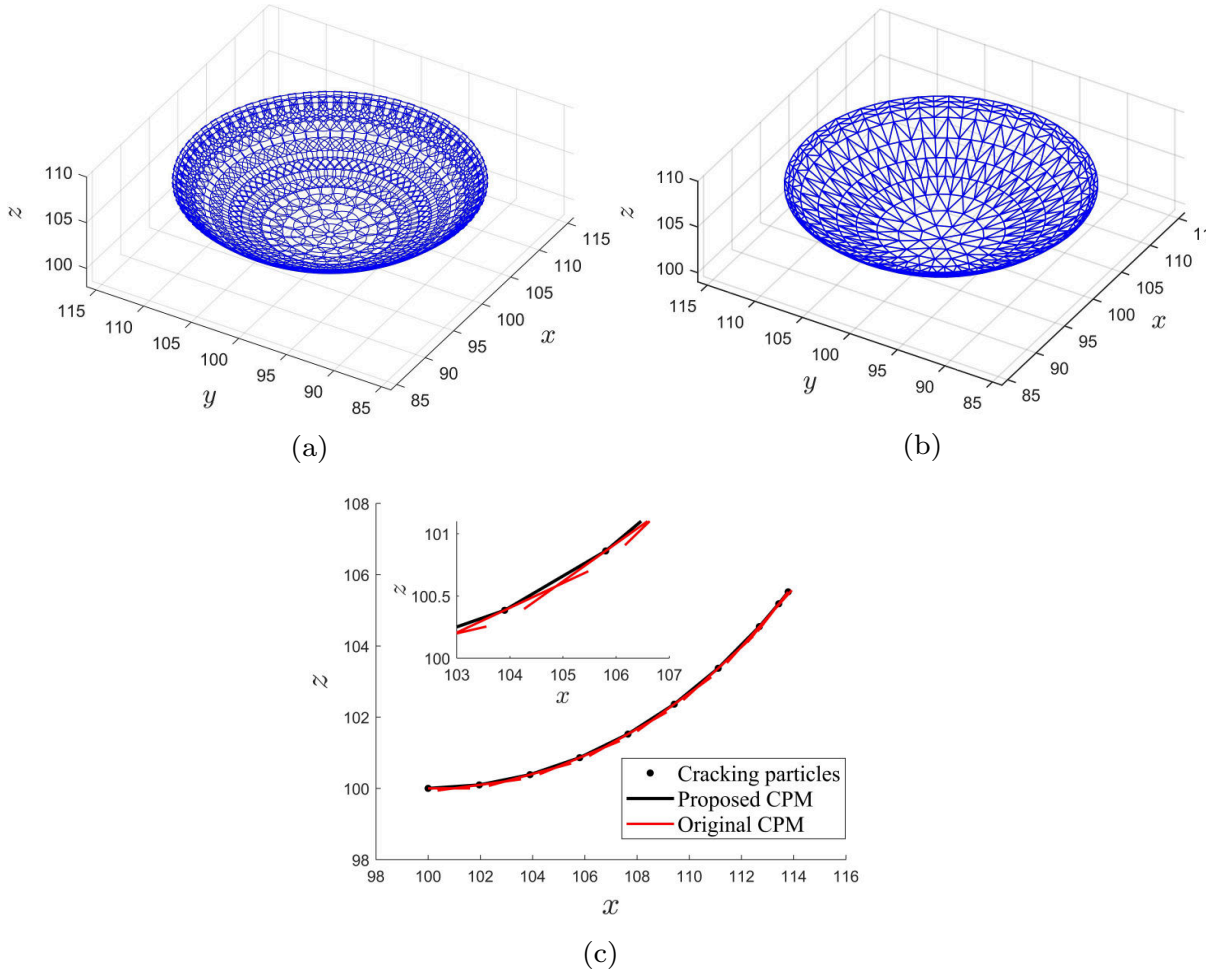

Figure 6.17: Comparison of crack surface description between the original CPM and the proposed CPM for the lens-shaped crack: (a) original CPM; (b) proposed CPM; (c) slice view at $y = 100$ (mm).

Some refinements of particles are predefined around the crack in the initial particle arrangement because it has a more complex shape than previous two examples. In the original CPM, the crack is represented by a set of planar discontinuous segments as shown in Figure 6.17 (a), while the new method makes use of a triangular mesh to model the crack, seen in Figure 6.17 (b). The difference between the two methods is illustrated in Figure 6.17 (c) using a "slice" view at $y = 100$mm, which shows that crack modelling by the original CPM is discontinuous while the proposed method provides a continuous path. This discontinuity leads to issues of implementation in the original CPM, as some integration points are isolated by the discontinuous segments. It is necessary to shift these points away from the crack to make them visible to surrounding particles, which is not necessary in the proposed method. The convergence rates of global error are included in

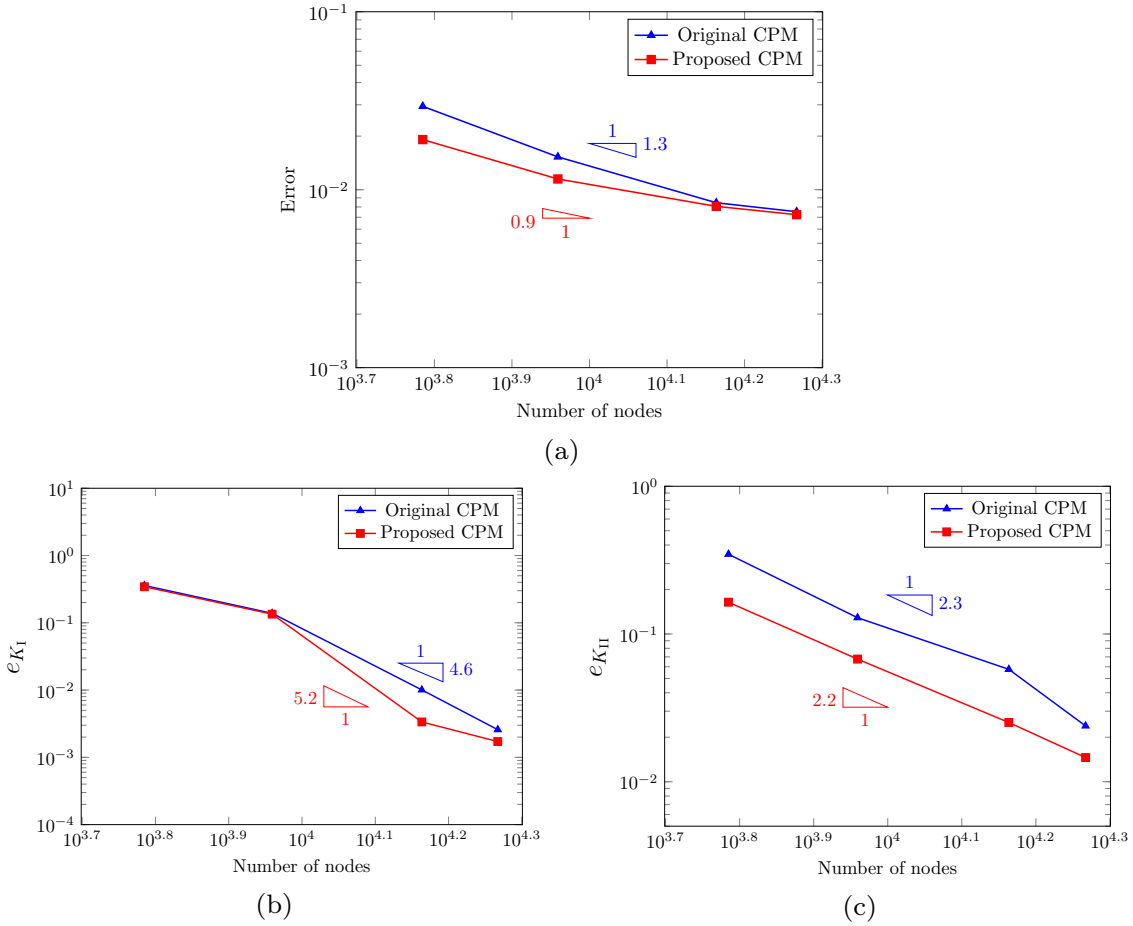

Figure 6.18: Comparison of results between the original CPM and the proposed CPM for the lens-shaped crack: (a) global error; (b) F_{I} at dashed line; (c) F_{II} at dashed line.

Figure 6.18 (a), which shows that the proposed method can provide results with lower errors than the original CPM, but the difference decreases when fine particle arrangements are used. The degradation in the convergence of global error is because the triangular cells for approximating the lens-shaped crack are not changed during the adaptivity process, and this part of error remains when using more Gauss points. It follows that the proposed method provides better accuracy in the calculation of SIFs as shown in Figures 6.18 (b-c), although similar results are obtained for K_{I} by the two methods using coarse particle arrangements which are not capable of detecting the difference in crack description of the two methods. The crack deformation predicted by the proposed CPM is given in Figure 6.19 with a slice view at $y = 100$mm in Figure 6.19 (c) to show the features of the crack opening. The SIFs of three modes along the crack front are obtained by the proposed method as shown in Figure 6.20, showing good agreement with the reference values. When

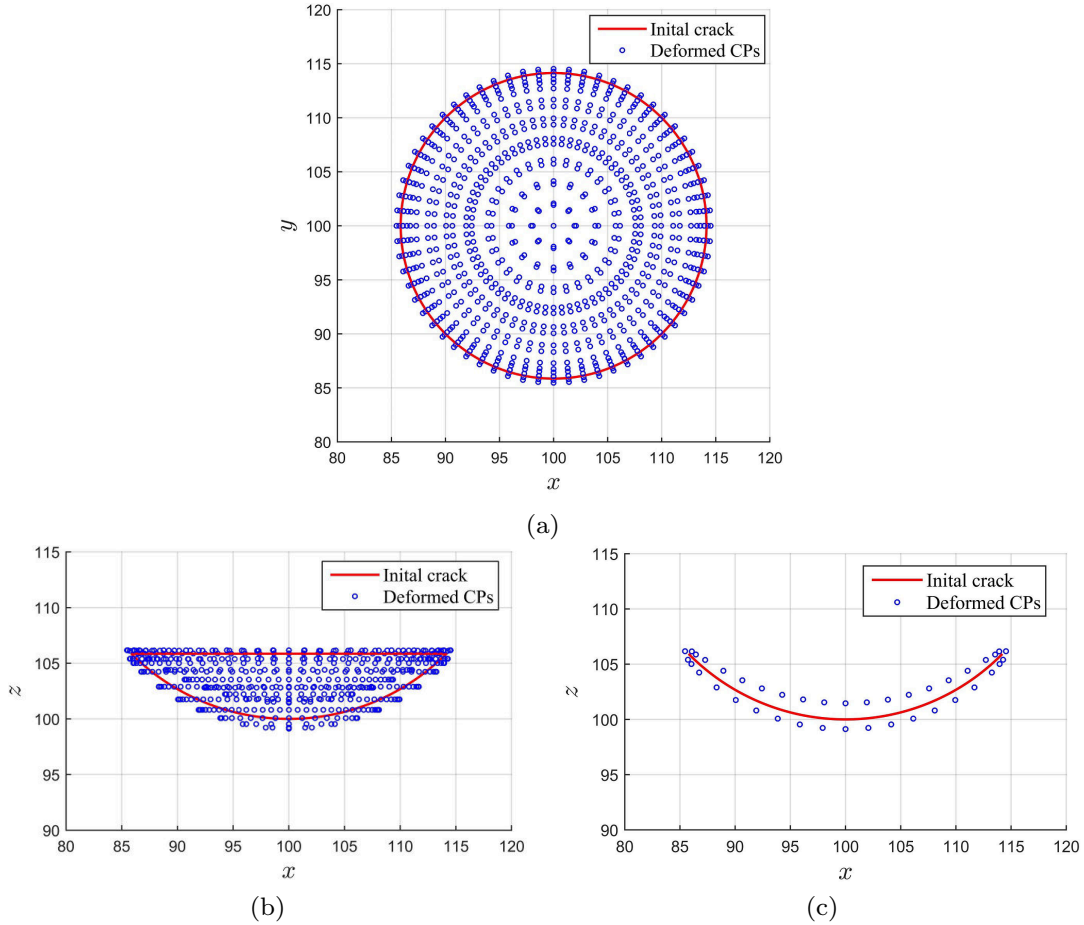

Figure 6.19: Deformation multiplied by 50 times of the lens-shaped crack under quadratic tensile loading: (a) xy view; (b) xz view; (c) slice view at $y = 100$ (unit mm).

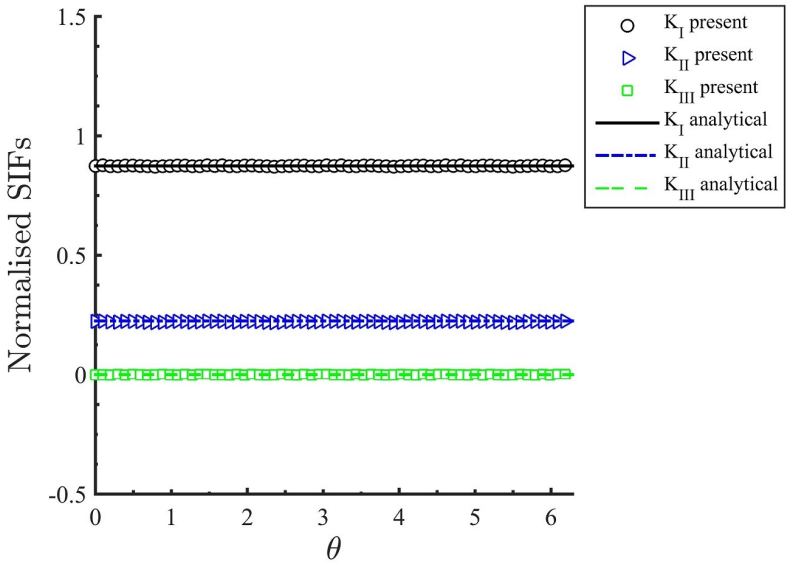

Figure 6.20: Validation of calculated SIFs along the crack front of the lens-shaped crack.

fine particle arrangements are used around the crack front, both the original CPM and the proposed method can provide results with a good accuracy. The advantage of the proposed method is the capacity to align the crack segments so that a better description of crack patterns is achieved, especially for modelling cracks with high curvatures.

6.5 Summary

An adaptive CPM for 3D fracture modelling has been proposed, which provides an explicit description for 3D crack propagation. The methodology makes use of triangular facets as discontinuous segments, which are located by particles, to represent 3D crack surfaces. Particles on crack surfaces are assumed to be cracking and are split into two parts. Influence domains of these particles are divided by the discontinuous segments, and discontinuities at cracks are obtained by using the visibility criterion. The geometry of new crack surfaces during crack propagation steps is described through a triangular mesh which is built from the original crack front. The triangular mesh is nonplanar and can record the angular change of the crack geometry by adjusting the orientations of these discontinuous segments. For particles inside a triangular facet, their influence domains are divided equally the same way as the original CPM, while for others on the edges of triangular facets, the supports are divided by nonplanar segments. An adaptivity approach for 3D problems has been introduced to the method to capture the stress gradients at the crack front. The original and the modified CPMs are compared using the lens-shaped crack problem, and the proposed methodology provides a higher convergence rate in global error with more accurate results of SIFs.

Chapter 7

Thermo-elastic fracture by an adaptive CPM without enrichments

7.1 Introduction

The study of thermo-elastic fracture mechanics is of great importance in the design of structures under thermal loadings, including aerospace components, turbines and nuclear vessels. When heat flow travels across a crack, thermal gradients are set up in the neighbourhood of the crack tip, as are thermal stresses [285]. The thermal stress concentration generated around the crack tip can lead to crack propagation and sudden failure of materials. For a crack in a thermoelastic solid, Sih [285] found that the local character of thermal stresses at the crack tip is of the same nature as mechanical stresses, and therefore Williams' expansions [286] for the asymptotic crack tip displacement field are applicable for temperature enrichment. In steady heat flux, crack surfaces can be considered to be fully insulated or perfectively conductive, for instance in [287, 288], which is one feature of thermal fracture mechanics and distinct from purely mechanical situations. A partial insulation crack model has been developed in [289, 290], where the cracked zone is considered to contain a medium capable of conducting heat, e.g. air inside the crack opening domain acting as a thermal conduction medium. The partial insulation coefficient concerned has a nonlinear relationship to the applied mechanical loading and heat flux [290]. During recent decades, cracking under steady thermal loading has been studied using conventional numerical methods, and much of the development is similar to the devel-

opment of non-thermal computational fracture. Examples of early numerical analysis of thermal fracture mechanics used the finite element method (FEM) as in [291, 292], where discontinuities of both temperature and displacement at cracks are modelled by element interfaces, so the issue of remeshing during crack propagation remains [293]. The boundary element method (BEM) is an alternative as in [294] for instance, but meets dilemmas for modelling thermal nonlinearity [295]. Crack tip enrichment functions in mechanical situations are also suitable to capture the thermal stress singularity at the crack tip, and have been introduced into the extended finite element method (XFEM) [288, 296, 297], the element free Galerkin method (EFGM) [298–301] and the numerical manifold method (NMM) [302, 303] for modelling thermoelastic fracture. These methods have been used for solving thermal fracture problems including dynamics cracks [297], ductile cracks [304], interface cracks at bimaterial bodies [298] and fatigue fracture in railway brake discs [305]. Using high order crack tip enrichments in the XFEM, the benefit in accuracy for thermoelastic problems is greater than for purely mechanical elastic problems, as mentioned in [296]. However, these enrichment functions bring extra unknowns leading to higher computational expense and make the global stiffness matrix ill-conditioned, as mentioned earlier in this thesis (e.g. Section 4.2). Apart from using extrinsic enrichments, intrinsic enrichments can be used in meshless methods to avoid these extra unknowns, which is the purpose of this chapter.

Here, an adaptive cracking particle method (CPM) for crack problems under thermal and mechanical loading is developed for 2D only for simplicity, which is based on the algorithm in Chapter 3. Temperature discontinuities at cracks are modelled by modifying the influence domain of particles and using the visibility criterion, and thermal stress singularities at the crack tip are captured by the adaptivity approach which is used to adjust the particle distribution, therefore extra unknowns from enrichment functions are avoided. Since the CPM is meshless, the adaptive approach is implemented easily, and transition elements in the FEM for elements with different sizes are not necessary (as mentioned in Section 1.3). Using crack segments to approximate crack paths, this method is capable of modelling multiple crack propagation under thermal loadings.

7.2 Governing equations

For linear thermo-elastic materials with small displacements, the equilibrium of the heat flux can be stated as

$$\nabla \cdot \mathbf{q} + Q = 0, \tag{7.1}$$

where Q is the heat source and $\mathbf{q}$ is the heat flux obtained from the gradient of temperature T as

$$\mathbf{q}^{\mathrm{T}} = -k_T \nabla T, \tag{7.2}$$

where k_T is the thermal conductivity. The temperature field in a body should satisfy the above and the following boundary conditions

$$T = \bar{T} \quad \text{on } \Gamma_T, \quad \mathbf{n} \cdot \mathbf{q} = \bar{q} \quad \text{on } \Gamma_q, \tag{7.3}$$

where $\bar{T}$ is the constraint at temperature boundary Γ_T, $\bar{q}$ is the external thermal loading at heat flux boundary Γ_q and $\mathbf{n}$ is the normal of the boundary contour. A material is deformed by temperature change due to thermal expansion, and the thermal strain vector $\boldsymbol{\varepsilon}_T$ in 2D using Voigt notation is

$$\boldsymbol{\varepsilon}_T = \alpha_T (T - T_0)[1, 1, 0]^{\mathrm{T}}, \tag{7.4}$$

where T_0 is the reference temperature before thermal loading and α_T is the coefficient of thermal expansion. Mechanical equilibrium in Equation (2.16) should also be satisfied in thermo-elastic problems, and the constitutive model in Equation (2.27) is modified by excluding thermal strains from engineering strains, as

$$\boldsymbol{\sigma} = \mathbf{D} \cdot (\boldsymbol{\varepsilon} - \boldsymbol{\varepsilon}_T). \tag{7.5}$$

Equations (2.16, 7.1) are therefore the governing equations for the thermo-elastic behaviour of homogeneous materials, and boundary conditions are in Equations (2.18-2.19, 7.3). Each particle is associated with three degrees of freedom for 2D problems, i.e. $\{u_x, u_y, T\}$, and a global stiffness matrix is assembled to get a solution for the coupled Equations (2.16, 7.1) as in [297, 299]. Mechanical and thermal governing equations can

be considered to be uncoupled as in [298, 306] with assuming infinite propagation speed for heat wave. In this approach, a solution for temperature distribution is obtained from Equation (7.1), and then the weak form of Equation (2.16) is solved to obtain the displacement and stress fields.

7.3 Review of enrichment functions for cracks under thermal loadings

Two types of cracks in steady heat flux are considered in thermoelastic solids, namely adiabatic crack and isothermal crack, where partially insulation crack is not included which brings thermal nonlinearity. The two cases result in different enrichment functions, which are applied according to the boundary conditions of the problem. These enrichment functions have been widely used in numerical methods including the XFEM and the EFGM to model the temperature and stress gradients near to a crack tip.

7.3.1 Adiabatic cracks

In an adiabatic crack, both temperature and displacement fields are discontinuous at the crack surface. In the temperature approximation, a node at one side of the crack has no influence on the other side. The heat flux is singular at the crack tip with the singularity $1/\sqrt{r}$ as in [285], and is similar to the situations in mechanical loadings, where r is the distance to the crack tip. The leading terms of the asymptotic expansion for temperature and heat flux near to the adiabatic crack tip are given in references [288, 307] as

$$T = -\frac{K_T}{k_T}\sqrt{\frac{2r}{\pi}}\sin\frac{\theta}{2}, \tag{7.6a}$$

$$\mathbf{q} = \frac{K_T}{\sqrt{2\pi r}}[\sin\frac{\theta}{2}, \cos\frac{\theta}{2}]^{\mathrm{T}}, \tag{7.6b}$$

where K_T is the thermal stress intensity factor and θ is the angle to the crack extension defined the same as in Equation (1.18).

To capture the thermal stress singularity at the crack tip, enrichment functions are used in either basis functions or the temperature/displacement approximation, which are similar to the enrichments in mechanical situations in Section 3.2. In the intrinsic enrichment approach, the basis function for temperature field is enriched using Equation

(4.4) as in [298] for instance. Considering the singularity of temperature in Equation (7.6a), a partially enriched basis function in [288] can be used alternatively to approximate the temperature field in 2D, as

$$\mathbf{p}(\mathbf{x}) = [1, x, y, \sqrt{r}\sin\frac{\theta}{2}]^{\mathrm{T}}, \tag{7.7}$$

and the displacement field is approximated using the fully enriched basis function in Equation (4.4). In addition, extrinsic enrichment functions have also been considered in both the EFGM and the XFEM for crack problems under thermal loadings in [288, 300, 301]. Enriched terms accounting for the discontinuities at cracks are added to the displacement approximation as in Equation (1.17). Similarly the trial function for temperature is enriched to

$$T^h(\mathbf{x}) = \sum_{i=1}^{n}\Phi_i(\mathbf{x})T_i + \sum_{i=1}^{n_1}\Phi_i(\mathbf{x})H(\mathbf{x})b_i + \sum_{i=1}^{n_c}\Phi_i(\mathbf{x})\Big(\sum_{k=1}^{4}R_k a_i^k\Big), \tag{7.8}$$

where shape function $\Phi_i(\mathbf{x})$ is used for both displacement and temperature fields, T_i is the temperature of ith particle, and $H(\mathbf{x})$, R_k, a_i^k and b_i are as defined in Equation (1.17). The crack-tip enrichments in R_k can be reduced to one term of $\sqrt{r}\sin\frac{\theta}{2}$ in the XFEM [288], due to the local character of temperature in Equation (7.6a). Extrinsic enrichment brings extra unknowns to the approximation and therefore increases the calculation expense, and these unknowns can make the global stiffness matrix ill-conditioned, which is the major difference to intrinsic enrichment.

7.3.2 Isothermal cracks

In the case of the isothermal crack, a crack surface is perfectly thermal conductive and is maintained at a specific temperature. Although the crack still blocks the heat flux, the difference with the adiabatic crack is from the angular variation of temperature field. The leading terms of the asymptotic expansion near to an isothermal crack tip [288] become

$$T = -\frac{K_T}{k_T}\sqrt{\frac{2r}{\pi}}\cos\frac{\theta}{2}, \tag{7.9a}$$

$$\mathbf{q} = \frac{K_T}{\sqrt{2\pi r}}[\cos\frac{\theta}{2}, \sin\frac{\theta}{2}]^{\mathrm{T}}. \tag{7.9b}$$

The crack surface has the same temperature and is a thermal essential boundary which is imposed on the weak form by Lagrange multipliers or the penalty approach in ways mentioned earlier in the thesis (Section 2.6). Nodes are required at the crack surface for the imposition of thermal essential boundary conditions. For modelling the thermal stress singularity at the isothermal crack tip, the basis function for displacement field is fully enriched with Equation (4.4) in [298], while the temperature field is given a partly enriched basis function in 2D as

$$\mathbf{p}(\mathbf{x}) = [1, x, y, \sqrt{r}\cos\frac{\theta}{2}]^{\mathrm{T}}. \tag{7.10}$$

For extrinsic enrichment, the sign function $H(\mathbf{x})$ is not applicable, since the temperature on the crack surface is continuous (but not the heat flux). Hence the enrichment function should be continuous across the crack surface but with a discontinuous derivative, have the maximum value along the crack surface and become zero away from the crack. For instance, these properties can be delivered using the normal level set function to replace $H(\mathbf{x})$ in the XFEM, as

$$\Lambda(\mathbf{x}) = \sum_{\mathrm{i}=1}^{n_1} \Phi_i(\mathbf{x})|\phi_i| - |\phi(\mathbf{x})|, \tag{7.11}$$

where $\phi(\mathbf{x})$ is the level set function describing the distance to the crack surface, $\Phi_i(\mathbf{x})$ is the shape function and n_1 is the number of nodes in an element, more details of which are given in reference [181].

Overall, the two types of cracks lead to different temperature distributions, so different enrichment functions are used. It has been shown by Duflot [288] that when enrichments of both type of cracks are contained in the discretisation and one type crack is chosen for boundary condition, the degrees of freedom associated with the other are set to zero by the Galerkin process. For instance if the isothermal condition is considered, the contribution from both crack surfaces of the adiabatic crack tip enrichments to the penalty term vanishes by symmetry.

7.4 Crack modelling by the CPM without enrichments

For the computational solution of crack problems under thermal loading, enrichment functions have been widely used in the XFEM and the EFGM. Although these enrichments provide solutions for modelling crack discontinuities, they also bring many issues, including extra unknowns, ill-conditioned stiffness matrices and an increasing order of basis functions, as stated earlier in the thesis. In addition, these enrichment functions require the coordinates of r and θ defining the relative location to the crack tip and their calculation becomes complex for multiple cracks or 3D cracks. Here the CPM developed in previous chapters is applied to this kind of problem. Discontinuities at cracks are obtained by using the visibility criterion for modifying the influence domain of particles so enrichment functions are not necessary, and the stress and temperature gradients around the crack tip are captured by the adaptivity approach. The proposed method is advantageous for modelling multiple cracks under thermal loading without using enrichment functions. Only the adiabatic crack is considered for simplicity, since there is little difference in the visibility criterion process for modelling crack discontinuity between the adiabatic and isothermal situations.

7.4.1 Weak form for mechanical and thermal governing equations

Similar to the development for mechanical equilibrium in Section 2.4, the weak form for the thermal equilibrium equation becomes

$$\int_\Omega \delta(\nabla T)^{\mathrm{T}}\mathbf{q}\mathrm{d}\Omega + \int_\Omega \delta T Q \mathrm{d}\Omega - \int_\Omega \delta T \bar{q}\mathrm{d}\Omega = 0, \tag{7.12}$$

where δ indicates the virtual state. Lagrange multipliers λ are used to impose the temperature boundary conditions, and the weak form becomes

$$\int_\Omega \delta(\nabla T)^{\mathrm{T}}\mathbf{q}\mathrm{d}\Omega + \int_\Omega \delta T Q \mathrm{d}\Omega - \int_\Omega \delta T \bar{q}\mathrm{d}\Omega + \int_\Omega \delta\lambda(T-\bar{T})\mathrm{d}\Omega + \int_\Omega \delta T \lambda \mathrm{d}\Omega = 0. \tag{7.13}$$

The discrete version of the weak form as in [298] is

$$\begin{bmatrix} \hat{\mathbf{K}}_T & \hat{\mathbf{G}} \\ \hat{\mathbf{G}}^{\mathrm{T}} & \mathbf{0} \end{bmatrix} \begin{Bmatrix} \mathbf{T} \\ \hat{\boldsymbol{\lambda}} \end{Bmatrix} = \begin{Bmatrix} \hat{\mathbf{f}} \\ \hat{\mathbf{q}} \end{Bmatrix}, \tag{7.14}$$

where

$$\hat{\mathbf{K}}_{ij} = \int_{\Omega} \begin{bmatrix} \Phi_{i,x} \\ \Phi_{i,y} \end{bmatrix}^{\mathrm{T}} \begin{bmatrix} k_T & 0 \\ 0 & k_T \end{bmatrix} \begin{bmatrix} \Phi_{i,x} \\ \Phi_{i,y} \end{bmatrix} \mathrm{d}\Omega, \tag{7.15a}$$

$$\hat{\mathbf{f}}_i = \int_{\Gamma_q} \Phi_i \bar{q} \mathrm{d}\Gamma_q + \int_{\Omega} \Phi_i Q \mathrm{d}\Omega, \tag{7.15b}$$

$$\hat{\mathbf{G}}_{ik} = -\int_{\Gamma_u} \Phi_i N_k \mathrm{d}\Gamma_T, \tag{7.15c}$$

$$\hat{\mathbf{q}}_k = -\int_{\Gamma_u} N_k \bar{T} \mathrm{d}\Gamma_T. \tag{7.15d}$$

and the hat indicates this to be for the thermal equilibrium distinct from the corresponding term in the mechanical governing equations. To take the contribution from thermal strains on the stress equilibrium equations into account, Equation (2.41b) is modified to

$$\mathbf{f}_i = \int_{\Gamma_T} \Phi_i \bar{\mathbf{t}} \, \mathrm{d}\Gamma_T + \int_{\Omega} \Phi_i \mathbf{b} \mathrm{d}\Omega + \int_{\Omega} \mathbf{B}_i^{\mathrm{T}} \mathbf{D} \boldsymbol{\varepsilon}_T \mathrm{d}\Omega. \tag{7.16}$$

Here mechanical and thermal governing equations are considered to be uncoupled, and the temperature and displacement fields are approximated using the same set of particles for problem discretisation. The stiffness matrices for temperature and displacement can be assembled in one loop, and shape functions and their derivatives are calculated for only one time at each Gauss point, so the computational expense for the temperature field is not high. The whole process is demonstrated in Algorithm 7.1.

7.4.2 Interaction integration for cracks under thermal loadings

The thermal stress intensity factors are calculated by the interaction integral [243], which is obtained from the J-integral and has been introduced in Section 3.4.3. For cracks under

Algorithm 7.1 Solve the temperature and displacement field

1: **for** i=1:n_g % Loop over each Gauss point
2: Find all particles connected to the Gauss point i
3: Calculate shape functions
4: Assemble global stiffness matrix for the displacement field using Equation (2.61)
5: Assemble global stiffness matrix for the temperature field using Equation (7.15)
6: **end for**
7: Solve the temperature field using Equation (7.14)
8: Use the solution of temperatures as input, obtain the displacement field using Equations (2.60)

thermal loadings, the domain form of the J-integral can be found from [308], as

$$J = \int_A \Big((\sigma_{ij} u_{j,1} - W\delta_{1i}) q_{,i} + q\bar{\alpha}_T \sigma_{kk} T_{,1} \Big) \mathrm{d}A, \quad i,j,k \in \{1,2\}, \tag{7.17}$$

and

$$\bar{\alpha}_T = \begin{cases} \alpha_T & \text{plane stress,} \\ (1+\nu)\alpha_T & \text{plane strain,} \end{cases} \tag{7.18}$$

where W is the strain energy, q is a weight function as defined in Equation (3.29) and the index notation is used with the Einstein summation. Comparing with the interaction integration in mechanical situations in Section 3.4.3, the difference for thermal situations is the inclusion of thermal terms as in [243, 296, 298]. The real state (as state 1) contains σ_{ij}, ε_{ij}, u_i, T_i, while the temperature in the auxiliary state (as state 2) is zero where the same auxiliary field of σ_{ij}^{aux}, $\varepsilon_{ij}^{\text{aux}}$, u_i^{aux} is used as in Appendix C. The superposition of the two states for the J-integral is equal to the sum of the two states,

$$J^{(1+2)} = J^{(1)} + J^{(2)} + I^{(1,2)}, \tag{7.19}$$

where the superscripts (1) and (2) represent the terms from state 1 and state 2 respectively. $I^{(1,2)}$ is the interaction integral between the two states, as

$$I^{(1,2)} = \int_A \Big((\sigma_{ij}^{(1)} u_{j,1}^{(2)} + \sigma_{ij}^{(2)} u_{j,1}^{(1)} - W^{(1,2)}\delta_{1i}) q_{,i} + q\bar{\alpha}_T \sigma_{kk}^{(2)} T_{,1}^{(1)} \Big) \mathrm{d}A, \quad i,j,k \in \{1,2\}, \tag{7.20}$$

and $W^{(1,2)}$ is the interaction strain energy density between the two states, where

$$W^{(1,2)} = \sigma_{ij}^{(1)} \varepsilon_{ij}^{(2)} = \sigma_{ij}^{(2)} \varepsilon_{ij}^{(1)}. \tag{7.21}$$

Considering the relationship between the SIFs and the interaction integral in Equation (3.30), the SIFs for a crack under mixed-mode loading are obtained by applying the specific auxiliary state, as in Section 3.4.3.

7.5 Numerical examples

Four numerical examples are presented in this section to demonstrate the performance of the proposed method. The first is an inclined crack under thermal loading, where mixed-mode fracture is considered. The second example contains a curved crack to test the abilities of the proposed method for cracks with complex geometries. Crack propagation is included in the third example, where the behaviour of a crack in a cruciform shaped plate under mechanical and thermal loadings are compared. The final example is extended from the third with one more crack, which is used to explore the performance of the proposed method for multiple cracks. Unless stated otherwise, all examples are under plane strain assumptions with linear elastic material properties, Young's modulus $E =$ 200GPa, Poisson's ratio $\nu = 0.3$, thermal conductivity $k_T = 100\text{W}/(\text{m}^\circ\text{C})$ and coefficient of thermal expansion $\alpha_T = 10^{-5\circ}\text{C}^{-1}$, all of which are used to normalise the results, and the reference environment temperature is zero. For all examples, a circular influence domain is used for every particle, and the size is $d_s = 2.2$. Rigid body translation and rotation are fixed as in [270] by setting

$$\int_\Omega u_x \mathrm{d}\Omega = 0, \quad \int_\Omega u_y \mathrm{d}\Omega = 0, \quad \int_\Omega \frac{\partial u_x}{\partial y} - \frac{\partial u_y}{\partial x} \mathrm{d}\Omega = 0, \tag{7.22}$$

where u_x and u_y are horizontal and vertical displacements respectively. These boundary conditions are imposed on the weak form by Lagrange multipliers with only three extra unknowns. Temperature and thermal stress gradients are captured by the adaptivity approach developed in Section 3.3, which is purely based on the elasticity equations, and Equation (7.5) is used to take the thermal effect into account.

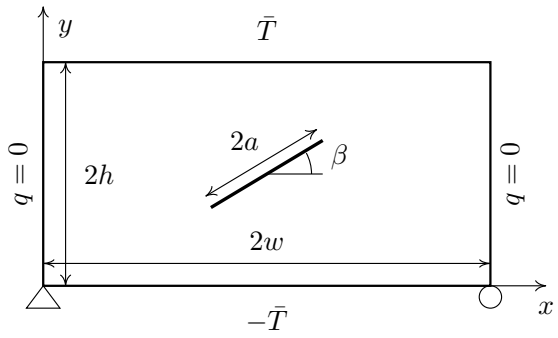

(a)

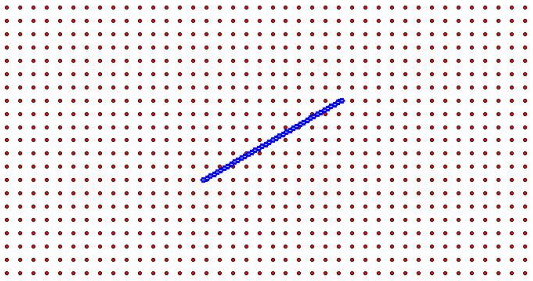

(b)

Figure 7.1: An inclined central crack under thermal loading: (a) configuration; (b) initial particle arrangement, with blue points for cracking particle.

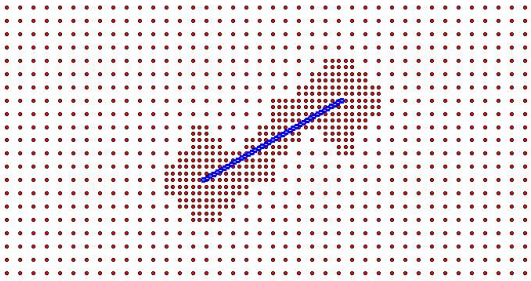

(a)

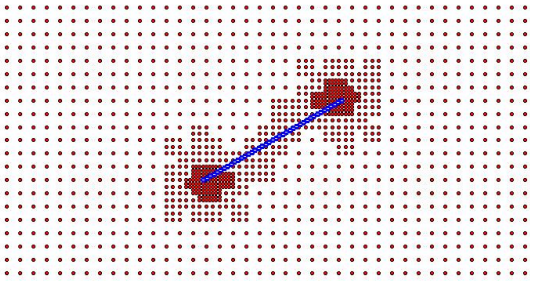

(b)

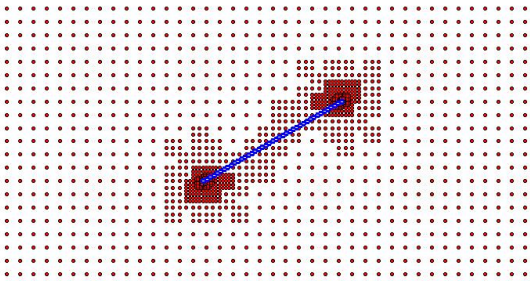

(c)

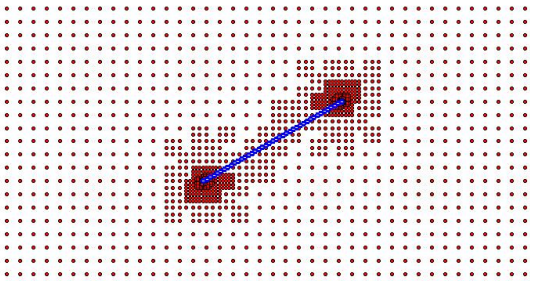

(d)

Figure 7.2: Adaptive particle arrangements for the inclined central crack (in blue, $\beta = 30°$) under thermal loading: (a) step 1; (b) step 2; (c) step 4; (d) step 7.

7.5.1 Inclined central crack

An inclined central crack is considered in a rectangular plate as shown in Figure 7.1. The configuration of this problem consists of $w = 0.1$m, $h = 0.5w$, $a = 0.3w$. The top of the plate is at a high temperature $\bar{T} = 100°$C, while the bottom is loaded by a low temperature $-\bar{T}$. The heat flux at the two sides of the plate is zero. The problem is initially discretised by 21×41 particles with 41 particles in blue along the crack as in Figure 7.1 (b).

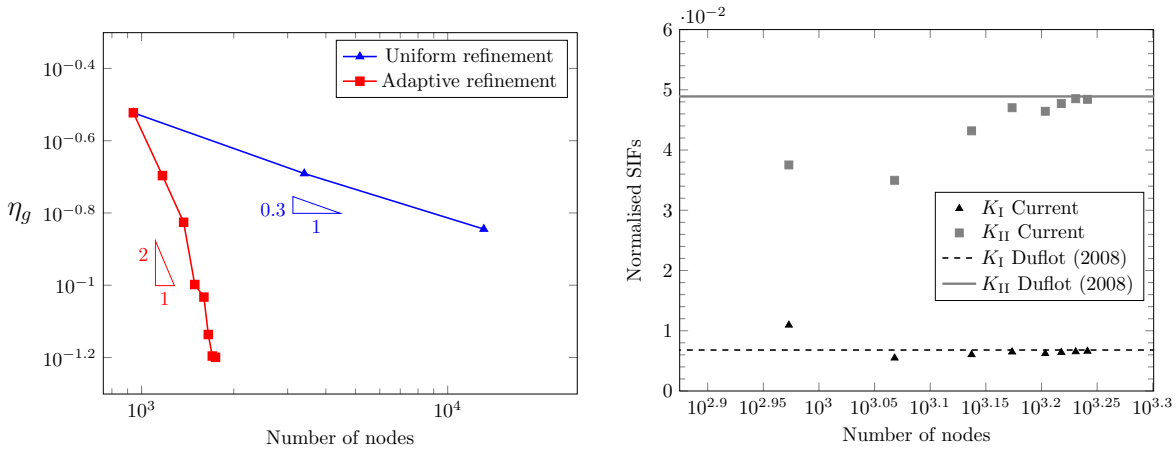

Figure 7.3: Adaptive results for the inclined central crack under thermal loading: (a) convergence rate for error; (b) SIFs.

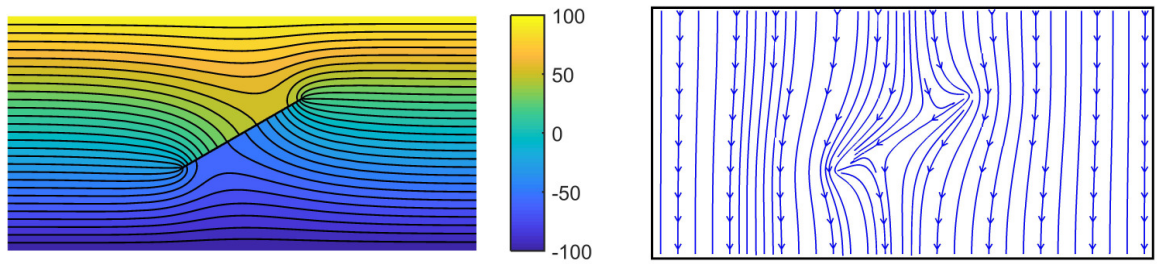

Figure 7.4: Thermal results of the inclined central crack: (a) temperature profile (°C); (b) heat flux.

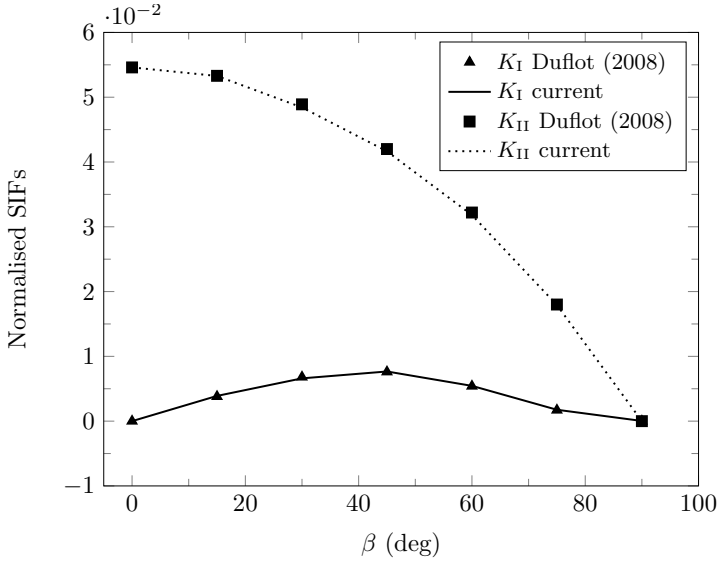

Figure 7.5: Normalised stress intensity factors for various crack inclinations.

Table 7.1: Validation of calculated SIFs for the inclined crack under thermal loading

	CPM		HXFEM [296]		XFEM [288]		BEM [294]	
θ	K'_{I}	K'_{II}	K'_{I}	K'_{II}	K'_{I}	K'_{II}	K'_{I}	K'_{II}
0°	0.00000	0.05532	0.00000	0.05471	0.00000	0.05460	0.00000	0.05400
30°	0.00664	0.04894	0.00670	0.04873	0.00680	0.04890	0.00640	0.04800
60°	0.00561	0.03200	0.00544	0.03209	0.00540	0.03220	0.00490	0.03200

The target error for the adaptivity approach is $\eta_t = 0.06$, and adaptive particle arrangements are given in Figure 7.2, where particle refinement is executed automatically around the two crack tips. Figures 7.3 illustrates the results during the adaptive steps, where it is shown that the convergence rate of error for the adaptivity approach is much higher than that for uniform refinement, and results for the SIFs converge to the reference values during adaptive steps. The SIFs at one crack tip are normalised by

$$K'_n = \frac{K_n}{\alpha_T \bar{T} E} \cdot \frac{h}{w\sqrt{2w}}, \quad n \in \{\mathrm{I}, \mathrm{II}\}. \tag{7.23}$$

and in Table 7.1 are compared with the results from other methods, including the XFEM from Duflot [288], the XFEM with high order enrichment functions (marked as HXFEM) from Zamani et al. [296] and the BEM from Prasad et al. [294]. The proposed method gives results with the same level of accuracy as using enrichment functions, and with adaptivity the maximum number of particles here is 1744 versus 1891 rectangular elements in the HXFEM [296], and 7000 triangular elements in the XFEM [288]. Figures 7.4 (a-b) illustrate the temperature distribution and heat flux in the problem domain. The calculated SIFs for the crack with various inclinations are presented in Figure 7.5 and good agreement with the results from [288] is achieved.

7.5.2 Curved central crack

The second example comprises an arc-shaped crack in a square domain as shown in Figure 7.6, the configuration of which consists of $w = 0.2$m, $2a = 0.1w$, $\beta = \pi/4$. The plate is under a constant and upward heat flux $\bar{q} = 10^4 \mathrm{W/m}^2$, where the bottom of the plate is at high temperature and the top is at low temperature. There is an analytical solution for

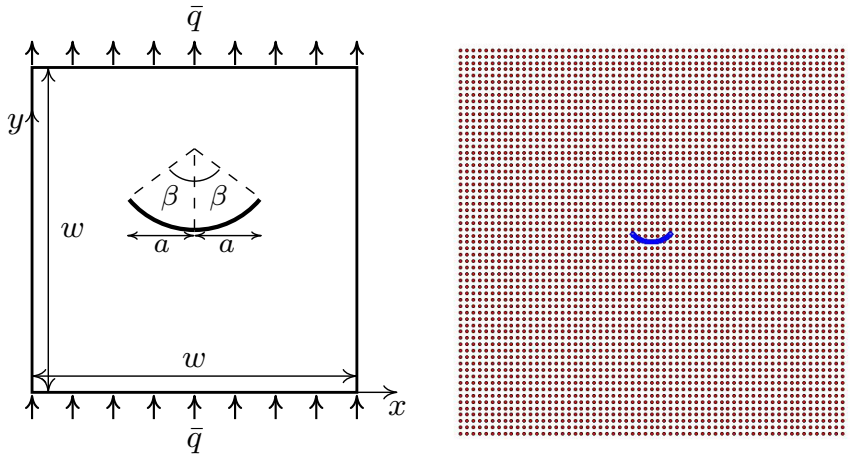

(a) (b)

Figure 7.6: A curved crack under constant heat flux: (a) configuration; (b) initial particle arrangement where cracking particles are in blue.

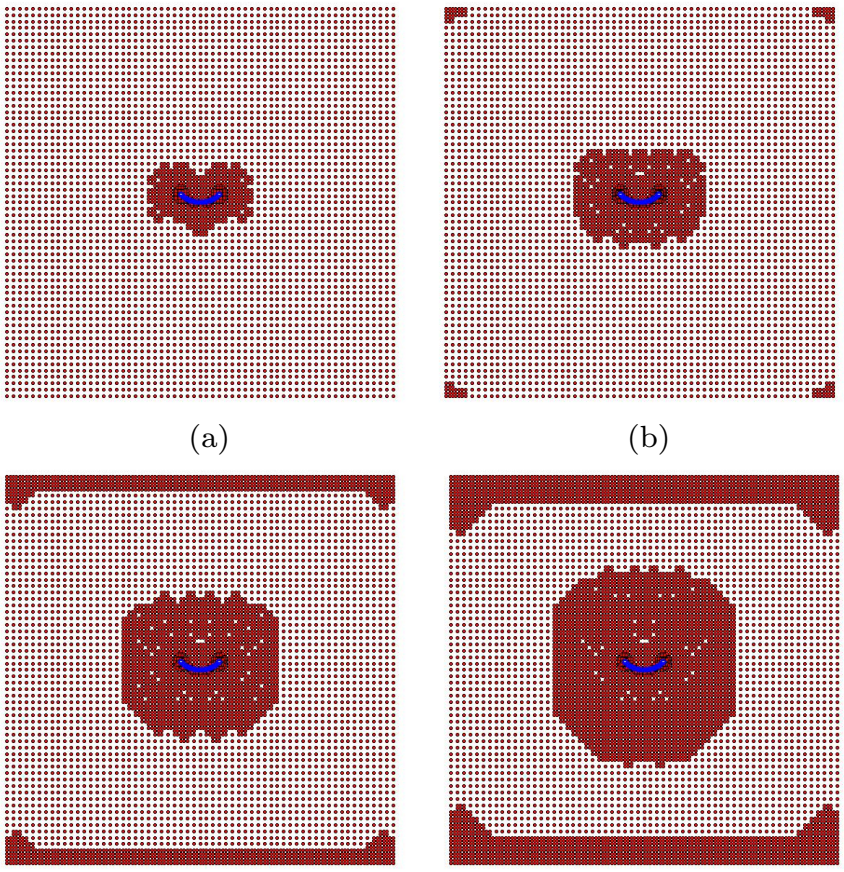

(a) (b)

(c) (d)

Figure 7.7: Adaptive particle arrangements for the curved crack problem: (a) step 2; (b) step 4; (c) step 6; (d) step 8.

Table 7.2: Normalised SIFs for a curved crack under thermal loading

	CPM		HXFEM [296]		Analytical [309]	
θ	K'_{I}	K'_{II}	K'_{I}	K'_{II}	K'_{I}	K'_{II}
30°	0.71745	0.79217	0.73962	0.82085	0.71904	0.80793
45°	0.96103	0.58276	0.97630	0.57770	0.97338	0.59995
60°	1.12586	0.34761	1.13546	0.33238	1.13750	0.35363

this problem from Chen and Hasebe [309] when this problem is considered in an infinite plate, as

$$K_{\mathrm{I}} = \frac{3+\cos\beta}{4}\Big(\sin\frac{\beta}{2} + \frac{4(1-\cos\beta)}{(3-\cos\beta)\cos\beta}\cos\frac{\beta}{2}\Big)\frac{E\alpha\bar{q}}{k_T}a\sqrt{\pi a}, \tag{7.24a}$$

$$K_{\mathrm{II}} = \frac{3+\cos\beta}{4}\Big(\cos\frac{\beta}{2} - \frac{4(1-\cos\beta)}{(3-\cos\beta)\sin\beta}\sin\frac{\beta}{2}\Big)\frac{E\alpha\bar{q}}{k_T}a\sqrt{\pi a}. \tag{7.24b}$$

For the sake of data analysis, the SIFs are normalised as

$$K'_n = \frac{K_n}{\alpha\bar{q}E}\cdot\frac{k_T}{a\sqrt{\pi a}}, \quad n \in \{\mathrm{I},\mathrm{II}\}. \tag{7.25}$$

Since the ratio between the size of the crack and the plate is $2a/w = 1/10$, the boundaries of this finite domain are far from the crack and the analytical solutions are applicable to this problem. The plate is initially discretised with 61×61 particles, from which the adaptivity approach proceeds. The curvature of the crack is modelled by 40 straight segments connecting cracking particles, which are in blue in Figure 7.6 (b).

The adaptivity approach uses a target error of $\eta_t = 0.12$ and adaptive particle distributions are shown in Figure 7.7. The local zone containing the crack is refined and two "masses" of particles are generated around the two crack tips. Particle refinement is also executed at both the top and bottom where the heat flux boundary condition is applied. The results of temperature profile and heat flux distribution are given in Figure 7.8, where it is shown that the crack disturbs the temperature profile at the centre of the plate and the heat flux travels encircling the crack surface. SIFs are calculated and compared with the results from Zamani et al. [296] using the HXFEM in Table 7.2. The same level of accuracy is obtained by the proposed method with 8391 particles compared with more than 10^4 nodes in the HXFEM [296]. For the curved crack with various curvatures, the

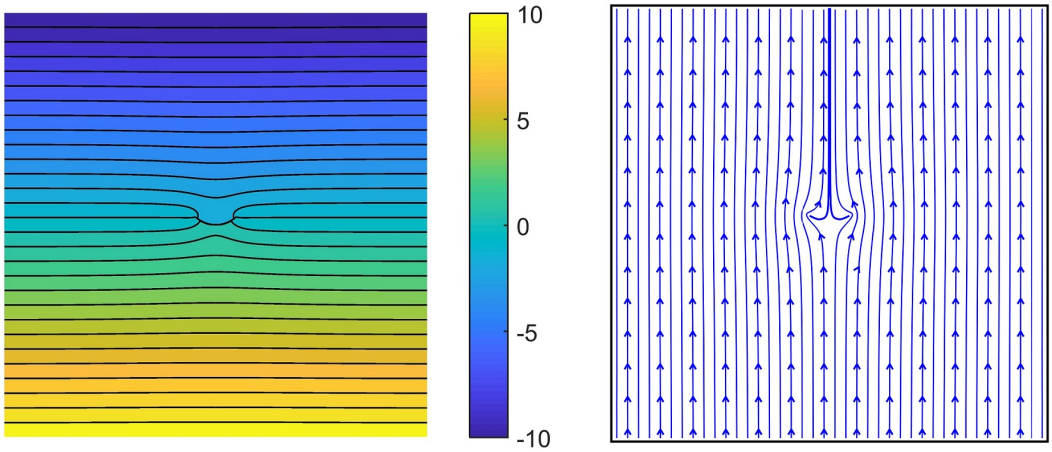

Figure 7.8: Thermal results for the curved crack problem: (a) temperature profile (°C); (b) heat flux.

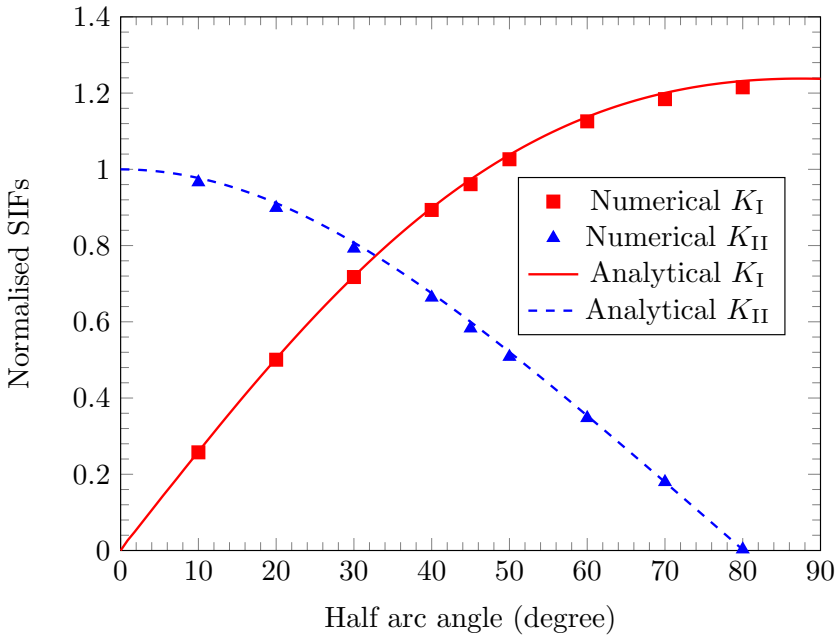

Figure 7.9: Normalised stress intensity factors for the curved crack with various values of the half arc angle.

proposed method delivers accurate SIFs compared to the analytical solution from Equation (7.24), as given in Figure 7.9. It has also been shown that, even with uniformly distributed particles, the proposed method is capable to capture the stress gradients at the crack tip of a curved crack.

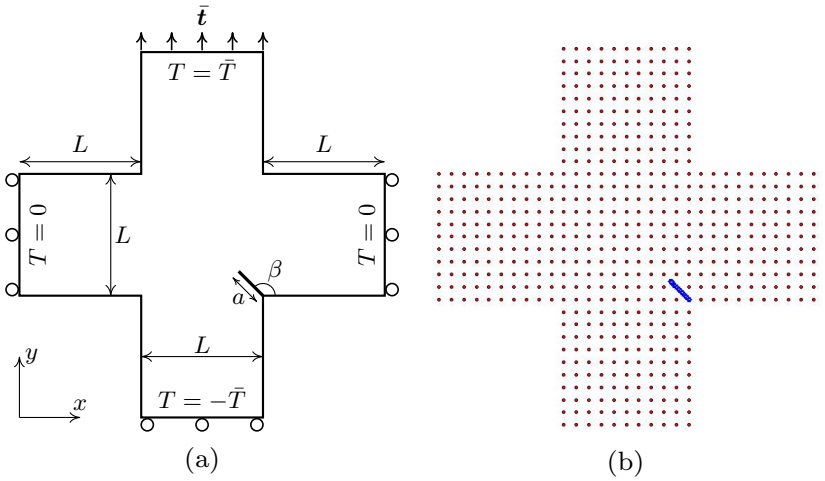

Figure 7.10: A crack in a cruciform shaped plate: (a) configuration; (b) initial particle arrangement (cracking particles are in blue).

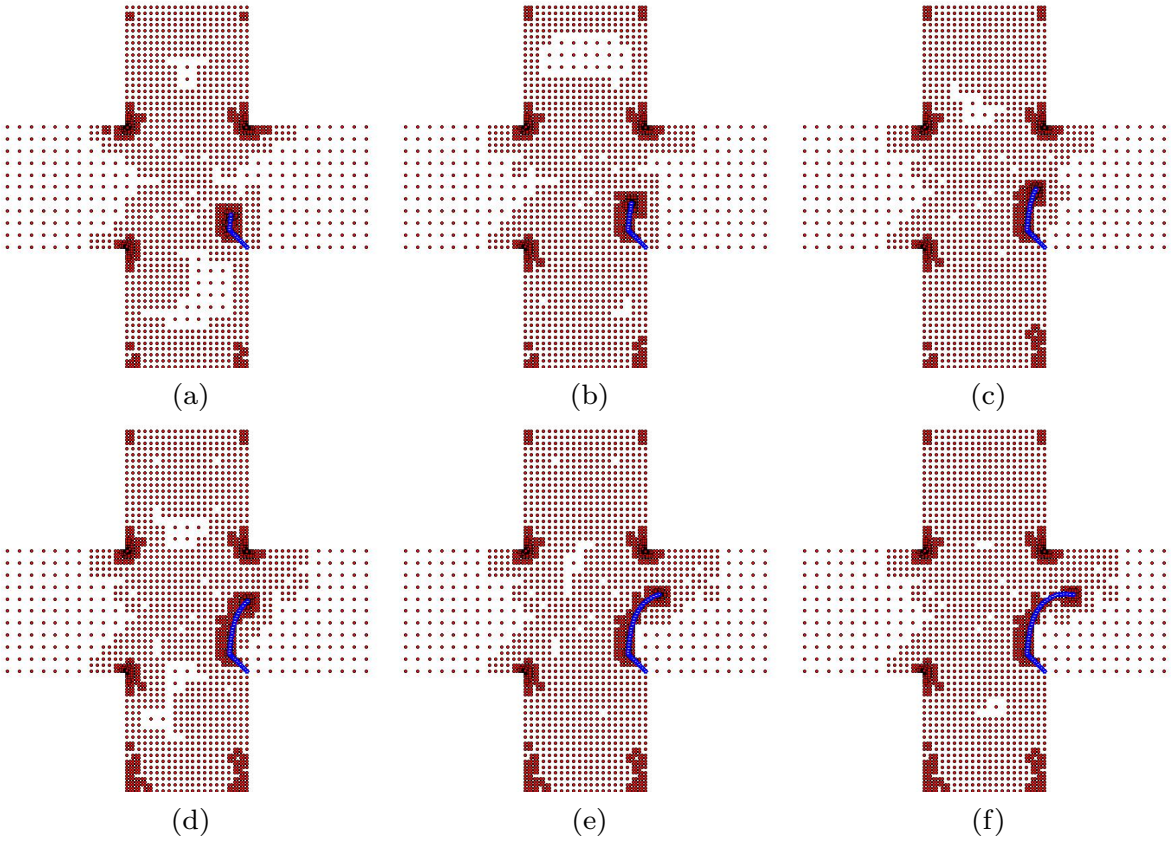

Figure 7.11: Adaptive particle arrangements of crack propagation steps for the cruciform shaped plate problem: (a-f) step=5, 10, 15, 20, 25, 30.

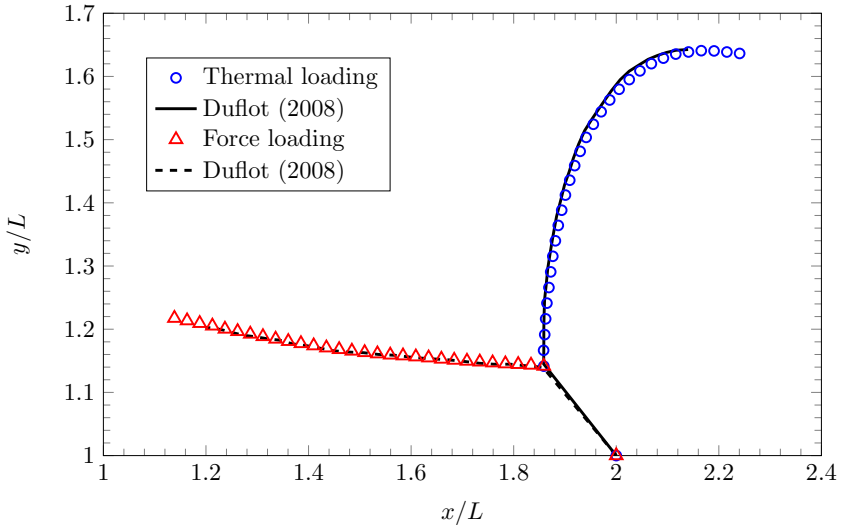

Figure 7.12: Comparison of crack growth in the cruciform shaped plate between under thermal loading and force loading.

7.5.3 Crack propagation in a cruciform shaped plate

Crack propagation under thermal loading is considered in the third example. The crack is located at the bottom-right corner of a cruciform shaped plate as shown in Figure 7.10 and the configuration is comprised of $L = 0.1$m, $a = 0.2L$ and $\beta = 3\pi/4$. The cruciform shaped plate is constrained in displacement at the bottom and both left and right sides. Two loading situations are considered: case 1, thermal loading with $\bar{T} \neq 0$, $\bar{t} = 0$; case 2, mechanical loading with $\bar{T} = 0$, $\bar{t} \neq 0$. The crack propagation direction is determined by the maximum circumferential stress criterion and the crack increment is set as $a/8$.

The adaptivity approach is defined with target error $\eta_t = 0.04$ and starts from the initial particle arrangement shown in Figure 7.10 (b). Adaptive particle arrangements during the crack propagation for case 1 are given in Figure 7.11, where particle distribution is refined at the three corners of the cruciform shaped plate and the crack tip. The crack propagates upward and then turns right after 15 propagation steps. The crack growth predicted by the proposed method is compared with the results from Duflot [288] using the XFEM, where good agreement is found and similar accuracy is obtained for case 2 as shown in Figure 7.12. Comparing the crack growth in the two cases, the crack propagates right under thermal loading while the mechanical loading leads the crack propagation to the left. The SIFs during crack propagation steps in two cases are calculated, which match well with the results from Prasad et al. [310] as shown in Figure 7.13. Thermal

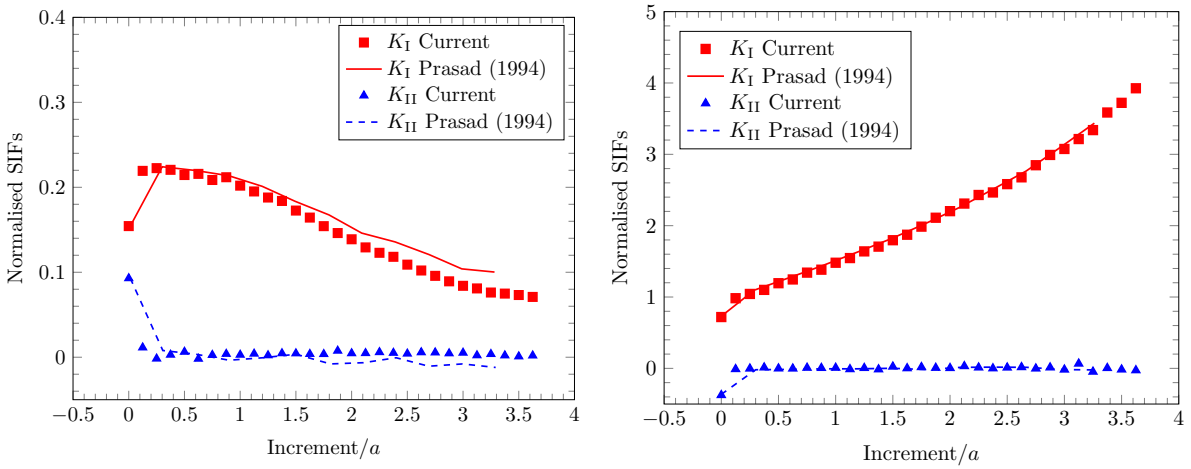

(a) (b)

Figure 7.13: normalised SIFs during crack propagation for the cruciform shaped plate problem: (a) thermal loading; (b) force loading.

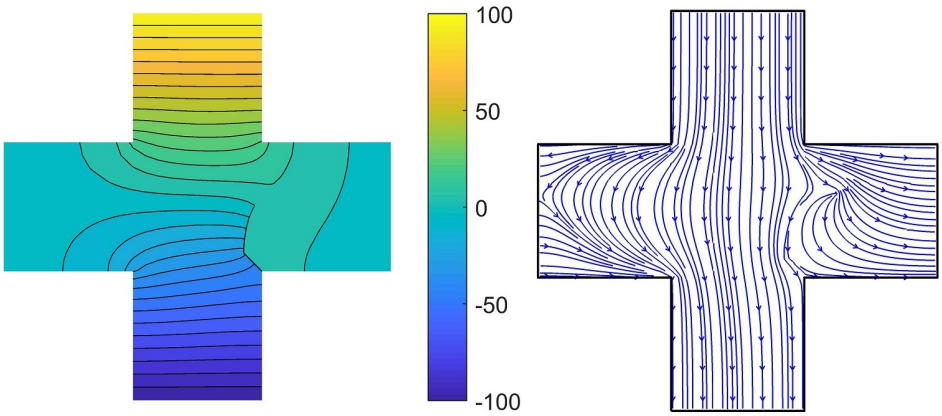

(a) (b)

Figure 7.14: Thermal results for the final crack propagation step in the cruciform shaped plate: (a) temperature profile (°C); (b) heat flux.

results including temperature profile and heat flux for the final crack propagation step are given in Figure 7.14.

7.5.4 Two cracks in a cruciform shaped plate

The fourth example comes from the third problem with one extra crack in consideration as shown in Figure 7.15, and other aspects including displacement boundary conditions and material properties are not changed. There are also two loading conditions involved, which are thermal loading and mechanical loading, and the difference is in case 1 where the top and bottom sides of the plate are loaded by a low temperature $\bar{T}$.

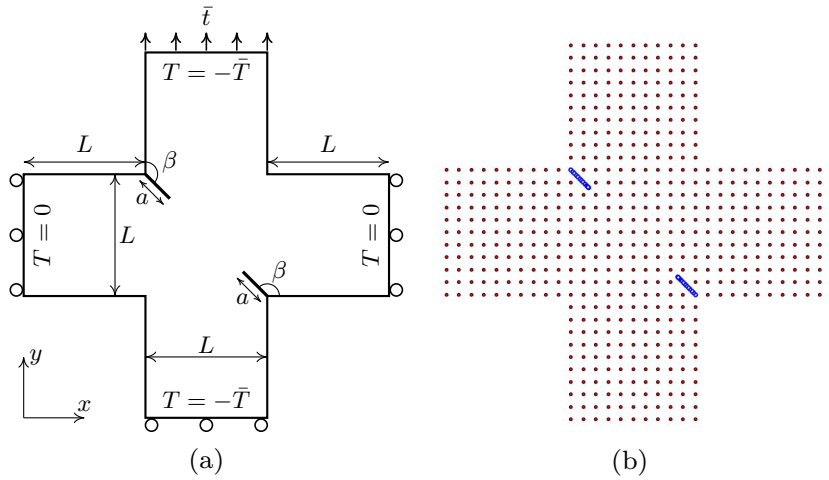

Figure 7.15: Two cracks in a cruciform shaped plate: (a) configuration; (b) initial particle arrangement.

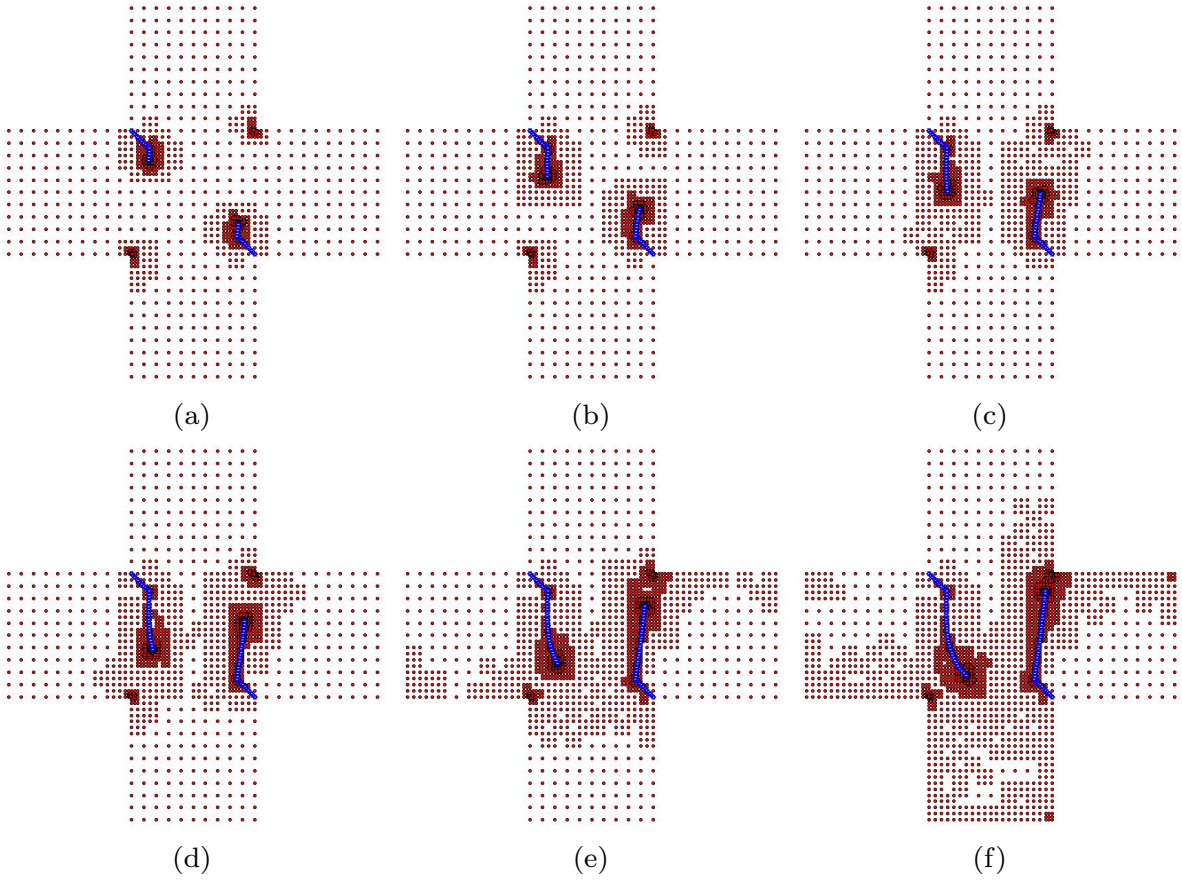

Figure 7.16: Adaptive particle arrangements for the two cracks in a cruciform shaped plate: (a-f) step=5, 10, 15, 20, 25, 30.

Adaptive particle distributions for the propagation of two cracks in case 1 are given in Figure 7.16, where again there are two "masses" of particles generated around the two

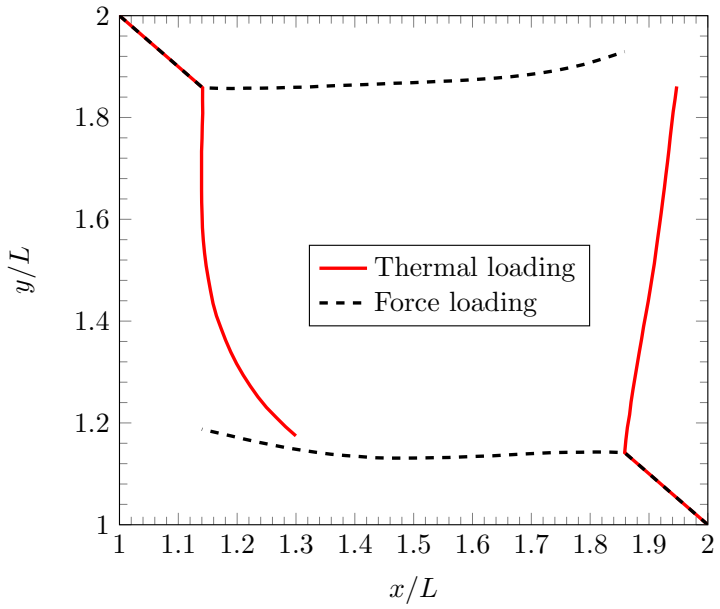

Figure 7.17: Propagation of two cracks in the cruciform shaped plate under thermal loading and force loading.

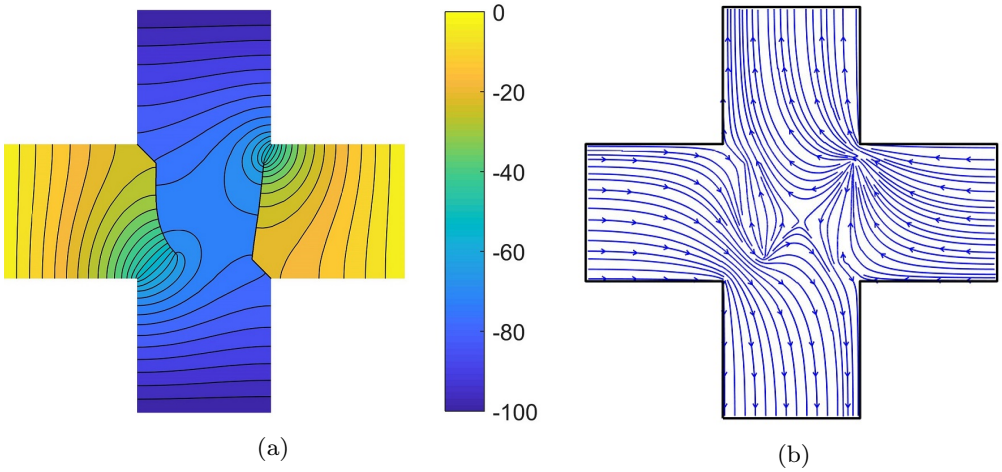

Figure 7.18: Thermal results at the final propagation step for two cracks in the cruciform shaped plate: (a) temperature profile (°C); (b) heat flux.

crack tips which travel with the two crack tips during the crack propagation process. The crack on the right propagates straight upwards towards the upper-right corner, while the left crack descends and turns right after 20 propagation steps. The crack growths for both cases are given in Figure 7.17, where it is shown that the two cracks propagate vertically under the thermal loading here while the mechanical loading leads to horizontal crack propagation. The temperature profile and heat flux at the final propagation step for the two cracks are presented in Figure 7.18, where it is shown there is of great influence from

the two cracks on both temperature distribution and heat flux direction. No analytical solution has been found yet and this example is used here to test the ability of the proposed methodology for modelling multiple crack propagation.

7.6 Summary

An adaptive CPM for modelling thermo-elastic fracture in 2D has been developed in this chapter, where enrichment functions, which have been widely used in traditional numerical methods including the XFEM and the EFGM, are not required. The discontinuities of temperature and displacement at a crack are modelled by the CPM using the visibility criterion, and stress gradients are captured using a high density of particles around the crack tip, which is controlled by an adaptivity approach. The mixed-mode stress intensity factors under thermal loadings are calculated by the interaction integral and the proposed method can provide results of accuracy at the same level as the XFEM with high order enrichments and uses much fewer particles than the number in the standard XFEM. The proposed methodology has shown its potential to handle the crack propagation of multiple cracks under thermal loading.

Chapter 8

Conclusions and future directions

8.1 Main conclusions

Computational fracture modelling is of great importance in the study of material failure and lifespan analysis of engineering structures. The difficulties of this topic exist in modelling crack discontinuities, high stress gradients around the crack tip and non-linear behaviour of crack propagation, all of which challenge the traditional element-based numerical methods via issues of remeshing, mesh distortion and volumetric locking. This thesis considerably develops a meshless method to arrive at a framework for modelling cracks and crack propagation in 2D and 3D. In the first two chapters, the development, classification and features of meshless methods are demonstrated, and since in meshless methods only node data are required in the problem discretisation, the issues mentioned above in element-based methods can be avoided. Due to the use of high order continuous shape functions, meshless methods show better accuracy of stress predictions than the standard FEM. Several numerical methods have been developed for crack modelling, and crack discontinuities are modelled by either enrichment functions or modifying the influence domain of nodes using the visibility criterion (for meshless methods). However, enrichment functions bring extra unknowns which can lead to an ill-conditioned global stiffness matrix. For both approaches mentioned above, a method to describe crack paths is required, for instance by level sets, but updating level set functions is computationally time-consuming. The methods using enrichments or level sets meet dilemmas when used for multiple cracks, since each crack requires a set of enrichments or level sets and com-

putational cost then balloons with the number of cracks. The cracking particle method (CPM) uses a set of crack segments to approximate crack paths, which has a simple implementation and is therefore suitable for modelling multiple cracks. This simplification in crack description however also brings issues of spurious cracking results and a large number of particles are required to get accurate results. It is here that this thesis starts. The main achievements in this thesis are as follows:

- A modified CPM using bilinear discontinuous segments has been developed for describing crack patterns and influence domains of cracking particles are modified to sector shapes which record the angular change of crack path. Crack segments are aligned well to provide a smooth crack path and the issue of spurious cracking results in the original CPM is addressed.

- An adaptivity approach has been introduced into the CPM, by which particle distribution density is adjusted to capture the stress gradients around a crack tip. A coarsening scheme is included in the adaptivity approach to reduce particle distribution density when the crack tip propagates away for improving calculation efficiency.

- A multi-cracked particle method has been proposed to model branched cracks. A crack with a complex geometry or multiple cracks can be approximated by a set of discontinuous segments, and crack discontinuities are achieved by the visibility criterion rather than using complex enrichment functions.

- Different crack propagation criteria are discussed, and a configurational-force-driven CPM has been presented for modelling crack propagation. Crack propagation direction is directly determined by the configurational force, where there is no need to decompose the displacement and stress fields with respect to the crack surface for mixed-mode crack problems.

- A framework for explicitly describing 3D crack surfaces and crack propagation has been developed using the CPM. A set of triangular facets connecting cracking particles is used to represent crack surfaces, and spherical influence domains of particles are divided by nonplanar crack segments, which provide continuous crack surface approximation and again prevent spurious cracking results.

- The adaptive CPM has been applied to crack problems under thermal loadings without using enrichment functions. Temperature discontinuities at cracks are modelled by the CPM, and temperature gradients are handled by the adaptivity approach. This method can provide results with the same level of accuracy with the standard XFEM using enrichments and less number of particle is needed.

8.2 Future directions

The research work in this thesis can be extended to the following directions:

- A fast integration technique is desired for assembling the global stiffness matrices, since this integration process spends the most calculation time in meshless methods. Gaussian quadrature is currently performed over background cells which makes the proposed method not truly meshfree, although there is no need for the background integration grid to conform to domain boundaries. Alternatives are nodal integration [113, 114] or integration over supports [115, 222].

- The collocation methods [99, 106] could also be considered, where the strong form of governing equations are solved directly and no integration process is required. The main concern for collocation methods is the requirement of calculating second-order derivatives of shape functions and the accuracy of results.

- Efficient calculation of shape functions is in demand for meshless methods. Unlike the standard FEM which uses explicit and simple shape functions, meshless methods make use of the MLS or the RK approximation to build shape functions with matrix inversion involved (albeit of small matrices). It has been shown that explicit matrix inversion expressions [117, 118] can be used to speed up the calculation of shape functions. The advantages of other methods, including the natural neighbour radial point interpolation method [311] or the virtual element method [312] could be investigated for the problem approximation.

- How to define the optimized support size is problem-dependent and requires further study to make it applicable for various materials and problems. It has been shown in [125] that support size affects the accuracy of displacements and their derivatives, where the former requires a smaller support but the latter is more accurate with

a larger support. A technique has been developed by Rosolen et al. [313] to provide optimum support size by introducing support size into the maximum entropy approximation [314].

- The proposed method in this thesis uses a quasi-static code and could be extended to model problems of dynamic fracture. Early applications of the CPM to model dynamic fracture can be found in [202, 209, 315], and it would be interesting to see the performance of the modified CPM proposed in this thesis for crack problems under dynamic loadings.

- Cohesive zone model could also introduced into the proposed method, since crack opening is obtained easily by the relative displacement of cracking particles on the two sides of crack surfaces. Different traction-displacement curves in [133, 134, 136] could be considered for modelling crack growth and the crack closure effect could be studied as in [316].

- Crack initiation, junction and coalescence are features of fracture in real engineering problems and nature but still challenge current numerical methods because they bring severe topology changes. These issues have been approached using extrinsic enrichment functions in the XFEM [155] and the EFGM [207], but complex enrichment functions are used which brings difficulties in modelling multiple cracks. The proposed method in this thesis makes use of intrinsic enrichment to model crack discontinuities rather than using complex enrichment functions and is suitable for modelling crack coalescence. Crack initiation is difficult to model in the XFEM when the crack initiation is inside one element, but this is not an issue in meshless methods and it follows the loss of hyperbolicity criterion [317].

- Parallel computing could be used to accelerate the meshless simulations although the focus in this thesis has been on accuracy rather than efficiency. It divides the computation of large problems into small parts and solves them at the same time, which therefore makes use of the full power of high-performance computer clusters. This technique has been widely used in the FEM [318], but its application to meshless methods is limited, one example can be found in Ullah et al. [319].

- Shape functions in the current CPM are obtained by the MLS approximation, which do not possess the Kronecker delta property. Therefore, Lagrange multipliers are required to impose essential boundary conditions into the weak form of governing equations, which can lead to an ill-conditioned system stiffness matrix, as mentioned in Section 2.6.1. This issue can be addressed by using the maximum entropy approach [314, 320, 321], which provides weak Kronecker delta property at boundaries, so essential boundary conditions can be imposed directly.

- There are sharp corners at the joints of crack segments in the current CPM, which can lead to artificial stress concentrations. Methods to improve the smoothness of the crack path are needed, and one possible solution is through spline functions for describing crack geometries borrowing ideas from the IGA [32, 322].

Appendix A

Implementation of the moving least squares approximation

A function for calculating shape functions in the EFGM by the MLS approximation is included here for 2D problems, which is implemented in MATLAB. The implementation of the EFGM can also be found in [55].

```
function [phi,dphix,dphiy]=MLS_SF(gpos,v)
% Input: gpos - location of node;
%        v - the list of nodes with support covering gpos
% Output: phi - shape functions;
%        dphix, dphiy - first derivatives of shape functions
% Global variables: x - coordinates of all nodes
%        support - support sizes of all nodes
global x support;
L=length(v);
phi=zeros(1,L); dphix=phi; dphiy=phi;
r=zeros(1,L); drdx=r;
p=[ones(1,L);x(v,1:2)'];
r=realsqrt( (x(v,1)'-gpos(1)).^2+(x(v,2)'-gpos(2)).^2 )./support(1,v);
% weight function using the 4th order spline
w=zeros(1,L); dwdr=w;
w=1-6*r.^2+8*r.^3-3*r.^4;
```

```
b=[w;w;w].*p;
aa=([w;w;w].*p)*p';
pg=[1.0d0;gpos(1);gpos(2)];
phi=pg'/aa*b;

% derivatives of shape functions
drdx=(gpos(1)-x(v,1)')./r./support(1,v)./support(1,v);
drdy=(gpos(2)-x(v,2)')./r./support(1,v)./support(1,v);
dwdr=-12*r+24*r.^2-12*r.^3;
dwdx=dwdr.*drdx;
dwdy=dwdr.*drdy;
daax=([dwdx;dwdx;dwdx].*p)*p';
daay=([dwdy;dwdy;dwdy].*p)*p';
dbx=[dwdx;dwdx;dwdx].*p;
dby=[dwdy;dwdy;dwdy].*p;
gama=pg'/aa;
dgamax=[0,1,0]/aa-gama*daax/aa;
dgamay=[0,0,1]/aa-gama*daay/aa;
dphix=dgamax*b+gama*dbx;
dphiy=dgamay*b+gama*dby;
```

Appendix B

Path independence of J-integral

Here a proof for path independence of the J-integral is presented. The J-integral in Equation (3.22) is rewritten as

$$J = \int_{\Gamma} (W\delta_{1j} - \sigma_{jk}\frac{\partial u_k}{\partial x_1})n_j \mathrm{d}\Gamma, \quad j,k \in \{1,2\} \tag{B.1}$$

Using Green's theorem (the 2D divergence theorem), the J-integral becomes

$$J = \int_A \frac{\partial}{x_j}(W\delta_{1j} - \sigma_{jk}\frac{\partial u_k}{\partial x_1})\mathrm{d}A = \int_A (\frac{\partial W}{x_1} - \frac{\partial \sigma_{jk}}{\partial x_j}\frac{\partial u_k}{\partial x_1} - \sigma_{jk}\frac{\partial^2 u_k}{\partial x_1 \partial x_j})\mathrm{d}A, \tag{B.2}$$

where A is the domain surrounded by the contour Γ. Considering the stress equilibrium equation in Equation (2.17) with no body force, i.e. $\partial\sigma_{jk}/\partial x_j = 0$ and the compatibility condition in Equation (2.31), we have

$$\sigma_{jk}\frac{\partial \varepsilon_{jk}}{\partial x_1} = \frac{1}{2}(\sigma_{jk}\frac{\partial^2 u_k}{\partial x_1 \partial x_j} + \sigma_{jk}\frac{\partial^2 u_j}{\partial x_1 \partial x_k}). \tag{B.3}$$

The balance of angular momentum yields $\sigma_{jk} = \sigma_{kj}$, then

$$\sigma_{jk}\frac{\partial \varepsilon_{jk}}{\partial x_1} = \frac{1}{2}(\sigma_{jk}\frac{\partial^2 u_k}{\partial x_1 \partial x_j} + \sigma_{kj}\frac{\partial^2 u_j}{\partial x_1 \partial x_k}) = \sigma_{jk}\frac{\partial^2 u_k}{\partial x_1 \partial x_j}. \tag{B.4}$$

Hence, the J-integral becomes

$$J = \int_A (\frac{\partial W}{\partial x_1} - \sigma_{jk}\frac{\partial \varepsilon_{jk}}{\partial x_1})\mathrm{d}A. \tag{B.5}$$

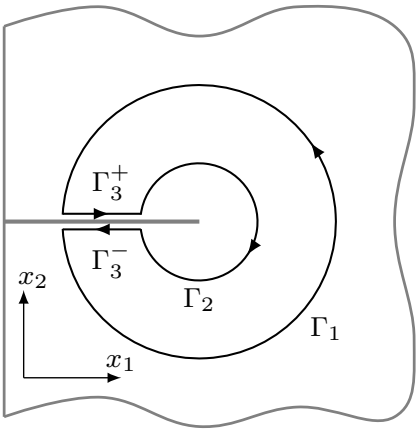

Figure B.1: Integration paths around a crack in 2D.

Using the chain rule of differentiation and considering the relationship between stress and stored energy function, we have

$$\sigma_{jk}\frac{\partial \varepsilon_{jk}}{\partial x_1} = \frac{\partial W}{\partial \varepsilon_{jk}}\frac{\partial \varepsilon_{jk}}{\partial x_1} = \frac{\partial W}{\partial x_1}. \tag{B.6}$$

Substituting Equation (B.6) to Equation (B.5), it is concluded that $J = 0$ for an arbitrary contour enclosing a simply connected domain. Considering a contour $\Gamma = \Gamma_1 + \Gamma_2 + \Gamma_3^+ + \Gamma_3^-$, which encloses a simply connected region, as given in Figure B.1, the J-integral over this contour is zero, hence

$$J = \int_{\Gamma_1+\Gamma_2+\Gamma_3^+ +\Gamma_3^-} (W\delta_{1j} - \sigma_{jk}\frac{\partial u_k}{\partial x_1})n_j \mathrm{d}\Gamma = 0. \tag{B.7}$$

Since the paths of Γ_3^+ and Γ_3^- are parallel to the x_1 axis, one component of the normal to these crack surfaces is $n_1 = 0$. These crack surfaces are assumed traction free, i.e. $\sigma_{jk}n_j = 0$, therefore

$$\int_{\Gamma_1+\Gamma_2} (W\delta_{1j} - \sigma_{jk}\frac{\partial u_k}{\partial x_1})n_j \mathrm{d}\Gamma = -\int_{\Gamma_3^- +\Gamma_3^+} (Wn_1 - \sigma_{jk}\frac{\partial u_k}{\partial x_1})n_j \mathrm{d}\Gamma = 0. \tag{B.8}$$

If the integration over a counter-clockwise path is defined with a positive sign, we have

$$\int_{\Gamma_1} (W\delta_{1j} - \sigma_{jk}\frac{\partial u_k}{\partial x_1})n_j \mathrm{d}\Gamma = \int_{-\Gamma_2} (W\delta_{1j} - \sigma_{jk}\frac{\partial u_k}{\partial x_1})n_j \mathrm{d}\Gamma. \tag{B.9}$$

Finally, it is proven that the J-integral is path-independent.

Appendix C

Auxiliary field in the interaction integral

The interaction integral, which is the superimposition of the real state and the auxiliary state, provides a general method to compute mixed mode SIFs through a domain integral. The auxiliary stresses field in 3D are

$$\begin{cases} \sigma_{11}^{\text{aux}} = \frac{1}{\sqrt{2\pi r}}\Big[K_{\text{I}}^{\text{aux}} \cos\frac{\theta}{2}(1 - \sin\frac{\theta}{2}\sin\frac{3\theta}{2}) - K_{\text{II}}^{\text{aux}} \sin\frac{\theta}{2}(2 + \cos\frac{\theta}{2}\cos\frac{3\theta}{2})\Big], \\ \sigma_{22}^{\text{aux}} = \frac{1}{\sqrt{2\pi r}}\Big[K_{\text{I}}^{\text{aux}} \cos\frac{\theta}{2}(1 + \sin\frac{\theta}{2}\sin\frac{3\theta}{2}) + K_{\text{II}}^{\text{aux}} \sin\frac{\theta}{2}\cos\frac{\theta}{2}\cos\frac{3\theta}{2}\Big], \\ \sigma_{12}^{\text{aux}} = \frac{1}{\sqrt{2\pi r}}\Big[K_{\text{I}}^{\text{aux}} \sin\frac{\theta}{2}\cos\frac{\theta}{2}\cos\frac{3\theta}{2} + K_{\text{II}}^{\text{aux}} \cos\frac{\theta}{2}(1 - \sin\frac{\theta}{2}\sin\frac{3\theta}{2})\Big], \\ \sigma_{23}^{\text{aux}} = \frac{K_{\text{III}}^{\text{aux}}}{2\pi r}\cos\frac{\theta}{2}, \\ \sigma_{13}^{\text{aux}} = -\frac{K_{\text{III}}^{\text{aux}}}{2\pi r}\sin\frac{\theta}{2}, \\ \sigma_{33}^{\text{aux}} = \nu(\sigma_{11}^{\text{aux}} + \sigma_{22}^{\text{aux}}), \end{cases} \tag{C.1}$$

where r is the distance to the crack front point, θ is the angle to the local x_1 axis as in Figure 3.8, and the associated auxiliary displacements are

$$\begin{cases} u_1^{\text{aux}} = \frac{1}{2\mu}\sqrt{\frac{r}{2\pi}}\Big[K_{\text{I}}^{\text{aux}} \cos\frac{\theta}{2}(\kappa - 1 + 2\sin^2\frac{\theta}{2}) + K_{\text{II}}^{\text{aux}} \sin\frac{\theta}{2}(\kappa + 1 + 2\cos^2\frac{\theta}{2})\Big], \\ u_2^{\text{aux}} = \frac{1}{2\mu}\sqrt{\frac{r}{2\pi}}\Big[K_{\text{I}}^{\text{aux}} \sin\frac{\theta}{2}(\kappa + 1 - 2\cos^2\frac{\theta}{2}) - K_{\text{II}}^{\text{aux}} \cos\frac{\theta}{2}(\kappa - 1 - 2sin^2\frac{\theta}{2})\Big], \\ u_3^{\text{aux}} = \frac{1}{\mu}\sqrt{\frac{r}{2\pi}}K_{\text{III}}^{\text{aux}} \sin\frac{\theta}{2}, \end{cases} \tag{C.2}$$

where μ is the shear modulus and κ is a material constant, as

$$\kappa = \begin{cases} 3 - 4\nu & \text{plane strain,} \\ (3-\nu)/(1+\nu) & \text{plane stress.} \end{cases} \tag{C.3}$$

The auxiliary strains are

$$\begin{cases} \varepsilon_{11}^{\text{aux}} = \frac{\partial u_1^{\text{aux}}}{\partial x_1}, \quad \varepsilon_{22}^{\text{aux}} = \frac{\partial u_2^{\text{aux}}}{\partial x_2}, \quad \varepsilon_{12}^{\text{aux}} = \frac{1}{2}(\frac{\partial u_2^{\text{aux}}}{\partial x_1} + \frac{\partial u_1^{\text{aux}}}{\partial x_2}), \\ \varepsilon_{13}^{\text{aux}} = \frac{1}{2}\frac{\partial u_3^{\text{aux}}}{\partial x_1}, \quad \varepsilon_{23}^{\text{aux}} = \frac{1}{2}\frac{\partial u_3^{\text{aux}}}{\partial x_2}, \quad \varepsilon_{33}^{\text{aux}} = 0. \end{cases} \tag{C.4}$$

For 2D cases, the auxiliary field can be obtained by the equations above but setting all items regarding to the x_3 direction to zero, i.e.

$$\begin{cases} \sigma_{23}^{\text{aux}} = \sigma_{23}^{\text{aux}} = \sigma_{23}^{\text{aux}} = 0, \quad u_3^{\text{aux}} = 0, \\ \varepsilon_{23}^{\text{aux}} = \varepsilon_{23}^{\text{aux}} = \varepsilon_{23}^{\text{aux}} = 0. \end{cases} \tag{C.5}$$

Bibliography

[1] Bathe KJ. *Finite Element Procedures*. Prenticle Hall, New Jersey 07458, 1996.

[2] Belytschko T, Lu Y, Gu L. Element-free Galerkin methods. *International Journal for Numerical Methods in Engineering* 1994; **37**(2):229–256.

[3] Belytschko T, Krongauz Y, Organ D, Fleming M, Krysl P. Meshless methods: an overview and recent developments. *Computer Methods in Applied Mechanics and Engineering* 1996; **139**(1):3–47.

[4] Nguyen VP, Rabczuk T, Bordas S, Duflot M. Meshless methods: a review and computer implementation aspects. *Mathematics and Computers in Simulation* 2008; **79**(3):763–813.

[5] Chen JS, Hillman M, Chi S. Meshfree methods: Progress made after 20 years. *Journal of Engineering Mechanics* 2017; **143**(4):04017 001.

[6] Stolarski T, Nakasone Y, Yoshimoto S. *Engineering analysis with ANSYS software*. Butterworth-Heinemann, 2011.

[7] Hibbitt, Karlsson, Sorensen. *ABAQUS/standard 6.2 User's Manual*. Pawtucket, USA, 1996.

[8] Hallquist JO. LS-DYNA theory manual. *Livermore software technology corporation* 2006; **3**:25–31.

[9] Hrennikoff A. Solution of problems of elasticity by the framework method. *Journal of Applied Mechanics* 1941; **8**(4):169–175.

[10] Courant R. Variational methods for the solution of problems of equilibrium and vibrations. *Bulletin of the American Mathematical Society* 1943; **49**(1):1–23.

[11] Turner M. Stiffness and deflection analysis of complex structures. *Journal of the Aeronautical Sciences* 1956; **23**:805–823.

[12] Melosh RJ. A stiffness matrix for the analysis of thin plates in bending. *Journal of the Aeronautical Sciences* 1961; **28**(1):34–42.

[13] Grafton PE, Strome DR. Analysis of axisymmetrical shells by the direct stiffness method. *AIAA Journal* 1963; **1**(10):2342–2347.

[14] Melosh RJ. Structural analysis of solids. *Journal of the Structural Division* 1963; **89**(4):205–248.

[15] Clough RW. The finite element method in plane stress analysis. *Proceedings, American Society of Civil Engineers, 2nd Conference on Electronic Computation, Pittsburgh, PA* 1960; :345378.

[16] Zienkiewicz O, Huang M, Pastor M. Localization problems in plasticity using finite elements with adaptive remeshing. *International Journal for Numerical and Analytical Methods in Geomechanics* 1995; **19**(2):127–148.

[17] Golla DF, Hughes P. Dynamics of viscoelastic structuresa time-domain, finite element formulation.

Journal of Applied Mechanics 1985; **52**(4):897–906.

[18] Huiskes R, Chao E. A survey of finite element analysis in orthopedic biomechanics: the first decade. *Journal of Biomechanics* 1983; **16**(6):385–409.

[19] Remacle JF, Geuzaine C, Compère G, Marchandise E. High-quality surface remeshing using harmonic maps. *International Journal for Numerical Methods in Engineering* 2010; **83**(4):403–425.

[20] Maligno A, Rajaratnam S, Leen S, Williams E. A three-dimensional (3D) numerical study of fatigue crack growth using remeshing techniques. *Engineering Fracture Mechanics* 2010; **77**(1):94–111.

[21] Wrobel L, Aliabadi M. The boundary element methods in engineering. *McGrawHill College* 2002; .

[22] Jaswon M. Integral equation methods in potential theory. I. *Proceedings of the Royal Society of London A: Mathematical, Physical and Engineering Sciences*, vol. 275, The Royal Society, 1963; 23–32.

[23] Cruse TA. Application of the boundary-integral equation method to three dimensional stress analysis. *Computers & Structures* 1973; **3**(3):509–527.

[24] Lachat J, Watson J. Effective numerical treatment of boundary integral equations: A formulation for three-dimensional elastostatics. *International Journal for Numerical Methods in Engineering* 1976; **10**(5):991–1005.

[25] Tan C, Fenner R. Elastic fracture mechanics analysis by the boundary integral equation method. *Proceedings of the Royal Society of London A: Mathematical, Physical and Engineering Sciences*, vol. 369, The Royal Society, 1979; 243–260.

[26] Mi Y, Aliabadi M. Dual boundary element method for three-dimensional fracture mechanics analysis. *Engineering Analysis with Boundary Elements* 1992; **10**(2):161–171.

[27] Alatawi I, Trevelyan J. A direct evaluation of stress intensity factors using the extended dual boundary element method. *Engineering Analysis with Boundary Elements* 2015; **52**:56–63.

[28] Liu Y, Rizzo F. A weakly singular form of the hypersingular boundary integral equation applied to 3-D acoustic wave problems. *Computer Methods in Applied Mechanics and Engineering* 1992; **96**(2):271–287.

[29] Bluck M, Walker S. Analysis of three-dimensional transient acoustic wave propagation using the boundary integral equation method. *International Journal for Numerical Methods in Engineering* 1996; **39**(8):1419–1431.

[30] Rizzo F, Shippy D. An advanced boundary integral equation method for three-dimensional thermoelasticity. *International Journal for Numerical Methods in Engineering* 1977; **11**(11):1753–1768.

[31] Czygan O, Von Estorff O. Fluid-structure interaction by coupling BEM and nonlinear FEM. *Engineering Analysis with Boundary Elements* 2002; **26**(9):773–779.

[32] Hughes TJ, Cottrell JA, Bazilevs Y. Isogeometric analysis: CAD, finite elements, NURBS, exact geometry and mesh refinement. *Computer Methods in Applied Mechanics and Engineering* 2005; **194**(39):4135–4195.

[33] Verhoosel CV, Scott MA, Hughes TJ, De Borst R. An isogeometric analysis approach to gradient

damage models. *International Journal for Numerical Methods in Engineering* 2011; **86**(1):115–134.

[34] Bazilevs Y, Calo V, Zhang Y, Hughes TJ. Isogeometric fluid–structure interaction analysis with applications to arterial blood flow. *Computational Mechanics* 2006; **38**(4-5):310–322.

[35] Temizer I, Wriggers P, Hughes T. Contact treatment in isogeometric analysis with NURBS. *Computer Methods in Applied Mechanics and Engineering* 2011; **200**(9):1100–1112.

[36] Kim HJ, Seo YD, Youn SK. Isogeometric analysis for trimmed CAD surfaces. *Computer Methods in Applied Mechanics and Engineering* 2009; **198**(37):2982–2995.

[37] Nguyen VP, Anitescu C, Bordas SP, Rabczuk T. Isogeometric analysis: an overview and computer implementation aspects. *Mathematics and Computers in Simulation* 2015; **117**:89–116.

[38] Liu GR. *Mesh free methods: moving beyond the finite element method*. CRC press, 2002.

[39] Askes H, de Borst R, Heeres O. Conditions for locking-free elasto-plastic analyses in the element-free galerkin method. *Computer Methods in Applied Mechanics and Engineering* 1999; **173**(1-2):99–109.

[40] Dolbow J, Belytschko T. Volumetric locking in the element free galerkin method. *International Journal for numerical methods in engineering* 1999; **46**(6):925–942.

[41] Lucy LB. A numerical approach to the testing of the fission hypothesis. *The Astronomical Journal* 1977; **82**:1013–1024.

[42] Gingold RA, Monaghan JJ. Smoothed particle hydrodynamics: theory and application to non-spherical stars. *Monthly Notices of the Royal Astronomical Society* 1977; **181**(3):375–389.

[43] Monaghan J, Gingold R. Shock simulation by the particle method SPH. *Journal of Computational Physics* 1983; **52**(2):374–389.

[44] Gingold R, Monaghan J. Kernel estimates as a basis for general particle methods in hydrodynamics. *Journal of Computational Physics* 1982; **46**(3):429–453.

[45] Swegle J, Attaway S. On the feasibility of using smoothed hydrodynamics paticle methods in hydrodynamics. *Computational Mechanics* 1995; **17**:151–168.

[46] Johnson GR, Beissel SR. Normalized smoothing functions for SPH impact computations. *International Journal for Numerical Methods in Engineering* 1996; **39**(16):2725–2741.

[47] Bonet J, Kulasegaram S. Correction and stabilization of smooth particle hydrodynamics methods with applications in metal forming simulations. *International Journal for Numerical Methods in Engineering* 2000; **47**(6):1189–1214.

[48] Chen J, Pan C, Wu C. Large deformation analysis of rubber based on a reproducing kernel particle method. *Computational Mechanics* 1997; **19**(3):211–227.

[49] Swegle J, Hicks D, Attaway S. Smoothed particle hydrodynamics stability analysis. *Journal of Computational Physics* 1995; **116**(1):123–134.

[50] Violeau D, Rogers BD. Smoothed particle hydrodynamics (SPH) for free-surface flows: past, present and future. *Journal of Hydraulic Research* 2016; **54**(1):1–26.

[51] Tartakovsky AM, Trask N, Pan K, Jones B, Pan W, Williams JR. Smoothed particle hydrodynamics and its applications for multiphase flow and reactive transport in porous media. *Computers &*

Geosciences 2016; **20**(4):807–834.

[52] Nayroles B, Touzot G, Villon P. Generalizing the finite element method: diffuse approximation and diffuse elements. *Computational Mechanics* 1992; **10**(5):307–318.

[53] Lancaster P, Salkauskas K. Surfaces generated by moving least squares methods. *Mathematics of Computation* 1981; **37**(155):141–158.

[54] Lu Y, Belytschko T, Gu L. A new implementation of the element free Galerkin method. *Computer Methods in Applied Mechanics and Engineering* 1994; **113**(3):397–414.

[55] Dolbow J, Belytschko T. An introduction to programming the meshless element free Galerkin method. *Archives of Computational Methods in Engineering* 1998; **5**(3):207–241.

[56] Barry W, Saigal S. A three-dimensional element-free Galerkin elastic and elastoplastic formulation. *International Journal for Numerical Methods in Engineering* 1999; **46**(5):671–693.

[57] Kargarnovin M, Toussi H, Fariborz S. Elasto-plastic element-free Galerkin method. *Computational Mechanics* 2004; **33**(3):206–214.

[58] Belytschko T, Gu L, Lu Y. Fracture and crack growth by element free Galerkin methods. *Modelling and Simulation in Materials Science and Engineering* 1994; **2**(3A):519–534.

[59] Belytschko T, Lu Y, Gu L, Tabbara M. Element-free Galerkin methods for static and dynamic fracture. *International Journal of Solids and Structures* 1995; **32**(17):2547–2570.

[60] Belytschko T, Organ D, Gerlach C. Element-free Galerkin methods for dynamic fracture in concrete. *Computer Methods in Applied Mechanics and Engineering* 2000; **187**(3-4):385–399.

[61] Krysl P, Belytschko T. Analysis of thin shells by the element-free Galerkin method. *International Journal of Solids and Structures* 1996; **33**(20-22):3057–3080.

[62] Chen X, Liu G, Lim S. An element free Galerkin method for the free vibration analysis of composite laminates of complicated shape. *Composite Structures* 2003; **59**(2):279–289.

[63] Amirani MC, Khalili S, Nemati N. Free vibration analysis of sandwich beam with FG core using the element free Galerkin method. *Composite Structures* 2009; **90**(3):373–379.

[64] Qin C, Yang X, Feng J, Liu K, Liu J, Yan G, Zhu S, Xu M, Tian J. Adaptive improved element free Galerkin method for quasi-or multi-spectral bioluminescence tomography. *Optics Express* 2009; **17**(24):21 925–21 934.

[65] Xuan L, Zeng Z, Shanker B, Udpa L. Element-free Galerkin method for static and quasi-static electromagnetic field computation. *IEEE Transactions on Magnetics* 2004; **40**(1):12–20.

[66] Singh I, Sandeep K, Prakash R. Heat transfer analysis of two-dimensional fins using meshless element free Galerkin method. *Numerical Heat Transfer: Part A: Applications* 2003; **44**(1):73–84.

[67] Singh A, Singh IV, Prakash R. Meshless element free Galerkin method for unsteady nonlinear heat transfer problems. *International Journal of Heat and Mass Transfer* 2007; **50**(5):1212–1219.

[68] Liu WK, Jun S, Zhang YF. Reproducing kernel particle methods. *International Journal for Numerical Methods in Fluids* 1995; **20**(8-9):1081–1106.

[69] Chen JS, Pan C, Wu CT, Liu WK. Reproducing kernel particle methods for large deformation

analysis of non-linear structures. *Computer Methods in Applied Mechanics and Engineering* 1996; **139**(1-4):195–227.

[70] Jun S, Liu WK, Belytschko T. Explicit reproducing kernel particle methods for large deformation problems. *International Journal for Numerical Methods in Engineering* 1998; **41**(1):137–166.

[71] Chen JS, Pan C, Wu CT. Application of reproducing kernel particle method to large deformation contact analysis of elastomers. *Rubber Chemistry and Technology* 1998; **71**(2):191–213.

[72] Wang HP, Wu CT, Chen JS. A reproducing kernel smooth contact formulation for metal forming simulations. *Computational Mechanics* 2014; **54**(1):151–169.

[73] Guan P, Chi S, Chen J, Slawson T, Roth M. Semi-Lagrangian reproducing kernel particle method for fragment-impact problems. *International Journal of Impact Engineering* 2011; **38**(12):1033–1047.

[74] Chi SW, Lee CH, Chen JS, Guan PC. A level set enhanced natural kernel contact algorithm for impact and penetration modeling. *International Journal for Numerical Methods in Engineering* 2015; **102**(3-4):839–866.

[75] Duarte CA, Oden JT. Hp clouds-an hp meshless method. *Numerical methods for partial differential equations* 1996; **12**(6):673–706.

[76] Duarte CA, Oden JT. An hp adaptive method using clouds. *Computer Methods in Applied Mechanics and Engineering* 1996; **139**(1-4):237–262.

[77] Garcia O, Fancello EA, de Barcellos CS, Duarte CA. hp-clouds in mindlin's thick plate model. *International Journal for Numerical Methods in Engineering* 2000; **47**(8):1381–1400.

[78] Oden JT, Duarte C, Zienkiewicz OC. A new cloud-based hp finite element method. *Computer Methods in Applied Mechanics and Engineering* 1998; **153**(1-2):117–126.

[79] Chen J, Hu W, Puso M. Orbital hp-clouds for solving schrödinger equation in quantum mechanics. *Computer Methods in Applied Mechanics and Engineering* 2007; **196**(37):3693–3705.

[80] Atluri SN, Zhu T. A new meshless local Petrov-Galerkin (mlpg) approach in computational mechanics. *Computational Mechanics* 1998; **22**(2):117–127.

[81] Zhu T, Zhang JD, Atluri S. A local boundary integral equation (LBIE) method in computational mechanics, and a meshless discretization approach. *Computational Mechanics* 1998; **21**(3):223–235.

[82] Atluri SN, Kim H, Cho JY. A critical assessment of the truly meshless local Petrov-Galerkin (mlpg), and local boundary integral equation (lbie) methods. *Computational Mechanics* 1999; **24**(5):348–372.

[83] Tadeu A, Stanak P, Sladek J, Sladek V. Coupled BEM–MLPG acoustic analysis for non-homogeneous media. *Engineering Analysis with Boundary Elements* 2014; **44**:161–169.

[84] Shivanian E. Meshless local petrov–Galerkin (MLPG) method for three-dimensional nonlinear wave equations via moving least squares approximation. *Engineering Analysis with Boundary Elements* 2015; **50**:249–257.

[85] Sladek J, Sladek V, Solek P, Zhang C. Fracture analysis in continuously nonhomogeneous magneto-

electro-elastic solids under a thermal load by the MLPG. *International Journal of Solids and Structures* 2010; **47**(10):1381–1391.

[86] Sladek J, Sladek V, Krahulec S, Pan E. The MLPG analyses of large deflections of magnetoelectroelastic plates. *Engineering Analysis with Boundary Elements* 2013; **37**(4):673–682.

[87] Vaghefi R, Baradaran G, Koohkan H. Three-dimensional static analysis of thick functionally graded plates by using meshless local petrov–Galerkin (MLPG) method. *Engineering Analysis with Boundary Elements* 2010; **34**(6):564–573.

[88] Li QH, Chen SS, Kou GX. Transient heat conduction analysis using the MLPG method and modified precise time step integration method. *Journal of Computational Physics* 2011; **230**(7):2736–2750.

[89] Shibahara M, Atluri S. The meshless local petrov-Galerkin method for the analysis of heat conduction due to a moving heat source, in welding. *International Journal of Thermal Sciences* 2011; **50**(6):984–992.

[90] Sladek J, Stanak P, Han Z, Sladek V, Atluri S. Applications of the MLPG method in engineering & sciences: a review. *Comput. Model. Eng. Sci* 2013; **92**(5):423–475.

[91] Franke R. Scattered data interpolation: tests of some methods. *Mathematics of Computation* 1982; **38**(157):181–200.

[92] Kansa EJ. Multiquadricsa scattered data approximation scheme with applications to computational fluid-dynamicsI surface approximations and partial derivative estimates. *Computers & Mathematics with Applications* 1990; **19**(8-9):127–145.

[93] Kansa EJ. Multiquadricsa scattered data approximation scheme with applications to computational fluid-dynamicsII solutions to parabolic, hyperbolic and elliptic partial differential equations. *Computers & Mathematics with Applications* 1990; **19**(8):147–161.

[94] Franke C, Schaback R. Solving partial differential equations by collocation using radial basis functions. *Applied Mathematics and Computation* 1998; **93**(1):73–82.

[95] Franke C, Schaback R. Convergence order estimates of meshless collocation methods using radial basis functions. *Advances in Computational Mathematics* 1998; **8**(4):381–399.

[96] Zhang X, Song KZ, Lu MW, Liu X. Meshless methods based on collocation with radial basis functions. *Computational Mechanics* 2000; **26**(4):333–343.

[97] Zerroukat M, Power H, Chen C. A numerical method for heat transfer problems using collocation and radial basis functions. *International Journal for Numerical Methods in Engineering* 1998; **42**(7):1263–1278.

[98] Tatari M, Dehghan M. A method for solving partial differential equations via radial basis functions: Application to the heat equation. *Engineering Analysis with Boundary Elements* 2010; **34**(3):206–212.

[99] Wang L, Chen JS, Hu HY. Subdomain radial basis collocation method for fracture mechanics. *International Journal for Numerical Methods in Engineering* 2010; **83**(7):851–876.

[100] Wang L, Chu F, Zhong Z. Study of radial basis collocation method for wave propagation. *Engineering Analysis with Boundary Elements* 2013; **37**(2):453–463.

[101] Chi S, Chen J, Luo H, Hu H, Wang L. Dispersion and stability properties of radial basis collocation method for elastodynamics. *Numerical Methods for Partial Differential Equations* 2013; **29**(3):818–842.

[102] Wang L, Wang Z, Qian Z. A meshfree method for inverse wave propagation using collocation and radial basis functions. *Computer Methods in Applied Mechanics and Engineering* 2017; **322**:311–350.

[103] Aluru N. A point collocation method based on reproducing kernel approximations. *International Journal for Numerical Methods in Engineering* 2000; **47**(6):1083–1121.

[104] Zhang X, Liu XH, Song KZ, Lu MW. Least-squares collocation meshless method. *International Journal for Numerical Methods in Engineering* 2001; **51**(9):1089–1100.

[105] Kim DW, Kim Y. Point collocation methods using the fast moving least-square reproducing kernel approximation. *International Journal for Numerical Methods in Engineering* 2003; **56**(10):1445–1464.

[106] Hu HY, Chen JS, Hu W. Error analysis of collocation method based on reproducing kernel approximation. *Numerical Methods for Partial Differential Equations* 2011; **27**(3):554–580.

[107] Chi SW, Chen JS, Hu HY, Yang JP. A gradient reproducing kernel collocation method for boundary value problems. *International Journal for Numerical Methods in Engineering* 2013; **93**(13):1381–1402.

[108] Krongauz Y, Belytschko T. Enforcement of essential boundary conditions in meshless approximations using finite elements. *Computer Methods in Applied Mechanics and Engineering* 1996; **131**(1-2):133–145.

[109] Noguchi H, Kawashima T, Miyamura T. Element free analyses of shell and spatial structures. *International Journal for Numerical Methods in Engineering* 2000; **47**(6):1215–1240.

[110] Fernández-Méndez S, Huerta A. Imposing essential boundary conditions in mesh-free methods. *Computer Methods in Applied Mechanics and Engineering* 2004; **193**(12):1257–1275.

[111] Kaljević I, Saigal S. An improved element free Galerkin formulation. *International Journal for Numerical Methods in Engineering* 1997; **40**(16):2953–2974.

[112] Zhuang X, Zhu H, Augarde C. An improved meshless Shepard and least squares method possessing the delta property and requiring no singular weight function. *Computational Mechanics* 2014; **53**(2):343–357.

[113] Beissel S, Belytschko T. Nodal integration of the element-free Galerkin method. *Computer Methods in Applied Mechanics and Engineering* 1996; **139**(1):49–74.

[114] Chen J, Wu C, Yoon S, You Y. A stabilized conforming nodal integration for Galerkin mesh-free methods. *International Journal for Numerical Methods in Engineering* 2001; **50**(2):435–466.

[115] Carpinteri A, Ferro G, Ventura G. The partition of unity quadrature in element-free crack mod-

elling. *Computers & Structures* 2003; **81**(18):1783–1794.

[116] Zhuang X, Augarde C. Aspects of the use of orthogonal basis functions in the element-free Galerkin method. *International Journal for Numerical Methods in Engineering* 2010; **81**(3):366–380.

[117] Breitkopf P, Rassineux A, Touzot G, Villon P. Explicit form and efficient computation of mls shape functions and their derivatives. *International Journal for Numerical Methods in Engineering* 2000; **48**(3):451–466.

[118] Zhou J, Wang X, Zhang Z, Zhang L. Explicit 3-D rkpm shape functions in terms of kernel function moments for accelerated computation. *Computer Methods in Applied Mechanics and Engineering* 2005; **194**(9):1027–1035.

[119] Zienkiewicz OC, Zhu JZ. The superconvergent patch recovery and a posteriori error estimates. part 1: The recovery technique. *International Journal for Numerical Methods in Engineering* 1992; **33**(7):1331–1364.

[120] Zienkiewicz OC, Zhu JZ. The superconvergent patch recovery and a posteriori error estimates. part 2: Error estimates and adaptivity. *International Journal for Numerical Methods in Engineering* 1992; **33**(7):1365–1382.

[121] Chung H, Belytschko T. An error estimate in the EFG method. *Computational Mechanics* 1998; **21**(2):91–100.

[122] Lee CK, Zhou C. On error estimation and adaptive refinement for element free Galerkin method: Part i: stress recovery and a posteriori error estimation. *Computers & Structures* 2004; **82**(4):413–428.

[123] Lee C, Zhou C. On error estimation and adaptive refinement for element free Galerkin method: Part ii: adaptive refinement. *Computers & Structures* 2004; **82**(4):429–443.

[124] Krysl P, Belytschko T. Element-free galerkin method: Convergence of the continuous and discontinuous shape functions. *Computer Methods in Applied Mechanics and Engineering* 1997; **148**(3-4):257–277.

[125] Zhuang X, Heaney C, Augarde C. On error control in the element-free Galerkin method. *Engineering Analysis with Boundary Elements* 2012; **36**(3):351 – 360.

[126] Liebowitz H, Sandhu J, Lee J, Menandro F. Computational fracture mechanics: research and application. *Engineering Fracture Mechanics* 1995; **50**(5):653–670.

[127] Inglis CE. Stresses in a plate due to the presence of cracks and sharp corners. *Transactions of the institute of naval architects* 1913; **55**(219-241):193–198.

[128] Griffith AA. The phenomena of rupture and flow in solids. *Philosophical Transactions of the Royal Society of London. Series A, Containing Papers of a Mathematical or Physical Character* 1921; **221**:163–198.

[129] Irwin GR. Fracutre dynamics. *Fracturing of Metals* 1948; **152**.

[130] Irwin GR. Analysis of stresses and strains near the end of a crack traversing a plate. *Journal of Applied Mechanics* 1957; **24**(3):361–364.

[131] Dugdale DS. Yielding of steel sheets containing slits. *Journal of the Mechanics and Physics of Solids* 1960; **8**(2):100–104.

[132] Barenblatt GI. The mathematical theory of equilibrium cracks in brittle fracture. *Advances in Applied Mechanics* 1962; **7**:55–129.

[133] Hillerborg A, Modéer M, Petersson PE. Analysis of crack formation and crack growth in concrete by means of fracture mechanics and finite elements. *Cement and Concrete Research* 1976; **6**(6):773–781.

[134] Moës N, Belytschko T. Extended finite element method for cohesive crack growth. *Engineering Fracture Mechanics* 2002; **69**(7):813–833.

[135] Zi G, Belytschko T. New crack-tip elements for xfem and applications to cohesive cracks. *International Journal for Numerical Methods in Engineering* 2003; **57**(15):2221–2240.

[136] Salih S, Davey K, Zou Z. Rate-dependent elastic and elasto-plastic cohesive zone models for dynamic crack propagation. *International Journal of Solids and Structures* 2016; **90**:95–115.

[137] Elices M, Guinea G, Gomez J, Planas J. The cohesive zone model: advantages, limitations and challenges. *Engineering Fracture Mechanics* 2002; **69**(2):137–163.

[138] Park K, Paulino GH. Cohesive zone models: a critical review of traction-separation relationships across fracture surfaces. *Applied Mechanics Reviews* 2011; **64**(6):060 802.

[139] Ewing J, Humfrey J. The fracture of metals under repeated alternations of stress. *Philosophical Transactions of the Royal Society of London. Series A, Containing Papers of a Mathematical or Physical Character* 1903; **200**:241–250.

[140] Basquin O. The exponential law of endurance tests. *Proceeding of the American Society for Testing and Materials*, vol. 10, 1910; 625–630.

[141] Paris PC, Gomez MP, Anderson WE. A rational analytic theory of fatigue. *The trend in engineering* 1961; **13**(1):9–14.

[142] Fleck N, Shin C, Smith RA. Fatigue crack growth under compressive loading. *Engineering Fracture Mechanics* 1985; **21**(1):173–185.

[143] Wolf E. Fatigue crack closure under cyclic tension. *Engineering Fracture Mechanics* 1970; **2**(1):37–45.

[144] Maiti S, Geubelle PH. Cohesive modeling of fatigue crack retardation in polymers: crack closure effect. *Engineering Fracture Mechanics* 2006; **73**(1):22–41.

[145] McDowell D, Dunne F. Microstructure-sensitive computational modeling of fatigue crack formation. *International Journal of Fatigue* 2010; **32**(9):1521–1542.

[146] Herbig M, King A, Reischig P, Proudhon H, Lauridsen EM, Marrow J, Buffière JY, Ludwig W. 3-d growth of a short fatigue crack within a polycrystalline microstructure studied using combined diffraction and phase-contrast x-ray tomography. *Acta Materialia* 2011; **59**(2):590–601.

[147] Sangid MD. The physics of fatigue crack initiation. *International Journal of Fatigue* 2013; **57**:58–72.

[148] Cui W. A state-of-the-art review on fatigue life prediction methods for metal structures. *Journal*

of Marine Science and Technology 2002; **7**(1):43–56.

[149] Zienkiewicz OC, Taylor RL. *The Finite Element Method*, vol. 3. McGraw-hill London, 1977.

[150] Xu X, Needleman A. Numerical simulations of dynamic crack growth along an interface. *International Journal of Fracture* 1995; **74**(4):289–324.

[151] Ortiz M, Pandolfi A. Finite-deformation irreversible cohesive elements for three-dimensional crack-propagation analysis. *International Journal for Numerical Methods in Engineering* 1999; **44**(9):1267–1282.

[152] Schöllmann M, Fulland M, Richard H. Development of a new software for adaptive crack growth simulations in 3D structures. *Engineering Fracture Mechanics* 2003; **70**(2):249–268.

[153] Belytschko T, Black T. Elastic crack growth in finite elements with minimal remeshing. *International Journal for Numerical Methods in Engineering* 1999; **45**(5):601–620.

[154] Dolbow J, Belytschko T. A finite element method for crack growth without remeshing. *International Journal for Numerical Methods in Engineering* 1999; **46**(1):131–150.

[155] Daux C, Moes N, Dolbow J, Sukumar N, Belytschko T. Arbitrary branched and intersecting cracks with the extended finite element method. *International Journal for Numerical Methods in Engineering* 2000; **48**:1741–1760.

[156] Sukumar N, Chopp DL, Moës N, Belytschko T. Modeling holes and inclusions by level sets in the extended finite-element method. *Computer Methods in Applied Mechanics and Engineering* 2001; **190**(46):6183–6200.

[157] Moës N, Belytschko T. Extended finite element method for cohesive crack growth. *Engineering Fracture Mechanics* 2002; **69**(7):813–833.

[158] Dolbow J, Moës N, Belytschko T. An extended finite element method for modeling crack growth with frictional contact. *Computer Methods in Applied Mechanics and Engineering* 2001; **190**(51):6825–6846.

[159] Laborde P, Pommier J, Renard Y, Salaün M. High-order extended finite element method for cracked domains. *International Journal for Numerical Methods in Engineering* 2005; **64**(3):354–381.

[160] Stazi F, Budyn E, Chessa J, Belytschko T. An extended finite element method with higher-order elements for curved cracks. *Computational Mechanics* 2003; **31**(1):38–48.

[161] Moës N, Gravouil A, Belytschko T. Non-planar 3D crack growth by the extended finite element and level sets - part I: Mechanical model. *International Journal for Numerical Methods in Engineering* 2002; **53**(11):2549–2568.

[162] Areias P, Belytschko T. Analysis of three-dimensional crack initiation and propagation using the extended finite element method. *International Journal for Numerical Methods in Engineering* 2005; **63**(5):760–788.

[163] Fries TP, Belytschko T. The extended/generalized finite element method: an overview of the method and its applications. *International Journal for Numerical Methods in Engineering* 2010; **84**(3):253–304.

[164] Boettinger WJ, Warren JA, Beckermann C, Karma A. Phase-field simulation of solidification. *Annual Review of Materials Research* 2002; **32**(1):163–194.

[165] Aranson I, Kalatsky V, Vinokur V. Continuum field description of crack propagation. *Physical Review Letters* 2000; **85**(1):118.

[166] Karma A, Kessler DA, Levine H. Phase-field model of mode iii dynamic fracture. *Physical Review Letters* 2001; **87**(4):045 501.

[167] Henry H, Levine H. Dynamic instabilities of fracture under biaxial strain using a phase field model. *Physical Review Letters* 2004; **93**(10):105 504.

[168] Francfort GA, Marigo JJ. Revisiting brittle fracture as an energy minimization problem. *Journal of the Mechanics and Physics of Solids* 1998; **46**(8):1319–1342.

[169] Kuhn C, Müller R. A continuum phase field model for fracture. *Engineering Fracture Mechanics* 2010; **77**(18):3625–3634.

[170] Miehe C, Welschinger F, Hofacker M. Thermodynamically consistent phase-field models of fracture: Variational principles and multi-field FE implementations. *International Journal for Numerical Methods in Engineering* 2010; **83**(10):1273–1311.

[171] de Borst R, Verhoosel CV. Gradient damage vs phase-field approaches for fracture: Similarities and differences. *Computer Methods in Applied Mechanics and Engineering* 2016; **312**:78–94.

[172] Ambati M, Kruse R, De Lorenzis L. A phase-field model for ductile fracture at finite strains and its experimental verification. *Computational Mechanics* 2016; **57**(1):149–167.

[173] Wilson ZA, Landis CM. Phase-field modeling of hydraulic fracture. *Journal of the Mechanics and Physics of Solids* 2016; **96**:264–290.

[174] Miehe C, Dal H, Schänzel LM, Raina A. A phase-field model for chemo-mechanical induced fracture in lithium-ion battery electrode particles. *International Journal for Numerical Methods in Engineering* 2016; **106**(9):683–711.

[175] Raina A, Miehe C. A phase-field model for fracture in biological tissues. *Biomechanics and Modeling in Mechanobiology* 2016; **15**(3):479–496.

[176] Ambati M, Gerasimov T, De Lorenzis L. A review on phase-field models of brittle fracture and a new fast hybrid formulation. *Computational Mechanics* 2015; **55**(2):383–405.

[177] Miehe C, Hofacker M, Welschinger F. A phase field model for rate-independent crack propagation: Robust algorithmic implementation based on operator splits. *Computer Methods in Applied Mechanics and Engineering* 2010; **199**(45):2765–2778.

[178] Ventura G, Xu J, Belytschko T. A vector level set method and new discontinuity approximations for crack growth by efg. *International Journal for Numerical Methods in Engineering* 2002; **54**(6):923–944.

[179] Zhuang X, Augarde C, Bordas S. Accurate fracture modelling using meshless methods, the visibility criterion and level sets: formulation and 2D modelling. *International Journal for Numerical Methods in Engineering* 2011; **86**(2):249–268.

[180] Zhuang X, Augarde C, Mathisen K. Fracture modeling using meshless methods and level sets in 3D: framework and modeling. *International Journal for Numerical Methods in Engineering* 2012; **92**(11):969–998.

[181] Duflot M. A study of the representation of cracks with level sets. *International Journal for Numerical Methods in Engineering* 2007; **70**(11):1261–1302.

[182] Stolarska M, Chopp D, Moës N, Belytschko T. Modelling crack growth by level sets in the extended finite element method. *International Journal for Numerical Methods in Engineering* 2001; **51**(8):943–960.

[183] Gravouil A, Moës N, Belytschko T. Non-planar 3D crack growth by the extended finite element and level sets - part II: Level set update. *International Journal for Numerical Methods in Engineering* 2002; **53**(11):2569–2586.

[184] Shi GH. Modeling rock joints and blocks by manifold method. *The 33th US Symposium on Rock Mechanics (USRMS)*, American Rock Mechanics Association, 1992; 639–648.

[185] Shi GH. Discontinuous deformation analysis: a new numerical model for the statics and dynamics of deformable block structures. *Engineering Computations* 1992; **9**(2):157–168.

[186] Chiou YJ, Lee YM, Tsay RJ. Mixed mode fracture propagation by manifold method. *International Journal of Fracture* 2002; **114**(4):327–347.

[187] Zhang H, Li L, An X, Ma G. Numerical analysis of 2-D crack propagation problems using the numerical manifold method. *Engineering Analysis with Boundary Elements* 2010; **34**(1):41–50.

[188] Zheng H, Liu F, Li C. The mls-based numerical manifold method with applications to crack analysis. *International Journal of Fracture* 2014; **190**(1-2):147–166.

[189] Fan H, He S, Jiang Z. A high-order numerical manifold method with nine-node triangular meshes. *Engineering Analysis with Boundary Elements* 2015; **61**:172–182.

[190] Ma G, An X, He L. The numerical manifold method: a review. *International Journal of Computational Methods* 2010; **7**(01):1–32.

[191] Silling SA. Reformulation of elasticity theory for discontinuities and long-range forces. *Journal of the Mechanics and Physics of Solids* 2000; **48**(1):175–209.

[192] Silling SA, Askari E. A meshfree method based on the peridynamic model of solid mechanics. *Computers & Structures* 2005; **83**(17):1526–1535.

[193] Silling SA, Epton M, Weckner O, Xu J, Askari E. Peridynamic states and constitutive modeling. *Journal of Elasticity* 2007; **88**(2):151–184.

[194] Silling SA, Lehoucq RB. Convergence of peridynamics to classical elasticity theory. *Journal of Elasticity* 2008; **93**(1):13–37.

[195] Parks ML, Lehoucq RB, Plimpton SJ, Silling SA. Implementing peridynamics within a molecular dynamics code. *Computer Physics Communications* 2008; **179**(11):777–783.

[196] Ganzenmüller GC, Hiermaier S, May M. On the similarity of meshless discretizations of peridynamics and smooth-particle hydrodynamics. *Computers & Structures* 2015; **150**:71–78.

[197] Ren H, Zhuang X, Cai Y, Rabczuk T. Dual-horizon peridynamics. *International Journal for Numerical Methods in Engineering* 2016; **108**(12):1451–1476.

[198] Sun S, Sundararaghavan V. A peridynamic implementation of crystal plasticity. *International Journal of Solids and Structures* 2014; **51**(19):3350–3360.

[199] Bobaru F, Zhang G. Why do cracks branch? a peridynamic investigation of dynamic brittle fracture. *International Journal of Fracture* 2015; **196**(1-2):59–98.

[200] Wildman RA, OGrady JT, Gazonas GA. A hybrid multiscale finite element/peridynamics method. *International Journal of Fracture* 2017; **207**(1):41–53.

[201] Tupek M, Rimoli J, Radovitzky R. An approach for incorporating classical continuum damage models in state-based peridynamics. *Computer Methods in Applied Mechanics and Engineering* 2013; **263**:20–26.

[202] Rabczuk T, Belytschko T. Cracking particles: a simplified meshfree method for arbitrary evolving cracks. *International Journal for Numerical Methods in Engineering* 2004; **61**(13):2316–2343.

[203] Rabczuk T, Belytschko T. A three-dimensional large deformation meshfree method for arbitrary evolving cracks. *Computer Methods in Applied Mechanics and Engineering* 2007; **196**(29):2777–2799.

[204] Rabczuk T, Zi G, Bordas S, Nguyen-Xuan H. A simple and robust three-dimensional cracking-particle method without enrichment. *Computer Methods in Applied Mechanics and Engineering* 2010; **199**(37):2437–2455.

[205] Rabczuk T, Zi G. A meshfree method based on the local partition of unity for cohesive cracks. *Computational Mechanics* 2007; **39**(6):743–760.

[206] Rabczuk T, Bordas S, Zi G. A three-dimensional meshfree method for continuous multiple-crack initiation, propagation and junction in statics and dynamics. *Computational Mechanics* 2007; **40**(3):473–495.

[207] Bordas S, Rabczuk T, Zi G. Three-dimensional crack initiation, propagation, branching and junction in non-linear materials by an extended meshfree method without asymptotic enrichment. *Engineering Fracture Mechanics* 2008; **75**(5):943–960.

[208] Amiri F, Anitescu C, Arroyo M, Bordas S, Rabczuk T. XLME interpolants, a seamless bridge between XFEM and enriched meshless methods. *Computational Mechanics* 2014; **53**(1):45–57.

[209] Kumar V, Ghosh A. Modeling of dynamic fracture based on the cracking particles method. *Theoretical and Applied Fracture Mechanics* 2015; **75**:22–31.

[210] Rabczuk T, Areias P, Belytschko T. A simplified mesh-free method for shear bands with cohesive surfaces. *International Journal for Numerical Methods in Engineering* 2007; **69**(5):993–1021.

[211] Chen L, Zhang Y. Dynamic fracture analysis using discrete cohesive crack method. *International Journal for Numerical Methods in Biomedical Engineering* 2010; **26**(11):1493–1502.

[212] Kumar V, Drathi R. A meshless cracking particles approach for ductile fracture. *KSCE Journal of Civil Engineering* 2014; **18**(1):238–248.

[213] Xu S. Stable cracking particles method based on stabilized nodal integration and updated Lagrangian kernel. *Mathematical Problems in Engineering* 2014; **article-ID 646514**:1–10.

[214] Combescure A, Gravouil A, Grégoire D, Rethore J. X-FEM a good candidate for energy conservation in simulation of brittle dynamic crack propagation. *Computer Methods in Applied Mechanics and Engineering* 2008; **197**(5):309–318.

[215] Potapov S, Faucher V, Daudeville L. Advanced simulation of damage of reinforced concrete structures under impact. *European Journal of Environmental and Civil Engineering* 2012; **16**(9):1090–1101.

[216] Cai Y, Wu J, Atluri S. A new implementation of the numerical manifold method (NMM) for the modeling of non-collinear and intersecting cracks. *Computer Modeling in Engineering & Sciences* 2013; **92**(1):63–85.

[217] Belytschko T, Lu Y, Gu L. Crack propagation by element-free Galerkin methods. *Engineering Fracture Mechanics* 1995; **51**(2):295–315.

[218] Fries TP, Matthies HG. *Classification and Overview of Meshfree Methods*. Institute of Scientific Computing, Technical University Braunschweig, Brunswick, Germany, 2004.

[219] Golub GH, Welsch JH. Calculation of gauss quadrature rules. *Mathematics of Computation* 1969; **23**(106):221–230.

[220] Le CV, Askes H, Gilbert M. Adaptive element-free Galerkin method applied to the limit analysis of plates. *Computer Methods in Applied Mechanics and Engineering* 2010; **199**(37):2487–2496.

[221] Racz D, Bui TQ. Novel adaptive meshfree integration techniques in meshless methods. *International Journal for Numerical Methods in Engineering* 2012; **90**(11):1414–1434.

[222] Carpinteri A, Ferro G, Ventura G. The partition of unity quadrature in meshless methods. *International Journal for Numerical Methods in Engineering* 2002; **54**(7):987–1006.

[223] Zhu T, Atluri S. A modified collocation method and a penalty formulation for enforcing the essential boundary conditions in the element free Galerkin method. *Computational Mechanics* 1998; **21**(3):211–222.

[224] Belytschko T, Organ D, Krongauz Y. A coupled finite element-element-free galerkin method. *Computational Mechanics* 1995; **17**(3):186–195.

[225] Ullah Z, Coombs W, Augarde C. An adaptive finite element/meshless coupled method based on local maximum entropy shape functions for linear and nonlinear problems. *Computer Methods in Applied Mechanics and Engineering* 2013; **267**:111–132.

[226] Organ D, Fleming M, Terry T, Belytschko T. Continuous meshless approximations for nonconvex bodies by diffraction and transparency. *Computational Mechanics* 1996; **18**(3):225–235.

[227] Ai W, Augarde CE. An adaptive cracking particle method for 2D crack propagation. *International Journal for Numerical Methods in Engineering* 2016; **108**(13):1626–1648.

[228] Rabczuk T, Samaniego E. Discontinuous modelling of shear bands using adaptive meshfree methods. *Computer Methods in Applied Mechanics and Engineering* 2008; **197**(6):641–658.

[229] Lee G, Chung H, Choi C. Adaptive crack propagation analysis with the element-free Galerkin method. *International Journal for Numerical Methods in Engineering* 2003; **56**(3):331–350.

[230] Rossi R, Alves MK. An h-adaptive modified element-free Galerkin method. *European Journal of Mechanics-A/Solids* 2005; **24**(5):782–799.

[231] Ullah Z, Augarde C. Finite deformation elasto-plastic modelling using an adaptive meshless method. *Computers & Structures* 2013; **118**:39–52.

[232] Häussler-Combe U, Korn C. An adaptive approach with the element-free-Galerkin method. *Computer Methods in Applied Mechanics and Engineering* 1998; **162**(1):203–222.

[233] Rabczuk T, Belytschko T. Adaptivity for structured meshfree particle methods in 2D and 3D. *International Journal for Numerical Methods in Engineering* 2005; **63**(11):1559–1582.

[234] Zienkiewicz O, Boroomand B, Zhu J. Recovery procedures in error estimation and adaptivity part I: Adaptivity in linear problems. *Computer Methods in Applied Mechanics and Engineering* 1999; **176**(1):111–125.

[235] Boroomand B, Zienkiewicz O. Recovery procedures in error estimation and adaptivity. part II: Adaptivity in nonlinear problems of elasto-plasticity behaviour. *Computer Methods in Applied Mechanics and Engineering* 1999; **176**(1):127–146.

[236] Krysl P, Belytschko T. Element-free Galerkin method: Convergence of the continuous and discontinuous shape functions. *Computer Methods in Applied Mechanics and Engineering* 1997; **148**(3):257–277.

[237] Fleming M, Chu Y, Moran B, Belytschko T, Lu Y, Gu L. Enriched element-free Galerkin methods for crack tip fields. *International Journal for Numerical Methods in Engineering* 1997; **40**(8):1483–1504.

[238] Afshar M, Naisipour M, Amani J. Node moving adaptive refinement strategy for planar elasticity problems using discrete least squares meshless method. *Finite Elements in Analysis and Design* 2011; **47**(12):1315–1325.

[239] You Y, Chen JS, Lu H. Filters, reproducing kernel, and adaptive meshfree method. *Computational Mechanics* 2003; **31**(3-4):316–326.

[240] Rice JR. A path independent integral and the approximate analysis of strain concentration by notches and cracks. *Journal of Applied Mechanics* 1968; **35**(2):379–386.

[241] Yan A, Nguyen-Dang H. Multiple-cracked fatigue crack growth by BEM. *Computational Mechanics* 1995; **16**(5):273–280.

[242] Berković M. Determination of stress intensity factors using finite element method. *Structural Integrity and Life* 2004; **4**(2):57–62.

[243] Yau J, Wang S, Corten H. A mixed-mode crack analysis of isotropic solids using conservation laws of elasticity. *Journal of Applied Mechanics* 1980; **47**(2):335–341.

[244] Yu H, Wu L, Guo L, Du S, He Q. Investigation of mixed-mode stress intensity factors for non-homogeneous materials using an interaction integral method. *International Journal of Solids and*

Structures 2009; **46**(20):3710–3724.

[245] Bouchard PO, Bay F, Chastel Y. Numerical modelling of crack propagation: automatic remeshing and comparison of different criteria. *Computer Methods in Applied Mechanics and Engineering* 2003; **192**(35):3887–3908.

[246] Peco C, Millán D, Rosolen A, Arroyo M. Efficient implementation of Galerkin meshfree methods for large-scale problems with an emphasis on maximum entropy approximants. *Computers & Structures* 2015; **150**:52–62.

[247] Westergaard HM. Bearing pressures and cracks. *Journal of Applied Mechanics* 1939; **6**(2):A49–A53.

[248] Tada H, Paris P, Irwin G. The analysis of cracks handbook. *New York: ASME Press* 2000; .

[249] Muravin B, Turkel E. Multiple crack weight for solution of multiple interacting cracks by meshless numerical methods. *International Journal for Numerical Methods in Engineering* 2006; **67**(8):1146–1159.

[250] Barbieri E, Petrinic N, Meo M, Tagarielli V. A new weight-function enrichment in meshless methods for multiple cracks in linear elasticity. *International Journal for Numerical Methods in Engineering* 2012; **90**(2):177–195.

[251] Barbieri E, Petrinic N. Three-dimensional crack propagation with distance-based discontinuous kernels in meshfree methods. *Computational Mechanics* 2014; **53**(2):325–342.

[252] Singh I, Mishra B, Pant M. A modified intrinsic enriched element free Galerkin method for multiple cracks simulation. *Materials & Design* 2010; **31**(1):628–632.

[253] Budyn E, Zi G, Moës N, Belytschko T. A method for multiple crack growth in brittle materials without remeshing. *International Journal for Numerical Methods in Engineering* 2004; **61**(10):1741–1770.

[254] An X, Fu G, Ma G. A comparison between the NMM and the XFEM in discontinuity modeling. *International Journal of Computational Methods* 2012; **9**(02):1240 030.

[255] Rabczuk T, Belytschko T. An adaptive continuum/discrete crack approach for meshfree particle methods. *Latin American Journal of Solids and Structures* 2003; **1**(1):141–166.

[256] Ooi ET, Song C, Tin-Loi F, Yang Z. Polygon scaled boundary finite elements for crack propagation modelling. *International Journal for Numerical Methods in Engineering* 2012; **91**(3):319–342.

[257] Dai S, Augarde C, Du C, Chen D. A fully automatic polygon scaled boundary finite element method for modelling crack propagation. *Engineering Fracture Mechanics* 2015; **133**:163–178.

[258] Ma G, An X, Zhang H, Li L. Modeling complex crack problems using the numerical manifold method. *International Journal of Fracture* 2009; **156**(1):21–35.

[259] Erdogan F, Sih G. On the crack extension in plates under plane loading and transverse shear. *Journal of Fluids Engineering* 1963; **85**(4):519–525.

[260] Sih G, Macdonald B. Fracture mechanics applied to engineering problems-strain energy density fracture criterion. *Engineering Fracture Mechanics* 1974; **6**(2):361–386.

[261] Wu CH. Fracture under combined loads by maximum-energy-release-rate criterion. *Journal of Ap-*

plied Mechanics 1978; **45**(3):553–558.

[262] Heintz P. On the numerical modelling of quasi-static crack growth in linear elastic fracture mechanics. *International Journal for Numerical Methods in Engineering* 2006; **65**(2):174–189.

[263] Miehe C, Gürses E, Birkle M. A computational framework of configurational-force-driven brittle fracture based on incremental energy minimization. *International Journal of Fracture* 2007; **145**(4):245–259.

[264] Miehe C, Gürses E. A robust algorithm for configurational-force-driven brittle crack propagation with R-adaptive mesh alignment. *International Journal for Numerical Methods in Engineering* 2007; **72**(2):127–155.

[265] Tillberg J, Larsson F, Runesson K. On the role of material dissipation for the crack-driving force. *International Journal of Plasticity* 2010; **26**(7):992–1012.

[266] Kaczmarczyk Ł, Nezhad MM, Pearce C. Three-dimensional brittle fracture: configurational-force-driven crack propagation. *International Journal for Numerical Methods in Engineering* 2014; **97**(7):531–550.

[267] Özenç K, Kaliske M, Lin G, Bhashyam G. Evaluation of energy contributions in elasto-plastic fracture: a review of the configurational force approach. *Engineering Fracture Mechanics* 2014; **115**:137–153.

[268] Eshelby JD. The force on an elastic singularity. *Philosophical Transactions of the Royal Society of London A: Mathematical, Physical and Engineering Sciences* 1951; **244**(877):87–112.

[269] Heintz P, Larsson F, Hansbo P, Runesson K. Adaptive strategies and error control for computing material forces in fracture mechanics. *International Journal for Numerical Methods in Engineering* 2004; **60**(7):1287–1299.

[270] Bird R, Coombs W, Giani S. A quasi-static discontinuous galerkin configurational force crack propagation method for brittle materials. *International Journal for Numerical Methods in Engineering* 2018; **113**(7):1061–1080.

[271] Sukumar N, Moës N, Moran B, Belytschko T. Extended finite element method for three-dimensional crack modelling. *International Journal for Numerical Methods in Engineering* 2000; **48**(11):1549–1570.

[272] Krysl P, Belytschko T. The element free Galerkin method for dynamic propagation of arbitrary 3-d cracks. *International Journal for Numerical Methods in Engineering* 1999; **44**(6):767–800.

[273] Duflot M. A meshless method with enriched weight functions for three-dimensional crack propagation. *International Journal for Numerical Methods in Engineering* 2006; **65**(12):1970–2006.

[274] Fries TP, Baydoun M. Crack propagation with the extended finite element method and a hybrid explicit–implicit crack description. *International Journal for Numerical Methods in Engineering* 2012; **89**(12):1527–1558.

[275] Yang Y, Tang X, Zheng H, Liu Q, He L. Three-dimensional fracture propagation with numerical manifold method. *Engineering Analysis with Boundary Elements* 2016; **72**:65–77.

[276] Yang S, Cao M, Ren X, Ma G, Zhang J, Wang H. 3d crack propagation by the numerical manifold method. *Computers & Structures* 2018; **194**:116–129.

[277] Ren B, Wu C, Askari E. A 3D discontinuous Galerkin finite element method with the bond-based peridynamics model for dynamic brittle failure analysis. *International Journal of Impact Engineering* 2017; **99**:14–25.

[278] Rabczuk T, Belytschko T. Application of particle methods to static fracture of reinforced concrete structures. *International Journal of Fracture* 2006; **137**(1-4):19–49.

[279] Ai W, Augarde CE. A multi-cracked particle method for complex fracture problems in 2D. *Mathematics and Computers in Simulation* 2018; **150**:1–24.

[280] Brighenti R. Application of the element-free Galerkin meshless method to 3-d fracture mechanics problems. *Engineering Fracture Mechanics* 2005; **72**(18):2808–2820.

[281] Sukumar N, Moran B, Black T, Belytschko T. An element-free Galerkin method for three-dimensional fracture mechanics. *Computational Mechanics* 1997; **20**(1):170–175.

[282] Gosz M, Moran B. An interaction energy integral method for computation of mixed-mode stress intensity factors along non-planar crack fronts in three dimensions. *Engineering Fracture Mechanics* 2002; **69**(3):299–319.

[283] Hu Y, Yang Z. An element-free Galerkin method for 3D crack propagation simulation under complicated stress conditions. *International Journal for Numerical Methods in Engineering* 2012; **91**(12):1251–1263.

[284] Richard H, Fulland M, Sander M. Theoretical crack path prediction. *Fatigue & fracture of engineering materials & structures* 2005; **28**(1-2):3–12.

[285] Sih GC. On the singular character of thermal stresses near a crack tip. *Journal of Applied Mechanics* 1962; **29**:587.

[286] Williams ML, Pasadena C. On the stress distribution at the base of a stationary crack. *Journal of Applied Mechanics* 1957; **24**(1):109–114.

[287] Kuo AY. Effects of crack surface heat conductance on stress intensity factors. *Journal of Applied Mechanics* 1990; **57**(2):354–358.

[288] Duflot M. The extended finite element method in thermoelastic fracture mechanics. *International Journal for Numerical Methods in Engineering* 2008; **74**(5):827–847.

[289] Zhong XC, Lee KY. A thermal-medium crack model. *Mechanics of Materials* 2012; **51**:110–117.

[290] Li XF, Lee KY. Effect of heat conduction of penny-shaped crack interior on thermal stress intensity factors. *International Journal of Heat and Mass Transfer* 2015; **91**:127–134.

[291] Emmel E, Stamm H. Calculation of stress intensity factors of thermally loaded cracks using the finite element method. *International Journal of Pressure Vessels and Piping* 1985; **19**(1):1–17.

[292] Magalhaes J, Emery A. Transient thermoelastic fracture of brittle substrates bonded to brittle films. *Journal of Thermal Stresses* 1997; **20**(1):35–45.

[293] Chen H, Wang Q, Liu G, Wang Y, Sun J. Simulation of thermoelastic crack problems using singular

edge-based smoothed finite element method. *International Journal of Mechanical Sciences* 2016; **115**:123–134.

[294] Prasad N, Aliabadi M, Rooke D. The dual boundary element method for thermoelastic crack problems. *International Journal of Fracture* 1994; **66**(3):255–272.

[295] Wrobel L, Brebbia C. The dual reciprocity boundary element formulation for nonlinear diffusion problems. *Computer Methods in Applied Mechanics and Engineering* 1987; **65**(2):147–164.

[296] Zamani A, Gracie R, Eslami MR. Higher order tip enrichment of extended finite element method in thermoelasticity. *Computational Mechanics* 2010; **46**(6):851–866.

[297] Zamani A, Eslami MR. Implementation of the extended finite element method for dynamic thermoelastic fracture initiation. *International Journal of Solids and Structures* 2010; **47**(10):1392–1404.

[298] Pant M, Singh I, Mishra B. Numerical simulation of thermo-elastic fracture problems using element free Galerkin method. *International Journal of Mechanical Sciences* 2010; **52**(12):1745–1755.

[299] Wang S, Zhang H. Partition of unity-based thermomechanical meshfree method for two-dimensional crack problems. *Archive of Applied Mechanics* 2011; **81**(10):1351–1363.

[300] Bouhala L, Makradi A, Belouettar S. Thermal and thermo-mechanical influence on crack propagation using an extended mesh free method. *Engineering Fracture Mechanics* 2012; **88**:35–48.

[301] Wang H. An extended element-free galerkin method for thermo-mechanical dynamic fracture in linear and nonlinear materials. *Computational Materials Science* 2015; **98**:366–371.

[302] Zhang H, Ma G, Ren F. Implementation of the numerical manifold method for thermo-mechanical fracture of planar solids. *Engineering Analysis with Boundary Elements* 2014; **44**:45–54.

[303] Zhang H, Ma G, Fan L. Thermal shock analysis of 2d cracked solids using the numerical manifold method and precise time integration. *Engineering Analysis with Boundary Elements* 2017; **75**:46–56.

[304] Simkins D, Li S. Meshfree simulations of thermo-mechanical ductile fracture. *Computational Mechanics* 2006; **38**(3):235–249.

[305] Wu S, Zhang S, Xu Z. Thermal crack growth-based fatigue life prediction due to braking for a high-speed railway brake disc. *International Journal of Fatigue* 2016; **87**:359–369.

[306] Rabizadeh E, Bagherzadeh AS, Rabczuk T. Goal-oriented error estimation and adaptive mesh refinement in dynamic coupled thermoelasticity. *Computers & Structures* 2016; **173**:187–211.

[307] Yosibash Z. Numerical thermo-elastic analysis of singularities in two-dimensions. *International Journal of Fracture* 1996; **74**(4):341–361.

[308] Shih C, Moran B, Nakamura T. Energy release rate along a three-dimensional crack front in a thermally stressed body. *International Journal of Fracture* 1986; **30**(2):79–102.

[309] Chen Y, Hasebe N. Solution for a curvilinear crack in a thermoelastic medium. *Journal of Thermal Stresses* 2003; **26**(3):245–259.

[310] Prasad N, Aliabadi M, Rooke D. Incremental crack growth in thermoelastic problems. *International Journal of Fracture* 1994; **66**(3):R45–R50.

[311] Dinis L, Jorge RN, Belinha J. Analysis of 3d solids using the natural neighbour radial point interpolation method. *Computer Methods in Applied Mechanics and Engineering* 2007; **196**(13):2009–2028.

[312] Beirão da Veiga L, Brezzi F, Cangiani A, Manzini G, Marini LD, Russo A. Basic principles of virtual element methods. *Mathematical Models and Methods in Applied Sciences* 2013; **23**(01):199–214.

[313] Rosolen A, Millán D, Arroyo M. On the optimum support size in meshfree methods: A variational adaptivity approach with maximum-entropy approximants. *International Journal for Numerical Methods in Engineering* 2010; **82**(7):868–895.

[314] Sukumar N. Construction of polygonal interpolants: a maximum entropy approach. *International Journal for Numerical Methods in Engineering* 2004; **61**(12):2159–2181.

[315] Rabczuk T, Song J, Belytschko T. Simulations of instability in dynamic fracture by the cracking particles method. *Engineering Fracture Mechanics* 2009; **76**(6):730–741.

[316] Maiti S, Geubelle PH. Cohesive modeling of fatigue crack retardation in polymers: crack closure effect. *Engineering Fracture Mechanics* 2006; **73**(1):22–41.

[317] Belytschko T, Chen H, Xu J, Zi G. Dynamic crack propagation based on loss of hyperbolicity and a new discontinuous enrichment. *International Journal for Numerical Methods in Engineering* 2003; **58**(12):1873–1905.

[318] Cecka C, Lew AJ, Darve E. Assembly of finite element methods on graphics processors. *International Journal for Numerical Methods in Engineering* 2011; **85**(5):640–669.

[319] Ullah Z, Coombs W, Augarde C. Parallel computations in nonlinear solid mechanics using adaptive finite element and meshless methods. *Engineering Computations* 2016; **33**(4):1161–1191.

[320] Arroyo M, Ortiz M. Local maximum-entropy approximation schemes: a seamless bridge between finite elements and meshfree methods. *International Journal for Numerical Methods in Engineering* 2006; **65**(13):2167–2202.

[321] Sukumar N, Wright R. Overview and construction of meshfree basis functions: from moving least squares to entropy approximants. *International Journal for Numerical Methods in Engineering* 2007; **70**(2):181–205.

[322] Peng X, Atroshchenko E, Kerfriden P, Bordas S. Isogeometric boundary element methods for three dimensional static fracture and fatigue crack growth. *Computer Methods in Applied Mechanics and Engineering* 2017; **316**:151–185.